DEVELOPMENTS OF THE ISOLDE RILIS FOR RADIOACTIVE ION BEAM PRODUCTION AND THE RESULTS OF THEIR APPLICATION IN THE STUDY OF EXOTIC MERCURY ISOTOPES

A thesis submitted to the University of Manchester
for the degree of Doctor of Philosophy
in the Faculty of Science and Engineering

2017

Thomas Day Goodacre
School of Physics and Astronomy

Contents

Word count 42184

List of Tables

List of Figures

The University of Manchester

Thomas Day Goodacre
Doctor of Philosophy
Developments of the ISOLDE RILIS for radioactive ion beam production and the results of their application in the study of exotic mercury isotopes
November 3, 2016

This work centres around development and applications of the Resonance Ionization Laser Ion Source (RILIS) of the ISOLDE radioactive ion beam facility based at CERN.

The RILIS applies step-wise resonance photo-ionization, to achieve an unparalleled degree of element selectivity, without compromising on ion source efficiency. Because of this, it has become the most commonly used ion source at ISOLDE, operating for up to 75% of ISOLDE experiments. In addition to its normal application as an ion source, the RILIS can be exploited as a spectroscopic tool for the study of nuclear ground state and isomer properties, by resolving the influence of nuclear parameters on the atomic energy levels of the ionization scheme. There are two avenues of development by which to widen the applicability of the RILIS: laser ionization scheme development, enabling new or more efficient laser ionized ion beams and the development of new laser-atom interaction regions. New ionization schemes for chromium, tellurium, germanium, mercury and radium have been determined. Additionally, for the first time, the anode cavity of the VADIS, ISOLDE's variant of the FEBIAD type arc discharge ion source was used as the laser-atom interaction region. A new element selective RILIS mode of operation was established, enabling the ISOLDE RILIS to be coupled with molten targets for the first time, increasing the flexibility of ISOLDE operation and opening a direction for future developments. This combined ion source was termed the VADLIS or Versatile Arc Discharge and Laser Ion Source.

A combination of the developments presented in this thesis: an improvement of the laser ionization efficiency and the ability to couple the RILIS with molten targets, satisfied the pre-requisites for the long-awaited extension of the laser spectroscopy studies of exotic mercury isotopes. A sudden onset of extreme shape staggering in the neutron deficient mercury isotopes was revealed by optical pumping and laser spectroscopy experiments at ISOLDE in the 1970s and 1980s, with measurements conducted down to ^{181}Hg. Despite this being one of the most remarkable examples of shape coexistence in the nuclear chart, in the intervening decades the cessation point of this odd-even staggering had yet to be unambiguously determined through measurements of nuclear ground state charge radii. This open question was successfully resolved using the ISOLDE RILIS for in-source resonance ionization spectroscopy. The experiment was performed as part of a large collaboration, using the Leuven Windmill system for α-detection; direct ion counting with the ISOLTRAP multi-reflection time-of-flight mass spectrometer (MR-ToF MS); and ion beam current measurements using the ISOLDE Faraday cups. The sensitivity of the technique enabled the measurements to be extended down to ^{177}Hg, providing a definitive answer, that the extreme shape staggering stops at ^{180}Hg.

In addition to extending the measurements at the neutron deficient end of the mercury isotope chain, the relative mean square charge radii of both ^{207}Hg and ^{208}Hg was determined. This extended the measurements beyond the N = 126 shell closure, enabling the characterization of the "kink" in the trend of the isotope shifts.

Declaration

No portion of the work referred to in the thesis has been submitted in support of an application for another degree or qualification of this or any other university or other institute of learning.

Copyright Statement

i. The author of this thesis (including any appendices and/or schedules to this thesis) owns certain copyright or related rights in it (the "Copyright") and s/he has given The University of Manchester certain rights to use such Copyright, including for administrative purposes.

ii. Copies of this thesis, either in full or in extracts and whether in hard or electronic copy, may be made **only** in accordance with the Copyright, Designs and Patents Act 1988 (as amended) and regulations issued under it or, where appropriate, in accordance with licensing agreements which the University has from time to time. This page must form part of any such copies made.

iii. The ownership of certain Copyright, patents, designs, trade marks and other intellectual property (the "Intellectual Property") and any reproductions of copyright works in the thesis, for example graphs and tables ("Reproductions"), which may be described in this thesis, may not be owned by the author and may be owned by third parties. Such Intellectual Property and Reproductions cannot and must not be made available for use without the prior written permission of the owner(s) of the relevant Intellectual Property and/or Reproductions.

iv. Further information on the conditions under which disclosure, publication and commercialisation of this thesis, the Copyright and any Intellectual Property and/or Reproductions described in it may take place is available in the University IP Policy (see http://documents.manchester.ac.uk/DocuInfo.aspx?DocID=487), in any relevant Thesis restriction declarations deposited in the University Library, The University Library's regulations (see http://www.manchester.ac.uk/library/aboutus/regulations) and in The University's Policy on Presentation of Theses.

Acknowledgements

There are a huge number of people who have been instrumental to the work presented in this thesis.

Starting closest to the work, I first have to thank Bruce for being a constant source of encouragement, support and enthusiasm as a supervisor. The ISOLDE RILIS team over the last four years (Valentin, Bruce, Sebastian, Ralf, Daniel, Christoph, Kati, Dima, Anatoly, Maxim, Pavel, Nobu, Julia, Annie, Sasha and Pierre) has been a fantastic place to work and learn, it's been a pleasure to get to know all you. Despite demanding requirements for on-line operation it feels like we have been able to achieve a lot. I have to additionally thank Anatoly for all of his help and assistance with the data analysis. To my supervisor Jon and co-supervisors Kieran and Thomas at Manchester, thank you for all of the advice, support and wine over the last few years. Finally a big thank you to the whole in-source RIS collaboration at ISOLDE, they've been great experiments to be involved in.

Closer to home, beginning in Geneva a massive thank you to Maria for putting up with the nights and weekends I've spent at CERN or on call, together with weeks of travelling. Additionally for the amount of time (and money) spent joining me in Geneva coffee shops during the "free" weekends! Moving further from CERN and Geneva, a huge thanks to my Mum for the unwavering support over the years. I've always had a home to go back to in Manchester, which has made life much easier when moving away as it's felt like I've never left. To my Nan, Uncle Howard and Auntie Sarah, thank you all for your help, understanding and short notice availability during my far too brief day trips to Oxford from Geneva. To all of the friends I've barely seen over the last couple of years, I look forward to seeing you soon!

Finally I've not forgotten the requirements of LA^{3}NET "this project has received funding through the European Union's Seventh Framework Programme for Research,

Technological Development and demonstration under Grant Agreement 289191". It was a lot more than just funding though, the people involved in LA^{3}NET and the opportunities provided by the Marie Curie Fellowship, made it an incredible three years.

Chapter 1

Introduction

Radioactive ion beam facilities have been described by colleagues in various ways: from "a playground for alchemists" to "exotic isotope factories". Fundamentally, they use nuclear reactions to create rare and short lived isotopes of elements: nuclei where the ratio of protons and neutrons result in an instability of the nucleus. As an example, the combination of 79 protons (Z) and 118 neutrons (N) results in a nucleus of $^{N+Z=197}$Au the stable isotope of gold. Adding or removing a neutron, results in $^{N+Z=198}$Au or $^{N+Z=196}$Au, still isotopes of gold but with half-lives of 2.69 days and 6.17 days respectively. Removing 26 neutrons results in a nucleus of $^{N+Z=171}$Au, a gold isotope with a half life of just 17 (+9-5) µs. Radioactive ion beam facilities provide scientists with the opportunity to conduct experiments on or with these exotic isotopes. Experiments range from the investigation of promising new cancer treatments [1] to nuclear astrophysics [2].

Lasers play an increasingly integral role at such facilities, both in the production of radioactive ion beams and the study of the exotic isotopes themselves. Considering light as packets of energy (photons), the colour of the light corresponds to the energy contained within the photon. One of the advantageous properties of lasers is their ability to produce monochromatic light or, equivalently, photons with a very narrow range of energies. Spectral absorption lines correspond to the excitation of an atomic electron and are unique to a particular element, a photon energy matching the excitation energy of the transition is required in order to induce the excitation. Thus, photons with a matching energy could be considered like a key to a lock, with a specific photon energy required to excite an atomic electron of a certain element. Lasers can therefore be used to target a specific atomic absorption line, promoting an electron to an excited energy level.

A commonly used laser-atom interaction region at radioactive ion beam facilities is a metal tube with an internal diameter of 3 mm. Taking typical parameters, laser light with an average power of 3 W, a wavelength of 580 nm and a spectral line width of 0.01 nm is directed into such a metal tube to target an atomic transition. The specific requirement of a laser for this role can be better understood by a comparison to sunlight. The spectral irradiance of the sun at sea level over this wavelength range is $\approx$1.1 Wm^{-2}nm^{-1} [3], or 39,000,000 times lower than the power of the laser over the 0.01 nm spectral range, directed into the metal tube.

It is possible to use multiple lasers to target a sequence of atomic lines, here the analogy shifts from that of a lock and a key, to a safe where a unique combination is required to unlock it. With a sufficient number of excitation steps, it is possible transfer enough energy to an atomic electron for it to break free of the Coulomb attraction of the nucleus, liberating it and transforming the atom into a charged particle (a singly charged ion). This method of ionization enables an element of interest to be selectively ionized, using the combination of excitation steps unique to it. The ions can then be extracted from the cloud of reaction products produced in the nuclear reactions at the radioactive ion beam facilities. The ionized particles can then be manipulated with electric and magnetic fields, to enable their transport to experimental set-ups and the experiments to take place.

Atomic transitions are, to a varying degree, sensitive to nuclear properties. Therefore the atomic excitations can also be used as probes to study the nucleus. By varying the energy of the photons used to target a particular atomic transition, it is possible to determine part-per-million shifts in the electronic energy levels, enabling attometer-scale fluctuations in the nuclear charge radius to be identified. Such laser spectroscopy techniques enable the evolution of ground state nuclear structure to be charted across the nuclear landscape.

1.1 Developments for the ISOLDE RILIS

There are two directions by which to expand the applicability of the RILIS: laser ionization scheme development enabling new or more efficient laser ionized ion beams, or the development of new laser-atom interaction regions. In this thesis, RILIS ionization schemes for tellurium and germanium (Section 7.1), chromium (Section 7.2), mercury (Section 7.3) and radium (Section 7.4) are presented. Additionally, the investigations and results from the coupling of the RILIS with the VADIS, ISOLDE's variant of the FEBIAD type arc discharge ion source are presented (Chapter 6). A new element selective RILIS mode of operation has been established, through off-line testing with gallium and barium and on-line experiments with mercury, cadmium and magnesium. This development enabled the ISOLDE RILIS to be coupled with molten targets for the first time, increased flexibility of ISOLDE operation and opened a direction for future developments.

1.2 In-source resonance ionization spectroscopy of mercury isotopes

In the field of nuclear structure physics, the neutron deficient lead region of the nuclear chart is renowned for shape coexistence [4]. It was first observed by Bonn et al. [5], as a strikingly large isotope shift in the nuclear mean square charge radius of ^{185}Hg, later determined to be an extreme odd-even staggering in the chain of isotopes starting from ^{186}Hg [6]. These discoveries led to an intense investigation of this region of the nuclear chart and remains the most pronounced example of this phenomena yet to be observed. Further optical pumping and laser spectroscopy experiments extended the measurements to span between ^{181}Hg and ^{206}Hg [7]. However, the cessation of the pronounced odd-even staggering had yet to be definitively determined.

The previous measurements of mercury charge radii are summarized in Chapter 8. The results, data extraction and analysis from the in-source resonance ionization spectroscopy experiment studying exotic mercury isotopes is presented in Chapter 9 and Appendix A. Finally the results of charge radii measurements of the neutron deficient and neutron rich mercury isotopes are discussed in Chapters 10 and 11 respectively.

1.3 Format and contributions

The work presented here is in the form of an alternative format thesis, therefore a portion of the work is included in the format of journal articles, while the remainder is presented in a conventional thesis format. The majority of the VADLIS characterization and developments are included in their published format in Section 6.1, with additional work and discussions in Sections 6.2 to 6.5. The ionization scheme development work is presented in both a publication format (tellurium and germanium in Section 7.1, chromium in Section 7.2, mercury and tellurium in Section 7.3) and in a standard thesis format (radium in Section 7.4). The in-source resonance ionization spectroscopy results and analysis from the study of exotic mercury isotopes are presented in a conventional thesis format (Chapters 8 to 11 and Appendix A).

As required by the alternative format thesis, my contribution to the work presented in publication form and the work of my co-authors is detailed below.

1.3.1 Paper I: Blurring the boundaries between ion sources: the application of the RILIS inside a FEBIAD type ion source at ISOLDE

Author list: T. Day Goodacre[1], J. Billowes[2], R. Catherall[3], T. E. Cocolios[2], B. Crepieux[3], D. Fedorov[1], V.N. Fedosseev[1], L.P. Gaffney[2], T. Giles[3], A. Gottberg[3], K.M. Lynch[2], B.A. Marsh[1], T.M. Mendonca[3], J.P. Ramos[3], R.E. Rossel[1], S. Rothe[1], S. Sels[2], C. Sotty[4], T. Stora[3], C. Van Beveren[2], M. Veinhard[1].

Author list composition and contribution: The author list includes myself as first author, members of the ISOLDE RILIS team, members of the in-source spectroscopy collaboration, members of the ISOLDE target team and the ISOLDE collaboration. The contributions were as follows:

[1] Laser set-up and operation, VADIS set-up and operation, discussion and interpretation of results.

[2] Planning, installation and operation of the decay spectroscopy apparatus.

[3] Production and operation of the VADIS ion sources, discussion of results.

[4] Beam tuning at ISOLDE.

Personal contribution

Off-line results As part of the RILIS team I worked on re-establishing the set-up for ion source development at the ISOLDE off-line separator and conducted the ion source tests. Following the measurements, I was responsible for both the extraction, collation and analysis of the data and the interpretation and presentation of the results.

On-line results: I planned the on-line RILIS test programme for mercury, including the laser set-up and the extrapolation of the isotope shift of ^{178}Hg to estimate the location of the resonance. I worked with other members of the RILIS team and the in-source spectroscopy collaboration to perform a verification "scan" of ^{178}Hg using an α-decay spectroscopy station for detection.

1.3.2 Paper II: Laser resonance ionization scheme development for tellurium and germanium at the dual Ti:Sa-Dye ISOLDE RILIS

Author list: T. Day Goodacre, D. Fedorov, V.N. Fedosseev, L. Forster, B.A. Marsh, R.E. Rossel, S. Rothe, M. Veinhard.

Author list composition and contribution: The author list includes myself as first author and the other members of the ISOLDE RILIS team at the time of the experiment as co-authors. The co-authors were involved in the set-up, data taking and the discussion of the results.

Personal contribution I planned and co-ordinated the RILIS ionization scheme development programme for tellurium and germanium, including the identification of potentially suitable atomic resonances listed in literature. I worked as part of the RILIS team to prepare the RILIS laser set-up and perform investigatory laser scans to identify suitable resonances of tellurium and germanium and efficiency measurements of the optimal germanium ionization scheme. Following the measurements, I was responsible for both the extraction, collation and analysis of the data and the interpretation and presentation of the results.

1.3.3 Paper III: The identification of autoionizing states of atomic chromium for resonance laser photo-ionization at the ISOLDE-RILIS

Author list: T. Day Goodacre, K. Chrysalidis, D.V. Fedorov, V.N. Fedosseev, B.A. Marsh, P.L. Molkanov, R.E. Rossel, S. Rothe, C. Seiffert.

Author list composition and contribution: The author list includes myself as first author and the other members of the ISOLDE RILIS team at the time of the experiment as co-authors. The co-authors were involved in the set-up, data taking and the discussion of the results.

Personal contribution I planned and co-ordinated the RILIS ionization scheme development programme for chromium, including the identification of potentially suitable atomic resonances listed in literature. I then worked as part of the RILIS team to prepare the laser set-up and perform investigatory laser scans to identify suitable resonances of chromium. Following the measurements, I was responsible for both the extraction, collation and analysis of the data and the interpretation and presentation of the results.

1.3.4 Paper IV: RILIS ionized mercury and tellurium beams at ISOLDE CERN

Author list: T. Day Goodacre, J. Billowes, D.V. Fedorov, V.N. Fedosseev, B.A. Marsh, P.L. Molkanov, R.E. Rossel, S. Rothe, K.D.A Wendt.

Author list composition and contribution: The author list includes myself as first author, the other members of the ISOLDE RILIS team at the time of the experiment and academic supervisors as co-authors. The co-authors were involved in the set-up, data taking and the discussion of the results.

Personal contribution I planned and co-ordinated the RILIS ionization scheme development programme for mercury, including the identification of potentially suitable atomic resonances listed in literature. I then worked as part of the RILIS team to prepare the laser set-up and perform investigatory laser scans to identify suitable resonances of mercury and efficiency measurements of the optimal mercury and tellurium ionization schemes. Following the measurements, I was responsible for both the extraction, collation and analysis of the data and the interpretation and presentation of the results.

Chapter 2

A theoretical understanding of nuclear structure

Nuclear models seek to explain and predict the structure and behaviour of nuclei. For heavier nuclei where ab initio calculations are not currently possible due to the computing power required, this is attempted via collective or single particle nuclear models and hybrids of the two. Collective models such as the liquid drop model focus on the structure and symmetries of the macroscopic nuclear system. Refinements and updates of the liquid drop model have been implemented in order to better reproduce specific behaviour observed experimentally. Single particle models such as the shell model are well suited to describing nuclei near shell closures and for nuclei below A $\approx$ 80, beyond this the number of valence nucleons makes single particle model calculations challenging. A truncation of the shell model space is required in order to enable such calculations, this technique is employed in models such as the interacting boson model IBM.

This chapter is largely based on the text books of K.S. Krane [8], R. Casten [9], B.R. Martin [10] and B. Povh et al. [11] and the review article of K. Heyde and J. Wood [4]. Additional sources are referenced within the text.

2.1 Liquid drop type models

The liquid drop model is a macroscopic model that takes a global view of the nucleus, modelling it as a quantum fluid composed of nucleons that interact with each other resulting in collective effects. Considering the nuclear force, there are a number of similarities between the nucleus and a liquid drop. The volume of a liquid drop is proportional to the number of its constituent molecules and there are no long range interactions between the molecules, thus each molecule interacts only with its neighbours. The liquid drop model was first proposed by G. Gamow [12], with the nuclear radius R equal to

$$R = R_0 A^{1/3}, \tag{2.1}$$

where R_0 is a constant ≈ 1.2 fm and A is the number of nucleons. The liquid drop model was further developed by C.F. von Weizsacker [13] in the 1930s, resulting in the semi empirical mass formula. This models the binding energy $B.E.$ of a nucleus and considers five contributions

$$B.E. = a_V A - a_S A^{2/3} - a_C \frac{Z^2}{A^{1/3}} - a_A \frac{(A-2Z)^2}{A} \pm \delta(A,Z). \tag{2.2}$$

The volume term ($a_V A$) and the surface term ($a_S A^{2/3}$) take into account the effect of the strong nuclear force within the nucleus and at the surface of the nucleus respectively, the Coulomb term ($a_C \frac{Z^2}{A^{1/3}}$) accounts for proton-proton repulsion, the asymmetry term ($a_A \frac{(A-2Z)^2}{A}$) takes into account the Pauli exclusion principle and favours a more equal number of protons and neutrons, finally the pairing term ($\delta(A,Z)$) accounts for the pairing of like nucleons. The volume term contributes towards the binding energy, while the surface, Coulomb and asymmetry terms contribute towards a reduction in the total binding energy. The pairing term can increase or decrease the binding energy for even-even and odd-odd nuclei respectively.

The strength of the liquid drop model is its ability to reproduce global trends in the binding energy per nucleon of the majority of stable nuclei. However, it is unable to reproduce deviations from the nuclear radius $r \propto A^{\frac{1}{3}}$ and phenomena such as asymmetric fission and nuclear magic numbers.

The liquid drop model was updated by W.D. Myers and W.J Swiatecki [14, 15, 16] to include non-uniform proton and neutron densities in addition to higher order terms and renamed the droplet model. This model includes an additional term $\bar{\varepsilon}$ made up of a number of empirically determined coefficients, included as

$$R = R_0 A^{1/3}(1+\bar{\varepsilon}). \tag{2.3}$$

The empirical coefficients were updated by D. Berdichevsky and F. Tondeur in 1985, to better agree with experimentally determined isotope shifts [17]. Further updates resulted in the finite range liquid drop model FRLDM and the finite range droplet model FRDM, which have themselves been further refined [18]. These later models represent a macroscopic-microscopic approach, well suited to the modelling of deformed nuclear ground states in the heavier region of the nuclear chart.

2.2 The shell model

The shell model considers independent nucleons in an attractive potential, which can be deduced from experimental data. The Woods-Saxon potential $V_{WS}(r)$ is commonly used [19] and can be expressed as

$$V_{WS}(r) = \frac{V_0}{1+e^{(r-r_0)/a}}, \tag{2.4}$$

where V_0, r_0 and a are constants with r_0 related to the nuclear size and a determining the diffuseness at the nuclear surface. The inclusion of a term for the spin orbit-interaction was proposed by M.G. Mayer and J.H.D. Jensen [20, 21], resulting in a potential $V(r)$

$$V(r) = \frac{V_0}{1+e^{(r-r_0)/a}} + V_{ls}(r)(\mathbf{l}\cdot\mathbf{s}), \tag{2.5}$$

where $\mathbf{l}$ and $\mathbf{s}$ are the orbital and spin angular momentum operators for a single nucleon.

Experimental results indicate an increased stability of nuclei with N or Z = 2, 8, 20, 28, 50, 82, 126 the “magic numbers”. These magic numbers are reproduced as successive shell gaps by solving the many body Schrödinger equation, including the potential $V_{ls}(r)$ [22]. The shell model considers filled shells as an inert core, with the properties of the nucleus determined by the unpaired valence nucleons. The consequence of considering independent particles in the manner of the shell model is that collective excitations are neglected. Using a modified Woods-Saxon or Nilsson potential, the deformed shell model considers independent particles moving in a deformed potential and enables the interpretation of collective excitations [23, 24].

2.3 The interacting boson model (IBM)

The interacting boson model (IBM), also known as the interacting boson approximation (IBA), is based on the shell model and was developed to model nuclei far from shell closures [25, 26]. The IBM achieves this by truncating the shell model space, vastly reducing the number of potential configurations.

2.4 Mean field theory

In the mean field approach, the nucleons are considered as independent particles interacting with a mean field created by the other nucleons. That is approximated by the Hartree-Fock (Bogoliubov) method and updated at each iteration until a minimal energy is reached. Thus unlike the shell model, there is no inert core. The effective nucleon-nucleon force is tuned to describe the properties of the nuclei and the interactions are included in the Hamiltonian as simplified parametrizations. In relativistic mean field theory the same approach is followed, but the nucleon-nucleon interactions occur via the exchange of mesons.

2.5 Shape coexistence

Shape coexistence occurs for a given isotope when there is a nucleon configuration (or in the case of ^{186}Pb two [27]) corresponding to a different nuclear shape “coexisting” within a few MeV of the nuclear ground state. The origin of shape coexistence studies in nuclear physics is identified by [28] to be a 1956 paper by H. Morinaga on the first excited state of ^{16}O [29].

One of the most striking examples of shape coexistence is that of the neutron deficient mercury isotopes. A combination of shell effects and residual nucleon-nucleon interactions result in dramatic shifts from a weakly deformed oblate ground state for the even isotopes, to a strongly deformed prolate ground state of the odd isotopes [5, 6]. This shape staggering is observable as pronounced isotope shifts between odd and even isotopes with reducing N from A = 186.

From a shell model interpretation, the shape coexistence in neutron deficient mercury is understood to be the result of an intruder band built on the excitation of two protons (p) from the zero proton two hole (h) proton configuration across the Z = 82 shell gap [30]. The excitation of the two protons is in turn the result of the increasing number of valence neutrons when moving further from the N = 126 neutron shell closure. The competing proton configurations are depicted graphically in Figure 2.1 for ^{185g}Hg and ^{185m}Hg.

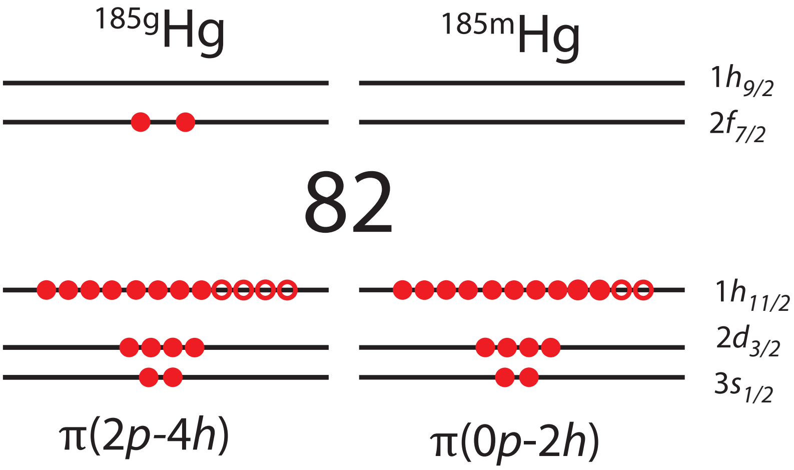

Figure 2.1: The proton configurations of the ground state and the isomer of ^{185}Hg based on the spherical shell model, level ordering from [9].

Intruder states in the lead region, such as the proton intruder state depicted in Figure 2.1, can be attributed to the attraction between protons and neutrons. In what could be considered to be the neutron midshell region around N = 104, the numerous valence neutrons are sufficient to excite a pair of protons across the shell gap. In the case of mercury there are therefore two competing proton configurations, one due to the near closed proton shell ($\pi(0p - 2h)$) and the other related to the open neutron shell around N = 104 ($\pi(2p - 4h)$).

Chapter 3

Nuclear characteristics in the optical spectrum

The charge radii and moments of the nucleus affect the energy levels of the atomic electrons, consequently information on the structure of the nucleus can be extracted from the study of these atomic energy levels. One method for such investigations is the study of atomic transitions which can be resonantly driven by laser light.

Unless otherwise stated, the following sections are predominantly based on the textbook of W.H. King [31] and the topical reviews of E.W. Otten [32], J. Billowes and P. Campbell [33], B. Cheal and K.T. Flanagan [34], B. Cheal, T.E. Cocolios, and S. Fritzsche [35] and P. Campbell, I.D. Moore and M.R. Pearson [36].

3.1 The isotope shift

There is a shift in the energy of the atomic fine structure levels between two isotopes of the same element. Considering isotopes A and A', the corresponding shift δ in the transition frequency ν from the atomic ground state can be written as

$$\delta\nu^{A,A'} = \nu^{A'} - \nu^{A}. \tag{3.1}$$

The isotope shift $\delta\nu^{A,A'}$ is a result of the change in the mass of the nuclei (mass shift $\nu_{MS}^{A,A'}$) and the change in the nuclear charge distribution (field shift $\nu_{FS}^{A,A'}$) between the two nuclei. It can therefore be approximated as arising from two distinct components

$$\delta\nu^{A,A'} = \nu_{MS}^{A,A'} + \nu_{FS}^{A,A'}. \tag{3.2}$$

The field shift contains the information on the nuclear charge distribution, however, both components of the isotope shift must be evaluated to enable information on the nuclear charge distribution to be extracted.

3.1.1 The mass shift

The angular momentum of an atomic level is fixed, thus a variation in the mass of a nucleus results in a change in the energy of the atomic energy level. This then corresponds to a variation in the transition frequency ν from the atomic ground state. $\nu_{MS}^{A,A'}$ is additionally separable into two components. The Normal Mass Shift (NMS) accounts for a change in the reduced mass correction, related to the finite mass of the nucleus and the Specific Mass Shift (SMS) accounts for changes in electron-electron correlations. $\nu_{MS}^{A,A'}$ can then be written as

$$\nu_{MS}^{A,A'} = (N+S)\frac{m^{A'} - m^{A}}{m^{A'}m^{A}}, \tag{3.3}$$

where N and S are constants related to the NMS and SMS respectively, m^A is the mass of isotope A and $m^{A'}$ is the mass of isotope A'. N is calculable, while S requires theoretical models or calibration using non-optical experimental data. From Equation 3.3, it can be seen that the magnitude of the mass shift has a $1/A^2$ dependence. Consequently, the contribution of $\nu_{MS}^{A,A'}$ to the total isotope shift decreases rapidly with increasing A.

3.1.2 The field shift

The electron wave function $\psi_e(r)$ overlaps with the nucleus, resulting in a sensitivity to changes in the nuclear charge distribution. Between isotopes of the same element, this manifests as the field shift $\nu_{FS}^{A,A'}$. The evaluation of $\nu_{FS}^{A,A'}$ can therefore enable nuclear structure investigations via the study of atomic energy levels. The field shift can be expressed as

$$\nu_{FS}^{A,A'} = \frac{Ze^2}{6h\epsilon_0}\Delta|\psi_e(0)|^2\delta\langle r^2\rangle^{A,A'}, \tag{3.4}$$

where Z is the number of protons, e is the magnitude of the elementary charge, h is the Planck constant, ϵ_0 is the permittivity of free space, $\Delta|\psi_e(0)|^2$ is the change in the electron density at the nucleus between the two atomic energy levels and $\delta\langle r^2\rangle^{A,A'}$ is the variation in the mean square charge radii between isotopes A and A'. For heavier nuclei, the approximation of a constant $\Delta|\psi_e(0)|^2$ across the nuclear volume becomes less reasonable. Equation 3.4 is then typically replaced by

$$\nu_{FS}^{A,A'} = F\lambda^{A,A'}, \tag{3.5}$$

where F is the electronic factor, a constant that is proportional to the change in electron density at the nucleus between the atomic energy levels and $\lambda^{A,A'}$ is the Seltzer moment [37] which can be approximated as

$$\lambda^{A,A'} = k\langle r^2\rangle^{A,A'}, \tag{3.6}$$

where k is a calculable constant. The variation in charge radii between isotopes A and A' can be compared to the expected variation from a spherical nucleus with an equal volume. To a second order approximation, $\langle r^2\rangle^{A,A'}$ can be expressed as

$$\langle r^2\rangle^{A,A'} = \langle r^2\rangle_0^{A,A'} + \langle r^2\rangle_0\frac{5}{4\pi}\delta\langle\beta_2^2\rangle^{A,A'}, \tag{3.7}$$

where $\langle r^2\rangle_0$ is the mean square charge radius of the spherical nucleus calculated using Equation 2.3 and $\delta\langle\beta_2^2\rangle^{A,A'}$ is the change in the mean square quadrupole deformation parameter between the two states. The determination of $\delta\langle\beta_2^2\rangle^{A,A'}$ offers the possibility of model independent determinations of changes in the shape of the nucleus as discussed in Section 2.5.

3.1.3 Isomer shifts

Isomer shifts are shifts in the atomic fine structure energy level between nuclear ground and isomeric excited states of the same isotope and can be expressed as $\delta\nu^{A^{g,m}}$. In the same manner as described in Section 3.1, the study of $\delta\nu^{A^{g,m}}$ enables the comparison of $\langle\beta_2^2\rangle$, which in turn enables the determination of the magnitude of nuclear shape changes between the ground state and the isomer. There is no mass shift component to the isomer shift, this is particularly relevant to the light region of the nuclear chart where the mass shift is dominant.

3.2 Atomic hyperfine structure

In addition to isotope shifts of the atomic fine structure levels, the nucleus can also induce a splitting of the atomic fine structure levels themselves, resulting in a hyperfine structure (HFS). The difference in the radius of the nucleus compared to that of the atom, results in only the electric monopole, magnetic dipole and electric quadrupole interactions being relevant to the HFS. The nucleus can only have even moments (M1, E2 etc.), because the nuclear wave function has good parity. Thus it is only those moments that contribute to the HFS. The isotope shift is determined from the substate weighted centroid of the hyperfine multiplet.

3.2.1 The magnetic dipole moment

Nuclei with a non-zero spin (I) have magnetic dipole moment μ_I. The nuclear magnetic moment interacts with the magnetic field of the orbiting electrons, lifting the degeneracy of the magnetic substates of the atomic level (when the total atomic angular momentum $J \neq 0$). The coupling of the atomic angular momentum and nuclear spin means a new quantum number is required. Thus, the states of the hyperfine multiplet are labelled with the total angular momentum quantum number $\boldsymbol{F} = \boldsymbol{I} + \boldsymbol{J}$. F can take values of

$$|I - J| \leqslant F \leqslant |I + J|. \tag{3.8}$$

The magnetic dipole moment shifts the F states from the fine structure energy by ΔE_A, which can be expressed as

$$\Delta E_A = \frac{A}{2}(F(F+1) - I(I+1) - J(J+1)), \tag{3.9}$$

where A is the hyperfine A factor. Equation 3.9 can be reduced to

$$\Delta E_A = \frac{AK}{2}, \tag{3.10}$$

where $K = (F(F+1) - I(I+1) - J(J+1))$. A is related to μ_I as

$$A = \frac{\mu_I B_J}{IJ}, \tag{3.11}$$

where B_J is the magnetic field produced by the electrons at the site of the nucleus.

3.2.2 The electric quadrupole moment

The contribution of an electric quadrupole moment to the hyperfine atomic structure is the result of an interaction between the average electric field gradient V_{JJ} of the atomic electrons at the site of the nucleus and non-spherical nuclear charge distributions. The electric quadrupole moment results in a perturbation of the HFS ΔE_B, where

$$\Delta E_B = B\frac{\frac{3}{4}K(K+1) - I(I+1)J(J+1)}{2(2I-1)(2J-1)IJ}, \tag{3.12}$$

where B is the hyperfine B factor. B is related to the spectroscopic quadrupole moment Q_s as

$$B = eQ_sV_{JJ}. \tag{3.13}$$

3.2.3 The hyperfine structure in an atomic line

The presence of HFS in an atomic fine structure transition can include contributions from the hyperfine splitting of both the upper and lower atomic energy levels. The total splitting of each level (ΔE_{HFS}) combines Equations 3.10 and 3.12, resulting in

$$\Delta E_{HFS} = \Delta E_A + \Delta E_B. \tag{3.14}$$

The expected structure for the 254 nm $5d^{10}6s^2\ {}^1S_0 \rightarrow 5d^{10}6s6p\ {}^3P_1^\circ$ transition in atomic ^{185g,m}Hg is presented in Figure 3.1.

The isotope shift $\delta\nu^{198,185}$ was unexpectedly small and the isomer shift of $\delta\nu^{185^{gm}}$ was unexpectedly large when first observed [5, 38]. The history of these measurements is discussed in Section 8.2. The ground state of atomic mercury has $J = 0$ thus, there is no hyperfine splitting. The hyperfine splitting of the $5d^{10}6s6p\ {}^3P_1^\circ$ excited atomic energy level of ^{185g}Hg is the result of the magnetic dipole moment. There is no contribution due to a spectroscopic quadrupole moment because the nuclear ground

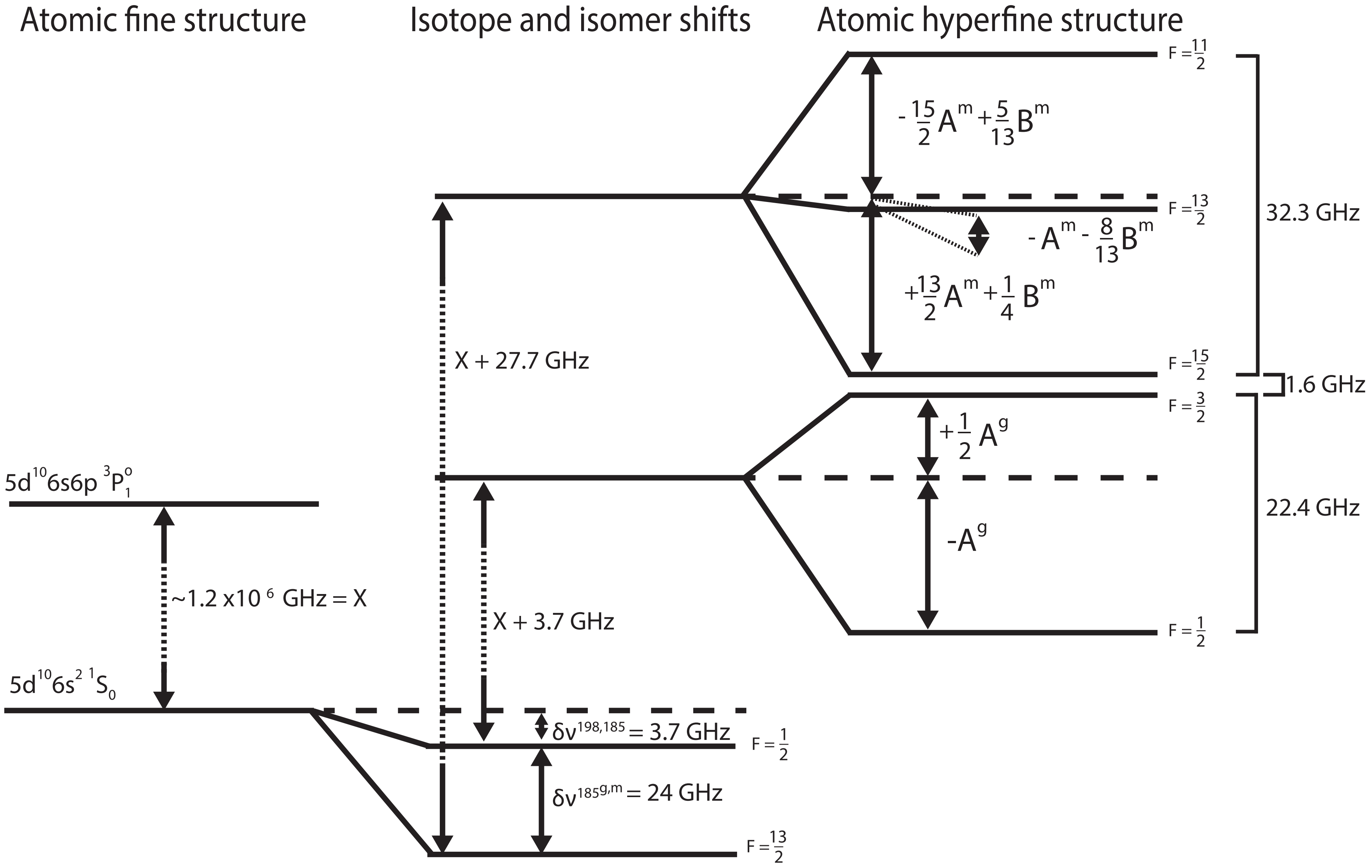

Figure 3.1: The hyperfine structure of 185Hg^{g,m}, the isotope shift $\delta\nu^{198,185}$ and the isomer shift $\delta\nu^{185g,m}$ are presented. Values for the hyperfine A and B factors were taken from [7] with an A factor of 14.96 GHz for the ground state of the nucleus and hyperfine A and B factors of -2.305 GHz and -0.14 GHz respectively for the isomeric state of the nucleus. The atomic ground state is depicted as fixed at an energy of 0 for convenience.

state has spin $I = 1/2$. In accordance with Equation 3.8, the hyperfine splitting results in two unique F levels. The hyperfine splitting of the $5d^{10}6s6p\ {}^3P_1^\circ$ excited state of ^{185m}Hg, is due to both the magnetic dipole and electric quadrupole moments, it has three components as from Equation 3.8 there are three unique F levels. It can also be observed that the magnetic dipole moment makes the dominant contribution to the hyperfine splitting of the ^{185m}Hg $5d^{10}6s6p\ {}^3P_1^\circ$ excited state.

Chapter 4

Resonance ionization spectroscopy for nuclear physics

4.1 Resonance ionization spectroscopy

The first multi-step selective photoionization was reported in 1971 by Ambartsumyan (Ambartzumian) et al. [39, 40], using ruby laser pumped tunable dye lasers. Advances in laser technology have enabled the now widespread application of the technique, two examples of which are outlined in Sections 4.2.1 and 4.2.2. Resonance ionization spectroscopy (RIS) is extensively explored in the book of V.S. Letokov [41]. Unless otherwise stated, this Section is predominantly based on that work.

RIS relies on two principles: for a particular element, the distribution of the atomic energy levels is unique and electronic transitions between energy levels can be induced if the atom is illuminated with photons matching the excitation energy. Photons from multiple lasers are typically used to stepwise excite and then liberate a valence electron from the element of interest. The selectivity of the ionization process is a direct consequence of the excitation of valence electrons via element-unique atomic transitions.

In order to maximize the ionization efficiency, the atomic transitions should be saturated. The energy flux required to saturate the transition between states a and b by optical illumination (Φ_{ab}) can be expressed as

$$\Phi_{ab} = \Phi_s^{ab} \frac{\Delta\omega_L^{ab}}{\Delta\omega_t^{ab}}, \tag{4.1}$$

where Φ_s^{ab} is the required saturation energy flux of the transition itself, $\Delta\omega_L^{ab}$ is the spectral linewidth of the laser driving the transition and $\Delta\omega_t^{ab}$ is the spectral width of the transition between states a and b in the laser atom interaction region. $\Delta\omega_t^{ab}$ is sensitive to the temperature and pressure of the laser-atom interaction region. A complete spectral coverage of the available atoms $\Delta\omega_L^{ab} \geq \Delta\omega_t^{ab}$ is required in order to maximize the efficiency of a resonant excitation. From Equation 4.1 however, it also follows that Φ_{ab} increases with increasing laser linewidth. Φ_s^{ab} depends on multiple factors and can be defined as

$$\Phi_s^{ab} = \frac{\hbar\omega_{ab}}{2\sigma_{ab}}, \tag{4.2}$$

where $\hbar$ is the reduced Planck constant, ω_{ab} is the frequency of the laser light and σ_{ab} is the cross-section of the atomic transition. Based on Equation 4.2, it can be seen that the larger the σ_{ab} of a transition, the less laser power is required to achieve saturation. σ_{ab} is determined by parameters related to both the incident photons and the atomic transition, it can be expressed as

$$\sigma_{ab} = \frac{g_a}{g_b} \frac{\lambda_{ab}^2}{2\pi} \frac{A_{ba}}{\Delta\omega_t^{ab}}, \tag{4.3}$$

where g_a and g_b are the degeneracy of the levels a and b respectively, λ_{ab}^2 is the wavelength of the illuminating laser and A_{ba} is the Einstein A coefficient. Considering atomic transitions in the same environment, variations in σ_{ab} are dominated by changes in A_{ba}, which can differ by up to seven orders of magnitude between reported optical transitions. For optical spectroscopy experiments, the saturation of the spectroscopic transition is avoided as it results in a broadening of the resonance.

The methods of ionization typically applied for RIS are summarized in Figure 4.1. ω_1 represents the laser frequency required to reach the ionization potential (IP) of the element of interest. The combination of $\omega 2$ and $\omega 3$ represents resonance ionization

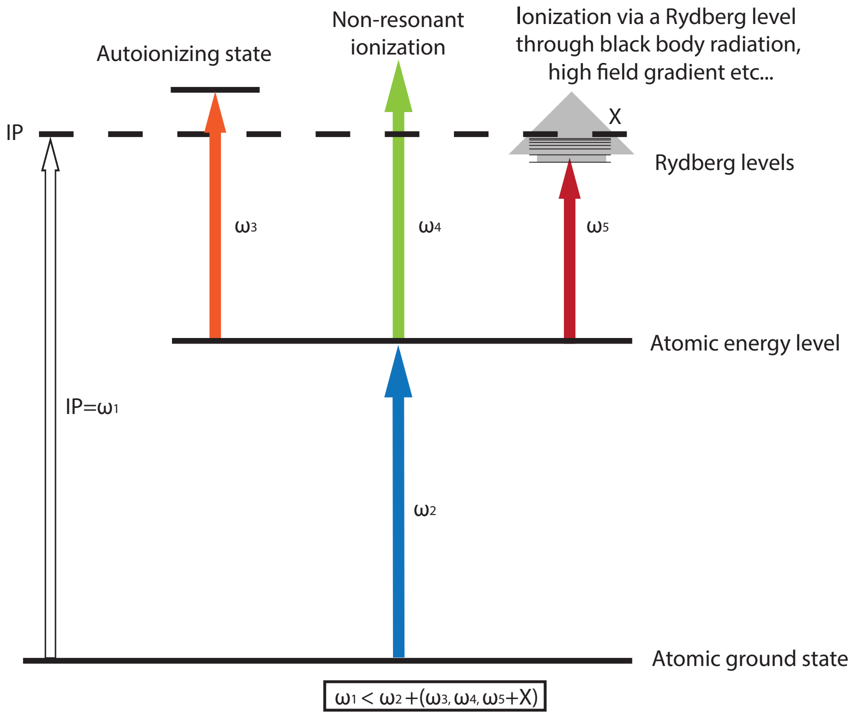

Figure 4.1: The principle of multi-step resonance photo-ionization. The photon energy required for each of the transitions is depicted as ω_x. More than one photon (ω_2 - ω_5) is required to excite a valence electron above the ionization potential (IP) = ω_1.

via an autoionizing state, which involves the excitation of two valence electrons, with a combined excitation energy above the first ionization potential of the element. In addition to a radiative decay of this doubly excited atomic state, it is possible for one of the excited electrons to transfer its energy to the other due to the Coulomb interaction between them, resulting in ionization [42]. Ionization via an autoionizing state is typically the most efficient method of resonance ionization, as the final step is a resonant transition. Consequently there is a greater chance of saturating it with the available laser power. The photo-absorption cross-section for resonant transitions in the "hot cavity" surface ion source environment, referred to here after as the hot cavity and discussed in Sections 4.2 and 5.2.1, can be up to 10^{-11} cm^{-2}. This is six to eight orders of magnitude larger than the photo-absorption cross-section for non-resonant ionization to the continuum in this environment, represented as the combination of $\omega 2$ and $\omega 4$ in Figure 4.1. Ionization can also be achieved via a resonant excitation to a Rydberg level (represented by the combination of $\omega 2$ and $\omega 5$ in Figure 4.1) lying of the order of meVs below the ionization potential. Ionization from Rydberg levels is achieved passively via external factors (X) including: black body radiation from the walls of the hot cavity, the effects of the extraction field gradient or collision with other particles in the atomic vapour. The final laser step in such schemes is a resonant transition, therefore despite the requirement of an additional ionizing contribution, the ionization efficiency can in some cases exceed that of a non-resonant transition to the continuum (depending on the available laser power).

4.2 Radioactive ion beam production

RIS was first proposed as a method of on-line radioactive ion beam production at the "On-line in 1985 and beyond - a workshop on the ISOLDE programme" event [43]. The technique was demonstrated at the Leningrad Nuclear Physics Institute (now PNPI) in 1988 [44] and at ISOLDE in 1990 [45]. Once established, the experimental set-ups were named Resonance Ionization Laser Ion Sources (RILIS). The technique involves multiple laser beams being directed into a heated metal tube (hot cavity), that is connected to the target where the reaction products are produced. The wider application of RILIS' for radioactive ion beam production was recently summarized in [46], including the combination with gas cells/catchers. This section will only consider hot cavity RILIS (HC-RILIS), as this is the principal method of application discussed in this work.

4.2.1 Ion beam production

The hot cavity, a resistively heated refractory metal tube, provides a defined laser-atom interaction region: confining the reaction products following effusion from the target container via a transfer line. It is typically heated to ∼2000°C, to minimize the wall sticking times of reaction products during their effusion and aid ion survival and extraction. This is discussed in more detail in Section 5.2.1. The simplicity of the structure is of particular value for use at radioactive ion beam facilities, where access to the target/ion source for maintenance is typically restricted following operation due to radiation protection concerns. The selectivity of the HC-RILIS can be compromised by competing surface ionization processes (also discussed in Section 5.2.1). This can pose a significant problem for certain experiments, particularly if surface ionized contaminants have production yields several orders of magnitude higher than the isotope of interest. To address this, alternative laser-atom interaction regions have been developed for specific cases, these are discussed in Chapters 5 and 6.

4.2.2 In-source resonance ionization spectroscopy

In addition offering an element selective method of ionization, the use of resonant atomic transitions results in a sensitivity of the process to the nuclear observables discussed in Chapter 3. Atomic s $\leftrightarrow$ p transitions are typically used as the spectroscopic transition, because the wave functions of s electrons have the largest overlap with the nucleus. The efficiency of the ionization process and therefore the ion rate are directly related to the matching of the photon energy of the laser light with the atomic resonances. This enables the isotope shifts and hyperfine splitting of the atomic lines to be investigated.

In-source RIS is typically applied on an atomic vapour in a hot cavity environment, resulting in a limitation of the achievable precision of the measurements due to the Doppler broadening ($\Delta\omega_D$) of the atomic lines. This can be calculated as

$$\Delta\omega_D = 7.16 \times 10^{-7}\omega_0(T/M)^{1/2}, \tag{4.4}$$

where ω_0 is the frequency of the atomic resonance, T is the temperature and M is the atomic mass [42, 47]. In the hot cavity environment, it is the frequency corresponding to the atomic resonance and the mass that are the dominant factors in variations of $\Delta\omega_D$. At ISOLDE, the RILIS laser wavelength coverage is between 210-950 nm and its application has ranged from lithium (Z = 3) to radium (Z = 88). By comparison, changes in the temperature of the hot cavity are small: unlikely to vary outside the range of 2000-2400 K. The influence of these parameters is depicted in Figure 4.2a, together with the contributions to the isotope shift from the mass and field shift (discussed in Section 3.1) in Figure 4.2b.

Based on Figure 4.2a and b, it is clear that in-source RIS is most applicable in the heavier region of the nuclear chart, where the resonances are less affected by Doppler broadening and the field shift component of the isotope shift dominates the mass shift. The decrease in the mass shift with increasing atomic number can be understood from Equation 3.3, where the mass shift can be seen to vary as $1/A^2$. The field shift by comparison varies as $Z^2/A^{\frac{1}{3}}$ [32, 48], with a relativistic correction described by [49].

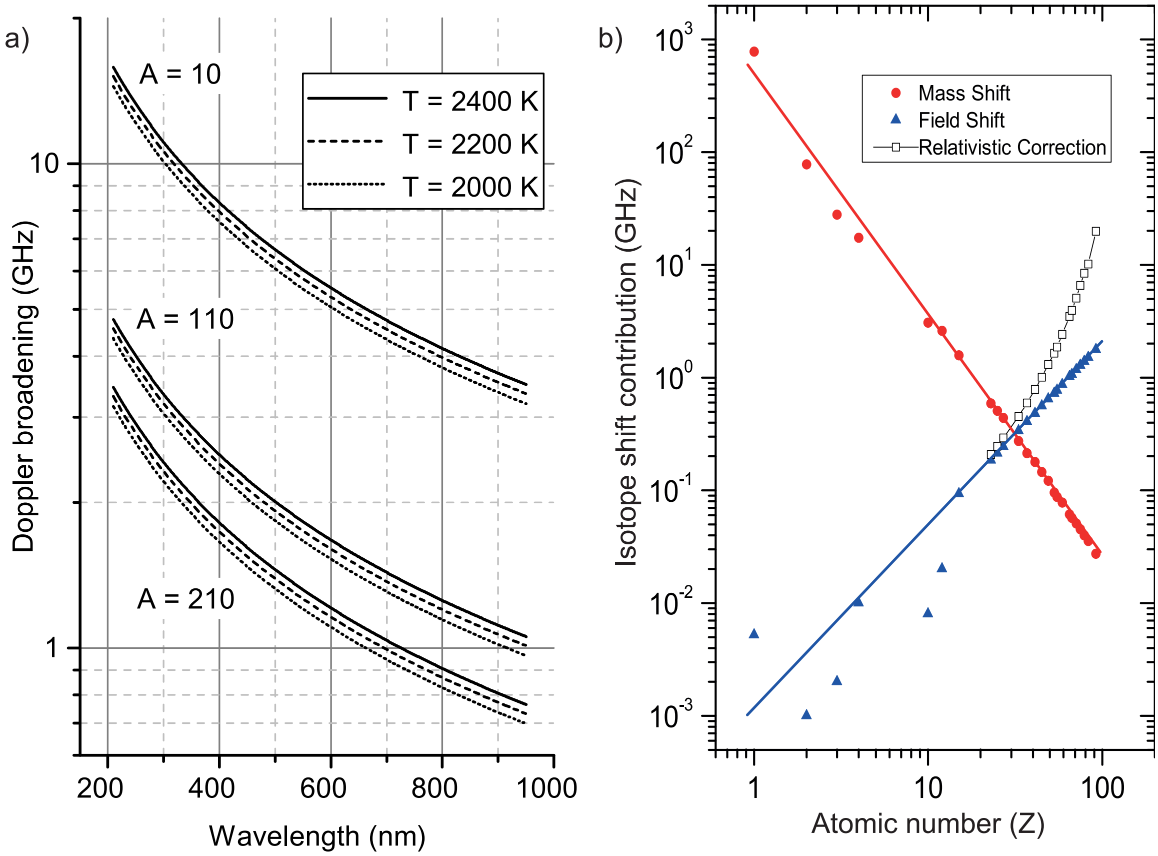

Figure 4.2: a) The variation in Doppler broadening for mass (A), temperature (K) and wavelength (nm), calculated from Equation 4.4, b) variation in the contribution to the isotope shift with atomic number (Z). Figure b) taken from [48], © for The Royal Swedish Academy of Sciences. Reproduced by permission of IOP Publishing. All rights reserved.

Alternative techniques such as collinear laser spectroscopy or laser spectroscopy on trapped ions (summarised in [36]) offer the possibility of achieving a spectral resolution limited by the natural linewidth of the transition. Therefore when feasible, such techniques offer a significantly higher precision than in-source RIS and are applicable across the nuclear chart. The strength of the in-source RIS technique is its sensitivity. Taking ISOLDE as an example, the isotope with the lowest yield measured by in-source RIS was ^{191}Po, with a rate of 0.01 ions/s on resonance [50], compared to the current reported record for collinear laser spectroscopy of ∼100 ions/s [51]. The improving stability, both of the lasers and the experimental set-ups, combined with the sophistication of the detection methods, means the feasibility of experiments is in many cases becoming limited by the required measurement times.

Chapter 5

ISOLDE and RILIS

5.1 The ISOLDE facility

ISOLDE [52] is a world leading radioactive ion beam facility based at CERN that has, in various incarnations, been in operation since 1967 [53]. Sadly the TRISTAN radioactive ion beam facility [54], a contemporary the original ISOLDE facility, is no longer operational. There are a growing number of radioactive ion beam facilities worldwide, offering scientists from disciplines ranging between nuclear structure and nuclear astrophysics to materials and medical sciences the opportunity to conduct experiments with short-lived and exotic isotopes [55]. The planned and currently operating facilities are summarized in [56]. As the name indicates, ISOLDE is an isotope separator on-line, or ISOL type, radioactive ion beam facility. It is classified as a “thick target” ISOL facility, as the target material is of sufficient thickness/density to stop and thermalize the reaction products produced by the impinging “driver beam”.

The working principles of ISOLDE are depicted in Figure 5.1. A pulsed proton beam originating from the Linac 2 accelerator [57], is further accelerated by the Proton Synchrotron Booster (PSB) [58] to an energy of 1.4 GeV and directed to the ISOLDE facility. The CERN accelerator complex operates a pulsed proton “supercycle” with proton pulses from the PSB separated by 1.2 s. Typically up to 40% of the proton pulses extracted from the PSB are directed to ISOLDE to be impinged on a target.

The majority of the targets used at the ISOLDE facility are uranium carbide (UCx) as depicted in Figure 5.1. Reaction products are primarily created by proton driver

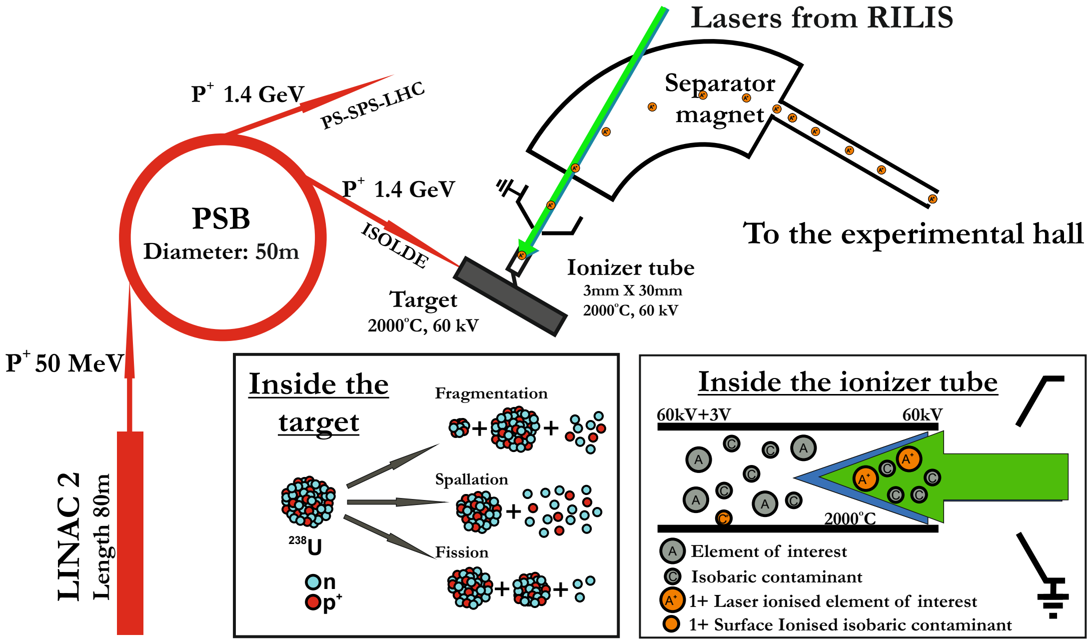

Figure 5.1: The fundamentals of radioactive ion beam production at ISOLDE. The acceleration stages of the proton driver beam are represented by red arrows. The production and ionization of reaction products is depicted in the inserts. Further discussion in the text.

beam induced fragmentation, spallation or fission of nuclei in the target material. Secondary reactions also take place however, increasing the yield for certain isotopes [59]. The target material is typically heated to between 500°C and 2200°C depending on the type. Sufficiently volatile reaction products diffuse out of the target material and then effuse via a transfer line to the ion source, typically for ionization to a 1+ charge state.

The ion source used in the process depicted in Figure 5.1 is the ISOLDE RILIS, the principle of which is discussed in Section 4.2. The entire target and ion source assembly is maintained at a voltage between 30 kV-60 kV, with a grounded extraction electrode positioned at the exit of the ion source. The ions are accelerated by the electric field resulting in the extraction of a radioactive ion beam. The ions are then directed through a dipole mass separator, where they are filtered by mv/Q (momentum/charge), before being directed to experiments located in the ISOLDE experimental hall.

5.2 ISOLDE ion sources

This section will focus on the three most commonly used ion sources at the ISOLDE facility: the hot cavity surface ion source, the RILIS and the VADIS (Versatile Arc Discharge Ion Source). Other less frequently used ion sources, such as negative ion sources [60], the COMIC ion source [61] and the Helicon ion source [62] will not be discussed.

5.2.1 Surface ion sources

At ISOLDE, hot cavity surface ion sources are used in both their originally envisaged role for surface ionization of sufficiently low IP elements and as the standard laser-atom interaction region for the ISOLDE-RILIS, this is depicted in Figure 5.1. The ISOLDE hot cavity surface ion source is a refractory metal tube, 34 mm in length, with an internal diameter of 3 mm, that is typically heated to ∼2000°C. The heating method is resistive, resulting in a longitudinal potential along the length. This potential accelerates ions created inside the hot cavity towards the extraction aperture.

The efficiency of the surface ion source for a particular element can be estimated using a modified Saha-Langmuir equation, with corrections for the hot cavity environment [63, 64]. An effective IP (IP_{ef}) [65] is used, that takes into account the atomic and ionic excited states. The IP_{ef} can be calculated as

$$IP_{ef} = IP - kT\ln(Q_i/Q_a), \tag{5.1}$$

where k is the Boltzmann constant, T is the temperature and Q_i and Q_a are partition functions accounting for the influence of the ground and excited states of the ion or the atom respectively. The partition functions can be calculated as

$$Q_x = \sum_j g_j \exp(-E_j/kT), \tag{5.2}$$

where, g is the degeneracy (2J+1) of the atomic or ionic state and E_j is the excitation energy of a particular state j. The IP_{ef} can then be inserted into the modified Saha-Langmuir equation to give an expected surface ionization efficiency E_{surf}, where

$$E_{surf} = \psi/(1+\psi), \tag{5.3}$$

$$\psi = N\xi(\exp((\phi - IP_{ef})/kT)), \tag{5.4}$$

where N is the number of collisions with the cavity walls (estimated as the ratio of the surface area of the cavity walls divided by the cross-sectional area of the exit aperture) [63], ξ is the ion survival probability and ϕ is the work function of the cavity surface.

The ion survival probability, ξ, is related to the so-called "hot cavity effect": if the electron emission from the walls is sufficiently greater than the number of ions, then a negative plasma potential is understood to build up at the walls, reducing the likelihood of ion-wall collisions and therefore enhancing the ion survival and extraction efficiency [45, 63, 66]. This effect is also applicable to laser ions created in the hot cavity surface ion source environment. Sufficient data (RILIS and surface ionization efficiencies) has been obtained experimentally for scandium [67], to enable an estimate to be made of $\xi \approx 0.1$ in a tungsten hot cavity heated to 2400 K.

Inaccuracies in this calculation could stem from several factors. ξ, has been demonstrated to be dependent on cavity temperature, surface contamination, ion load and the neutral pressure within the cavity [63], all of which can vary over time. Electron impact ionization has been determined as an additional ionization mechanism, although, ions arising from this process will account for a negligible component of the total ion rate unless $E_{surf} << 1$.

The work functions of the standard ISOLDE hot cavity materials are listed in Table 5.1. From these values it is apparent why, where possible, tantalum is used as the cavity material for the laser ion source, since the lower work function results in a reduced surface ion rate and an increased electron emission at a given temperature.

Table 5.1: Work functions of surface ion source materials determined by thermionic methods for polycrystalline material. Data taken from [68].

Element	Work function (ϕ) (eV)
Tantalum	4.25
Tungsten	4.55
Rhenium	4.72

5.2.2 The ISOLDE RILIS

The ISOLDE RILIS [45] has become the principal ion source of the ISOLDE radioactive ion beam facility. It was upgraded in 2012 with the addition of solid state pump lasers and a complementary suite of titanium:sapphire (Ti:Sa) lasers [69]. A full description can be found in the latest review article [70]. There are six broadly tunable lasers. This ensures both a good spectral coverage and a sufficient degree of flexibility in the system to meet the requirements of routine operation during the majority of the ISOLDE physics programme. A schematic of the RILIS set-up is presented in Figure 5.2.

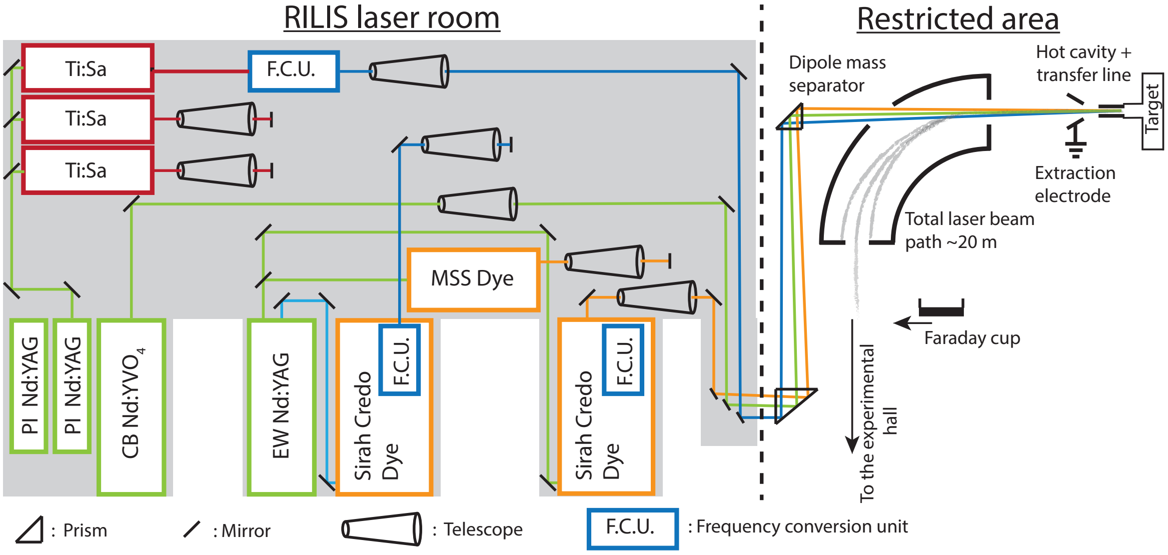

Figure 5.2: The ISOLDE RILIS, a complete description is given in the text.

The dye lasers and Ti:Sa lasers are typically pumped by frequency doubled ($2\omega =$ 532 nm) Nd:YAG lasers pulsed at 10 kHz. The 10 kHz repetition rate is approximately the frequency required to ensure atoms effusing through the ion source are illuminated by a minimum of one set of laser pulses. Though this is not sufficient for the lightest elements such as beryllium [71]. The pulsed laser light enables sufficient peak intensities for single pass 2ω, 3ω, 4ω frequency conversion, which in combination with the option to pump the dye lasers with the third harmonic of the Nd:YAG ($3\omega = 355$ nm), enables unbroken spectral coverage between 210-950 nm. This range is suitable for the majority of elements other than the noble gasses, where the only available transitions from the atomic ground states are for wavelengths <180 nm. An independent 40 W average power, TEM_{00}, frequency doubled ($2\omega = 532$ nm) Nd:YVO$_4$ Lumera Blaze laser, is available for ionization schemes using a non-resonant ionizing transition [72].

Table 5.2: ISOLDE RILIS laser parameters. The EdgeWave (EW) and Photonics Industries (PI) Nd:YAG lasers are typically used to pump the dye and Ti:Sa lasers respectively. The Nd:YVO_4 Coherent Blaze laser (CB) is typically applied for ionization schemes requiring a non-resonant transition to the ionization continuum.

Laser	Output wavelengths (nm)	Pulse length (ns)	Linewidth (GHz)
EW Nd:YAG	355, 532, 1064	8	-
PI Nd:YAG	532	170	-
CB Nd:YVO_4	532	17	-
Sirah Credo dye	372-900	7	9
MSS dye	540-900	10	0.8, 15, >60
Ti:Sa (CERN/Mainz)	690-950	40	5, 0.8

An overview of the RILIS laser parameters is presented in Table 5.2, further details can be found in [70].

The laser wavelengths are measured using HighFinesse/Ångstrom WS6 and WS7 wavelength meters. A UV grade fused silica plate, not included in Figure 5.2, is mounted half way between the laser room and the hot cavity. As the laser beams pass through this plate, two reference beams are generated (Fresnel reflections from each from each surface). The plate is wedged so that the two reference beams are separated by approximately 20 mm when they enter the reference beam observation area inside the RILIS laboratory. This enables the positions of the laser beams to be stabilized and monitored during the operation of the RILIS. Quadrant photodiodes are used as position sensitive detectors (PSDs), which in combination with piezo-actuated mirrors maintain the laser beam positions.

5.2.3 FEBIAD-type ion sources

A schematic of the principles of FEBIAD-type (Forced Electron Beam Induced Arc Discharge) ion sources [73] is presented in Figure 5.3. The latest iteration of this ion source at ISOLDE is the VADIS (Versatile Arc Discharge Ion Source) [74]. Electrons are emitted by a cathode heated to ∼2000°C. The anode is a cylindrical electrode held at 100-150 V, the anode wall facing the cathode is a grid which allows the passage of the accelerated electrons into the ionizer volume [73, 74, 75]. A source magnet is used to focus the electrons into helical orbits to increase their path length and therefore the probability of electron-atom collisions inside the anode volume. Reaction products inside the anode volume are ionized by the 100-150 eV electrons from the cathode.

Ions are extracted from the 1.5 mm aperture (at the opposite end to the grid) by the penetrating electric field of the ion source casing, that is held at the same voltage as the cathode return (the high voltage platform potential). Similarly to the surface ion source, the entire target unit is maintained at 30-60 kV. The electric field, resulting from a grounded extraction electrode located several centimetres from the exit aperture, extracts and accelerates the ions to create a radioactive ion beam.

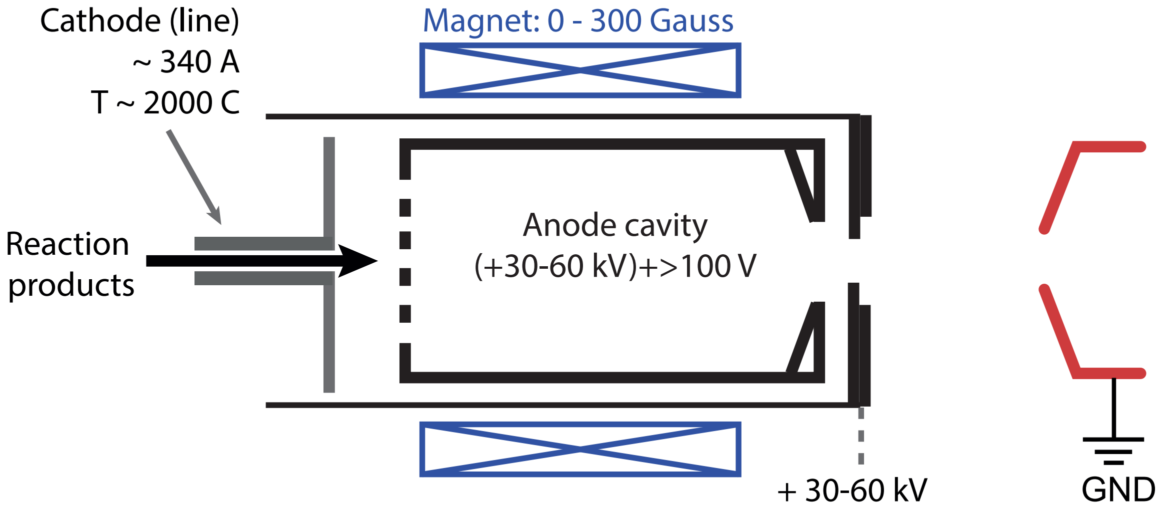

Figure 5.3: The principle of FEBIAD-type ion sources

The VADIS offers a universal method of ionization, particularly useful for the noble gases. However, because of this universal nature of the ionization process, VADIS ionized radioactive ion beams often suffer from isobaric contamination. Depending on the element of interest, temperature controlled transfer lines can be applied for increased selectivity [75].

5.3 In-source spectroscopy at ISOLDE

The set-up for in-source spectroscopy at ISOLDE is detailed in [72]. The laser targeting the spectroscopic transition is scanned in a stepwise manner, while the frequencies of the other transitions are maintained constant. This results in an ion rate of the element of interest that is dependent on the frequency of the laser probing the spectroscopic transition. The resulting ion beam is directed through an ISOLDE dipole mass separator for mass selection and then on to a detection device for the determination of the ion rate at each laser frequency step. Three methods of detection are used. For isotopes with yields greater than 1×10^6 ions/s, an ISOLDE Faraday cup can be used if the isotope of interest is the main component of the mass separated ion beam. For long lived and β emitting isotopes, the ISOLDE Multi-Reflection Time-of-Flight Mass Separator (MR-ToF MS) is used (Section 5.3.2). For α-emitters with a sufficiently short half-life, the Windmill detector is used (Section 5.3.3).

5.3.1 "Narrowband" RILIS operation

The fundamentals of the RILIS narrowband (~1 GHz) Ti:Sa (NB-Ti:Sa) are given in detail in [76]. The wavelength of the laser is scanned using a thin (0.3 mm) and a thick (6 mm) etalon, mounted in motorized mirror mounts and controlled by a LabVIEW program running on the Control PC. A laser scan management and data recording program, described in detail in [77], enables the automation of the laser scan: setting the laser frequency step size and coordinating with the Faraday cup, Windmill, or MR-ToF MS detectors. A schematic of the NB-Ti:Sa laser set-up is presented in Figure 5.4.

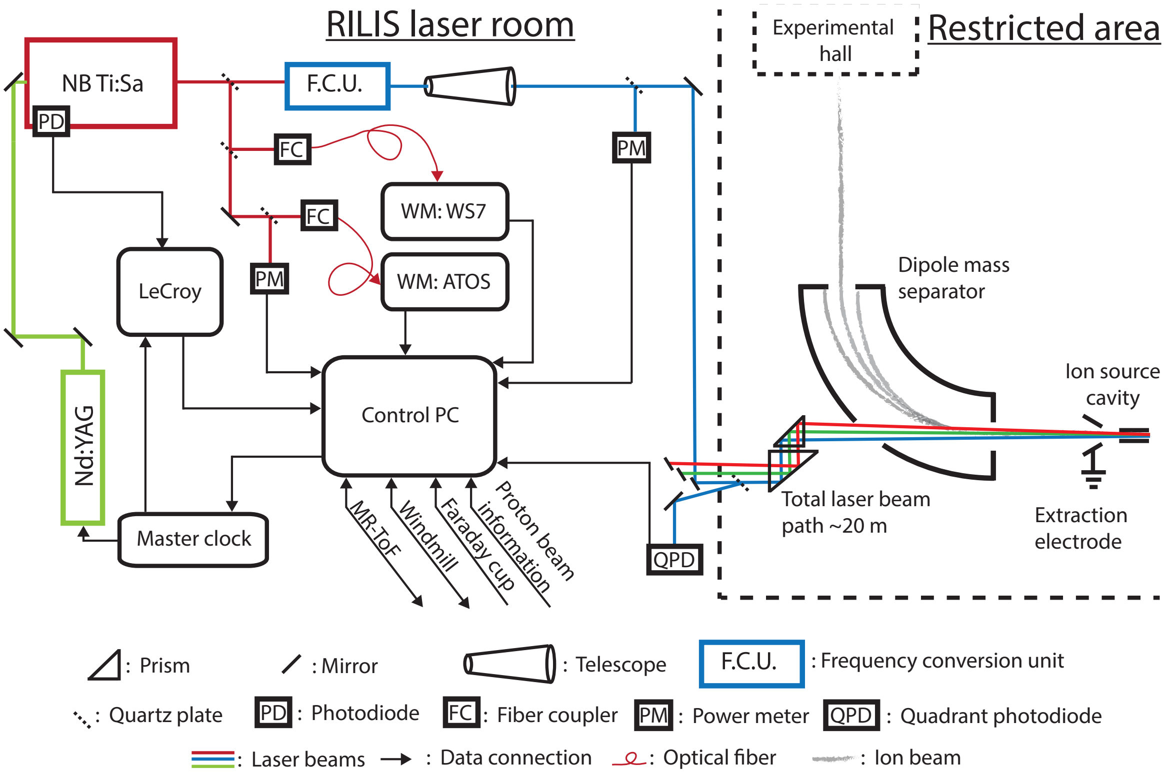

Figure 5.4: Simplified experimental set-up of the scanning laser during in-source RIS experiments at ISOLDE, the direction of the arrows indicates the direction of data flow.

The laser light is sampled in multiple locations using UV grade fused silica plates to take two 4% reflections (one from each uncoated surface). The fundamental laser power and the wavelength of the scanning laser are measured before the frequency conversion set-up as depicted in Figure 5.4. The laser power is then measured a second time on the laser table following frequency conversion and a third time by measuring the power of the reference beam reflected back into the laser room, taking a power reading from the quadrant photodiode PSD used to stabilize the laser beam position. The timing synchronization of the NB-Ti:Sa, with respect to the lasers used for the other excitation steps, is monitored with a photodiode (PD) connected to LeCroy Oscilloscope, that determines the synchronization to nanosecond precision. A LabVIEW program running on the Control PC actively corrects the synchronization of the NB-Ti:Sa during the laser scan. This is achieved by altering the delay on the master clock digital delay generator, which provides the Q-switch trigger for the pump laser.

At each measurement point, the scanning software associates the laser frequency with the ion rate (from either the Faraday cup, the Windmill or the MR-ToF MS), the three laser power measurements, the timing synchronization and the parameters of the proton driver beam. A more refined post analysis of the count rate data is performed following the experiment, however, the live information acquired mid-scan enables the quality and stability of the scan to be determined as the scan progresses.

5.3.2 The ISOLTRAP MR-ToF MS

The ISOLTRAP MR-ToF MS [78] enables the selective detection of longer lived and β-emitting isotopes, using a MagneTOF detector installed after a mass spectrometer. The ions are reflected between electrostatic plates $\sim 10^3$ times, separating isobaric contaminants by picosecond differences in the $\sim$30 ms flight time arising from the mass differences between isobars. In most cases, gating on the ion arrival time at the detector enables the determination of the ion rate of the ion beam component of interest, free of isobaric contamination. The use of the MR-ToF MS for in-source RIS is discussed in detail in [79]. A representative time-of-flight mass spectra from one of the measurement points of a scan of ^{208}Hg is presented in Figure 5.5. The separation of the ^{208}Hg ions from the ^{208}Pb isobaric contamination is clearly apparent.

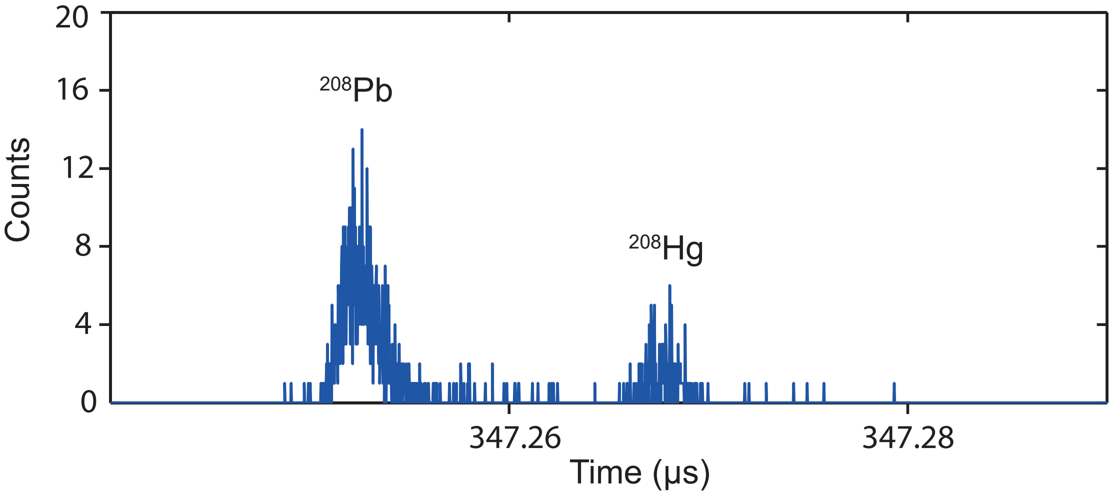

Figure 5.5: Time-of-flight spectra from a scan of ^{208}Hg. Image courtesy of F. Wienholtz.

5.3.3 The Windmill detector

The Windmill detector consists of a rotating wheel containing 10 thin carbon foils (20 μg/cm^2). The application of the Windmill detector for in-source RIS is described in detail in [80]. The ion beam is deposited onto one of the foils and the α-decay energies are measured by silicon detectors. At the position of deposition, a carbon foil is sandwiched between two silicon detectors: an annular detector to enable the transmission of the ion beam to the carbon foil and a solid detector at the rear. The movement of the wheel is synchronized with the PSB supercycle and the laser scanning the spectroscopic transition. Gates are set on the α-energies, enabling the determination of the frequency dependent ion rate of the isotope of interest. A representative energy spectra of ^{179}Hg is presented in Figure 5.6.

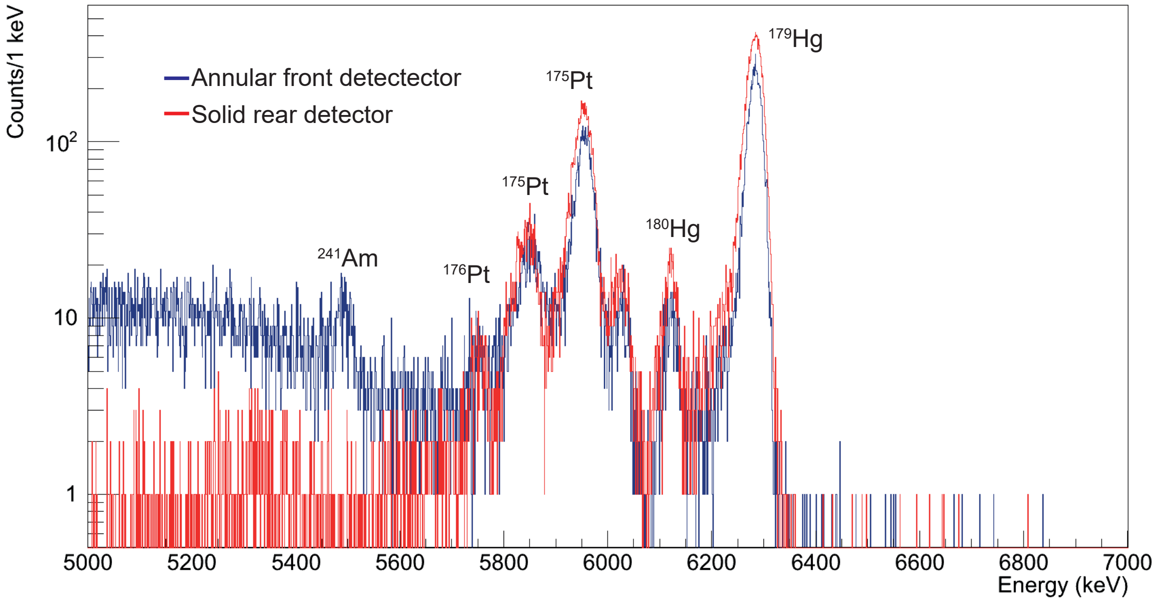

Figure 5.6: Energy spectra from the measurements of ^{179}Hg. Image courtesy of S. Sels.

Chapter 6

The VADLIS ion source

The development of alternative laser-atom interaction regions offers the possibility of increasing the applicability of the ISOLDE RILIS. A successful example of this is the LIST (Laser Ion Source and Trap) [81], which has been demonstrated to reduce significantly the surface ionized contamination often present during HC-RILIS operation. Despite a reduction in yield of one to two orders of magnitude, the selectivity offered by the LIST enabled the successful in-source RIS of ^{217}Po and ^{219}Po [82]. This Chapter presents the investigation, characterization and early application of the coupling of the RILIS with the VADIS ion source, resulting in a new laser atom interaction region. This combination that has been termed the VADLIS (Versatile Arc Discharge and Laser Ion Source).

6.1 Coupling the RILIS and VADIS ion sources

Paper I

Blurring the boundaries between ion sources: the application of the RILIS inside a FEBIAD type ion source at ISOLDE [83]

Nuclear Instruments and Methods in Physics Research B 376 (2016) 39–45

Contents lists available at ScienceDirect

Nuclear Instruments and Methods in Physics Research B

journal homepage: www.elsevier.com/locate/nimb

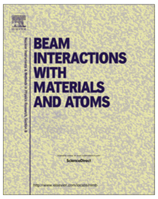

BEAM INTERACTIONS WITH MATERIALS AND ATOMS

Blurring the boundaries between ion sources: The application of the RILIS inside a FEBIAD type ion source at ISOLDE

T. Day Goodacre[a,b,*], J. Billowes[b], R. Catherall[a], T.E. Cocolios[b], B. Crepieux[a], D.V. Fedorov[c], V.N. Fedosseev[a], L.P. Gaffney[e,1], T. Giles[a], A. Gottberg[a], K.M. Lynch[a], B.A. Marsh[a], T.M. Mendonça[a], J.P. Ramos[a,d], R.E. Rossel[a,f,g], S. Rothe[a], S. Sels[e], C. Sotty[e], T. Stora[a], C. Van Beveren[e], M. Veinhard[a]

[a] *CERN, CH-1211 Geneva 23, Switzerland*
[b] *School of Physics and Astronomy, The University of Manchester, Manchester M13 9PL, United Kingdom*
[c] *Petersburg Nuclear Physics Institute, 188350 Gatchina, Russia*
[d] *Laboratory of Powder Technology, EPFL, CH-1015 Lausanne, Switzerland*
[e] *KU Leuven, Instituut voor Kern- en Stralingsfysica, 3001 Leuven, Belgium*
[f] *Institut für Physik, Johannes Gutenberg Universität, D-55099 Mainz, Germany*
[g] *Faculty of Design, Computer Science and Media, Hochschule RheinMain, 65197 Wiesbaden, Germany*

ARTICLE INFO

Article history:
Received 2 September 2015
Received in revised form 15 February 2016
Accepted 3 March 2016
Available online 11 April 2016

Keywords:
RILIS
VADLIS
Resonance laser ionization
Ion source
ISOLDE

ABSTRACT

For the first time, the laser resonance photo-ionization technique has been applied inside a FEBIAD-type ion source at an ISOL facility. This was achieved by combining the ISOLDE RILIS with the ISOLDE variant of the FEBIAD ion source (the VADIS) in a series of off-line and on-line tests at CERN. The immediate applications of these developments include the coupling of the RILIS with molten targets at ISOLDE and the introduction of two new modes of FEBIAD operation: an element selective RILIS mode and a RILIS + VADIS mode for increased efficiency compared to VADIS mode operation alone. This functionality has been demonstrated off-line for gallium and barium and on-line for mercury and cadmium. Following this work, the RILIS mode of operation was successfully applied on-line for the study of nuclear ground state and isomer properties of mercury isotopes by in-source resonance ionization laser spectroscopy. The results from the first studies of the new operational modes, of what has been termed the Versatile Arc Discharge and Laser Ion Source (VADLIS), are presented and possible directions for future developments are outlined.

1. Introduction

The Resonance Ionization Laser Ion Source (RILIS) has become the principal ion source of the ISOLDE radioactive ion beam facility [1]. At ISOLDE, resonance laser ionization is typically applied inside a hot cavity surface ion source: a metal tube 34 mm in length with an inner diameter of 3 mm, made from tungsten or tantalum with a standard operational temperature in the region of 2000 °C. The increasing ubiquity of the RILIS stems from its combination of element selective ionization with efficiencies in the region of 10%. There are two avenues by which to expand the RILIS capabilities. The first is laser ionization scheme development, enabling new or more efficiently produced laser ionized ion beams. The second avenue for development is the exploration of alternative laser/atom interaction and ion extraction conditions, of which the results reported here are an example.

The recent studies presented here demonstrate the possibility to blur the boundaries between ion sources at ISOLDE. The RILIS [2] has been combined with the Versatile Arc Discharge Ion Source (VADIS) [3], ISOLDE's variant of the Forced Electron Beam Induced Arc Discharge (FEBIAD) type ion source [4], enabling laser resonance ionization to be achieved inside the VADIS anode cavity. The combination, termed the Versatile Arc Discharge and Laser Ion Source (VADLIS), offers both immediate applications and promising directions for further development to meet the laser ion source requirements of the future.

The original motivation for coupling the RILIS and the VADIS was as a step towards the production of refractory metal ion beams at ISOLDE: extracting refractory elements as molecules [5], dissociation to atomic form using the VADIS, then selective ionization using the RILIS lasers. While this work continues, the initial

---

[*] Corresponding author at: CERN, CH-1211 Geneva 23, Switzerland.
E-mail address: thomas.day.goodacre@cern.ch (T. Day Goodacre).

[1] Present address: School of Engineering, University of the West of Scotland, Paisley PA1 2BE, United Kingdom.

http://dx.doi.org/10.1016/j.nimb.2016.03.005
0168-583X/

promising results obtained for resonance laser ionization of non-refractory elements has led to both immediate applications and additional opportunities. Here we introduce the VADLIS as a new ion source option for ISOLDE and provide a summary of the modes of operation that have been characterized thus far. The immediate applications and the progress towards future opportunities are also discussed.

2. The ISOLDE RILIS and VADIS

At ISOLDE, reaction products created inside the target effuse via a transfer line to an ion source for ionization. The principles of FEBIAD type ion sources, described in detail by Kirchner and Roeckl [4], are schematically outlined in Fig. 1. Electrons are emitted by a cathode, typically heated to over 2000 °C. The anode is a cylindrical electrode held at 100–150 V with respect to the cathode. The face of the anode cylinder directly opposite the cathode is a grid, allowing the passage of accelerated electrons into the anode cavity. A portion of the reaction products inside the anode volume are ionized in the arc discharge resulting from electrons accelerated from the cathode [4,6]. Ions are extracted from the anode cavity through a 1.5 mm aperture at the opposite end to the grid.

The anode geometries of all ISOLDE VADIS type ion sources are identical to that of the MK5 FEBIAD [7,8], though with molybdenum rather than graphite components. The material modification was implemented because of the apparent sensitivity of the FEBIAD to the outgassing of CO [3,7]. As such, the results presented here are expected to be equally applicable to FEBIAD variants used at radioactive beam facilities worldwide.

The ISOLDE RILIS, described by Rothe et al. in these proceedings [9], uses tunable lasers to target a progressive series of resonant atomic transitions, before a final ionizing transition, either to an autoionizing state or a non-resonant transition to the ionization continuum. The lasers are pulsed with a repetition rate of 10 kHz, which is well suited to the mean effusion time of 100 µs for atoms along the length of the hot cavity. The hot cavity walls confine the atoms, providing a complete overlap of the RILIS lasers with the reaction products. If the RILIS lasers are instead transmitted through the 1.5 mm VADIS exit aperture, the geometry of the VADIS anode cavity limits the laser-atom overlap region to just 7% of the anode volume. However, assuming saturation of the directed into the anode volume, the efficiency of the laser ionization within the cavity is independent of the area of the extraction aperture [2,10]. Neglecting wall sticking times, the mean atom residence time within this volume is expected to be of the order of 10 ms [4].

3. Experimental set-up

Here we describe the experimental set-up used for the first VADLIS tests, which were conducted at the ISOLDE off-line separator. This is representative of the set-up used for the subsequent tests performed at the ISOLDE GPS separator (off-line and on-line) [11]. Significant differences in the experimental set-ups are highlighted individually. The off-line facility is a replica of the ISOLDE on-line front-end, attached to a dipole mass separator magnet. For simplicity, the ionization of gallium in the VADIS anode cavity was investigated during all tests at the off-line separator. Gallium ionization in both the hot cavity (surface and laser ionization) [12] and the Laser Ion Source Trap (LIST) [13] has been well characterized before. The ionization potential of 6 eV ensures that gallium is surface ionized at a typical hot cavity operating temperature of 2000 °C, but with low efficiency (<1%), thereby providing a benchmark by which to judge the relative efficiencies of other ionization methods. The boiling point and the natural isotope abundance signature of gallium make it a reliable and easily identifiable ion beam for ion source development work. Furthermore, the two-step laser ionization scheme $\{\lambda_1 \mid \lambda_2\} = \{294\,\text{nm} \mid 532\,\text{nm}\}$ [1] requires only one tunable RILIS laser. The experimental set-up is summarized in Fig. 2.

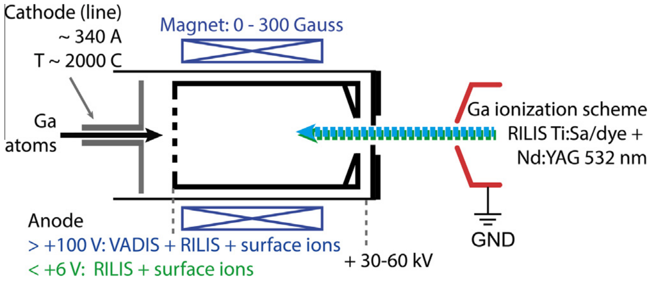

Fig. 1. A schematic of the VADLIS ion source.

Light from a titanium-doped sapphire (Ti:Sa) laser was frequency tripled to produce the first step of 294 nm. The non-resonant final step transition of 532 nm was provided by a frequency doubled Nd:YAG laser (Edgewave). The wavelength of the Ti:Sa laser was measured using a HighFinnesse/Angstrom WS6 wavelength meter. The laser beams were directed through a window in the dipole mass separator magnet, into the anode cavity of a VADIS via the exit aperture as depicted in Fig. 1. A sample of stable gallium was evaporated from a resistively heated refractory metal capillary (mass-marker) attached at the rear of the ion source. The laser parameters (beam position, average power, wavelength, timing) were maintained constant whilst the VADIS parameters (anode voltage, cathode heating, magnetic field strength) were varied to determine the optimal conditions for the extraction of laser ions. At the off-line separator depicted in Fig. 2, the target and ion source construction was held at +32 kV so that the grounded extraction electrode, located downstream of the anode aperture, accelerated the positive ions, creating a 32 keV ion beam.

A LeCroy Waverunner 104MXi oscilloscope was synchronized with the 10 kHz laser trigger and used to record a time structure histogram of the ion signal, measured with a microchannel plate (MCP) detector installed in the focal plane of the mass separator. The ion current incident on the MCP detector was limited to below 1 pA. For ion currents in excess of 1 pA, a Faraday cup was used as a more robust measurement device, but without the time resolution capabilities of the MCP detector.

4. Off-line testing and characterization

With the presence of the RILIS laser light in the VADIS anode cavity, gallium atoms may be ionized by three distinct processes: arc discharge ionization, surface ionization and resonance laser ionization. At a constant cathode temperature, adjusting the anode voltage influences both the total ion quantity and the relative contribution from each ionization process. Operation in the 1–5 V region offers a selective RILIS mode of operation, where only laser and surface ionization is observed. A sufficient positive voltage on the anode grid provides active suppression of surface ions ionized outside of the anode cavity, leaving only the internal anode walls, radiatively heated by the cathode, as a point of origin for surface ions extracted from the source. Arc discharge ionization can occur once the electrons emitted from the cathode are accelerated with a sufficient anode voltage. The effect of increasing the anode voltage on the arc discharge related ion current typically saturates between 100 V and 160 V, this is the standard VADIS mode of operation. The introduction of the RILIS lasers while in VADIS mode has been demonstrated to increase the overall ion current and is referred to hereafter as the RILIS + VADIS mode of operation.

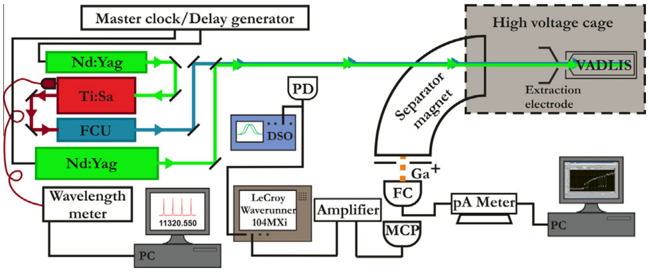

Fig. 2. Experimental set-up used at the ISOLDE off-line separator. DSO: digital storage oscilloscope, FC: Faraday cup, FCU: frequency conversion unit, MCP: microchannel plate, PD: photo diode.

The distinct modes of operation are observable in the measurement of the ^{71}Ga ion rate during a scan of the anode voltage with the cathode heated with 340 A (Fig. 3a). Other than the anode voltage, all VADIS parameters were maintained constant during the scan. At each anode voltage step, measurements were made with the 294 nm resonant first step transition both blocked and unblocked to enable a determination of the laser ionized fraction (red curve) and the VADIS ionized fraction (black curve) from the total ion current (dashed blue curve).

As depicted in Fig. 3a, the maximum ion current of ^{71}Ga was observed with the lasers directed into the ion source and an anode voltage of 2 V. With increasing anode voltage, resonance laser ionization was observed to dominate the ionization mechanisms until 60 V was reached, at which point arc discharge ionization became the dominant process for ionization. Both the RILIS related and arc discharge related ion currents dropped in the step from 23 V to 24 V, the RILIS related ion current from 176 pA to 100 pA and the arc discharge related ion current from 34 pA to 20 pA. Similarly, following the step from 55 V to 60 V, both the RILIS related and arc discharge related ion currents increased: the RILIS related ion current increased from 36 pA to 80 pA and the arc discharge related ion current increased from 55 pA to 330 pA. The coincidence of the decrease and increase in both currents, indicates a change in the extraction efficiency of the ions at these voltage steps, rather than a particular increase or decrease of the ionization efficiency of either types of ionization mechanism.

The cathode heating current was then increased to 360 A and the anode scan was repeated. The result, shown in Fig. 3b, demonstrates a partial loss of the RILIS mode of operation. Here, we observe the onset of an increase in the efficiency of laser ion extraction, coincident with an improved extraction or ionization rate of arc discharge ionized gallium between 10 V and 15 V. An increase in the maximum achievable VADIS mode ion current of 485 pA was also observed following the increase in the cathode heating current to 360 A, however, this ion current did not exceed the maximum recorded RILIS mode ion current of 530 pA achieved with a cathode heating current of 340 A.

To some extent, the features that appear in Fig. 3a can be interpreted by an analysis of the time structure of the ion beam, relative to the laser pulse arrival time. The time structure measurements required an MCP and were therefore performed with ion currents three orders of magnitude below those recorded in the anode scans presented in Fig. 3a and b. The time structures recorded at the maxima and minima in the laser ion signal (0 V, 2 V, 5 V and 15 V), observed in the anode voltage scan with the 340 A cathode heating, are presented in Fig. 4. The histograms have been normalized to 35,000 counts over the 100 μs time window.

Similarly to laser ionization in a hot cavity, the first peak in the time structures shown in Fig. 4 is understood to correspond to laser ions created at the exit aperture of the cavity, in a region where penetration of the extraction field is possible [14]. The second peak observed in the time structure measurements recorded at 5 V and 15 V and the slow release component, observed as a continuous background of ~17 counts, are features believed to correspond to the potential distribution along the axis of the anode cavity.

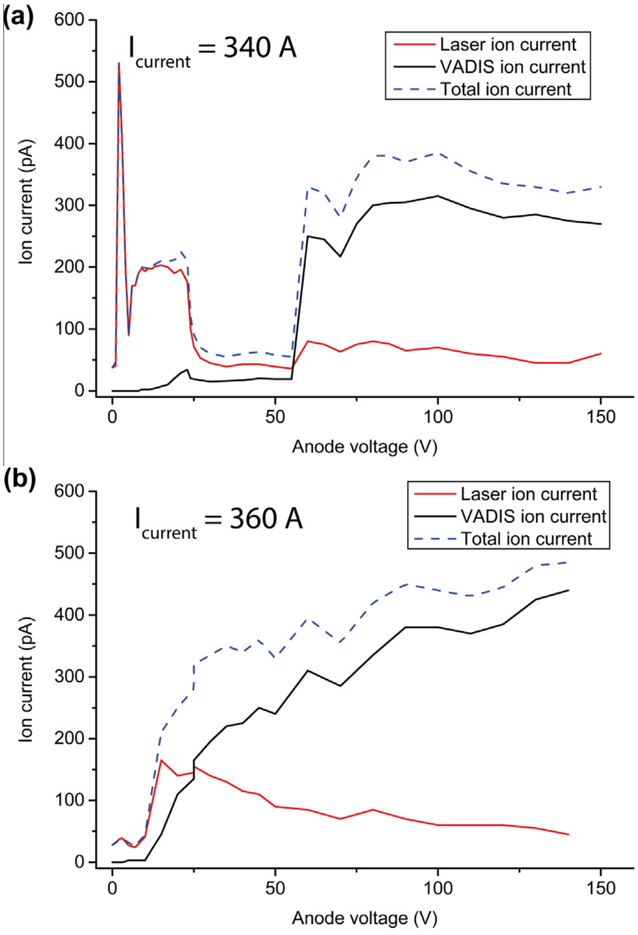

Fig. 3. Anode voltage vs ^{71}Ga ion current for an applied cathode heating current of 340 A (a) and 360 A (b). The laser ion current was determined by measuring the reduction in the total ion current following the blocking of the 294 nm laser beam.

Ion survival in a hot cavity is understood to be strongly dependent on electron emission from the inner walls creating a negative potential well along the central axis, with respect to the positively charged walls, that prevents the positive ions from colliding with the walls [2,15]. VADIS simulations indicate a similar, but completely enclosed, potential well at the center of the anode cavity when the VADIS is operated with 150 V applied to the anode [3]. It was concluded that only the ions created in the region outside of this central potential well could be extracted efficiently.

A qualitative understanding of the features observed in the time structures presented in Fig. 4, can be formulated by assuming the existence of such a potential well when lower voltages are applied to the anode cavity. Under conditions where laser ions can escape the potential well, the average laser ion survival is enhanced, though the extraction of these ions is retarded by the electric field distribution, resulting in a DC component of the laser ion current, observable as the ~17 count background in the time structures taken at 2 V and 15 V. In conditions where the potential well is too deep and laser ions are unable to escape, the total laser ion rate is reduced due to the poor extraction efficiency and the prompt release component is dominant. This can be observed in the time structures taken at 0 V and 5 V, anode voltages that correspond to minima in the ion current. The second peak, visible in the time

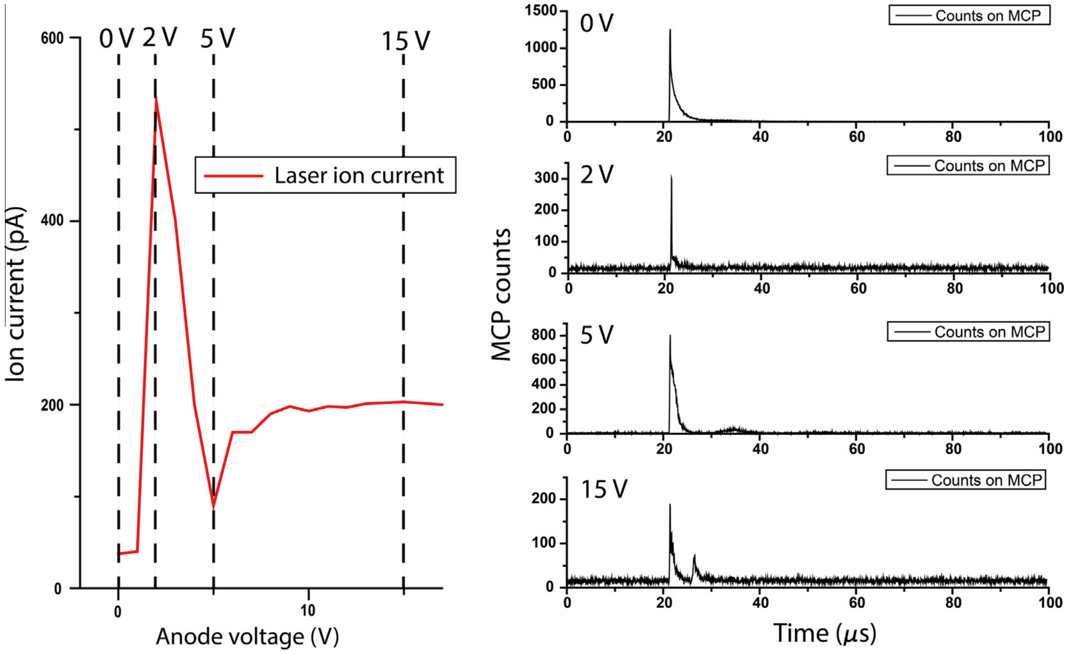

Fig. 4. Time structure measurements of the ^{71}Ga laser ionized beam, cathode 340 A. The distinct voltages at which the time structures were obtained are highlighted in the anode voltage scan (detailed view from Fig. 3a). Details are given in the text.

structures measured at 5 V and 15 V, is understood to correspond to laser ions created at the rear of the anode cavity, outside of the central potential well.

The differing ion current dependence on the anode voltage between Fig. 3a and b could therefore be understood as the result of a variation in the electron density within the anode cavity. The increased electron density in the anode cavity due to an increase in the cathode heating current to 360 A, resulted in a potential well too deep for the laser ions to escape until ions of other elements, produced after the onset of arc discharge ionization began to occupy the central potential well, thereby balancing the influence of the additional electrons.

To illustrate the dependence of RILIS mode efficiency on extraction from the assumed potential well at the center of the anode cavity, the laser ion signal is plotted with the percentage of the MCP counts relating to the slow release DC component in Fig. 5a and b, for operation at 340 A and 360 A respectively.

The time structure measurements corresponding to the dashed (blue) line in Fig. 5a and b were recorded with ion currents three orders of magnitude below that of the Faraday cup measurements, due to the limits of the MCP; however, between 0 V and 15 V there is still a clear correlation between the fraction of the total counts coming from the slow release DC component of the time structure and the ^{71}Ga ion rate measured on a Faraday cup. This indicates a requirement for the extraction of what are understood to be ions from the center of the cavity for the most efficient RILIS mode operation. In Fig. 5a, this can be seen in the minima at 0 V and after 5 V, and the maxima at 2 V and 10 V in both the ion current measured with a Faraday cup and the contribution of the DC background to the total count rate recorded in the time structure measurements. Similarly, in Fig. 5b it can be seen in the increase after 10 V is applied to the anode. The sensitivity of the laser ion extraction to the electron distribution within the anode cavity was confirmed by an observed influence of the source magnet on the extracted laser ion current by up to a factor of two or more. Electron trajectories are significantly affected by the weak magnetic field but any direct influence on ion dynamics is expected

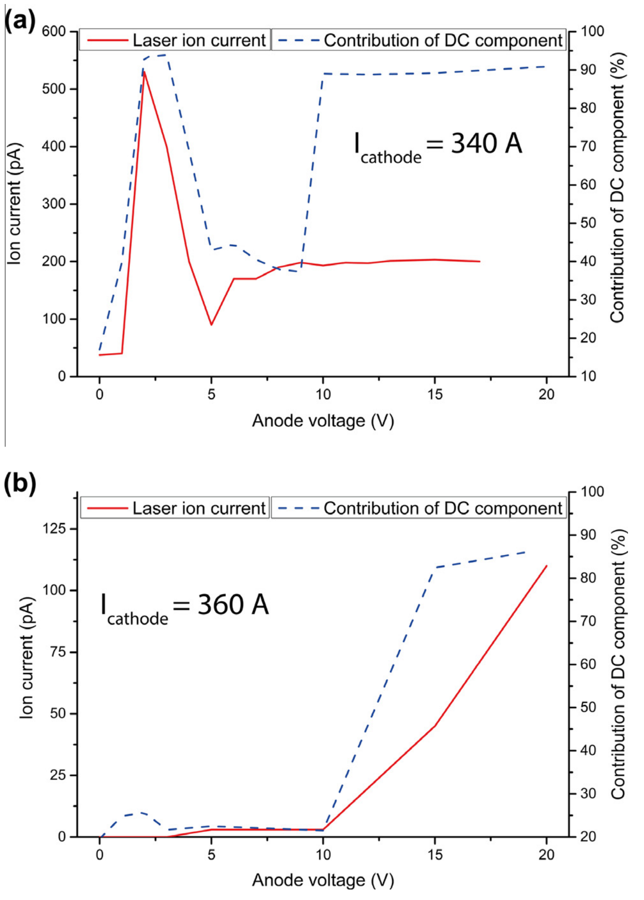

Fig. 5. Correspondence of the RILIS related ^{71}Ga ion current with the DC slow release component observed in time structure measurements, cathode heated with 340 A (a) and 360 A (b).

to be negligible. The understanding and optimization of the RILIS mode of operation will be the subject of further investigation.

In addition to the standard VADIS mode of operation, two new operating modes have therefore been established: the predominantly element selective RILIS mode, with the anode voltage set below the threshold for electron impact ionization to occur and a RILIS + VADIS mode, with the RILIS laser light whilst a nominal VADIS mode anode voltage is applied. The RILIS + VADIS mode was observed to result in the highest ion current during the on-line operation, as discussed in Section 6. Surface ionization can also contribute to the total ion production however, this is strongly dependent on the ionization potential of the element.

5. VADLIS for selective RILIS operation

The VADLIS modes of operation were investigated off-line at ISOLDE with barium. The RILIS lasers were tuned to ionize barium with a two-step $\{\lambda_1 \mid \lambda_2\} = \{350\,\text{nm} \mid 532\,\text{nm}\}$ scheme [16] and the laser beams were directed into the anode cavity of a VADIS mounted on the ISOLDE HRS front end [11]. The results are presented in Fig. 6.

At 2.5 V, corresponding to the maximum recorded ion current, the application of the RILIS lasers enhanced the barium related signal by a factor of 8. By comparison, off-line tests of barium laser ionization in a hot cavity using the same scheme resulted in a laser enhancement of the barium ion current of less than 1.5. The enhanced selectivity of the VADLIS is thus far understood to be the consequence of a reduced efficiency for surface ionization compared to that of a standard hot cavity surface ion source, combined with surface ion suppression by the anode grid. The signal reduction when the lasers were blocked, with 150 V applied to the anode, was below 10%, indicating that the majority of the ions extracted at this voltage were ionized by arc discharge ionization.

The dominance of a RILIS mode of operation for barium is apparent from the results depicted in Fig. 6. Reduced FEBIAD efficiencies for alkali metals, following the application of a VADIS mode anode voltage, was reported by Burkard et al. [17]. It would appear that this behavior is consistent for barium which also has a comparatively low ionization potential of 5.2 eV. The repelling action of the anode voltage was also observed during the same VADIS test for surface-ionized ^{133}Cs where the largest ion current was observed at 0 V. The mechanism behind these effects is under investigation.

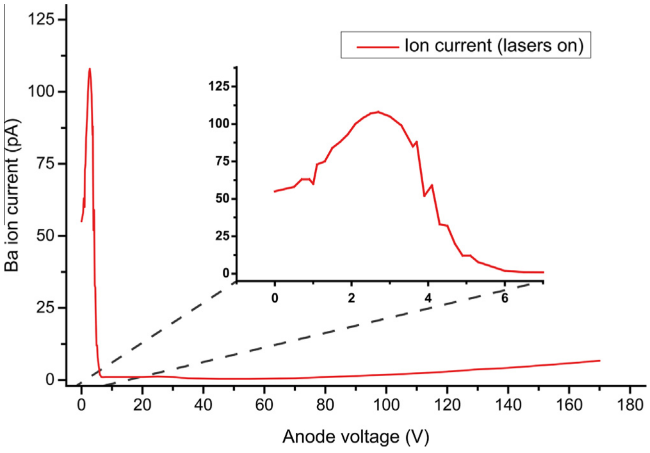

Fig. 6. ^{138}Ba ion current during an anode voltage scan with RILIS lasers directed into the anode cavity. The total signal was recorded without distinction between laser ionization and other ionization mechanisms.

The use of the VADLIS as a laser ion source, has the potential to both increase selectivity compared to hot cavity RILIS operation and expand the applicability of the laser resonance ionization technique to elements currently surface ionized at ISOLDE. We intend to investigate the performance of the VADLIS with an inverted-polarity transfer line cathode, combined with a low work function material for the VADLIS anode cavity such as thoriated or lanthanated tungsten.

6. On-line testing and verification

Following successful off-line testing, an immediate application of the VADLIS developments is the possibility to couple the RILIS with molten metal targets at ISOLDE. The RILIS mode of VADLIS operation was demonstrated on-line at ISOLDE on three occasions during 2015: yield checks of mercury and the study of mercury isotopes by in-source resonance ionization laser spectroscopy using a molten lead target [18] and a test of the VADLIS modes of operation with radiogenic ^{114}Cd from a molten tin target. Fig. 7 is a comparison of the VADLIS modes of operation, observed for the two different target units during mercury yield checks and cadmium ionization tests. The ^{178}Hg rate was measured by α-decay spectroscopy in the CRIS DSS 2.0 set-up [19], while the ^{114}Cd signal was measured using a Faraday cup located after the ISOLDE GPS dipole magnet.

The on-line tests described here took place in-between scheduled ISOLDE experiments. The VADIS parameters were therefore maintained at the optimized values for on-line VADIS mode operation. All RILIS mode operation has thus far been validated by comparison to VADIS mode ion currents, for which the absolute efficiency has not yet been determined. Fig. 7 demonstrates a comparable efficiency for RILIS mode and VADIS mode operation under on-line conditions. A mercury ionization efficiency of 60% was reported at ISOLDE with the MK6 FEBIAD variant [8]. The MK6 however, differs in anode design and component material compared to the VD3 VADIS variant, currently used to ionize mercury at ISOLDE. An efficiency measurement of the RILIS ionization scheme for mercury in a hot cavity gave a lower limit efficiency of 6%. Fig. 7 demonstrates the comparable on-line ionization efficiencies of RILIS mode and VADIS mode operation for mercury and cadmium, with the highest ion currents observed in the RILIS + VADIS mode. Fig. 7 also includes the VADIS + Blaze effect of directing the 40 W laser into the VADIS anode, the increased

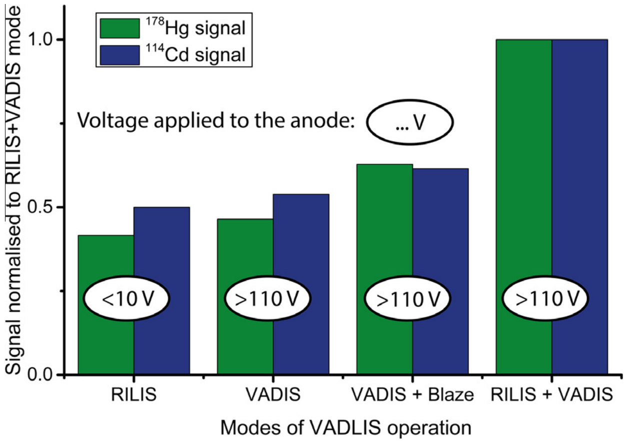

Fig. 7. Comparison of the VADLIS modes of operation. The Blaze is a 40 W frequency doubled Nd:YVO$_4$ laser, typically directed into a cavity for a non-resonant final step transition to the ionization continuum.

VADIS mode signal is thought to be due the incident laser beam increasing the temperature of the cathode surface.

7. On-line application and further development

The coupling of the RILIS with molten targets, combined with what is essentially a new type of laser ion source cavity, has already enabled the study of nuclear ground state and isomer properties of mercury isotopes between ^{177}Hg and ^{208}Hg. The possibility of switching between RILIS and VADIS modes of operation also has a wider significance for ISOLDE operation. Element selective and in some cases isomer selective ionization is now available from molten metal targets at ISOLDE, offering the possibility to significantly reduce isobaric and isomeric contamination in extracted ion beams.

The application of the RILIS requested for signal identification as part of a Coulomb excitation experiment using a VADIS ion source [20]. Using the VADLIS, combined with the new RILIS ionization scheme for tellurium [21], enables this to be accomplished using a single target/ion source assembly, in one continuous experimental run.

An enlarged anode aperture of 2.5 mm was trialed during the initial round of testing (not reported in this proceedings) in order to better match the focusing limitations of the RILIS lasers at a distance of ~20 m but at the expense of mass resolving power [4]. Following these successful initial tests, in order to maximize the flexibility of the ion source and enable immediate on-line application, the focus of the investigations moved towards optimizing modes of operation compatible with current VADIS anode geometries, the results of which have been reported here. It is therefore important to note that so far, only the optimal operating conditions for the existing VADIS design that have been investigated. There are numerous areas for further ion source development and testing:

- Selective ionization of refractory metal beams at ISOLDE: extraction from the target as a volatile molecule and dissociation in the VADIS before chemically selective resonance laser ionization.
- Selective RILIS: a low work function anode cavity combined with an inverted polarity cathode transfer line. The enhanced selectivity could potentially widen the range of RILIS applicable elements to those that are typically surface ionized at ISOLDE.
- Efficiency measurements: a series of RILIS mode and VADIS mode efficiency measurements are required to enable the absolute efficiencies of the hot cavity RILIS and VADLIS operation to be compared.
- Optimization of the anode cavity geometry and electrical configuration for RILIS and VADIS mode operation: the results reported here all took place using unmodified VADIS units, it is therefore unlikely that the existing design is optimal for RILIS mode operation. Simulations of the RILIS mode of operation would significantly aid understanding and streamline the design process. Resonance laser ionization could also be used to probe the electric field distribution inside the VADIS anode during VADIS mode operation, offering a minimally invasive method of study.
- Two-photon spectroscopy: it has been demonstrated that polished molybdenum is moderately reflective ($\geqslant 50\%$) across a broad spectral range, including at temperatures exceeding 1500 °C (private communication Maxim Seliverstov). The VADIS anode grid is a perforated molybdenum disc with 37 holes. Omitting the central hole, on-axis with the laser beam path, and polishing the molybdenum surface may enable "Doppler free" two-photon spectroscopy inside the anode cavity volume.

8. Conclusion

The ISOLDE RILIS has been successfully combined with the VADIS, ISOLDE's variant of the FEBIAD type ion source. The combination, termed the VADLIS has been tested off-line with gallium and barium isotopes and on-line with mercury and cadmium isotopes. Three distinct modes of operation are now available: an element selective RILIS mode, the standard VADIS mode and a combined RILIS + VADIS mode for enhanced on-line efficiencies. The RILIS mode of operation has been investigated, the efficiency appears to depend strongly on the possibility of extracting laser ions from the full anode cavity. This is related to the cathode temperature, anode voltage and source magnet current. The selectivity of the RILIS mode has been demonstrated, potentially widening the range of RILIS applicable elements to those that are typically surface ionized at ISOLDE. The possibility to further suppress surface ions will be investigated. The results presented here mark the beginning of a series of further VADLIS developments and optimization.

Acknowledgments

This project has received funding through the European Union's Seventh Framework Programme for Research and Technological Development under Grant Agreements: 262010 (ENSAR), 267194 (COFUND), and 289191 (LA^{3}NET). K.M.L. and L.P.G. acknowledges FWO-Vlaanderen (Belgium) as FWO Pegasus Marie Curie Fellows. S.S acknowledges a Ph.D. grant of the Agency for Innovation by Science and Technology (IWT).

References

[1] V.N. Fedosseev, L.-E. Berg, D.V. Fedorov, D. Fink, O.J. Launila, R. Losito, B.A. Marsh, R.E. Rossel, S. Rothe, M.D. Seliverstov, A.M. Sjödin, K.D.A. Wendt, Upgrade of the resonance ionization laser ion source at ISOLDE on-line isotope separation facility: new lasers and new ion beams, Rev. Sci. Instrum. 83 (2) (2012) 02A903.

[2] V.I. Mishin, V.N. Fedoseyev, H.-J. Kluge, V.S. Letokhov, H.L. Ravn, F. Scheerer, Y. Shirakabe, S. Sundell, O. Tengblad, Chemically selective laser ion-source for the CERN-ISOLDE on-line mass separator facility, Nucl. Instr. Meth. Phys. Res. Sect. B: Beam Interact. Mater. Atoms 73 (4) (Apr 1993) 550–560.

[3] L. Penescu, R. Catherall, J. Lettry, T. Stora, Development of high efficiency versatile arc discharge ion source at CERN ISOLDE, Rev. Sci. Instrum. 81 (2) (2010) 02A906.

[4] R. Kirchner, E. Roeckl, Investigation of gaseous discharge ion sources for isotope separation on-line, Nucl. Instrum. Meth. 133 (2) (Mar 1976) 187–204.

[5] H.L. Ravn, S. Sundell, L. Westgaard, Target techniques for the isolde on-line isotope separator, Nucl. Instr. Meth. 123 (1) (Jan 1975) 131–144.

[6] R. Kirchner, E. Roeckl, A novel isol ion source, Nucl. Instrum. Meth. 139 (Dec 1976) 291–296.

[7] T. Bjrnstad, E. Hageb, P. Hoff, O.C. Jonsson, E. Kugler, H.L. Ravn, S. Sundell, B. Vosicki, the ISOLDE Collaboration, Methods for production of intense beams of unstable nuclei: new developments at ISOLDE, Phys. Scr. 34 (6A) (Dec 1986) 578–590.

[8] S. Sundell, H. Ravn, Ion source with combined cathode and transfer line heating, Nucl. Instr. Meth. Phys. Res. Sect. B: Beam Interact. Mater. Atoms 70 (1–4) (Aug 1992) 160–164.

[9] S. Rothe, T. Day Goodacre, D. Fedorov, V.N. Fedosseev, B.A. Marsh, P.L. Molkanov, M.D. Seliverstov, R.E. Rossel, S. Rothe, M. Veinhard, K.D.A. Wendt, Laser ion beam production at CERN-ISOLDE: new features – more possibilities, Nucl. Instr. Meth. Phys. Res. Sect. B 376 (2016) 91–96.

[10] F. Ames, T. Brumm, K. Jager, H.J. Kluge, B.M. Suri, H. Rimke, N. Trautmann, R. Kirchner, A high-temperature laser ion source for trace analysis and other applications, Appl. Phys. B Photophys. Laser Chem. 51 (3) (1990) 200–206.

[11] E. Kugler, The ISOLDE facility, Hyperfine Interact. 129 (1/4) (2000) 23–42.

[12] F. Schwellnus, R. Catherall, B. Crepieux, V.N. Fedosseev, B.A. Marsh, Ch. Mattolat, M. Menna, F.K. Österdahl, S. Raeder, T. Stora, K. Wendt, Study of low work function materials for hot cavity resonance ionization laser ion sources, Nucl. Instr. Meth. Phys. Res. Sect. B: Beam Interact. Mater. Atoms 267 (10) (May 2009) 1856–1861.

[13] K. Blaum, C. Geppert, H.-J. Kluge, M. Mukherjee, S. Schwarz, K. Wendt, A novel scheme for a highly selective laser ion source, Nucl. Instrum. Meth. Phys. Res. Sect. B: Beam Interact. Mater. Atoms 204 (May 2003) 331–335.

[14] J. Lettry, R. Catherall, U. Köster, U. Georg, O. Jonsson, S. Marzari, V. Fedosseev, Alkali suppression within laser ion-source cavities and time structure of the

laser ionized ion-bunches, Nucl. Instrum. Meth. Phys. Res. Sect. B: Beam Interact. Mater. Atoms 204 (May 2003) 363–367.

[15] G.D. Alkhazov, E.Ye. Berlovich, V.N. Panteleyev, A new highly efficient selective laser ion source, Nucl. Instr. Meth. Phys. Res. Sect. A: Accel., Spectrometers, Detectors Assoc. Equip. 280 (1) (Aug 1989) 141–143.

[16] T. Day Goodacre, J. Ballof, D. Fedorov, V.N. Fedosseev, B.A. Marsh, R.E. Rossel, S. Rothe, C. Seiffert. Laser ionized ion beams of Li+, Ba+ and Ba2+ using the ISOLDE-RILIS. Unpublished results.

[17] K.H. Burkard, W. Dumanski, R. Kirchner, O. Klepper, E. Roeckl, The mass separator facility on-line to the heavy-ion accelerator UNILAC at Darmstadt, Nucl. Instr. Meth. 139 (Dec 1976) 275–280.

[18] L.P. Gaffney, T. Day Goodacre, A. Andreyev, M. Seliverstov, N. Althubiti, B. Andel, S. Antalic, D. Atanasov, A.E. Barzakh, J. Billowes, K. Blaum, T.E. Cocolios, J. Cubiss, G. Farooq-Smith, V.N. Fedosseev, D.V. Fedorov, R. Ferrer, K.T. Flanagan, L. Ghys, A. Gottberg, C. Granados, F. Herfurth, M. Huyse, D.G. Jenkins, D. Kisler, S. Kreim, T. Kron, Yu. Kudryavtsev, D. Lunney, K.M. Lynch, V. Manea, B.A. Marsh, T.M. Mendonca, P.L. Molkanov, D. Neidherr, R. Raabe, S. Raeder, J.P. Ramos, E. Rapisarda, M. Rosenbusch, R.E. Rossel, S. Rothe, L. Schweikhard, S. Sels, T. Stora, I. Tsekhanovich, C. Van Beveren, P. Van Duppen, M. Veinhard, R. Wadsworth, F. Wienholtz, A. Welker, K. Wendt, G.L. Wilson, S. Witkins, R. Wolf, K. Zuber, In-source laser spectroscopy of mercury isotopes, CERN INTC, 2014. p. 424. Available: <http://cds.cern.ch/record/1953719>.

[19] K.M. Lynch, T.E. Cocolios, N. Althubiti, G.J. Farooq-Smith, A.J. Smith. A simple chamber for decay spectroscopy at CRIS-ISOLDE. Unpublished results.

[20] T. Ahn, H. Al-Azri, T. Bloch, P.A. Butler, N. Bree, T. Bäck, S. Bönig, J. Cederkäll, B. Cederwall, I.G. Darby, J. Diriken, D. O'Donnell, C. Fahlander, L.P. Gaffney, T. Grahn, B. Hadinia, M. Huyse, D.G. Jenkins, A. Johnson, P. Joshi, D.T. Joss, R. Julin, T. Kröll, J. Leske, B.S. Nara Singh, A. Nicholls, R.D. Page, J. Pakarinen, E.S. Paul, N. Pietralla, P. Rahkila, E. Rapisarda, M. Sandzelius, M. Scheck, J. Simpson, J.F. Smith, R. Wadsworth, P. Van Duppen, D. Voulot, F. Wenander, V. Werner, Coulomb Excitation of 116 Te: A Study of Collectivity Above the Z = 50 Shell Gap, CERN-INTC, 2011. p. 11. Available: <http://cds.cern.ch/record/1319097>.

[21] T. Day Goodacre, D. Fedorov, V.N. Fedosseev, L. Forster, B.A. Marsh, R.E. Rossel, S. Rothe, M. Veinhard, Laser resonance ionization scheme development for tellurium and germanium at the dual Ti:Sa-Dye ISOLDE RILIS, Nucl. Instr. Meth. Phys. Res. Sect. A: Accel., Spectrometers, Detectors Assoc. Equip. (in press), http://dx.doi.org/10.1016/j.nima.2015.10.066.

6.2 Further RILIS-mode characterization and application

Ion beam time structure measurements, measuring the extracted ion arrival time at a detector with respect to the laser pulses, offer a valuable probe to study laser-atom interaction regions. Such measurements, taken when in the RILIS mode of VADLIS operation, were discussed extensively in Section 6.1. By reducing the repetition rate of the laser applied for ionization from the standard 10 kHz, it is possible to observe the ion beam time structure over a longer period of time. Such measurements are presented in Figure 6.1, where ion beam time structure measurements from a standard HC-RILIS are plotted, with the ionizing laser operating at either 5 kHz and 10 kHz and from RILIS mode VADLIS operation with the ionizing laser operating at 2 kHz. The background observable in the HC-RILIS time structure is predominantly due to surface ionization, whereas in the RILIS mode of VADLIS operation it is nearly 100% laser related. The time structure of RILIS mode VADLIS operation presented in this Section was measured with a modified VADIS with an enlarged extraction aperture (from 1.5 mm to 2.5 mm) to better accommodate the RILIS lasers. Nevertheless, since the change in aperture size resulted in no observed difference in the ion source behaviour (efficiency, parameter optimization), the time structure measurements were deemed relevant.

The time structures were recorded with an MCP, using the experimental set-up and techniques discussed in Section 6.1. Two distinct components are visible in the time structures measured in HC-RILIS operation (Figure 6.1a). The first sharp component corresponds to the ionization of atoms at the extraction electrode and the mouth of the hot cavity. The second, broader component, corresponds to atoms ionized along the length of the hot cavity. These ions are accelerated towards the extraction aperture due to the longitudinal potential discussed in Section 5.2.1. The HC-RILIS time structure measurements confirm the understanding that the majority of the laser related ions are extracted within the 100 µs duty cycle of the lasers.

Figure 6.1b presents the time structure measurements of the laser ions extracted when operating the VADLIS in RILIS mode, with the ionizing laser operated with a 2 kHz repetition rate. It is clear that the laser ion residency time greatly exceeds 500 µs.

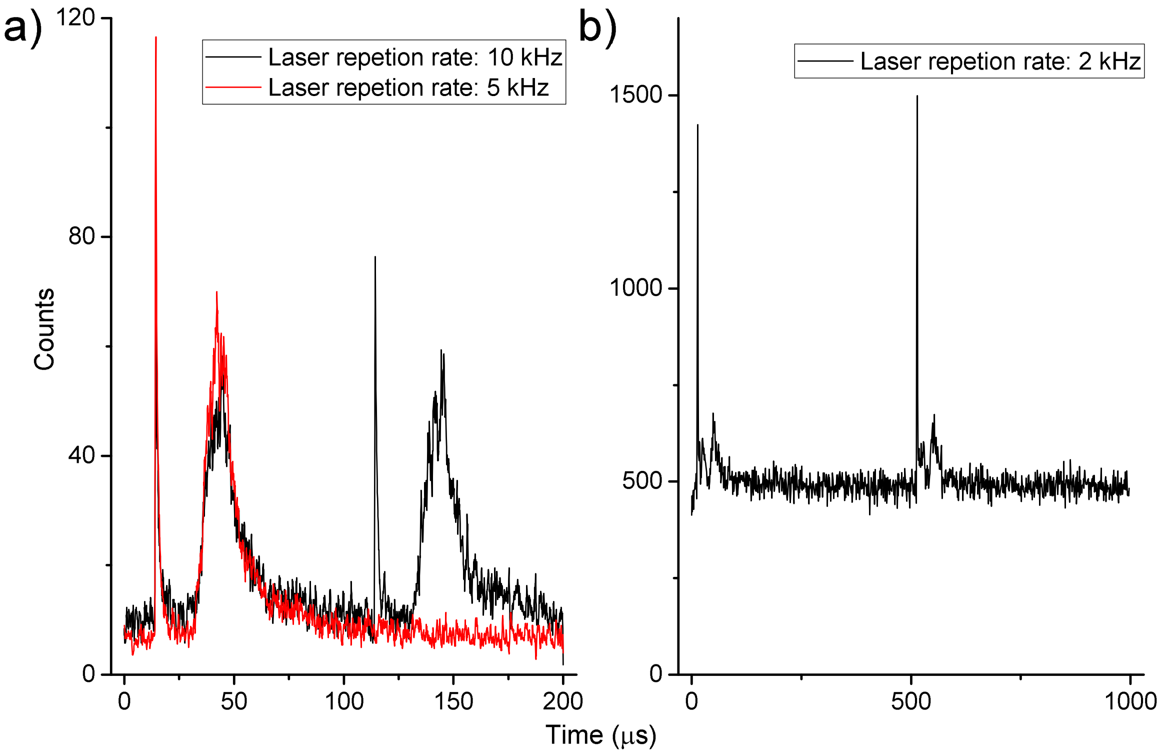

Figure 6.1: Ion beam time structures from a) HC-RILIS operation and b) RILIS mode VADLIS operation.

The discussion in Section 6.1 suggests that the extended residence time compared to that of the hot cavity is the result of a central potential well. Such a potential well had previously been suggested in VADIS mode operation, based on the simulation results of L. Penescu [74] using the charged particle optics software CPO [84]. The ion beam time structure measurements, presented in Section 6.1 and Figure 6.1b, support the idea that a similar potential well exists in the anode volume when operating in RILIS mode (anode voltage $\sim$ 5V). A new simulation campaign was initiated with the goal of gaining insights into both the RILIS mode of the VADLIS operation and FEBIAD sources in general.

The particle-in-cell (PIC) software VSIM [85] was identified as suitable for this task. A precursor to VSIM (VORPAL) was originally used by L. Penescu to study space charge effects in FEBIAD sources [86]. The potential benefits of VSIM compared to electrostatic simulation software such as CPO, is the capability of including the required physics to model plasmas, electron impact ionization and collisional ionization/neutralization, thus enabling a greater range of conditions to be taken into account. In PIC simulations a grid or mesh is overlaid on the structures in the simulation. The particles move throughout the simulation region in predefined time steps and at each time step the electromagnetic fields are calculated at the nodes of the grid boundaries and updated. The Courant condition [87] is typically applied, restricting the particles to no more than one grid boundary crossing per time step. As the mass of an electron is 3-5 orders of magnitude lower than that of an atom or ion, its velocity is correspondingly greater. The Courant condition therefore limits the possible duration of the time step, hindering attempts to obtain meaningful results within a reasonable time frame when simulating both ions and electrons, based on the available computer resources.

The nature of FEBIAD ion sources, compared to the previously used Modified Nielsen Ion Sources (MNIS) [88], reduced the need for the simultaneous simulation of the electrons with the ions and atoms. The major improvement the FEBIAD offered was the introduction of the anode grid [73], which enables the ion source to operate with a range of internal pressures, down to 10^{-5} mbar and ion currents below 1 µA. The relative insensitivity of the FEBIAD ion sources to variations in the pressure and ion load, implies the possibility to consider an electron dominated regime. In the RILIS mode of operation, the electron current is lower because of the reduction in the voltage applied to the anode. However, the extracted ion current is similarly reduced due to the selective nature of the RILIS mode of operation and does not typically exceed 10 nA.

An initial VSim simulation code was written working in collaboration with J. Smith from TechX. The further development and subsequent application of the code for FEBIAD optimization will form part of the PhD thesis of Y. Martinez. Early results from the VSim simulations are presented in Figure 6.2b, together with the results of simulations with CPO reported in [74] for comparison (Figure 6.2a).

For the VSim simulations, electrons were introduced from the rear of the anode cavity at each time step. The anode voltage and electron energies were set as 150 V and 5 V for the VADIS mode and RILIS mode simulations respectively. The simulations were run until the electron population within the anode cavity reached steady state conditions. Comparing the simulation results for VADIS mode operation between the CPO and VSIM simulations, a similar potential well is observable at the rear of the

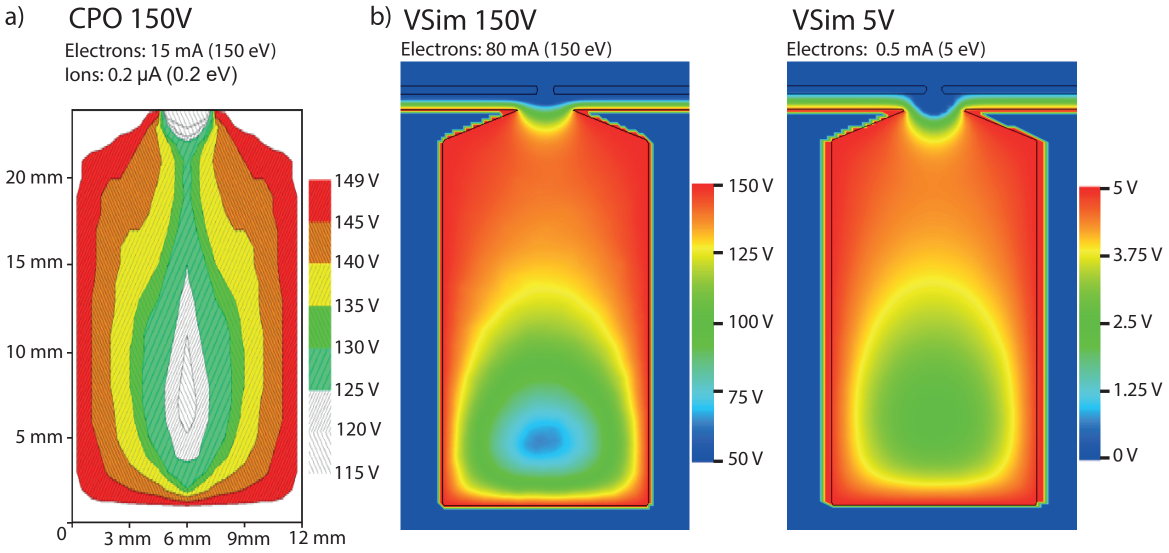

Figure 6.2: Simulation of the electric potential inside the VADLIS anode cavity in VADIS mode using CPO (from [74]) and VSim and in RILIS mode using VSim. Input parameters are discussed in the text.

anode cavity, with a similar potential distribution across the anode volume. There were several differences in the input parameters for the VSim simulations compared to the previous CPO simulations. The electron current was increased to 80 mA based on the current measured on the anode voltage supply during operation in VADIS mode and the ion contribution to the electric potential was not considered (based on the capability of the source to operate over a wide range of ion currents). These assumptions require further verification, however, despite this and the simulations being conducted using different software, the results are comparable, suggesting the validity of the approach.

When operating in RILIS mode, the electron current is no longer within the range of measurement using the anode voltage supply. Instead, the electron current resulting from the application of 5 V to the anode was estimated using Child's law for space charge limited electron emission, which states that the electron emission is proportional to $V^{3/2}$. Applying this relationship, the electron current was reduced to 0.5 mA. Comparing the VSim simulations for VADIS mode and RILIS mode operation (Figure 6.2b, a similar potential well is observable with 5 V applied to the anode. This is in good agreement with the interpretation of the time structure measurements. The results presented in Figure 6.2b represent only the results of initial proof of concept simulations. For example, the axial magnetic field created by the source magnet was not included and ion tracing within the electric potential is yet to be attempted. However, the simulation results support the discussion in Section 6.1 and indicate the suitability of this approach for future ion source optimization.

6.3 A truly versatile ion source

In addition to its application for the in-source RIS of exotic mercury isotopes, discussed in Chapters 9 to 11, the VADLIS developments have also been applied on-line at ISOLDE for an ISOLTRAP experiment. Ion beams of magnesium, sodium and neon were required for the study of the Q-values of mirror transitions for fundamental interaction studies [89]. A VD5 “hot plasma” (∼2000°C transfer line) VADIS was installed, coupled to a SiC target to try to achieve this. However, the contamination on mass A = 23 when operating in VADIS mode was too great for the measurement of ^{23}Mg. By switching to the RILIS mode of operation and applying the $\{\lambda_1\,|\lambda_2|\,\lambda_3\} = \{285\text{ nm}|553\text{ nm}|532\text{ nm}^{NR}\}$ RILIS ionization scheme for magnesium [90], the isobaric contamination was sufficiently reduced and the experiment could take place. Thus it was possible to make effective use of surface ionized, electron impact ionized and laser ionized radioactive ion beams from the same target-ion source unit.

An anode voltage scan was made in a similar manner to those described in Section 6.1, with 345 A applied to the cathode (∼1980°C). However, during this scan, the source magnet was optimized at each measurement point. The results are presented in Figure 6.3.

There is a smooth increase in the VADIS mode ion current with increasing anode voltage. Considering the laser ionized component, a clear low voltage RILIS mode of operation is once again observable. Under on-line conditions the RILIS mode and VADIS mode were again demonstrated to have to comparable efficiencies, with a doubling of the ion rate possible when operating in the RILIS + VADIS mode.

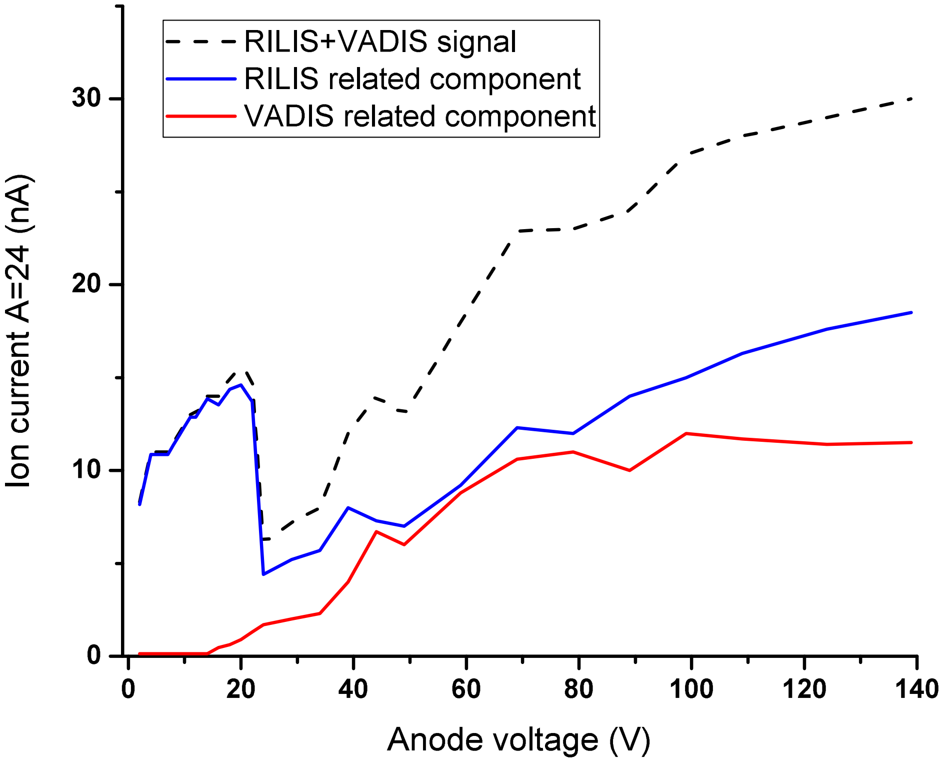

Figure 6.3: On-line VADLIS anode voltage scan for magnesium.

6.4 Outlook

A number of possibilities for future developments are discussed in Section 6.1. The comparable RILIS mode and VADIS mode ion signals presented in Sections 6.1 and 6.3, indicate a reasonable RILIS mode ionization and extraction efficiency, based on the understanding that the VADIS is a universal ion source [75]. This does not however, imply that the scope for optimization is limited. The time structure measurements indicate the efficiency of RILIS mode operation is linked to an ion survival time of >> 500µs, compensating for the slow extraction of laser ionized ions. One of the avenues of potential interest is the use of the VADIS mode to break up molecules and then the RILIS mode of operation to selectively ionize the constituent of interest, as discussed in Section 6.1. Ideas for achieving this involve the pulsing of the voltage applied to the anode to provide electrons with sufficient energy for molecular breakup, followed by ionization and extraction in the RILIS mode of operation. Such a method does not appear compatible with the current RILIS mode of operation due to the slow extraction of RILIS related ions. Optimization of the anode cavity to reduce the ion extraction time is therefore crucial for such developments to take place. Additionally, were extraction in the range of 10 µs to be achieved, then it could enable time-gating methods [91] to be applied for enhanced selectivity.

6.5 Conclusion

The coupling of the RILIS with the VADIS has now been demonstrated off-line for gallium and barium and on-line for mercury, cadmium and magnesium. The VADLIS is now an established ion source option at ISOLDE. The efficiency of the RILIS mode of operation appears to be linked to laser-ion survival times of >>500µs within the anode cavity. Early results from the simulation of the ion source, operating in both RILIS mode and VADIS mode, appear promising and are in agreement with the interpretation of ion beam time structure measurements: that the ion survival and comparatively slow extraction in RILIS mode is the result of a potential well forming at the rear of the anode cavity.

Chapter 7

Ionization scheme development for the ISOLDE RILIS

Ionization scheme development is required in order for new or more efficient ion beams to be produced by the ISOLDE RILIS. The selective nature of the ionization process requires an ionization scheme to be developed for each element of interest. This chapter presents the results of ionization scheme development for tellurium, germanium, chromium, mercury and radium.

7.1 Tellurium and germanium

Paper II

Laser resonance ionization scheme development for tellurium and germanium at the dual Ti:Sa-Dye ISOLDE RILIS [92]

Nuclear Instruments and Methods in Physics Research A 830 (2016) 510–514

Contents lists available at ScienceDirect

Nuclear Instruments and Methods in Physics Research A

journal homepage: www.elsevier.com/locate/nima

Laser resonance ionization scheme development for tellurium and germanium at the dual Ti:Sa–Dye ISOLDE RILIS ☆

T. Day Goodacre [a,b,*], D. Fedorov [c], V.N. Fedosseev [a], L. Forster [a], B.A. Marsh [a], R.E. Rossel [a,d,e], S. Rothe [a], M. Veinhard [a]

[a] CERN, CH-1211 Geneva 23, Switzerland
[b] School of Physics and Astronomy, The University of Manchester, Manchester M13 9PL, United Kingdom
[c] Petersburg Nuclear Physics Institute, 188350 Gatchina, Russia
[d] Institut für Physik, Johannes Gutenberg Universität, D-55099 Mainz, Germany
[e] Faculty of Design, Computer Science and Media, Hochschule RheinMain, Wiesbaden, Germany

ARTICLE INFO

Available online 26 October 2015

Keywords:
RILIS
ISOLDE
Germanium
Tellurium
Autoionizing
Laser ionization

ABSTRACT

The resonance ionization laser ion source (RILIS) is the principal ion source of the ISOLDE radioactive beam facility based at CERN. Using the method of in-source laser resonance ionization spectroscopy, a transition to a new autoionizing state of tellurium was discovered and applied as part of a three-step, three-resonance, photo-ionization scheme. In a second study, a three-step, two-resonance, photo-ionization scheme for germanium was developed and the ionization efficiency was measured at ISOLDE. This work increases the range of ISOLDE RILIS ionized beams to 31 elements. Details of the spectroscopy studies are described and the new ionization schemes are summarized.

1. Introduction

1.1. The RILIS at ISOLDE

ISOLDE is an ISOL (isotope separator on-line) type, radioactive ion beam facility based at CERN [1]. A pulsed 1.4 GeV proton beam of up to 2 μA is impacted upon a thick target, creating reaction products via spallation, fragmentation and fission, that are stopped and thermalized within the target material. Depending on the type and composition, the target is heated to between 400 °C and 2400 °C. Higher temperatures reduce the release time of sufficiently volatile elements, which diffuse through the target material and then effuse, via a transfer line, to an ion source.

The resonance ionization laser ion source (RILIS) is the principal ion source of the ISOLDE facility [2]. Laser ion sources of this type are based on two principles: for a particular element, the distribution of the atomic energy levels is unique; and electronic transitions between energy levels can be induced if the atom is illuminated with photons of an energy that matches the transition energy [3]. The RILIS uses multiple laser beams to step-wise excite and then liberate a valence electron from the element of interest. The selectivity of the ionization process follows as a consequence of the element unique distribution of atomic energy levels [4].

The ISOLDE RILIS is a dual Ti:Sa–Dye laser system with six tunable lasers, three Titanium:Sapphire (Ti:Sa) and three dye. All of the lasers produce pulsed light at 10 kHz and are pumped by frequency doubled Nd:YAG (532 nm) lasers, with the option to UV pump the dye lasers at 355 nm. The combination of Ti:Sa and dye lasers with 2ω, 3ω and 4ω frequency conversion enables continuous spectral coverage between 210 nm and 950 nm [2]. An independent 40 W, 10 kHz, TEM_{00}, frequency doubled $Nd{:}YVO_4$ (532 nm) Lumera Blaze laser, is available for ionization schemes which rely on a non-resonant ionizing step [5]. A schematic of the RILIS laser system and the experimental setup used for the scheme development is depicted in Fig. 1.

At ISOLDE, the RILIS laser ligth is are transported over a distance of approximately 20 m to converge within a hot-cavity ion source: a tantalum or tungsten tube 3 mm in diameter and 34 mm in length, which is connected to the target container via a transfer line. The entire target and ion source assembly is mounted on an ISOLDE frontend and maintained at a voltage between 20 kV and 60 kV, with a grounded extraction electrode positioned ~60 mm from the exit of the ion source. Resistive heating along the length of the hot cavity creates a voltage drop of ~2 V between the entrance and exit, causing ions to drift towards the penetrating field of the extraction electrode, where they are extracted and accelerated to form an ion beam. Ions generated upstream of the influence of the extraction field are therefore extracted with a low

---

☆ This paper was selected for a special edition of NIMA for LA^3NET.

* Corresponding author.
E-mail address: thomas.day.goodacre@cern.ch (T. Day Goodacre).

http://dx.doi.org/10.1016/j.nima.2015.10.066

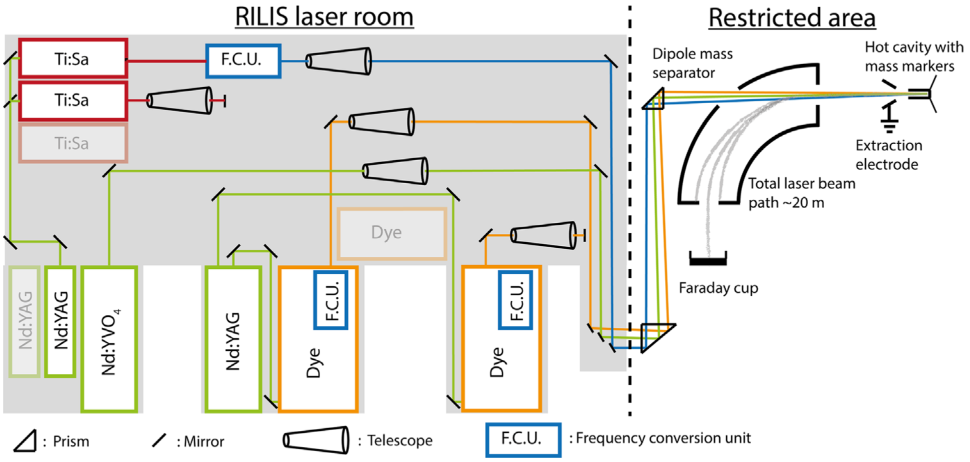

Fig. 1. Schematic of the RILIS layout and the experimental setup for the laser spectroscopy and efficiency measurements.

energy spread (typically <3 V). The ion beam passes through either one or two dipole mass separators, for isotope separation, before being directed to an experiment located in the ISOLDE Hall.

A consequence of the element-selective nature of the RILIS, is that a laser resonance ionization scheme must be developed and tested for each element. It is practical to use stable isotopes for scheme development, rather than relying on radiogenic production with a pulsed proton beam. A mass-marker capillary, containing a stable atomic sample, is connected to the transfer line between the target and ion source hot cavity. During RILIS scheme development, the laser beams are overlapped in the hot cavity and the mass-marker is evaporated while the laser wavelengths are scanned and the ion current is monitored using a Faraday cup located after the mass separator magnet, as depicted in Fig. 1. The laser wavelengths are measured using a HighFinesse WS7 wavemeter.

The spectroscopic studies described here were conducted using laser powers and linewidths identical to standard RILIS operation, to ensure the applicability of the results to on-line radioactive ion beam production at ISOLDE. A comprehensive description of the RILIS laser system can be found in the papers of Fedosseev et al. [2] and Rothe et al. [6].

1.2. Scheme development for the ISOLDE RILIS

The procedure for laser resonance ionization scheme development is described in detail by Fedosseev et al. [7]. The process begins with an assessment of literature data on atomic lines and energy levels. The primary sources of information are the Kurucz and NIST atomic line databases [8,9]. There are a number of relevant factors that determine the suitability of an atomic level or transition for use within an ionization scheme. The possibility to saturate a transition with the available laser power, can be estimated by considering literature data on transition strengths. Candidate transitions are compared to transitions used in existing RILIS ionization schemes, for which the laser power required for saturation has been measured. Thermally populated atomic levels divide the atomic population available to the first excitation step of the laser ionization scheme. In order to determine the optimal starting point of an ionization scheme, the percentage of atoms, P_a, with a valence electron excited to a thermally populated state, a, in the hot cavity environment can be calculated by applying Boltzmann's equation in a form given in the following equations:

$$\phi = g_a \exp(E_a/kT) \tag{1}$$

$$\Phi = \sum_i g_i \exp(E_i/kT) \tag{2}$$

$$P_a = (\phi/\Phi) \times 100 \tag{3}$$

where g is the degeneracy of the atomic state, the subscript a represents a specific atomic state, E is the energy of the atomic state, k is Boltzmann's constant, T is the temperature of the hot cavity in kelvin (K) and the subscript i represents the group of atomic states with a significant thermal population T. Where possible, an excitation path via states with progressively increasing total angular momentum (J) is preferable. This is because the theoretical maximum efficiency of an excitation is greater if the statistical weight $(2J+1)$ of the upper level of the atomic excitation is greater than that of the lower level. The width of an atomic transition in the hot cavity environment must also be considered, this is particularly important if a pronounced hyperfine splitting is expected. An incomplete spectral overlap of the excitation lasers with the resonant transition restricts the accessible atomic population, thereby reducing the ionization efficiency.

2. Tellurium

In addition to ion beam production, the RILIS can also serve as a tool for signal identification. RILIS ionized tellurium is required to enable signal identification for an approved Coulomb excitation experiment investigating ^{116}Te and ^{118}Te [10]. At ISOLDE, tellurium beams have thus far been produced using arc discharge ion sources, which do not offer the element selective capabilities of a RILIS [11]. Recent work at ISOLDE has demonstrated the possibility to couple the RILIS with the VADIS, the ISOLDE variant of the FEBIAD type arc discharge ion source, for laser resonance ionization inside the VADIS anode cavity [12]. The combination, termed the VADLIS or Versatile Arc Discharge and Laser Ion Source, has enabled the possibility of switching to an element selective RILIS-Mode of operation, should either a reduction in isobaric contamination or signal identification be required. The element selectivity of the RILIS provides the option to selectively reduce the tellurium ion rate when operating in RILIS-Mode, by blocking and unblocking one of the laser beams, offering an effective signal identification tool for the analysis of gamma spectra. The experimental setup used for this development work is shown in Fig. 1.

Laser resonance ionization of tellurium was applied previously at ISOLDE as part of a COMPLIS experiment where a two-resonance, three-step scheme of $\{\lambda_1 | \lambda_2 | \lambda_3\} = \{214.35\ \text{nm} | 591.53\ \text{nm} | 1064\ \text{nm}\}$ (vacuum wavelengths) was applied [13]. The experiment did not involve ionization inside a hot cavity, thus there were no measured efficiencies applicable to this work. A rich continuum of autoionizing states of tellurium was identified previously using flash pyrolysis and other non-laser light sources [14–16]. Autoionizing resonances have also been investigated at Oak Ridge National Laboratory (private communication Y. Liu).

Using Eqs. (1)–(3), in a hot cavity ion source at 2300 K we expect a 95% population of the $5P^4\ {}^3P_2$ ground state. Thus only schemes involving transitions from the atomic ground state were considered. According to the NIST database [9], the first-step transition from the atomic ground state within the RILIS wavelength range and with the largest photo absorption cross-section, is the 214.281 nm ($5p^4\ {}^3P_2 \longrightarrow 5p^3({}^4S^o)6s\ {}^3S_1^o$) transition. From the $5p^3({}^4S^0)6s\ {}^3S_1^0$ state, six second-step transitions, also listed in the databases, were observed while scanning a R6G dye laser from 16 805 cm^{-1} to 17 785 cm^{-1}. The four second-step transitions corresponding to the highest ion signals during the scan, were tested as part of three-step, two-resonance ionization schemes, using 532 nm photons from the Blaze laser for non-resonant ionization step. The ion currents recorded for each scheme are compared in Table 1. A search for autoionizing resonances was conducted by replacing the 532 nm third-step laser with a tunable Ti:Sa laser. The search was limited to transitions from the upper level of the two most effective second-step transitions of 573.360 nm and 578.922 nm. A new autoionizing state at 75 181.41 (20) cm^{-1} was identified as part of a {214.281 nm| 573.360 nm| 901.270 nm} scheme.

Comparing the measured ion currents, the autoionizing resonance was a factor of 2.5 more efficient than non-resonant ionization with an estimated 24 W in the ion source. Saturation was verified for the first two resonant transitions, the maximum RILIS laser powers delivered to the ion source for 214 nm light and 573 nm light were estimated to be 25 mW and 6 W respectively. The autoionizing resonance was not saturated with an estimated 1 W of laser light, at 901.270 nm, delivered to the source. The optimal scheme and scans of the 573.360 nm second-step transition and the autoionizing resonance are presented in Fig. 2.

Following this scheme development, the ISOLDE RILIS is now capable of offering signal identification of tellurium related signals, as requested by the IS516 Coulomb excitation experiment, and tellurium ion beam production. Further scheme development, to investigate alternative autoionizing states for a potentially more efficient scheme, is a possibility for future development.

3. Germanium

RILIS ionized germanium beams are required for the study of the β^+/EC decay of ^{64}Ge and ^{66}Ge by total absorption spectroscopy [18]. A three-step, Ti:Sa only, laser ionization scheme with a final step transition to an autoionizing state was developed at ORNL. An efficiency of 3.3% was reported for stable germanium [19].

Based on Eq. (1), and using information from the Kurucz and NIST databases [8,9], the majority of the thermal population at 2300 K is distributed between two atomic states, with 40% lying in the $4s^24p^2\ {}^3P_1$ state at 557.134 cm^{-1} and 39% lying in the $4s^24p^2\ {}^3P_2$ state at 1409.961 cm^{-1}. Consequently, schemes starting from either $4s^24p^2\ {}^3P_1$ or $4s^24p^2\ {}^3P_2$ were considered. A 275.459 nm transition ($4s^24p^2\ {}^3P_2 \longrightarrow 4s^24p5s\ {}^3P_1^0$) was selected from the atomic lines tabulated in literature because of an expectation of saturation and a wavelength that could be produced by frequency doubling the light from a dye laser pumped at 532 nm. From the $4s^24p5s\ {}^3P_1^0$ state, four second-step transitions, also documented in literature, were compared as part of two-resonance, three-step schemes with

Table 1
The resonant transitions tested during the tellurium scheme development. Spectroscopic information for known transitions is taken from [9].

Transition (cm^{-1})	Upper state config., term, *J*	Wavenumber (cm^{-1})	Air wavelength (nm)	Relative ion current
0–46 652.738	$5p^3({}^4S^o)6s$, $^3S^0$, 1	46 652.74	214.281	–
46 652.738–63 669.944	$5p^3({}^4S^o)7p$, b ^5P, 1	17 017.21	587.478[a]	0.35[b]
46 652.738–63 921.485	$5p^3({}^4S^o)7p$, ^3P, 2	17 268.75	578.922	1[b]
46 652.738–63 982.463	$5p^3({}^4S^o)7p$, ^3P, 0	17 329.73	576.883[a]	0.24[b]
46 652.738–64 088.997	$5p^3({}^4S^o)7p$, ^3P, 1	17 436.26	573.360	0.74[b]
64 088.997–75 181.41 (20)	New	11 092.41 (20)	901.270[a]	2.5

[a] Air wavelengths calculated using the equation of [17].

[b] Ion current measured with ~24 W of 532 nm light delivered to the ion source for the third, non-resonant, ionization step.

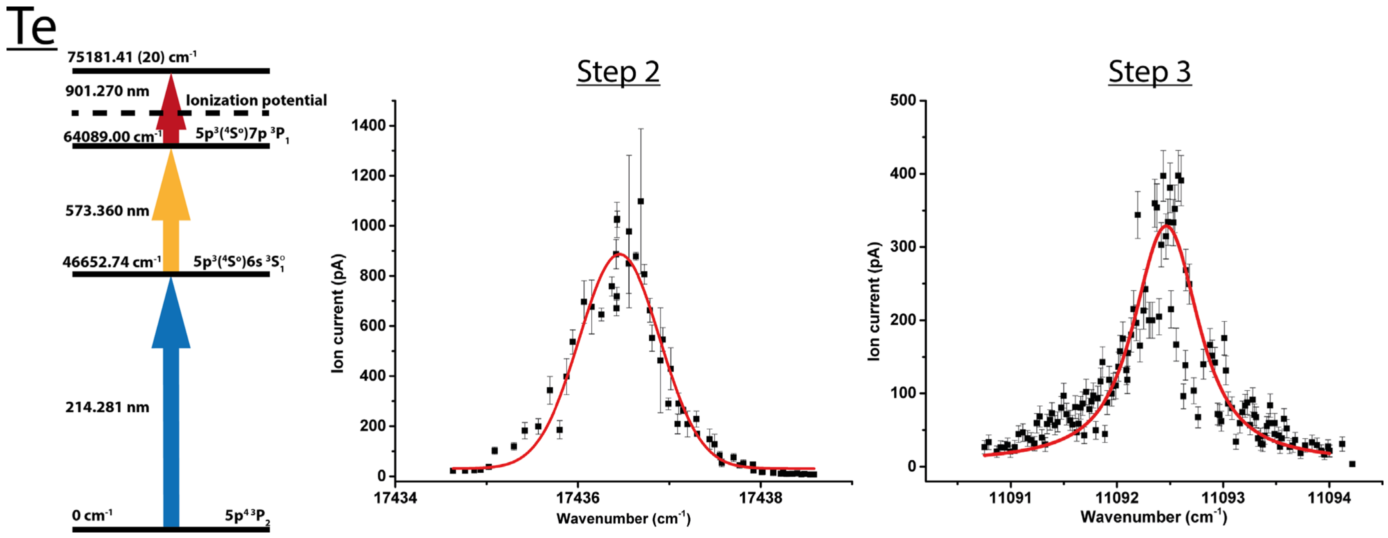

Fig. 2. The optimal tellurium RILIS scheme and laser scans of the second-step and the third-step, autoionizing resonance.

Table 2
The resonant transitions tested during the germanium scheme development. Spectroscopic information is taken from [9].

Transition (cm^{-1})	Upper state config., term, J	Wavenumber (cm^{-1})	Air wavelength (nm)	Relative ion current
1409.961–37 702.305	4s^{2}4p5s, ^{3}P^0, 1	36 292.34	275.459	–
37 702.305–54 935.848	4s^{2}4p6p, ^{3}D, 1	17 233.54	580.103	0.10[a]
37 702.305–55 235.834	4s^{2}4p6p, ^{1}P, 1	17 533.53	570.178	0.27[a]
37 702.305–55 266.090	4s^{2}4p6p, ^{3}D, 2	17 563.79	569.196	1[a]
37 702.305–55 503.203	4s^{2}4p6p, ^{3}P, 0	17 800.90	561.614	0.26[a]

[a] Ion current measured with ~24 W of 532 nm light delivered to the ion source for the third, non-resonant, ionization step.

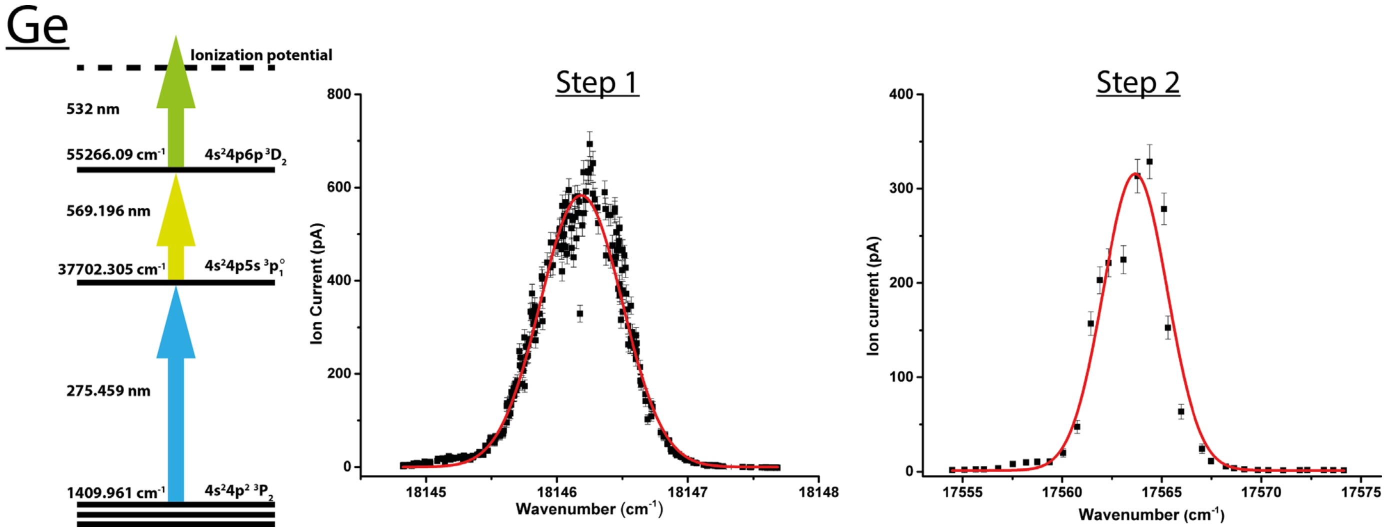

Fig. 3. The most efficient of the tested germanium ionization schemes and scans of the first and second resonances.

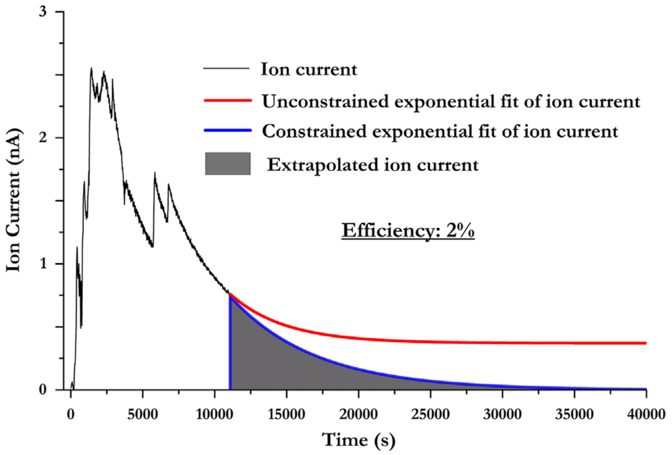

Fig. 4. Laser ionized ^{76}Ge ion current against time during the efficiency measurement.

532 nm photons from the Blaze laser for non-resonant ionization. The results are summarized and compared in Table 2.

The optimal RILIS scheme and laser scans of the first two steps are presented in Fig. 3. Our measurements indicate that the first and second-step transitions were strongly saturated with 580 mW and 14 W respectively on the laser table, estimated to correspond to 300 mW and 5.6 W in the source.

An efficiency measurement was performed for the RILIS scheme depicted in Fig. 3 using a calibrated mass marker of germanium. During the sample evaporation, the laser ion signal was measured on a Faraday cup located after the dipole mass separator magnet. The recorded ion current is plotted against measurement time in Fig. 4. The ion current was integrated over the measurement time in order to extract a lower limit for the ionization efficiency.

The sharp increases in the measured ion current, depicted in Fig. 4, are due to increases in the heating of the calibrated mass marker. Due to time constraints, the measurement was terminated before the sample had been fully evaporated. An extrapolation of the exponential decrease of the ion current was required. A conservative value for the efficiency was determined by constraining the extrapolation to reach zero. An unconstrained extrapolation converged on a 370 pA ion current, suggesting a significant quantity of un-evaporated germanium remaining in the system. The integration over time, of the measured ion current and the constrained extrapolated ion current depicted in Fig. 4, gives a lower limit estimate for the laser ionization scheme efficiency of 2%.

There are two possibilities for improving the efficiency of the germanium ionization scheme: a two-fold efficiency increase could be expected by accessing a larger fraction of the atomic population through the application of an additional first-step laser at 269.134 nm, to excite from the 40% populated (at 2300 K) 4s^{2}4p^2 ^{3}P$_1$ state to the 4s^{2}4p5s ^{3}P$^0_1$ state; or further ionization scheme development to identify useful autoionizing resonances. The application of an additional first-step, to access atoms in a thermally populated state, is standard practice at the ISOLDE RILIS for the ionization of gallium.

4. Conclusion

A new three-step, three-resonance RILIS ionization scheme for tellurium has been developed with a final step transition to a newly identified autoionizing state. The scheme provides sufficient enhancement of the tellurium ion rate to satisfy the needs of signal identification during Coulomb excitation studies at ISOLDE.

With approximately 1 W of laser power delivered to the ion source, the autoionizing resonance was a factor of 2.5 more efficient than a non-resonant ionization step using 24 W of 532 nm light in the source.

Secondly, a new three-step, two-resonance RILIS scheme for germanium was identified and tested using the ISOLDE RILIS. A laser ionization efficiency of $>2\%$ was measured. This efficiency can be increased by the application of an additional first-step to access another thermally populated low-lying atomic energy level, possibly increasing the efficiency of the scheme to $>4\%$. This work extends the range of RILIS ionized beams at ISOLDE to 31 elements.

Acknowledgements

This project has received funding from the European Union's Seventh Framework Programme for research, technological development and demonstration under grant agreements: 262010 (ENSAR), 267194 (COFUND) and 289191 (LA^{3}NET).

References

[1] E. Kugler, Hyperfine Interactions 129 (1/4) (2000) 23.
[2] V.N. Fedosseev, L.-E. Berg, D.V. Fedorov, D. Fink, O.J. Launila, R. Losito, B. A. Marsh, R.E. Rossel, S. Rothe, M.D. Seliverstov, A.M. Sjodin, K.D.A. Wendt, Review of Scientific Instruments 83 (2) (2012) 02A903.
[3] V.S. Letokhov, Laser Photoionization Spectroscopy, 1st ed., Academic Press Inc., London, 1987.
[4] V.N. Fedosseev, Yu. Kudryavtsev, V.I. Mishin, Physica Scripta 85 (May (5)) (2012) 058104.
[5] B. Marsh, T. Day Goodacre, D. Fink, S. Rothe, M. Seliverstov, N. Imai, M. Sjodin, R. Rossel, Suitability Test of a High Beam Quality Nd:YVO4 Industrial Laser for the ISOLDE RILIS Installation, Technical Report, CERN, Geneva, 2013.
[6] S. Rothe, T. Day Goodacre, V.N. Fedosseev, B.A. Marsh, R.E. Rossel, M. Veinhard, K.D.A. Wendt, Laser ion beam production at CERN-ISOLDE: new features—more possibilities. Nuclear Instruments and Methods in Physics Research Section B: Beam Interactions with Materials and Atoms, (Proceedings of The International Conference on Electromagnetic Isotope Separators and Related Topics (EMIS), Grand Rapids, Michigan, USA, May 11–15).
[7] V.N. Fedosseev, B.A. Marsh, D.V. Fedorov, U. Köster, E. Tengborn, Hyperfine Interactions 162 (April (1–4)) (2006) 15.
[8] P.L. Smith, H. Claas, J.R. Esmond, R.L. Kurucz, Atomic spectral line database.
[9] A. Kramida, Yu. Ralchenko, J. Reader, and the NIST ASD Team, NIST atomic spectra database (ver. 5.2), [Online], 2014.
[10] T. Ahn, H. Al-Azri, T. Bloch, P.A. Butler, N. Bree, T. BäcK, S. Bönig, B. Cederwäll, I. D. Darby, J. Diriken, D. O'Donnell, C. Fahlander, L.P. Gaffney, T. Grahn, B. Hadinia, M. Huyse, D. G. Jenkins, A. Johnson, P. Joshi, D. T. Joss, R. Julin, T. Kröll, J. Leske, B.S. Nara Singh, A. Nicholls, R.D. Page, J. Pakarinen, E.S. Paul, N. Pietralla, P. Rahkila, E. Rapisarda, M. Sandzelius, M. Scheck, J. Simpson, J.F. Smith, R. Wadsworth, P. Van Duppen, D. Voulot, F. Wenander, V. Werner, Coulomb Excitation of 116Te and 118Te: a Study of Collectivity Above the Z=50 Shell Gap, Technical Report, CERN-INTC, Geneva, 2011.
[11] U. Köster, U.C. Bergmann, D. Carminati, R. Catherall, J. Cederkäll, J.G. Correia, B. Crepieux, M. Dietrich, K. Elder, V.N. Fedoseyev, L. Fraile, S. Franchoo, H. Fynbo, U. Georg, T. Giles, A. Joinet, O.C. Jonsson, R. Kirchner, Ch. Lau, J. Lettry, H.J. Maier, V.I. Mishin, M. Oinonen, K. Peräjärvi, H.L. Ravn, T. Rinaldi, M. Santana-Leitner, U. Wahl, L. Weissman, Nuclear Instruments and Methods in Physics Research Section B: Beam Interactions with Materials and Atoms 204 (May) (2003) 303.
[12] T. Day Goodacre, J. Billowes, R. Catherall, T.E. Cocolios, B. Crepieux, D. Fedorov, V.N. Fedosseev, J.P. Ramos, L.P. Gaffney, A. Gottberg, K.M. Lynch, B.A. Marsh, T. M. Mendonca, R.E. Rossel, S. Roth, S. Sels, C. Sotty, T. Stora, C. Van Beverene, M. Veinhard, Extending the capabilities of the ISOLDE RILIS by blurring the boundaries between ion sources at ISOLDE, Nuclear Instruments and Methods in Physics Research Section B: Beam Interactions with Materials and Atoms, (Proceedings of The International Conference on Electromagnetic Isotope Separators and Related Topics (EMIS), Grand Rapids, Michigan, USA, May 11–15).
[13] R. Sifi, F. Le Blanc, N. Barré, L. Cabaret, J. Crawford, M. Ducourtieux, S. Essabaa, J. Genevey, G. Huber, M. Kowalska, C. Lau, J.K.P. Lee, G. Le Scornet, J. Oms, J. Pinard, B. Roussière, J. Sauvage, M. Seliverstov, H. Stroke, Hyperfine Interactions 171 (July (1–3)) (2006) 173.
[14] J. Berkowitz, C.H. Batson, G.L. Goodman, Physical Review A 24 (July (1)) (1981) 149.
[15] A.M. Cantú, M. Mazzoni, Y.N. Joshi, Physica Scripta 27 (April (4)) (1983) 261.
[16] M. Mazzoni, A.M. Cantu, Y.N. Joshi, Journal of Physics B: Atomic and Molecular Physics 16 (September (17)) (1983) 3183.
[17] K.P. Birch, M.J. Downs., Metrologia 30 (January (3)) (1993) 155.
[18] E. Nacher, C. Domingo, J.A. Algora, A. Briz, M. Carmona, A. Illana, A. Jungclaus, A. Peria, V. Pesudo, G. Ribeiro, J. Sanchez-del Rio, P. Sarriguren, J. Taprogge, O. Tengblad, J. Agramunt, G. Guibrone, V. Guadilla, A. Montaner, S.E.A. Orrigo, B. Rubio, J.L. Tain, E. Valencia, J. Jose, A. Parikh, L.M. Fraile, I. Marroquin, O. Moreno, B. Olaizola, V. Paziy, J.M. Udias, V. Vedia, M.J.G. Borge, T. Day Goodacre, V. Fedosseev, B. Marsh, E. Rapisarda, T. Stora, W. Gelletly, P. Regan, Z. Podolyak, S. Rice, R Orlandi, M. Carmona, et al., Beta Decay of the N=Z, rp-Process Waiting Points: 64Ge, 68Se and the N=Z+2: 66Ge, 70Se for Accurate Stellar Weak-Decay Rates, Technical Report, CERN-INTC, Geneva, 2013.
[19] Y. Liu, C. Baktash, J.R. Beene, H.Z. Bilheux, C.C. Havener, H.F. Krause, D. R. Schultz, D.W. Stracener, C.R. Vane, K. Brück, Ch. Geppert, T. Kessler, K. Wendt, Nuclear Instruments and Methods in Physics Research Section B: Beam Interactions with Materials and Atoms 243 (February (2)) (2006) 442.

7.2 Chromium

Paper III

The identification of autoionizing states of atomic chromium for resonance laser photo-ionization at the ISOLDE-RILIS

The identification of autoionizing states of atomic chromium for the resonance ionization laser ion source (RILIS) of the ISOLDE radioactive ion beam facility

T. Day Goodacre*[a,b], K. Chrysalidis[a,d], D.V. Fedorov[c], V. N. Fedosseev[a], B. A. Marsh[a], P.L. Molkanov[c], R. E. Rossel[a,d,e], S. Rothe[a], C. Seiffert[a]

[a] *CERN, CH-1211 Geneva 23, Switzerland*
[b] *School of Physics and Astronomy, The University of Manchester, Manchester, M13 9PL, United Kingdom*
[c] *Petersburg Nuclear Physics Institute, 188350 Gatchina, Russia*
[d] *Institut für Physik, Johannes Gutenberg Universität, D-55099 Mainz, Germany*
[e] *Faculty of Design, Computer Science and Media, Hochschule RheinMain, Wiesbaden, Germany*

Abstract

This paper presents the results of an investigation into autoionizing states of atomic chromium, in the service of the Resonance Ionization Laser Ion Source (RILIS): the principal ion source of the ISOLDE radioactive beam facility based at CERN. The multi-step resonance photo-ionization process enables element selective ionization which, in combination with mass separation, allows isotope specific selectivity in the production of radioactive ion beams at ISOLDE. The element selective nature of the process requires a multi-step "ionization scheme" to be developed for each element. Using the method of in-source resonance ionization spectroscopy, an optimal three-step, three-resonance photo-ionization scheme originating from the $3d^5(^6S)4s\ a^7S_3$ atomic ground state has been developed for chromium. The scheme uses an ionizing transition to one of the 15 newly observed autoionizing states reported here. Details of the spectroscopic studies are described and the new ionization scheme is summarized.

Keywords: Resonance ionization laser ion source, ISOLDE, chromium, autoionizing states, laser ionization

---

1. Introduction

The Resonance Ionization Laser Ion Source (RILIS) [1], of the ISOLDE radioactive beam facility [2], utilizes the technique of multi-step resonance photo-ionization for the element selective ionization of ISOLDE reaction products. We present here a new RILIS "ionization scheme" for atomic chromium, which will enable multiple experiments to take place at ISOLDE, in fields ranging from solid state physics to fundamental nuclear physics.

ISOLDE is an isotope separator on-line (ISOL) type radioactive ion beam facility, connected to the CERN accelerator complex. Radionuclides are produced with a pulsed 1.4 GeV proton beam of up to 2 μA average current that is impacted upon a "thick target". Reaction products, created via fragmentation, spallation and fission, are stopped and thermalized within the target material. The target is heated to enable sufficiently volatile elements to diffuse through the target material and then effuse, via a transfer line, to an ion source typically for 1+ ionization.

The RILIS is the principal ion source of the ISOLDE facility, used for >75 % of the ISOLDE physics experiments in 2015. The hot cavity RILIS is based on the following three principles:

1. The distribution of the atomic energy levels is unique to a particular element.
2. Electric dipole transitions between electronic states of the atom can be driven by an external photon field, when the photon energy corresponds to the transition energy.
3. Ion survival in the hot cavity environment (typically a 3 mm internal diameter refractory metal tube heated to between 2300 K and 2400 K) is enhanced by a radial potential well along the length of the cavity resulting from thermally induced electron emission [1].

The RILIS targets a progressive series of resonant atomic excitations, using multiple tunable lasers, before a final ionizing step: either a resonant transition to an autoionizing state or non-resonant excitation to the ionization continuum [3]. Ionization via an autoionizing resonance is preferred as the photo-absorption cross-section for resonant transitions can be orders of magnitude higher than for non-resonant ionization, often making saturation of the transition feasible with the typically available laser power [1].

The consequence of targeting the element unique electron energy levels is that the laser ionization process is element selective; however, it also requires a multi-step resonance photo-ionization scheme to be developed for each element the RILIS is applied for. The development of a RILIS scheme for chromium was initiated following a request from the ISOLTRAP collaboration: for the application of the RILIS in the production of chromium ion beams for mass measurements of neutron rich chromium isotopes [4] and interest from the ISOLDE solid state physics group: for the use of ^{48}Cr as a magnetic probe for Perturbed Angular Correlation (PAC) spectroscopy (private communication Karl John-

---

*thomas.day.goodacre@cern.ch

ston, ISOLDE Physics coordinator). Previous chromium production at ISOLDE used arc discharge ion sources, most recently a VD5 "hot plasma" variant of the ISOLDE Versatile Arc Discharge Ion Source (VADIS), coupled to a ZrO_2 or a Y_2O_3 target [5]. The "universal" ionization efficiency of the VD5 VADIS limits the achievable beam purity of the radioactive ion beams, due to isobaric contamination, particularly if a UC_x target is used [6]. Furthermore, the VADIS anode cavity is only heated radiatively and by electron bombardment, rather than by direct ohmic heating as used for the hot cavity. The effect of wall sticking times becomes increasingly significant with decreasing half-lives, particularly for less-volatile elements such as chromium. The achievable VADIS ionization efficiency may therefore be hindered more by wall sticking times than the achievable efficiency of RILIS ionization in a hot cavity. A viable RILIS scheme therefore enhances the purity of chromium ion beams at ISOLDE, offers the advantages of element selective ionization with the RILIS such as the ability to remove the laser ionized chromium component of the ion beam by blocking one of the resonant transitions, enabling measurements to be made both with the lasers blocked and unblocked for signal identification and can be expected to reduce the release time from the ion source assembly.

2. Ionization of chromium atoms in a hot cavity

2.1. Surface ionization

Chromium has a first ionization potential of 6.77 eV [7]. Consequently, with sufficient heating of a sample of stable chromium, a surface ion signal, measurable on an ISOLDE Faraday cup (>100 fA), is expected from a tungsten hot cavity ion source heated to 2400 K. The efficiency of the surface ionization process (E_{surf}) is largely dependent on the ionization potential (IP) of the element and the work function of the cavity surface, it can be estimated using a modified Saha-Langmuir equation which takes into account the hot cavity environment [8, 9]. This equation requires the effective ionization potential (IP_{ef}) to be calculated [10]:

$$Q_x = \sum_j g_j \exp(-E_j/kT) \tag{1}$$

$$IP_{ef} = IP - kT\ln(Q_i/Q_a) \tag{2}$$

where Q is a partition function accounting for the influence of the ground or excited states j of the atom ($x = a$) or the ion ($x = i$), g is the degeneracy of the atomic or ionic state, E_j is the excitation energy of a particular state, k is Boltzmann's constant and T is the temperature. The IP_{ef} can then be inserted into a modified Saha-Langmuir equation to give an expected surface ionization efficiency E_{surf}:

$$\psi = N \times \omega \times \exp((\phi - IP_{ef})/kT) \tag{3}$$

$$E_{surf} = \psi/(1 + \psi) \tag{4}$$

where N is the number of collisions with the cavity walls (estimated as the surface area of the cavity walls divided by the cross-sectional area of the exit aperture) [8], ω is the ion survival probability and ϕ is the work function of the cavity surface.

The ion survival probability, ω, is dependent on thermally induced electron emission from the cavity walls establishing a radial potential well for positive ions along the length of the cavity. This reduces the probability of ion-wall collisions and corresponding recombination rates, therefore improving the overall ion extraction efficiency [8, 1]. Sufficient data (RILIS and surface ionization efficiencies) has been obtained experimentally for scandium [11], to enable an estimate to be made of $\omega \approx 0.1$ in a tungsten hot cavity heated to 2400 K. This value is applicable for the estimation of the chromium efficiency under the assumption that, for stable isotopes, ω is cavity work function, rather than element, dependent and considering that scandium and chromium have a similar mass. Taking $\omega = 0.1$ and using Equations 1-4, the surface ionization efficiency of chromium in a tungsten hot cavity heated to 2400 K, was calculated to be ~0.01 %.

Inaccuracies in this calculation could stem from three factors. A poisoning of the surface of the hot cavity can change the work function ϕ. The ion survival rate ω, has been demonstrated to be dependent on cavity temperature, surface contamination, ion load and the neutral pressure within the cavity [8], all of which can vary over time. Wayne et al. [12] suggest an additional ionization process due to electron impact ionization, not considered in the modified Saha-Langmuir equation. This is in agreement with the extensive simulations of Turek [13], which also suggest that the contribution of electron impact ionization to the total ionized fraction increases with greater ionization potentials and decreasing half lifes. Consequently, electron impact ionization was not considered when estimating the efficiency of the surface ionization of ^{52}Cr for benchmarking RILIS ionization schemes for chromium.

2.2. RILIS Ionization

The procedure used for laser resonance ionization scheme development for the ISOLDE-RILIS was reviewed by Fedosseev et al. [11]. According to Boltzmann's equation, the $3d^5(^6S)4s\ a^7S_3$ atomic ground state of chromium is 97 % populated at 2400 K. Thus, all of the RILIS schemes considered for chromium originate from the atomic ground state. Extensive atomic line data is available for chromium, including numerous autoionizing states [14, 7, 15]. Following a review of these atomic lines and energy levels, suitable first and second steps for a RILIS scheme were identified, details of the transitions are presented in Table 1. The upper level of the second transition lies at an energy of 42 261.226 cm^{-1}, ~12 314 cm^{-1} (~812 nm) below the ionization threshold [7]. When considering the suitability of a transition, information concerning the photoabsorption cross-section of the candidate transition was compared to data for similar transitions used in existing RILIS schemes, for which a saturation measurement has been performed. This provides a reliable estimate of the feasibility of saturating a proposed transition with the laser power that is typically available from the RILIS lasers. Neglecting the polarization of the laser

Table 1: The first and second resonant transitions used in the chromium scheme development originating from the $3d^5(^6S)4s\ a^7S_3$ ground state. Spectroscopic information is taken from the NIST database [7].

Transition (cm^{-1})	Upper state configuration	Term	J	Wavenumber (cm^{-1})	Air wavelength (nm)
0 - 27 935.241	$3d^4(^5D)4s4p^3P°$	$y^7P°$	4	27 935.241	357.869
27 935.241 - 42 261.226	$3d^5(^6S)4d$	e^7D	5	14 325.985	697.840

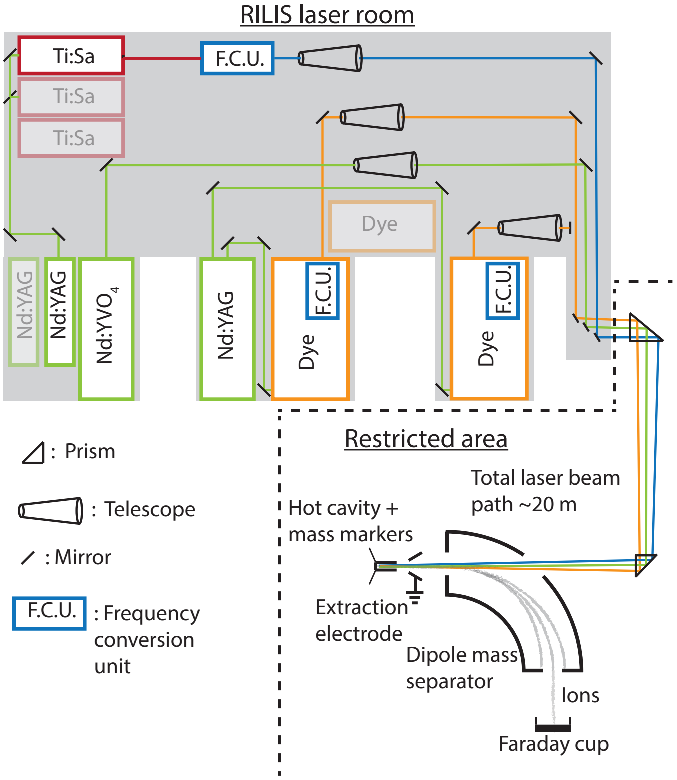

Figure 1: RILIS at ISOLDE. Schematic of the RILIS layout and the experimental set-up for the development of a RILIS scheme for chromium.

light, an excitation scheme consisting of states with progressively increasing statistical weights is preferred as this increases the maximum achievable ionization efficiency in the RILIS ionization geometry [16].

3. Experimental setup

The RILIS scheme development for chromium took place at ISOLDE using the RILIS laser system and a tungsten hot cavity ion source mounted on the ISOLDE General Purpose Separator (GPS) front-end [2]. The ISOLDE-RILIS is primarily made up of broadly tunable lasers to maximize the spectral range and flexibility of the system, with a combination of three dye lasers and three Titanium:Sapphire (Ti:Sa) lasers. The RILIS laser parameters are described in detail by Fedosseev et al. and Rothe et al. [17, 18].

An independent 40 W average power, TEM_{00}, frequency doubled $Nd:YVO_4$ (532 nm) Lumera Blaze laser, is available for ionization schemes using a non-resonant final ionizing step [19]. The lasers are pulsed at a repetition rate of 10 kHz, approximately the frequency required to ensure atoms effusing through the ion source are illuminated by a minimum of one set of laser pulses. The tunable lasers are typically pumped by frequency doubled Nd:YAG (532 nm) lasers, however, the dye lasers can also be pumped with the third harmonic of the Nd:YAG (355 nm) to extend their tuning range. Through the use of non-linear optics for 2nd, 3rd and 4th harmonic generation, an unbroken spectral coverage between 210 nm and 950 nm is achieved. The wavelengths of the RILIS lasers are measured using a HighFinesse/Ångstrom WS7 wavelength meter. Two dye lasers, one frequency doubled Ti:Sa laser and the 532 nm Blaze laser, highlighted in the schematic of the RILIS laser system presented in Figure 1, were used during the scheme development of chromium.

For RILIS scheme development, independently heated capillaries are loaded with “mass markers” of stable isotopes of the element of interest and connected to the rear of a hot cavity. Thus a continuous supply of atoms is delivered to the ion source as the mass markers are heated and evaporated. As depicted in Figure 1, the RILIS laser beams were directed through a window in the GPS dipole magnet, to converge within the hot cavity ion source. The ion source assembly was maintained at a voltage of 30 kV and a grounded extraction electrode was positioned ~ 60 mm from the exit of the ion source. Ions created in the ion source drifted towards the cavity exit under the influence of a longitudinal voltage drop resulting from the resistive heating of the hot cavity. At the exit of the hot cavity, the ions were extracted by the penetrating field of the extraction electrode and accelerated to form a 30 keV ion beam. The ions passed through the ISOLDE GPS dipole magnet for mass separation before being directed to a Faraday cup for measurement of the ion current.

The 358 nm light for the first step transition was produced by frequency doubling the output of a Ti:Sa laser using a Beta-Barium Borate (BBO) crystal. The 698 nm light for the second step transition was produced by a dye laser operated with an ethanol solution of Pyridine 1 with a typical average power of 3 W. A second dye laser, operated with an ethanol solution of either Rhodamine 6G, Pyrromethene 597 or DCM dye was used to scan above the ionization potential to search for autoionizing resonances. The typical average powers ranged between 0.5 - 10 W across the lasing range of the dyes. The ^{52}Cr ion current was measured while recording the scanning laser wavelength using the RILIS data acquisition system [20]. Since the purpose of the spectroscopic study was the identification of an optimal RILIS scheme for chromium beam production at ISOLDE, typical RILIS operating conditions were maintained (laser linewidths and power levels were not optimized for spectral resolution).

4. Results and discussion

4.1. RILIS scheme development

To verify the transitions listed in Table 1, a three step, two resonance scheme, with a non-resonant final step (^{NR}) at 532 nm was used ($\{\lambda_1 | \lambda_2 | \lambda_3\} = \{358\text{ nm}|698\text{ nm}|532\text{ nm}^{NR}\}$), verifying the suitability of the transitions found in literature with a laser to surface ion ratio of 1000:1. The 532 nm laser beam was then replaced with the tunable dye laser beam to excite from the $3d^5(^6S)4d\ e^7D_5$ level at 42 261.226 cm^{-1} and scan above the ionization potential. 15 transitions to new autoionizing states were observed in the scans between 16 526 cm^{-1} and 17 854 cm^{-1} (560 - 605 nm). The scan results are presented in Figure 2.

The autoionizing resonances were fitted using either Voigt or Breit-Wigner-Fano profiles. The details of the observed resonances are presented in Table 2. The uncertainties in the centroid positions for AI1 to AI10 take into account the standard deviation of the centroid positions of multiple scans of each resonance and the second step transition which was used as a reference. AI11 to AI15 were only scanned once in a scan that also included AI2 to AI10. The uncertainties in the centroid positions for AI11 to AI15 therefore consider the maximum differences between the centroid positions for AI2 to AI10 observed in this scan, to the centroid positions obtained subsequently following multiple scans of each resonance. Fitting errors and the signal to background ratios, defined as the ratio between the signal at the peak of the resonance to the signal from non-resonant ionization when the scanning laser was detuned, were also taken into account. The variation in the signal to background ratio of up to an order of magnitude and peaks AI11-AI15 being scanned only once results in significant differences in the uncertainties associated with the reported transitions. An increase in the background with increasing wavenumber visible in the combined spectra presented in Figure 2, the cause of this is not immediately clear. Any attempt to correct for the increasing background would still result in AI3 corresponding to the highest ion signal. The optimal scheme, corresponding to the highest observed ^{52}Cr ion current, is presented in Figure 3, along with laser scans of the three resonances.

4.2. Saturation of the transitions

The efficiency of a given ionization scheme is maximized when all of the atomic transitions are saturated. The laser power required to saturate the $\{358\text{ nm}|698\text{ nm}|579\text{ nm}^{AI}\}$ scheme, applying an autoionizing (^{AI}) final step, was investigated by measuring the ^{52}Cr ion current while varying the laser power delivered to the hot cavity by each laser independently. The results of the saturation measurements are presented in Figure 4.

Equation 5 was used to fit a curve to the saturation data. This is a commonly used function which relates the signal to the laser power delivered for each resonant transition by determining a saturation parameter $P_{1/2Sat}$ [22, 23]:

$$I = B + M(P/P_{1/2Sat})/(P/(P_{1/2Sat} + 1)) \tag{5}$$

Where I is the ion current, B is the background ion current when the transition is blocked, M is the maximum ion current achievable with a fully saturated transition, P is the laser power delivered to the hot cavity, $P_{1/2Sat}$ is the laser power required to achieve 50% of M. The equation assumes the dominant contribution to the ionization process is from resonant excitation.

The uncertainty in the $P_{1/2Sat}$ values are dominated by the uncertainty in the transmission of the laser light to the hot cavity. The transmission efficiency is assumed to be constant during the saturation measurement therefore it was not included as an uncertainty on each measurement point but rather in the error in the value for $P_{1/2Sat}$, with a transmission of between 40-60% considered. The plots shown in Figure 4 assume a 50% transmission efficiency, the effect of varying the transmission efficiency is included for the third step transition. The saturation measurements demonstrate a complete saturation of the first and second step transitions. For the third step transition, a saturation of 65(7)% was achieved. At this point the saturation is already in the non-linear regime, extrapolating from the saturation fit, doubling the power delivered to the source would increase the saturation level to 77%.

Despite not being fully saturated, the ion signal achieved when applying the $\{358\text{ nm}|698\text{ nm}|579\text{ nm}^{AI}\}$ scheme, was a factor of two greater than the ion signal observed when using the $\{358\text{ nm}|698\text{ nm}|532\text{ nm}^{NR}\}$ scheme with an estimated 24 W of 532 nm laser light transmitted to the ion source.

4.3. Ionization efficiency

Two attempts were made to measure the efficiency of the $\{358\text{ nm}|698\text{ nm}|579\text{ nm}^{AI}\}$ scheme, using calibrated samples of chromium loaded into the ion source and mass marker setup described in Section 3. Unfortunately it was not possible to extract meaningful data from these attempts due to excessive amounts of additional chromium present in the target ion source assembly. It is believed the additional chromium in the system was either due to impurities in the ion source material or contamination introduced from the machining of the ion source itself. In an attempt to benchmark the efficiency of the scheme, the RILIS enhancement of the surface ionized chromium ion current was considered. Using the scheme depicted in Figure 3, a laser to surface ionization ratio of 2200:1 was recorded with the hot cavity heated to 2400 K. Considering the estimated surface ionization efficiency for Cr of ~0.01 %, from Equations 1-4, a factor of 2200 enhancement of the surface ion current would indicate a RILIS scheme with an efficiency in the region of 20 %. A poisoning of the surface of the hot cavity resulting in a lowering of the work function is considered unlikely, as the tests were conducted without any heavily outgassing target materials connected to the ion source unit. Additionally, the unit was operated for a number of days with the hot cavity heated to >2000°C. An incorrect estimation of the ion survival probability would have a near proportional effect on the efficiency. Ion survival probabilities of $\omega = 0.05, 0.1$ or 0.2 correspond to efficiencies of 9 %, 18 % and 36 % respectively.

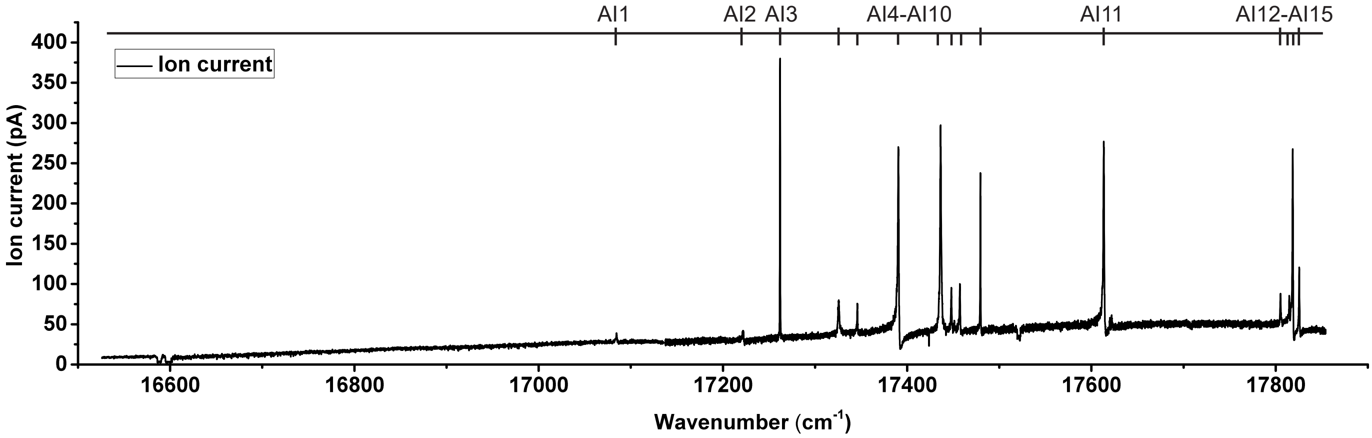

Figure 2: Autoionizing resonances of chromium. The combined spectra from laser scans between 16 526 cm^{-1} and 17 854 cm^{-1}, the observed autoionizing resonances were accessed via a single photon transition from the $3d^5(^6S)4d\ e^7D_5$ state at 42 261.226 cm^{-1}.

Table 2: Autoionizing states of chromium accessed via a single photon transition from the $3d^5(^6S)4d\ e^7D_5$ level at 42 261.226 cm^{-1}. Air wavelengths calculated using the equation of [21]. No attempt was made to deconvolve the 12 GHz linewidth of the scanning laser from the FWHM.

Identifier	Energy (cm^{-1})	Transition (cm^{-1})	Air wavelength (nm)	Relative signal	FWHM (cm^{-1})
AI1	59 345.91 (6)	17 084.68 (6)	585.157	4 (1)	1.11 (2)
AI2	59 483.52 (6)	17 222.29 (6)	580.482	10 (2)	0.92 (8)
AI3	**59 523.39 (3)**	**17 262.16 (3)**	**579.141**	**100**	**1.02 (1)**
AI4	59 587.00 (8)	17 325.77 (8)	577.015	28 (2)	2.1 (2)
AI5	59 606.7 (3)	17 345.5 (3)	576.357	12 (2)	1.5 (3)
AI6	59 652.25 (4)	17 391.02 (4)	574.850	80 (8)	1.48 (3)
AI7	59 697.74 (6)	17 436.51 (6)	573.350	84 (8)	1.85 (3)
AI8	59 709.5 (1)	17 448.3 (1)	572.963	12 (3)	1.1 (2)
AI9	59 718.6 (2)	17 457.4 (2)	572.665	0.20 (1)	1.1 (1)
AI10	59 740.93 (3)	17 479.70 (3)	571.933	40 (1)	0.67 (2)
AI11	59 874.8 (2)	17 613.6 (2)	567.587	65 (6)	1.0 (1)
AI12	60 066.4 (5)	17 805.2 (5)	561.478	12 (2)	0.86 (9)
AI13	60 076.0 (7)	17 814.8 (7)	561.175	8 (2)	0.64 (8)
AI14	60 079.8 (2)	17 818.6 (2)	561.055	63 (6)	0.71 (8)
AI15	60 086.8 (3)	17 825.6 (3)	560.835	25 (3)	0.61 (8)

4.4. On-line application at ISOLDE

The validity of the new RILIS scheme has been demonstrated on-line at ISOLDE by the measurement of RILIS ionized ^{52}Cr. A factor of 800 enhancement of the ion signal was observed, from an ion beam composed of multiple elements with the ion source cavity heated to 2400 K. Chromium extraction from ISOLDE UC_x targets has been verified, using both RILIS and surface ionization. The RILIS scheme reported here enabled a measurement of the mass of ^{59}Cr under challenging circumstances at ISOLDE [24], demonstrating the possibility of extracting chromium isotopes with half lives of the order of 100 ms. The scheme will be applied again for the production of radioactive ion beams for the extension of the chromium mass measurements by the ISOLTRAP collaboration [24] and also to explore the feasibility of solid state physics experiments using chromium isotopes at ISOLDE.

5. Conclusion

15 new autoionizing states of chromium have been observed during off-line testing at the ISOLDE-RILIS. From this work, an optimal three-step three-resonance $\{358\ nm|698\ nm|579\ nm^{AI}\}$ RILIS ionization scheme was identified, with an estimated efficiency of 20 %. The scheme was verified on-line at ISOLDE, using radiogenic chromium produced from a UC_x target. As a result, RILIS ionized chromium beams are now available for experiments at ISOLDE. The scheme has already been applied for the production of ^{59}Cr ion beams for mass measurements by the ISOLTRAP collaboration.

6. Acknowledgments

This project has received funding through the European Union's Seventh Framework Programme for Research and Technological Development under Grant Agreements 262010 (ENSAR), 267194 (COFUND), and 289191 (LA^3NET). The authors would like to thank Y. Liu for the interesting discussions on surface ionization in a hot cavity.

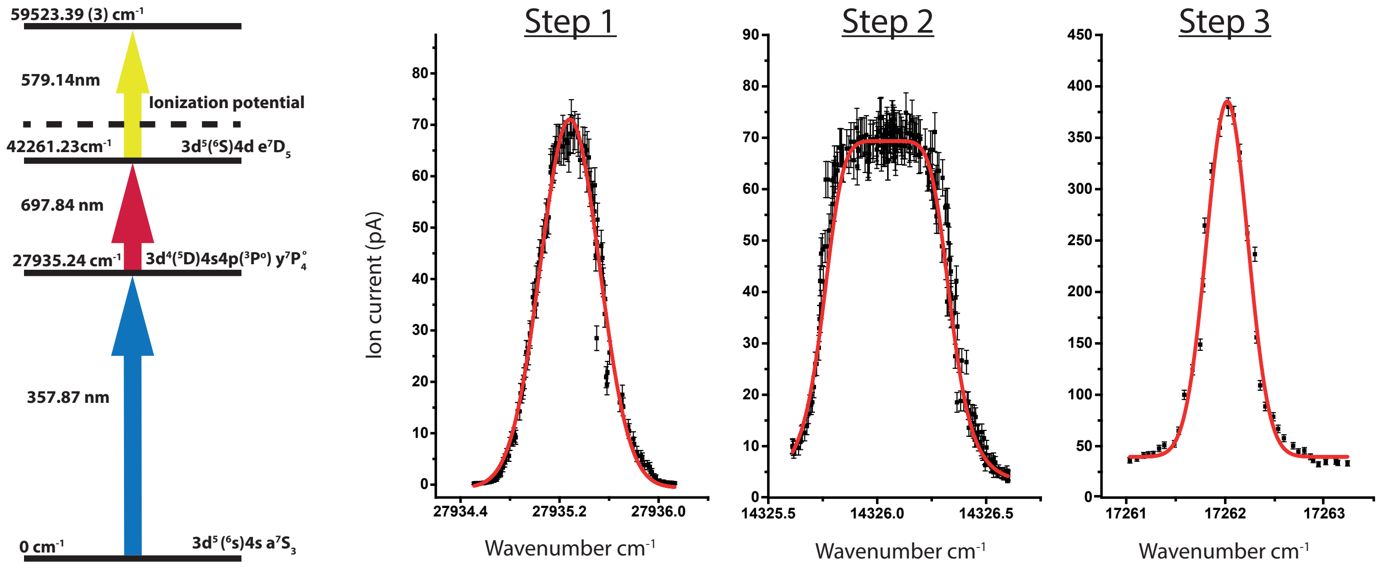

Figure 3: A new RILIS scheme for chromium. The optimal RILIS ionization scheme for chromium and scans of the three resonant transitions. The error bars are estimated based on the precision of the Faraday cup and the method of data acquisition.

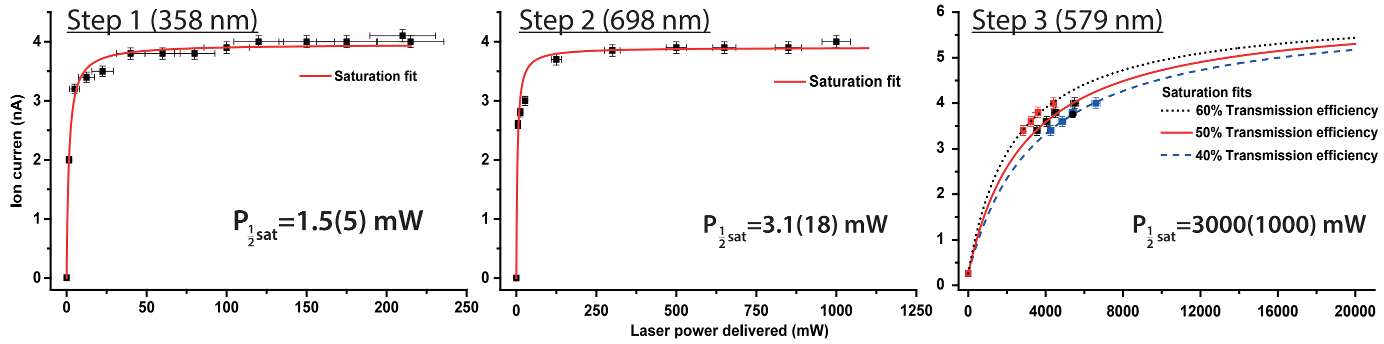

Figure 4: Saturation measurements plotting laser power delivered to the hot cavity ion source against ion current measured on a Faraday cup for each of the three resonant transitions in the {358 nm|698 nm|579 nm^{AI}}scheme. The error bars on individual measurement points are related to the precision of the measurement devices and the method of recording, the uncertainty in the value of $P_{1/2sat}$ is discussed in the text.

References

[1] V.I. Mishin, V.N. Fedoseyev, H.-J. Kluge, V.S. Letokhov, H.L. Ravn, F. Scheerer, Y. Shirakabe, S. Sundell, and O. Tengblad. Chemically selective laser ion-source for the CERN-ISOLDE on-line mass separator facility. *Nuclear Instruments and Methods in Physics Research Section B: Beam Interactions with Materials and Atoms*, 73(4):550–560, apr 1993. `doi:10.1016/0168-583X(93)95839-W`.

[2] E. Kugler. The ISOLDE facility. *Hyperfine Interactions*, 129(1/4):23–42, 2000. `doi:10.1023/A:1012603025802`.

[3] V. S. Letokhov. *Laser Photoionization Spectroscopy*. ACADEMIC PRESS INC., London, 1 edition, 1987.

[4] S. Kreim, D. Beck, K. Blaum, Ch. B\{”o}hm, Ch. Borgmann, M. Breitenfeldt, R. B. Cakirli, F. Herfurth, M. Kowalska, Y. Litvinov, D. Lunney, V. Manea, S. Naimi, D. Neidherr, M. Rosenbusch, L. Schweikhard, J. Stanja, T. Stora, F. Wienholtz, Wolf R. N., and K. Zuber. Seeking the Purported Magic Number N = 32 with High-Precision Mass Spectrometry. Technical report, CERN-INTC, Geneva, 2011. `doi:10.17181/CERN.P6YL.2W01`.

[5] T. Stora. Recent developments of target and ion sources to produce ISOL beams. *Nuclear Instruments and Methods in Physics Research Section B: Beam Interactions with Materials and Atoms*, 317:402–410, dec 2013. `doi:10.1016/j.nimb.2013.07.024`.

[6] R. Kirchner. Progress in ion source development for on-line separators. *Nuclear Instruments and Methods in Physics Research*, 186(1-2):275–293, jul 1981. `doi:10.1016/0029-554X(81)90916-2`.

[7] A. Kramida, Yu. Ralchenko, J. Reader, and the NIST ASD Team. NIST Atomic Spectra Database (ver. 5.2), [Online, accessed: 22/07/2016]. URL: `http://physics.nist.gov/asd`.

[8] R. Kirchner. On the thermoionization in hot cavities. *Nuclear Instruments and Methods in Physics Research Section A: Accelerators, Spectrometers, Detectors and Associated Equipment*, 292(2):203–208, jul 1990. `doi:10.1016/0168-9002(90)90377-I`.

[9] Y. Liu, H. Z. Bilheux, and Y. Kawai. Characterization of a tubular hot-cavity surface ion source. In *Proceedings of the 2005 IEEE Particle Accelerator Conference (PAC 05). 16-20 May 2005, Knoxville, Tennessee. 21st IEEE Particle Accelerator Conference, p.1581*, pages 1581–1583, Knoxville, 2005. URL: `http://accelconf.web.cern.ch/AccelConf/p05/PAPERS/TPPE018.PDF`.

[10] É. Ya. Zandberg and N. I. Ionov. Surface ionization. *Soviet Physics Uspekhi*, 2(2):255–281, feb 1959. `doi:10.1070/PU1959v002n02ABEH003123`.

[11] V. N. Fedosseev, B. A. Marsh, D. V. Fedorov, U. Köster, and E. Tengborn. Ionization Scheme Development at the ISOLDE RILIS. In *Laser 2004*, pages 15–27. Springer-Verlag, Berlin/Heidelberg, 2005. `doi:10.1007/3-540-30926-8_2`.

[12] D. M. Wayne, W. Hang, D. K. McDaniel, R. E. Fields, E. Rios, and V. Majidi. The thermal ionization cavity (TIC) source: elucidation of possible mechanisms for enhanced ionization efficiency. *International Journal of Mass Spectrometry*, 216(1):41–57, apr 2002. `doi:10.1016/S1387-3806(02)00551-1`.

[13] M. Turek. Ionization of short-lived isotopes in a hot cavity Numerical

simulations. *Vacuum*, 104:1–12, jun 2014. `doi:10.1016/j.vacuum.2013.12.016`.

[14] P. L. Smith, H. Claas, J. R. Esmond, and R. L. Kurucz. Atomic spectral line database [Online, accessed: 28/9/2015]. URL: `http://www.pmp.uni-hannover.de/cgi-bin/ssi/test/kurucz/sekur.html`.

[15] E. B. Saloman. Energy Levels and Observed Spectral Lines of Neutral and Singly Ionized Chromium, Cr I and Cr II. *Journal of Physical and Chemical Reference Data*, 41(4):043103, 2012. `doi:10.1063/1.4754694`.

[16] V. N. Fedosseev and A. K. Yusupov. Effect of polarization of laser emission on the multistage photoionization yield of ytterbium isotopes. *Optics and Spectroscopy (English translation of Optika i Spektroskopiya)*, 57:905–908, 1984.

[17] V. N. Fedosseev, L.-E. Berg, D. V. Fedorov, D. Fink, O. J. Launila, R. Losito, B. A. Marsh, R. E. Rossel, S. Rothe, M. D. Seliverstov, A. M. Sjodin, and K. D. A. Wendt. Upgrade of the resonance ionization laser ion source at ISOLDE on-line isotope separation facility: New lasers and new ion beams. *Review of Scientific Instruments*, 83(2):02A903, 2012. `doi:10.1063/1.3662206`.

[18] S. Rothe, T. Day Goodacre, V. N. Fedosseev, B. A. Marsh, R. E. Rossel, M. Veinhard, and K. D. A. Wendt. Laser ion beam production at CERN-ISOLDE: new features - more possibilities. *Nuclear Instruments and Methods in Physics Research Section B: Beam Interactions with Materials and Atoms*, (Proceedings of The International Conference on Electromagnetic Isotope Separators and Related Topics (EMIS), Grand Rapids, Michigan, USA, May 11-15), 2016. `doi:10.1016/j.nimb.2016.02.024`.

[19] B. Marsh, T. Day Goodacre, D. Fink, S. Rothe, M. Seliverstov, N. Imai, M. Sjodin, and R. Rossel. Suitability test of a high beam quality Nd:YVO4 industrial laser for the ISOLDE RILIS installation. Technical report, CERN, Geneva, 2013. `doi:10.17181/CERN.F65D.P3NR`.

[20] R. E. Rossel, V. N. Fedosseev, B. A. Marsh, D. Richter, S. Rothe, and K. D. A. Wendt. Data acquisition, remote control and equipment monitoring for ISOLDE RILIS. *Nuclear Instruments and Methods in Physics Research Section B: Beam Interactions with Materials and Atoms*, 317:557–560, dec 2013. `doi:10.1016/j.nimb.2013.05.048`.

[21] K P Birch and M J Downs. An Updated Edlén Equation for the Refractive Index of Air. *Metrologia*, 30(3):155–162, jan 1993. `doi:10.1088/0026-1394/30/3/004`.

[22] S Rothe. *An all-solid state laser system for the laser ion source RILIS and in-source laser spectroscopy of astatine at ISOLDE, CERN*. Doctoral thesis, J.G. University of Mainz, 2012. `doi:10.17181/CERN.0HNZ.7Z6X`.

[23] D. A. Fink. *Improving the Selectivity of the ISOLDE Resonance Ionization Laser Ion Source and In-Source Laser Spectroscopy of Polonium*. Doctoral thesis, Heidelberg University, 2014. `doi:10.17181/CERN.R8QG.WACQ`.

[24] D. Atanasov, K. Blaum, S. George, F. Herfurth, M. Kowalska, S. Kreim, D. Lunney, V. Manea, Z. Meisel, M. Mougeot, D. Neidherr, M. Rosenbusch, L. Schweikhard, A. Welker, F. Wienholtz, R. N. Wolf, and K. Zuber. IS532: Mass spectrometry of neutron-rich nuclides into the N = 40 "island of inversion". Technical report, CERN-INTC, Geneva, 2015. URL: `http://cds.cern.ch/record/2120143/`, `doi:10.17181/CERN.5DIK.UUTK`.

7.3 Mercury and tellurium

Paper IV

RILIS-ionized mercury and tellurium beams at ISOLDE CERN

RILIS-ionized mercury and tellurium beams at ISOLDE CERN

T. Day Goodacre*[a,b], J. Billowes[b], K. Chrysalidis[a,c], D.V. Fedorov[d], V. N. Fedosseev[a],
B. A. Marsh[a], P.L. Molkanov[d], R. E. Rossel[a,d,e], S. Rothe[a,b], C. Seiffert[a], K.D.A. Wendt[c]

[a] *CERN, CH-1211 Geneva 23, Switzerland*
[b] *School of Physics and Astronomy, The University of Manchester, Manchester, M13 9PL, United Kingdom*
[c] *Institut für Physik, Johannes Gutenberg Universität, D-55099 Mainz, Germany*
[d] *Petersburg Nuclear Physics Institute, 188350 Gatchina, Russia*
[e] *Faculty of Design, Computer Science and Media, Hochschule RheinMain, Wiesbaden, Germany*

Abstract

This paper presents the results of ionization scheme development for application at the ISOLDE Resonance Ionization Laser Ion Source (RILIS). Two new ionization schemes for mercury are presented: a three-step three-resonance ionization scheme, ionizing via an excitation to a Rydberg level and a three-step two-resonance ionization scheme, with a non-resonant final step to the ionization continuum that corresponded to a factor of four higher ionization efficiency. The efficiency of the optimal mercury ionization scheme was measured, together with the efficiency of a new three-step three resonance ionization scheme for tellurium. The efficiencies of the mercury and tellurium ionization schemes were determined to be 6% and >18% respectively.

1. Introduction

The Resonance Ionization Laser Ion Source (RILIS) [1, 2] is the principal ion source of the ISOLDE radioactive ion beam facility [3] based at CERN, scheduled for >75% of experiments in 2016. The RILIS targets sequential atomic resonances to achieve the step-wise excitation of a valence electron, followed by a final transition resulting in ionization. The final step transition is either an excitation to an autoionizing state, a Rydberg level or a non-resonant transition to the ionization continuum. The sequential series of atomic excitations is termed the "ionization scheme" of the element. The primary advantage of the RILIS, with respect to the other ionization mechanisms employed at ISOLDE, is the element selective nature of the ionization process. This is crucial, when the production of isobaric contaminants can be orders of magnitude higher than that of the isotope of interest. The prerequisite for applying the RILIS to a particular element is that a multi-step ionization scheme must be developed. Following the determination the ionization scheme corresponding to the highest ion signal, the absolute efficiency of the ionization scheme is measured. This enables an assessment of the suitability of the ionization scheme for application at ISOLDE.

1.1. Mercury

A pre-existing ionization scheme for mercury, was based on a publication by A.A. Podshivalov et al. [4]. It was determined to have an efficiency of 0.1% when tested at the ISOLDE

---

*thomas.day.goodacre@cern.ch

Preprint submitted to Hyperfine Interactions *February 14, 2017*

RILIS [5]. The three step ($\{\lambda_1|\lambda_2|\lambda_3\}$ = {254 nm|313 nm|626 nm}) ionization scheme from [4] uses the residual 626 nm fundamental light from the 2ω conversion process (producing the 313 nm second step) as the final ionizing transition. It was suggested that the 626 nm light accessed a favourable part of the ionization continuum due to the vicinity of autoionizing states. By comparison, the reported efficiency of the FEBIAD type ion source for mercury is 60% [6]. There was therefore limited interest for the application of the RILIS scheme on-line at ISOLDE. A more efficient ionization scheme was required to facilitate an in-source resonance ionization spectroscopy experiment of mercury isotopes, seeking to extend the optical measurements of the mercury isotope chain further into the neutron rich and neutron deficient regions of the nuclear chart [7]. The spectroscopic investigations that resulted in a new mercury ionization scheme are presented in Section 3.1 and the efficiency measurement of this ionization scheme is presented in Section 3.2.

1.2. Tellurium

A RILIS scheme for tellurium was requested to enable signal identification for a Coulomb excitation experiment [8]. Blocking one of the resonant transitions removes the laser ionized component of the ion beam directed to an experiment, while preserving the contamination ionized by other mechanisms, thereby enabling the identification of signals related to the isotope of interest. The tellurium ionization scheme development was detailed in [9]. In order to be applied for standard radioactive ion beam production at ISOLDE, the efficiency of the ionization scheme had to be determined. The results of the efficiency measurement are presented in Section 3.3.

2. Experimental method

The process of RILIS ionization scheme development at ISOLDE is outlined in [9] and [10]. Following the identification of potentially suitable atomic transitions based on literature data, spectroscopic studies and efficiency measurements are carried out. During standard ISOLDE operation for the production of radioactive isotopes, reaction products are produced by impinging 1.4 GeV protons onto the target material mounted inside the ISOLDE target units. The target material is heated depending on the material type, enabling the reaction products to diffuse through the target material and then effuse via a transfer line to the ion source. For RILIS operation and ionization scheme development, a hot cavity ion source (a tungsten or tantalum tube 34 mm in length with an internal diameter of 3 mm and heated to ~2000°C) is typically used. The ionization scheme development reported here took place at ISOLDE. A modified target was used, containing a hot cavity ion source with an independently heated refractory metal capillary attached to the rear, but no target for nuclear reactions. The capillary contained a stable sample "mass marker" of the element of interest. The modified target unit was mounted on a "front-end" connected to one of the dipole mass separators and optically to the ISOLDE RILIS laser system. This configuration for off-line ionization scheme development, ensures the applicability of the results to "on-line" ISOLDE operation. The RILIS lasers are a combination of tunable dye and titanium:sapphire (Ti:Sa) lasers and non-tunable Nd:YAG and Nd:YVO_4 lasers, all pulsed at 10 kHz. The full laser parameters can be found in [2]. A schematic of the experimental set-up is presented in Fig. 1.

As depicted in Fig. 1, laser light from the RILIS lasers is focussed using telescopes located in the laser room and directed via an optical launch and transport system, through a window in the dipole separator magnet, to converge in an ion source cavity. During ionization scheme

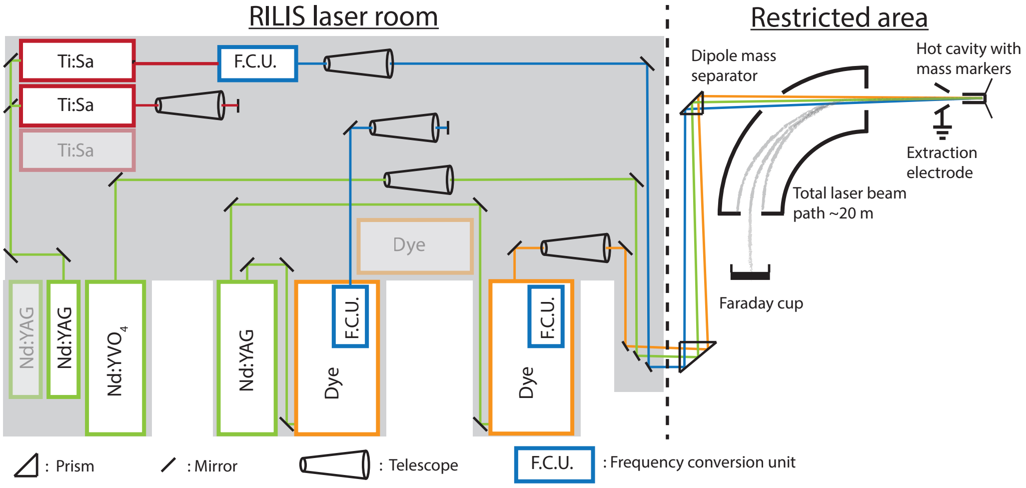

Figure 1: Schematic of the experimental set-up used for the development and testing of ionization schemes of mercury and tellurium for the ISOLDE RILIS.

development, a mass marker containing the equivalent of ~10000 nAh of the element of interest is used (assuming their 100% conversion to singly charged ions), to ensure a sufficient supply of atoms during the spectroscopic investigations. The known resonant transitions are verified by directing the lasers to the ion source while heating the excess mass marker and detecting the ions on a Faraday cup inserted in the focal plane of the dipole mass separator. Following this, a tunable final step laser is introduced to search for autoionizing states or investigate Rydberg levels. While the final step laser is scanned, the ion current is measured with the Faraday cup and the laser wavelengths are measured with a HighFinesse/Ångstrom WS7 wavelength meter. The various experimental parameters are combined and recorded by a LabVIEW based data recording system [11]. Once an optimal scheme has been determined, a calibrated mass marker of typically between 1000 nAh and 2000 nAh is evaporated, while the ion current is measured with a Faraday cup. A Faraday cup measurement is recorded periodically during the evaporation of the sample, to enable the determination of the average recorded signal and thus the efficiency of the ionization scheme. During the tests reported here, a Faraday cup measurement was recorded every 10 s and 1 s for the mercury and tellurium efficiency measurements respectively. The final efficiency value is therefore a combined efficiency of the ionization, extraction and ion beam transport through the dipole mass separator. No attempt is made to correct for these factors as they are intrinsic to the system, thus a corrected value would not provide a realistic determination of the achievable efficiency of the entire machine.

The use of ISOLDE front-ends, mass separators and beam lines is limited due to the annual demand for physics, development or commissioning work. Consequently, only one efficiency measurement per element is typically possible. In the standard (target-transfer line-hot cavity) configuration used for on-line ISOLDE experiments, there is an additional laser-atom overlap region in the transfer line, increasing the efficiency of the ionization process [12]. The efficiency measured with the (mass marker-hot cavity) configuration, used for scheme development, could therefore be considered a lower limit of ionization efficiency.

3. Results and discussion

3.1. RILIS ionization scheme development for mercury

The initial RILIS tests of the {254 nm|313 nm|626 nm} scheme took place prior to the upgrade to solid state pump lasers [1] and the addition of a complementary suite of Ti:Sa lasers [13]. Consequently, the ionization scheme was applied as suggested in [4], with the residual 626 nm laser light used for the final step transition (to what had been reported to be a favourable part of the ionization continuum). A full characterization of the scheme was possible in this work using the upgraded RILIS system. The first step 254 nm laser light was produced by 3ω frequency conversion of light from a Ti:Sa laser and the second step 313 nm light by 2ω frequency conversion of light produced by a Sirah Credo Dye laser, operated with an ethanol solution of DCM dye. The third step 626 nm light was produced by a second Sirah Credo Dye laser, also operated with an ethanol solution of DCM dye, enabling the wavelength of the final step to be scanned, while measuring the ion current. Scans of the third step revealed that the region of the ionization continuum around 87 293 cm^{-1} was not found to be additionally favourable for ionization when accessed via {254 nm|313 nm|626 nm}, with all three second steps tested exciting to $5d^{10}6s6d$ $^1D_2$, $^3D_1$, $^3D_2$. Consequently, a comprehensive ionization scheme development programme was embarked upon.

Ionization schemes applying each of the three second step transitions were tested. The final step dye laser was scanned to probe the ionization continuum from each of them, while operated with ethanol solutions of either Rhodamine 6G, DCM or Phenoxazone 9 dyes. Rydberg levels were also investigated, exciting from the $5d^{10}6s6d$ $^1D_2$ state. Finally, the effect of the addition of a non-resonant transition $^{(NR)}$ at 532 nm was tested, again exciting from each of the second steps, this is presented in Fig. 2 a). The resonances corresponding to the first step, three second steps and the Rydberg level corresponding to the largest ion signal are presented in Fig. 2 b).

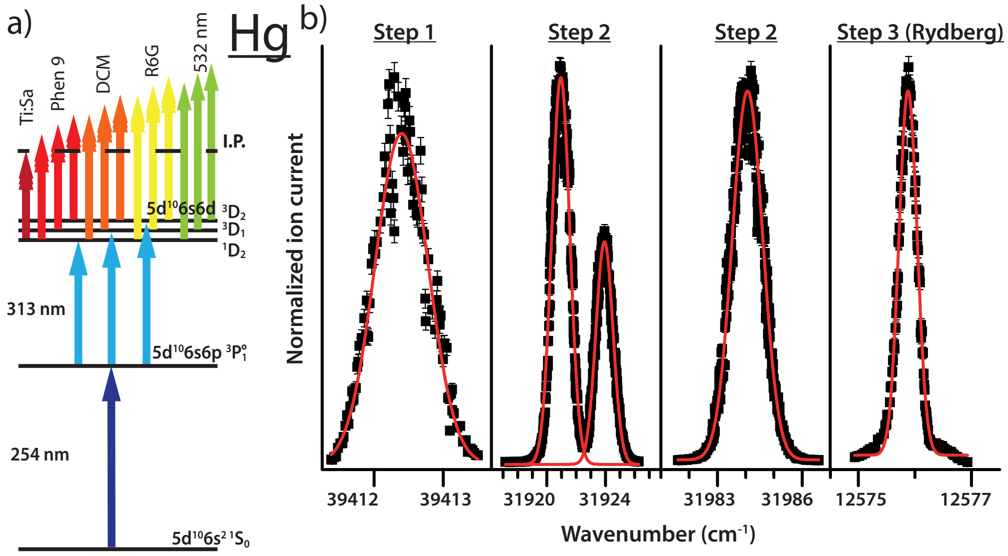

Figure 2: a) Schematic overview of the ionization scheme development for mercury. b) Scans of the first step, three second steps and the optimal Rydberg resonance. The resonances were scanned while being applied as part of the the schemes depicted in a).

The saturation of the second steps were verified. Saturation measurements of the first step were not fully conclusive, though saturation effects were observed with an estimated 15 mW of laser power delivered to the ion source. No autoionizing resonances were identified and the 88 759.6 cm^{-1} autoionizing state reported in literature [14] was not observed. Based on the reported odd parity and J = 1, this state should have been accessible from each of the 5d^{10}6s6d ^{1}D$_2$, ^{3}D$_1$, ^{3}D$_2$ states. The laser parameters used for the scheme development and efficiency measurement are presented in Table 1. The {254 nm|313.18 nm|795 nm} ionization scheme, ionizing via the Rydberg level shown in Fig. 2, was compared to the {254 nm|313.18 nm|532 nm^{NR}} scheme with a non-resonant final step to the ionization continuum using 532 nm light.

Table 1: The schemes originated from the 5d^{10}6s^{2} ^{1}S$_0$ atomic ground state. Spectroscopic information for known transitions is taken from [14]. The given laser power is an estimation of the power delivered to the ion source. *Transitions applied for the efficiency measurement. †Air wavelength calculated using the equation of [15].

Transition (cm^{-1})	Upper state config., term, J	Air wavelength (nm)	laser power mW
0 - 39 412.237*	5d^{10}6s6p, ^{3}P$^\circ_1$	253.652	80
39 412.237 - 71 333.053*	5d^{10}6s6d, ^{1}D$_2$	313.184	120
39 412.237 - 71 336.005	5d^{10}6s6d, ^{3}D$_1$	313.155	120
39 412.237 - 71 396.073	5d^{10}6s6d, ^{3}D$_2$	312.567	120
71 333.053 - 83 908.95 (4)	Rydberg	794.955† (25)	1 200
71 333.053 - ~90 121*	-	532	24 000

Ionization with the non-resonant final step exciting from the 5p^3(^{4}S°)7p ^{1}D$_2$ atomic state was determined to be four times more efficient than via the Rydberg level. This was achieved with an estimated 24 W of 532 nm laser light transmitted to the ion source from the Nd:YVO$_4$ Lumera Blaze laser [16], compared to an estimated 1.2 W of 795 nm laser light from a Ti:Sa laser. This discrepancy in the signal to power ratio can be understood as resulting from a higher cross-section of excitation to the Rydberg level. The {254 nm|313.18 nm|532 nm^{NR}} ionization scheme was therefore determined to be the optimal one for application at the ISOLDE RILIS.

3.2. RILIS ionization efficiency of mercury

The {254 nm|313.18 nm|532 nm^{NR}} scheme was applied and the dipole mass separator was set to ^{202}Hg, the isotope of mercury with the highest natural abundance (29.86 (26) % [17]). The laser parameters used for the efficiency measurement are indicated with an * in Table 1. A calibrated sample of 1336 nAh of mercury (≈400 nAh of ^{202}Hg) was evaporated from the independently heated mass marker described in Section 2, while the ion current was measured with a Faraday cup inserted downstream of the dipole mass separator. The results are presented in Fig. 3, together with a schematic of the ionization scheme applied during the efficiency measurement.
An average signal of 13.2 nA was recorded over a period of 1.88 h, this corresponds to an efficiency of 6%. This efficiency is a factor of 60 greater than the measured efficiency of the {254 nm|313.18 nm|626 nm} ionization scheme. During the previous efficiency measurement, the final ionizing transition was an estimated 1.3 W of 626 nm laser light delivered to the ion source. Considering the fact that the ionizing transitions are accessing different areas of the ionization continuum and the efficiency was only measured once for each scheme, this is within expectations.

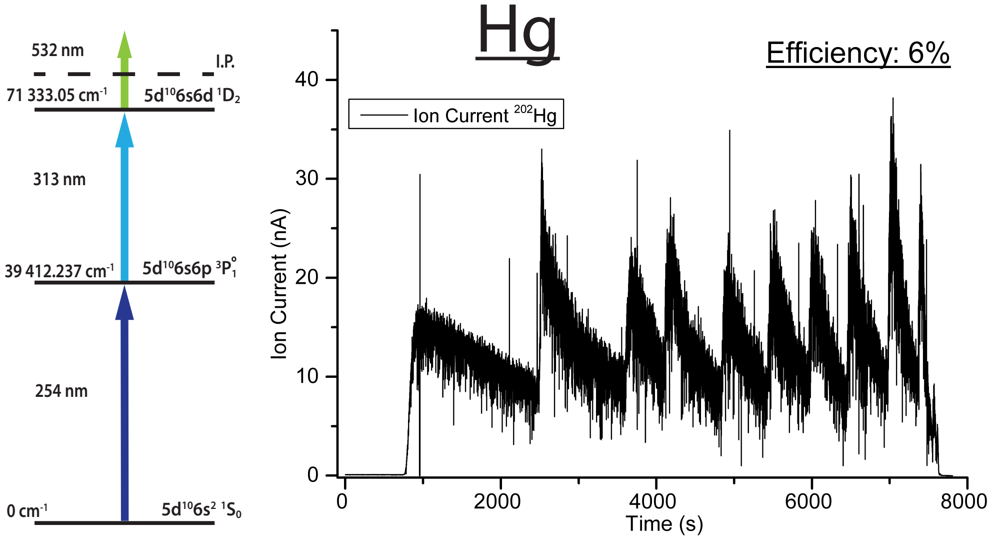

Figure 3: The measured ion current over the period of the efficiency measurement, together with a schematic of the ionization scheme that was applied. Additional laser parameters are presented in Table 1.

Following these results, the new RILIS scheme was applied using the anode cavity of a VADIS (ISOLDE's FEBIAD type) ion source as the laser atom interaction region, described in [18]. The extracted mercury ion currents when using either the arc discharge ionization process or the element selective RILIS ionization process were found to be equivalent, suggesting a comparative efficiency under on-line conditions. The new ionization scheme was then successfully applied for an in-source resonance ionization spectroscopy of mercury experiment, extending the hyperfine structure measurements four isotopes further towards the neutron dripline to ^{177}Hg and two isotopes further in the neutron rich direction up to ^{208}Hg [19].

3.3. RILIS ionization efficiency of tellurium

The new RILIS ionization scheme for tellurium of {214 nm|573 nm|901 nm} (described in [9]) was applied and the dipole mass separator was set to ^{130}Te, the isotope of tellurium with the highest natural abundance (34.08 (62) % [17]). The laser parameters during the tellurium efficiency measurements are presented in Table 2.

Table 2: The resonant transitions for the scheme originating from the 5p^4 ^{3}P$_2$ atomic ground state applied during the tellurium ionization scheme efficiency measurement. The given laser power is an estimation of the power delivered to the ion source. Spectroscopic information taken from [9].

Transition (cm^{-1})	Upper state config., term, J (cm^{-1})	Air wavelength (nm)	laser power (mW)
0 - 46 652.738	5p^3(^{4}S°)6s, ^{3}S°, 1	214.281	13
46 652.738 - 64 088.997	5p^3(^{4}S°)7p, ^{3}P, 1	573.360	4 000
64 088.997 - 75 181.41 (20)	-	901.270 (17)	1 300

A calibrated sample of 1000 nAh of tellurium (≈340 nAh of ^{130}Te) was evaporated from the independently heated mass marker described in Section 2, while the ion current was measured with a Faraday cup inserted downstream of the dipole mass separator. The results are presented in Fig. 4 together with a schematic of the ionization scheme that was applied during the measurements.

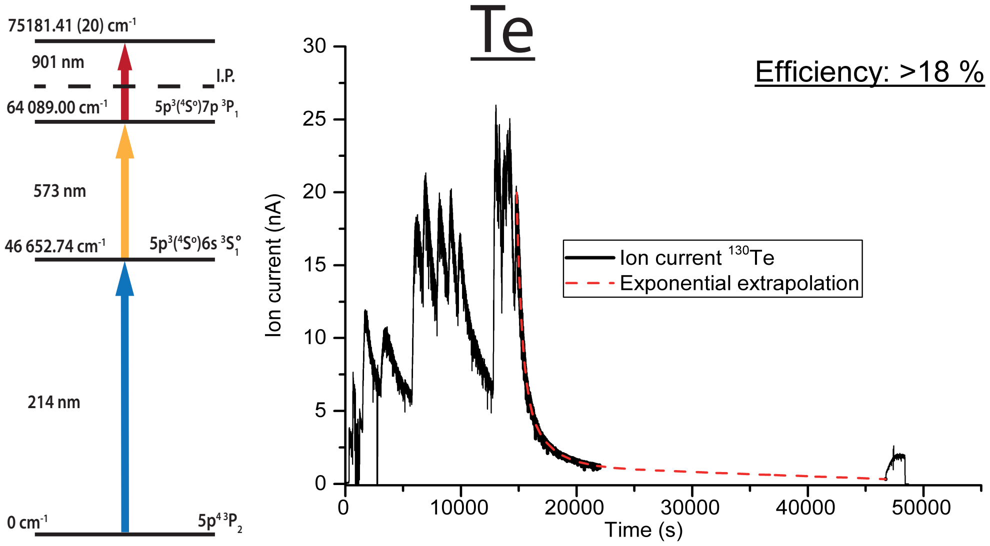

Figure 4: The measured ion current over the period of the efficiency measurement, together with a schematic of the ionization scheme that was applied. Additional laser parameters are presented in 2.

A data acquisition malfunction resulted in the loss of the Faraday cup measurements towards the end of the measurement. However, sufficient data was recorded to enable a reliable extrapolation of the ion current to cover the missing data points using an exponential decay function. This is depicted in Fig. 4 as a dashed (red) line. The accuracy of the extrapolation was aided by the possibility to measure the ion current once the correct functioning of the data acquisition system had been recovered, providing an end point for the exponential extrapolation. The increase in the ion signal at the end of the efficiency measurement corresponds to a final heating of the mass marker capillary. Due to time constraints, it was necessary to stop the measurement while the ion rate was stable and equivalent to 0.6% of efficiency/hour. This indicates there was a significant amount of tellurium remaining in the system. As there was not sufficient data to reliably extrapolate the decay of the ion rate following the final heating, only the data shown in Fig. 4 was included in the evaluation of the efficiency. An average signal of 4.8 nA was recorded over a period of 12.98 h, this corresponds to an efficiency of 18% which is considered to be a lower limit for the efficiency of the scheme.

4. Conclusions

An optimal RILIS ionization scheme of {254 nm|313.18 nm|532 nm^{NR}} was determined for mercury. A scheme of {254 nm|313.18 nm|795 nm}, ionizing via a Rydberg level corresponded to a factor of four lower ion current at typical laser power levels available at the ISOLDE RILIS for these wavelengths. No autoionizing resonances were observed, including the autoionizing state reported in literature at 88 759.6 cm^{-1}. The efficiency of the new RILIS ionization scheme for mercury of {254 nm|313.18 nm|532 nm^{NR}} was determined to be 6%, a factor of 60 higher than the previously measured efficiency of 0.1% with a scheme of {254 nm|313 nm|626 nm}. The efficiency of the new RILIS ionization scheme for tellurium ({214 nm|573 nm|901 nm} reported in [9]) was determined to be >18%, with a significant amount of tellurium remaining in the system at the end of the measurement. The mercury scheme has already been applied at ISOLDE for a successful in-source resonance ionization spectroscopy experiment. The scheme was demonstrated to have an ionization efficiency equivalent to that of the ISOLDE VADIS ion source under standard on-line conditions [18]. The application of the new mercury scheme has been requested for a number of future ISOLDE experiments, due to the selective method of ionization offered by the RILIS.

5. Acknowledgements

This project has received funding through the European Union's Seventh Framework Programme for Research, Technological Development and demonstration under Grant Agreements 262010 (ENSAR), 267194 (COFUND), and 289191 (LA^{3}NET).

References

[1] V.N. Fedosseev, L.E. Berg, D.V. Fedorov, D. Fink, O.J. Launila, R. Losito, B.A. Marsh, R.E. Rossel, S. Rothe, M.D. Seliverstov, A.M. Sjodin, and K.D.A. Wendt. Upgrade of the resonance ionization laser ion source at ISOLDE on-line isotope separation facility: New lasers and new ion beams. *Review of Scientific Instruments*, 83(2):02A903, 2012. `doi:10.1063/1.3662206`.

[2] S. Rothe, T. Day Goodacre, D.V. Fedorov, V.N. Fedosseev, B.A. Marsh, P.L. Molkanov, R.E. Rossel, M.D. Seliverstov, M. Veinhard, and K.D.A. Wendt. Laser ion beam production at CERN-ISOLDE: New features More possibilities. *Nuclear Instruments and Methods in Physics Research Section B: Beam Interactions with Materials and Atoms*, 376:91–96, 2016. `doi:10.1016/j.nimb.2016.02.024`.

[3] E. Kugler. The ISOLDE facility. *Hyperfine Interactions*, 129(1/4):23–42, 2000. `doi:10.1023/A:1012603025802`.

[4] A.A Podshivalov, O.I Matveev, B.W Smith, and J.D Winefordner. A novel and efficient excitation- and ionization-scheme for laser resonance ionization of mercury. *Spectrochimica Acta Part B: Atomic Spectroscopy*, 54(13):1793–1799, 1999. `doi:10.1016/S0584-8547(99)00112-3`.

[5] V.N. Fedosseev, L.E. Berg, N. Lebas, O.J. Launila, M. Lindroos, R. Losito, B.A. Marsh, F.K. Österdahl, T. Pauchard, G. Tranströmer, and J. Vannesjö. ISOLDE RILIS: New beams, new facilities. *Nuclear Instruments and Methods in Physics Research Section B: Beam Interactions with Materials and Atoms*, 266(19-20):4378–4382, 2008. `doi:10.1016/j.nimb.2008.05.038`.

[6] S. Sundell and H. Ravn. Ion source with combined cathode and transfer line heating. *Nuclear Instruments and Methods in Physics Research Section B: Beam Interactions with Materials and Atoms*, 70(1-4):160–164, 1992. `doi:10.1016/0168-583X(92)95926-I`.

[7] L.P. Gaffney, T. Day Goodacre, A. Andreyev, M. Seliverstov, N. Althubiti, B. Andel, S. Antalic, D. Atanasov, A.E. Barzakh, J. Billowes, K. Blaum, T.E. Cocolios, J. Cubiss, G. Farooq-Smith, V.N. Fedosseev, D.V. Fedorov, R. Ferrer, K.T. Flanagan, L. Ghys, A. Gottberg, C. Granados, F. Herfurth, M. Huyse, D.G. Jenkins, D. Kisler, S. Kreim, T. Kron, Yu. Kudryavtsev, D. Lunney, K.M. Lynch, V. Manea, B.A. Marsh, T.M. Mendonca, P.L. Molkanov, D. Neidherr, R. Raabe, S. Raeder, J.P. Ramos, E. Rapisarda, M. Rosenbusch, R.E. Rossel, S. Rothe, L. Schweikhard, S. Sels, T. Stora, I. Tsekhanovich, C. Van Beveren, P. Van Duppen, M. Veinhard, R. Wadsworth, F. Wienholtz, A. Welker, K. Wendt, G.L. Wilson, S. Witkins, R. Wolf, and K. Zuber. In-source laser spectroscopy of mercury isotopes. *CERN INTC*, (P-424), 2014. `doi:10.17181/CERN.DUGM.L69R`.

[8] T. Ahn, H. Al-Azri, T. Bloch, P.A. Butler, N. Bree, T. Bäck, S. Bönig, J. Cederkäll, B. Cederwall, I.G. Darby, J. Diriken, D. O'Donnell, C. Fahlander, L.P. Gaffney, T. Grahn, B. Hadinia, M. Huyse, D.G. Jenkins, A. Johnson, P. Joshi, D.T. Joss, R. Julin, T. Kröll, J. Leske, B.S. Nara Singh, A. Nicholls, R.D. Page, J. Pakarinen, E.S. Paul, N. Pietralla, P. Rahkila, E. Rapisarda, M. Sandzelius, M. Scheck, J. Simpson, J.F. Smith, R. Wadsworth, P. Van

Duppen, D. Voulot, F. Wenander, and V. Werner. Coulomb excitation of ^{116}Te and ^{118}Te: A study of collectivity above the Z=50 shell gap. *CERN-INTC*, page 11, 2011. `doi:10.17181/CERN.LT8P.T0OC`.

[9] T. Day Goodacre, D. Fedorov, V.N. Fedosseev, L. Forster, B.A. Marsh, R.E. Rossel, S. Rothe, and M. Veinhard. Laser resonance ionization scheme development for tellurium and germanium at the dual Ti:SaDye ISOLDE RILIS. *Nuclear Instruments and Methods in Physics Research Section A: Accelerators, Spectrometers, Detectors and Associated Equipment*, 830:510–514, 2016. `doi:10.1016/j.nima.2015.10.066`.

[10] V.N. Fedosseev, B.A. Marsh, D.V. Fedorov, U. Köster, and E. Tengborn. Ionization Scheme Development at the ISOLDE RILIS. *Hyperfine Interactions*, 162(1-4):15–27, 2006. `doi:10.1007/s10751-005-9204-2`.

[11] R.E. Rossel, V.N. Fedosseev, B.A. Marsh, D. Richter, S. Rothe, and K.D.A. Wendt. Data acquisition, remote control and equipment monitoring for ISOLDE RILIS. *Nuclear Instruments and Methods in Physics Research Section B: Beam Interactions with Materials and Atoms*, 317:557–560, 2013. `doi:10.1016/j.nimb.2013.05.048`.

[12] Y. Liu, C. Baktash, J.R. Beene, C.C. Havener, H.F. Krause, D.R. Schultz, D.W. Stracener, C.R. Vane, Ch. Geppert, T. Kessler, K. Wies, and K. Wendt. Time profiles of ions produced in a hot-cavity resonant ionization laser ion source. *Nuclear Instruments and Methods in Physics Research Section B: Beam Interactions with Materials and Atoms*, 269(23):2771–2780, 2011. `doi:10.1016/j.nimb.2011.08.009`.

[13] S. Rothe, B.A. Marsh, C. Mattolat, V.N. Fedosseev, and K.D.A. Wendt. A complementary laser system for ISOLDE RILIS. *Journal of Physics: Conference Series*, 312(5):052020, 2011. `doi:10.1088/1742-6596/312/5/052020`.

[14] A. Kramida, Yu. Ralchenko, J. Reader, and the NIST ASD Team. NIST Atomic Spectra Database (ver. 5.2), [Online, accessed: 22/07/2016], 2015. URL: `http://physics.nist.gov/asd`.

[15] K.P. Birch and M.J. Downs. An Updated Edlén Equation for the Refractive Index of Air. *Metrologia*, 30(3):155–162, 1993. `doi:10.1088/0026-1394/30/3/004`.

[16] B. Marsh, T. Day Goodacre, D. Fink, S. Rothe, M. Seliverstov, N. Imai, M. Sjodin, and R. Rossel. Suitability test of a high beam quality Nd:YVO4 industrial laser for the ISOLDE RILIS installation. Technical report, CERN, Geneva, 2013. `doi:10.17181/CERN.F65D.P3NR`.

[17] J.R de Laeter, J.K. Böhlke, P. De Bièvre, H. Hidaka, H.S. Peiser, K.J.R. Rosman, and P.D.P. Taylor. Atomic weights of the elements. Review 2000 (IUPAC Technical Report). *Pure and Applied Chemistry*, 75(6), 2003. `doi:10.1351/pac200375060683`.

[18] T. Day Goodacre, J. Billowes, R. Catherall, T.E. Cocolios, B. Crepieux, D.V. Fedorov, V.N. Fedosseev, L.P. Gaffney, T. Giles, A. Gottberg, K.M. Lynch, B.A. Marsh, T.M. Mendonça, J.P. Ramos, R.E. Rossel, S. Rothe, S. Sels, C. Sotty, T. Stora, C. Van Beveren, and M. Veinhard. Blurring the boundaries between ion sources: The application of the RILIS inside a FEBIAD type ion source at ISOLDE. *Nuclear Instruments and Methods in Physics Research Section B: Beam Interactions with Materials and Atoms*, 376:39–45, 2016. `doi:10.1016/j.nimb.2016.03.005`.

[19] T. Day Goodacre. *Developments of the ISOLDE-RILIS for radioactive ion beam production and the results of their application in the study of exotic mercury isotopes*. PhD thesis, The University of Manchester, 2017.

7.4 Radium

RILIS ionization of radium was requested for an experiment [93] on the CRIS beam line at ISOLDE [94]. The application of a RILIS for the ionization of radium was reported at TRIUMF, applying a $\{\lambda_1\,|\lambda_2|\,\lambda_3\} = \{483\,\mathrm{nm}|818\,\mathrm{nm}|532\,\mathrm{nm}^{NR}\}$ scheme [95]. A factor of three enhancement over the surface ionized background was achieved. The scheme development for radium presented here was undertaken using the general method reported in Sections 7.1 to 7.3. In this case, since no stable isotope of radium exists, the radium atoms were produced on-line by impinging 1.4 GeV protons on a UCx target as described in Section 5.1. The target and tantalum hot cavity were maintained at 1950°C and 2060°C respectively throughout these measurements.

The first and second step transitions were identified in literature [96]. A more convenient scheme to that applied at TRIUMF was tested, avoiding the need to produce 483 nm light. A dye laser operated with ethanol solutions of either Rhodamine 6G, Fluorescein 27 or DCM dyes was scanned to search for autoionizing resonances: {714 nm|784 nm|dye scan}. Initially it was believed that three autoionizing states had been discovered (the first to be reported), with schemes of {714 nm|784 nm|558 nm,581 nm,615 nm}. However, after unexpected results when the {714 nm|784 nm|615 nm} scheme was tested at the CRIS beam line (using a charge exchange cell to neutralize ions before re-ionization) and an additional review of the literature, it was determined that the 615 nm line was a known transition. However, it was a transition that could only be populated in HC-RILIS operation via a decay from the 7s8s $^3S_1$ level, suggesting optical pumping. The scans of the investigated resonant transitions are presented with a schematic of the schemes in Figure 7.1 and Table 7.1.

Table 7.1: The resonant transitions investigated during the radium ionization scheme development originating from the 7s^2 $^1S_0$ ground state (*the 615 nm transition originates from the 7s7p $^3P^\circ_2$ level). Spectroscopic information on known lines is taken from [96]. Air wavelengths of new resonances calculated using the equation of [97]. The uncertainties are dominated by the widths of the autoionizing resonances.

Transition (cm^{-1})	Upper state config.	Term	J	Air wavelength (nm)
0 - 13 999.357	7s7p	$^3P^\circ$	1	714.12167 (5)
13 999.357 - 26 754.01	7s8s	^3S	1	783.812 (2)
26 754.01 - 44 686 (4)	new		0,1,2	557.51 (13)
26 754.01 - 43 951 (6)	new		0,1,2	581.34 (21)
16 688.54* - 32 941.06	7p^2	^3P	2	615.119 (5)

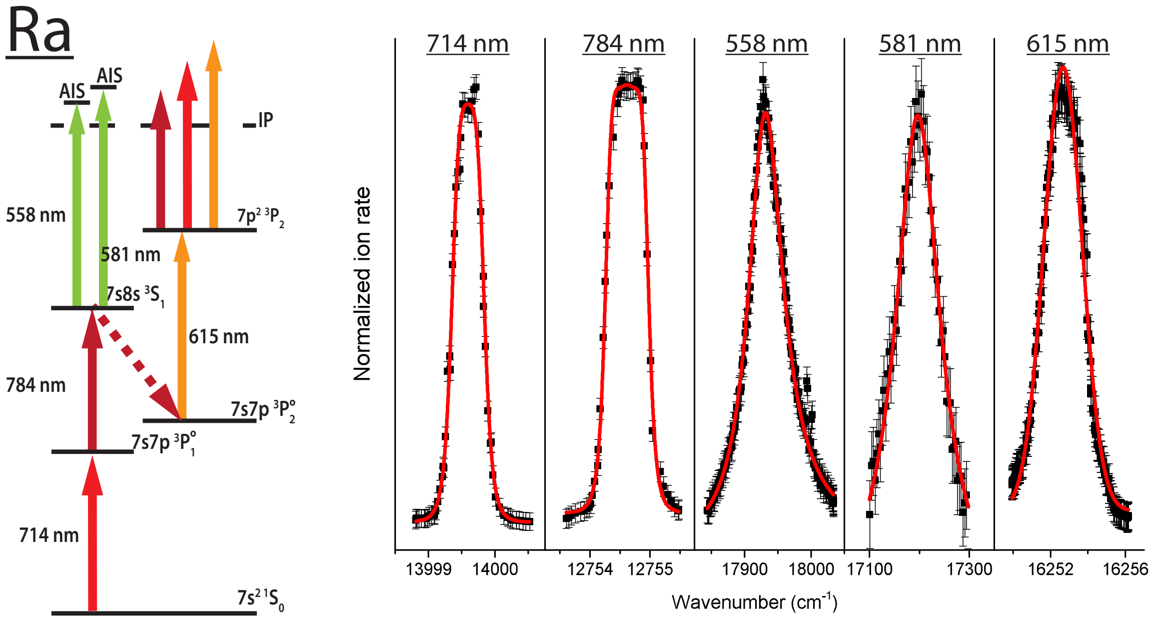

Figure 7.1: The resonant transitions investigated during the radium ionization scheme development and scans of the resonances. The error bars are estimated based on the precision of the Faraday cup and the method of data acquisition

In order to demonstrate optical pumping within the hot cavity environment, the 615 nm transition was delayed with respect to the 714 nm and 784 nm transitions while monitoring the ion current on a Faraday cup inserted after the dipole mass separator. The results are presented in Figure 7.2, together with the results from delaying the 558 nm transition in the same manner for comparison.

The unusual insensitivity of the {714 nm|784 nm|615 nm} scheme to the timing synchronization with respect to the first two transitions, can be understood as resulting from the lack of an allowed transition to the atomic ground state from the 7s7p $^3P^\circ_2$ state. Surprisingly, the {714 nm|784 nm|615 nm} scheme offered a similar factor of three enhancement as the ionization scheme employing the better of the two autoionizing states ({714 nm|784 nm|558 nm}). Saturation measurements of the 714 nm, 784 nm, 558 nm and 615 nm transitions were made by varying the laser power of each transition individually, while monitoring the ion current. The results are presented in Figure 7.3.

The saturation measurement curves presented in Figure 7.3 were fitted in the same manner as described in Section 7.2. The 714 nm, 784 nm and 615 nm transitions were demonstrated to be deeply saturated. Therefore the {714 nm|784 nm|615 nm} ionization scheme was chosen to enhance the radium yields for the CRIS experiment [93].

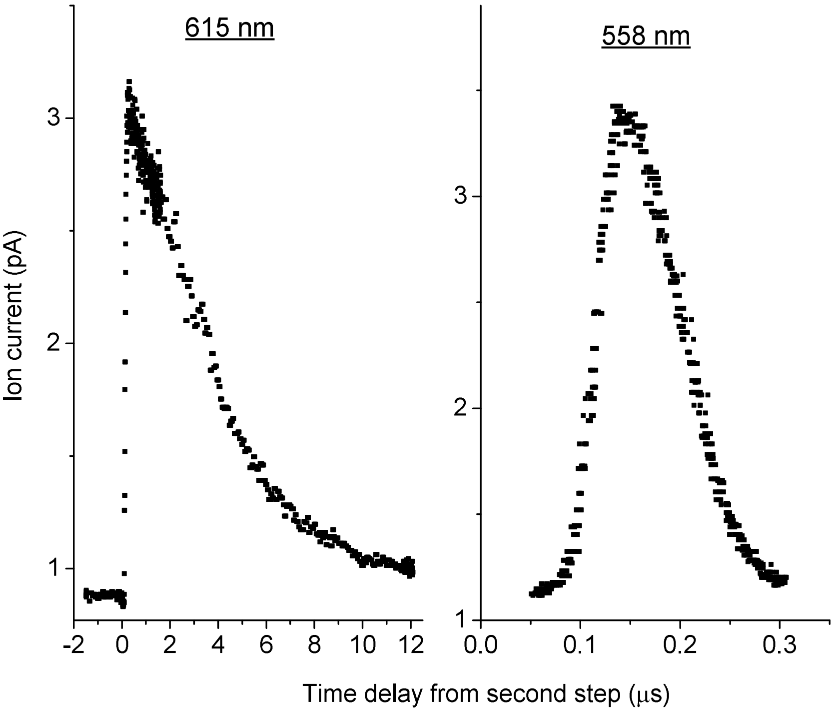

Figure 7.2: The change in ion current with a variation in the delay second and third step transitions. An off-set of ~100 ns with respect to the timing of the 714 nm and 784 nm transitions is the result of the laser pulse timing being measured at different locations.

The strong saturation of all of the transitions corresponds to a reduced sensitivity to any potential deterioration in the RILIS laser power over the course of the experiment. The {714 nm|784 nm|558 nm} ionization scheme was applied by the CRIS experiment for their spectroscopic investigations. The saturation and ionization efficiency of the 615 nm transition is difficult to understand unless it is capable of reaching a favourable part of the ionization continuum from the $7p^2\ ^3P_2$ excited state. The comparative insensitivity of the 615 nm transition, to delaying it with respect to the first two excitation steps, indicates this transition is also the dominant ionizing step in the {714 nm|784 nm|615 nm} ionization scheme.

Conclusion

Two new RILIS ionization schemes for radium have been developed ({714 nm|784 nm|615 nm}, {714 nm|784 nm|588 nm}), capable of enhancing the radium yield by a factor of three when applied in a tantalum hot cavity operated at 2060°C. During the course of the scheme development, what are believed to be the first two autoionizing states of radium were identified at 43 951 (6) cm^{-1} and 44 686 (4) cm^{-1}. Additionally, optical

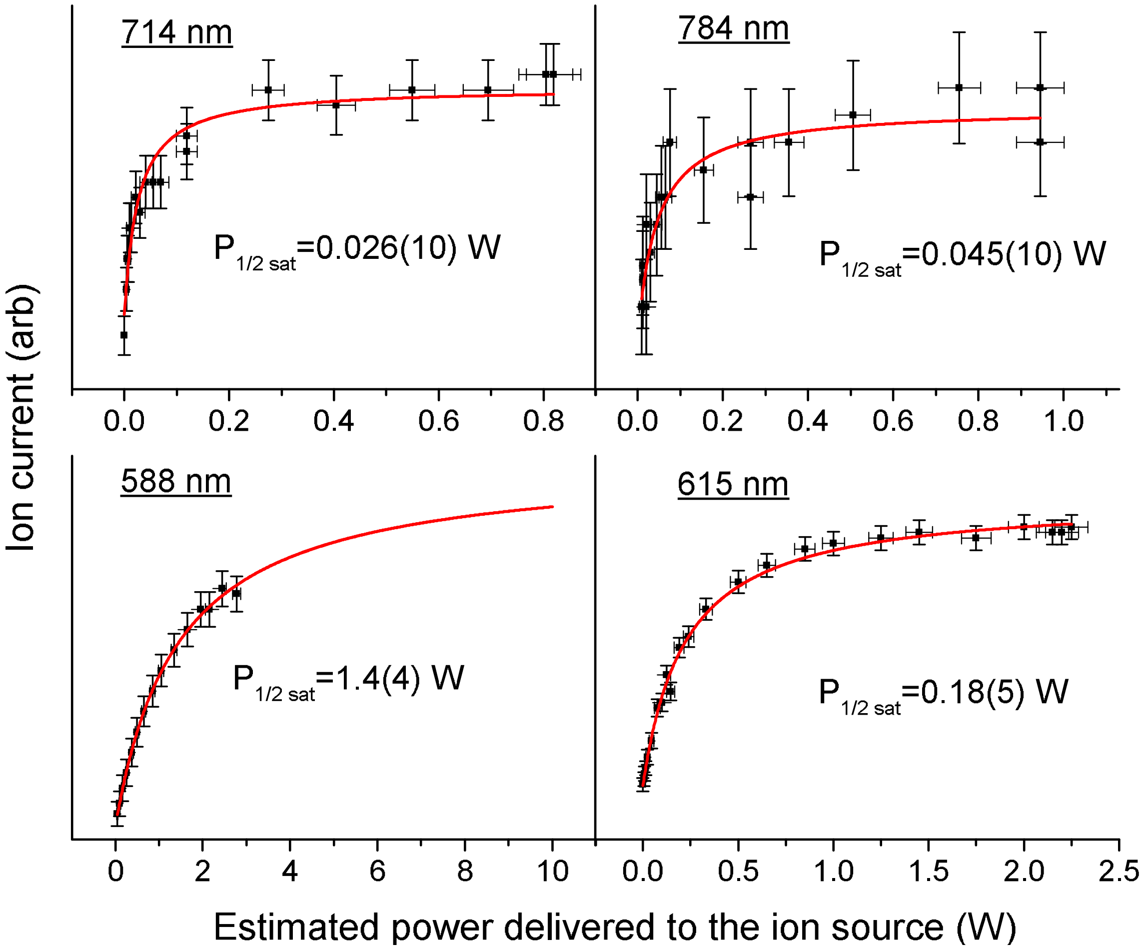

Figure 7.3: Saturation measurements plotting the laser power delivered to the hot cavity ion source against ion current measured on a Faraday cup for four of the investigated transitions. The uncertainty on individual measurement points is related to the precision of the measurement devices and the method of recording. An additional uncertainty is included for the $P_{1/2sat}$ values, considering a transmission efficiency of the laser light to the ion source between 40-60%.

pumping effects were observed within the hot cavity environment.

Chapter 8

Mercury isotopes “the playground of the optical spectroscopist”

Mercury isotopes were described as the playground of the optical spectroscopist by G. Fricke and K. Heilig in their compendium of nuclear charge radii data [98], an assessment based on the extensive history of optical studies of these isotopes. This Chapter presents a brief overview of the previous HFS investigations of mercury isotopes, concentrating particularly on the period following the identification of the unexpectedly large isotope shift between ^{187}Hg and ^{185}Hg in 1972 [5]. Much of the history is summarized in [7, 32].

8.1 Measurements pre 1972

The targeting of the 254 nm mercury line for isotope specific ionization was first reported in the early 1930s by K. Zuber [99], applying techniques pioneered by S. Mrozowski [100]. The advent of synthetic isotope production and the first generations of radioactive ion beam facilities increased the range of available isotopes [101, 102], while improved interferometric techniques enabled increasing precision in the measurement of the HFS and isotope shifts [103]. A compilation of the measurements can be found in [7]. The status of the mercury isotope shift measurements in 1971 is presented in Figure 8.1.

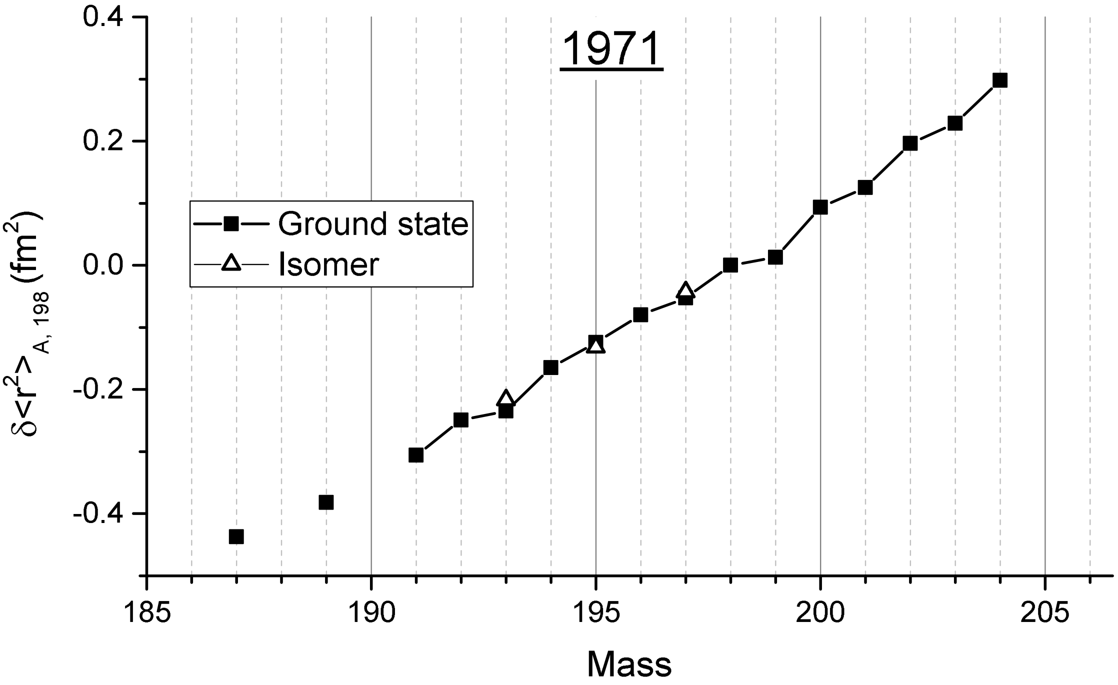

Figure 8.1: Isotope shifts of mercury isotopes measured before 1972. Data taken from [7].

8.2 Measurements 1972 - 1986

A sudden jump in the trend of charge radii between ^{187}Hg and ^{185}Hg was reported by Bonn et al. [5] using a pioneering pre laser β-RADOP (β-radiation detected optical pumping) technique, capable of studying isotopes with nuclear spin $I \neq 0$. The addition of their results is presented in Figure 8.2a and the technique is outlined in [104]. Various explanations for the magnitude of the isotope shift were suggested, including bubble nuclei [105] and an increase in the proton surface density [106]. The phenomenon was correctly interpreted by [107, 108, 109, 110, 111, 112] as a variation in the shape of the nuclei between a weak oblate deformation and a strong prolate deformation.

γ-spectroscopy identified an intruder rotational band, responsible for the shape coexistence and indicated that the ground state of ^{184}Hg corresponded to the band related to the weakly oblate deformation, therefore suggesting an odd-even shape staggering between ^{186}Hg and ^{184}Hg [113, 114]. This was confirmed optically by Kühl et al. [6], using laser spectroscopy which enabled an extension of the optical measurements to the $I = 0$ even isotopes.

The first "satisfactory" [32] explanation of the shape staggering was provided by

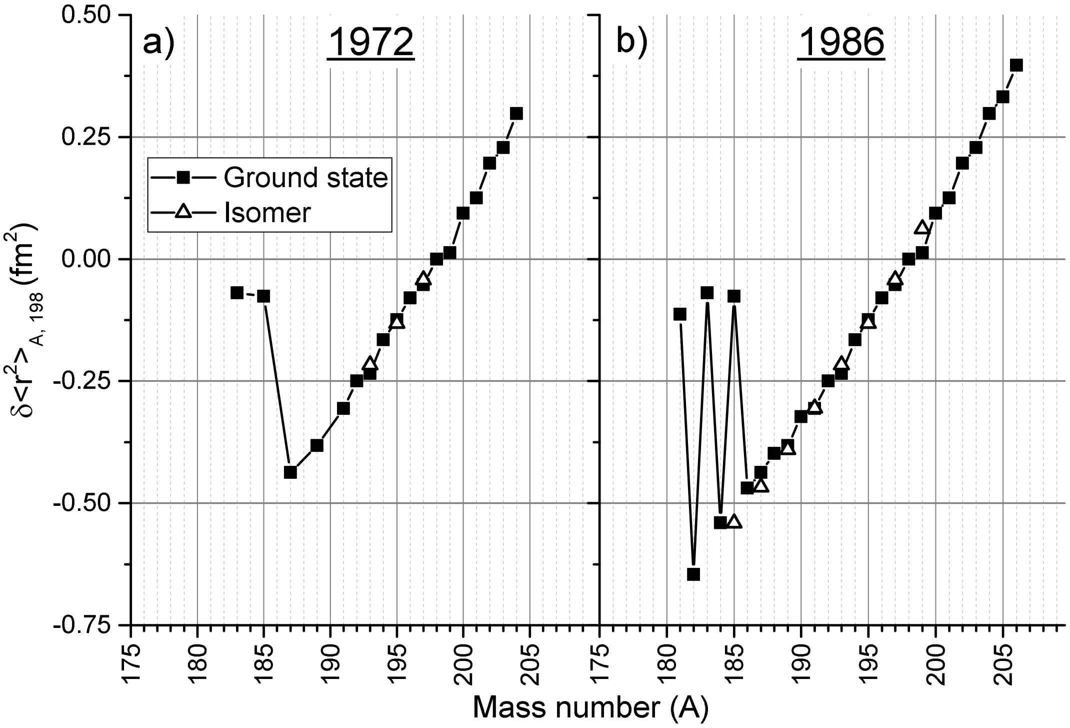

Figure 8.2: The status of the isotope shift measurements of mercury isotopes in 1972 (a) and 1986 (b). Data taken from [7].

Frauendorf and Pashkkevich [112] who modelled the nuclei by applying an approach combining the liquid drop model with Struinsky's shell correction [115]. They suggested that the shape staggering was the result of a differing loss in pairing energy between the two competing minima, following the addition of an unpaired neutron blocking the last Fermi level. The discrepancy in the pairing energy between the oblate and prolate minima was explained as the result of the differing densities of the single particle neutron levels for either the weakly deformed oblate, or the strongly deformed prolate deformations. The two minima are understood to be close (within a few hundred keV of each other), consequently the blocking effects are sufficient to tip the balance between the minima for the odd-A nuclei, resulting in the shape staggering.

Laser spectroscopy measurements extended the chain of $\delta\langle r^2\rangle^{198,A}$ measurements to span between ^{182}Hg and ^{206}Hg by 1986 [7, 116, 117], including the identification of the ∼24 GHz isomer shift in ^{185}Hg [38]. The status of the mercury isotope shift measurements by 1986 is presented in 8.2b.

The sudden and pronounced isotope and isomer shifts in neutron deficient mercury are considered to have made a significant contribution to the discovery of shape coexistence, as they provided a direct demonstration of the phenomenon [28]. It was described by K. Heyde and J.L. Wood as "one of the most remarkable discoveries in nuclear structure physics in the last 50 years" [118].

8.3 Motivation for extending the optical measurements

The optical $\delta\langle r^2\rangle^{198,A}$ measurements presented in 8.2b indicate two opportunities for further investigation:

- At the neutron deficient end of the mercury isotope chain, the cessation point of the odd-even shape staggering had yet to be definitively determined through the study of nuclear ground state properties. Further in-beam studies, revealed an increase in the level energies of the prolate intruder structure with decreasing N from ^{182}Hg [119]. The return to a weakly deformed shape for the odd mercury isotopes below A = 181 was suggested based on γ-spectroscopy [120, 121] and α-spectroscopy results [122]. Theoretical modelling was in agreement with the level energies of the prolate intruder structure [123] and a general reduction in deformation [18]. However, there was no definitive determination of whether the shape staggering would continue beyond ^{180}Hg.
- At the neutron rich end of the isotope chain, the experimentally measured isotopes extended as far as the N = 126 shell closure. An extension of these measurements would provide information on the nuclei following the shell closure and the characteristic "kink" in the charge radii.

Chapter 9 describes the experiment and the process of data extraction, and Chapters 10 and 11 discuss the results for the neutron deficient and neutron rich measurements respectively in the context of recent experimental work, theoretical predictions and the charge radii systematics of the region. The measurements presented in the following three chapters extend the isotope shift measurements of the mercury chain to span from ^{177}Hg to ^{208}Hg, the longest unbroken chain of optically determined isotope shifts in the nuclear chart.

Chapter 9

In-source resonance ionization spectroscopy of mercury

The in-source RIS experiment [124] discussed in the following chapters took place at the ISOLDE facility described in Section 5.1. Mercury isotopes were produced by impinging a pulsed 1.4 GeV proton “driver beam” on to a molten lead target. A staggered proton pulse substructure was used to maximize the release of short-lived isotopes from the molten target [125, 126]. For molten targets, the limit on the number of protons per pulse is reduced from 3.5×10^{13} to 1×10^{13} in order to preserve the target vessels [127]. Therefore, the achievable proton current is limited by the number of protons available from the CERN proton sharing supercycle (typically 35-40%), rather than by limits set by radiation protection requirements. Agreements with other CERN facilities enabled up to 68% of the proton pulses being made available to ISOLDE during periods of this experiment, in order to increase the mercury yields.

This experiment was the first on-line application of the VADLIS ion source: coupling the ISOLDE RILIS with the VADIS, ISOLDE's variant of the FEBIAD type arc discharge ion source. The developments leading to this capability are outlined in Section 6.1. The VADLIS developments enabled the RILIS to be coupled to a molten metal target for the first time. The specific benefits for this experiment are discussed in Section 9.1.

The first step transition ($5d^{10}6s^2\ {}^1S_0 \rightarrow 5d^{10}6s6p\ {}^3P_1^\circ$) of the three step ionization scheme, described in Section 7.3, was chosen as the spectroscopic transition due to its known sensitivity to variations in nuclear structure [98]. The 254 nm radiation

Table 9.1: The number of successful laser scans and the method of determining the laser frequency dependent ion rate for the measured isotopes. The Windmill determined the ion rate via the detection of α-decays, while the detector downstream of the MR-ToF MS and the Faraday cup determined it by detecting the charge of the incident ions.

Isotope	Half-life (time)	Number of successful scans	Method of ion rate determination
177	127.3 (18) ms	2	Windmill
178	266.5 (14) ms	3	Windmill
179	1.05 (3) s	4	Windmill
180	2.59 (1) s	4	Windmill
181	3.6 (1) s	3	Windmill
182	10.83 (6) s	2	Windmill
183	9.4 (7) s	2	MR-ToF MS
184	30.87 (26) s	3	MR-ToF MS
185g	49.1 (10) s	3	MR-ToF MS
185m	21.6 (15) s	3	MR-ToF MS
198	stable	9	Faraday cup
198	stable	8	MR-ToF MS
202	stable	2	MR-ToF MS
203	46.594 (12) days	2	MR-ToF MS
206	8.32 (7) min	3	MR-ToF MS
207	2.9 (2) min	3	MR-ToF MS
208	41 (+5-4) min	5	MR-ToF MS

required for this transition was generated by 3ω frequency conversion of the output of a Ti:Sa laser, operating in the dual etalon scanning mode described in Section 5.3.1. The laser was scanned in a stepwise manner and at each frequency step the ion rate was recorded either via direct ion measurement or α-decay spectroscopy. The technique is summarized in Sections 4.2.2 and 5.3.

The isotope ^{198}Hg was chosen as the reference isotope and all of the isotope shifts were determined relative to it, consequently, measurements of ^{198}Hg were repeated periodically during the experiment. The ion rate was determined with an ISOLDE Faraday cup for the first nine of the 17 reference measurements of ^{198}Hg. The ISOLTRAP MR-ToF MS [78] was used to determine the mercury ion rate for the remaining eight scans of ^{198}Hg. The scope of the experiment, including the number of successful scans of each isotope and the detection method employed is presented in Table 9.1.

The Windmill detector [128] (Section 5.3.3) was used to determine the ion rate for isotopes A $\leq$ 182. Gating on the α-decay energy enabled isotope specific detection. The MR-ToF MS (Section 5.3.2) was used to determine the ion rates of isotopes with

A $\geq$ 183, applying timing gates in order to separate mercury specific ion signals from isobaric contamination.

9.1 On-line application of the VADLIS ion source

Measurement of the neutron rich mercury isotopes, beyond the N=126 shell closure, would not have been possible with a UCx target due to the francium (Z=87) contamination on masses A=206-208. The ISOLTRAP MR-ToF MS is typically capable of separating the isotopes of interest from isobaric contamination, however, there is a limit to the maximum number of ions that can be injected into the MR-ToF MS. Consequently, there is a limit on the ratio of the isotope of interest to the isobaric contamination. Radioactive mercury ion beams produced in a molten lead (Z=82) target do not suffer from francium contamination. However, molten metal targets are currently incompatible with the surface ion sources typically used as the laser-atom interaction region at ISOLDE. This problem was overcome by the coupling of the ISOLDE RILIS with the VADIS ion source (described in Section 6.1) that is typically used with molten metal targets at ISOLDE.

The VADIS ion source was operated in the new RILIS mode of operation, presented in Section 6.1, to prevent arc discharge ionized stable lead from overwhelming the MR-ToF MS detection system. Operating in RILIS mode reduced the stable lead background by seven orders of magnitude, this can be observed in Figure 9.1.

Figure 9.1 also demonstrates the necessity of the MR-ToF MS to determine the ion rate. Without the isobaric separation of surface ionized contaminants present in the ion beam, determination of the ^{208}Hg related signal would have been close to impossible.

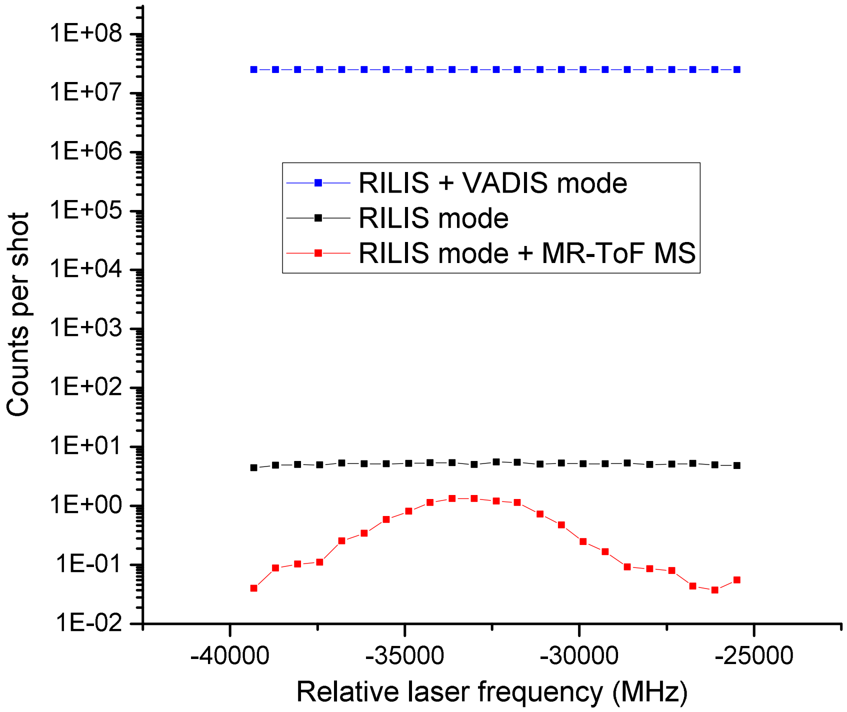

Figure 9.1: Ion rates on mass A = 208 at the detector down stream of the MR-ToF MS, both directly measured and estimated (the rate for RILIS + VADIS mode was calculated based on Faraday cup measurements).

9.2 Fitting procedure and $\delta\langle r^2\rangle^{198,A}$ extraction

The laser scans were fitted to extract the centre of gravity (CG) of the HFS, the hyperfine A factor and the hyperfine B factor using a program written in C by A. Barzakh for the Origin 2016 graphing and analysis software. The program considers the resonances to have Voigt profiles and includes 11 parameters to account for the nuclear spin, CG, hyperfine A factor, hyperfine B factor, Lorentzian contribution, Gaussian contribution, amplitude, peak amplitude ratios, a constant and a linearly varying background. The program was applied within the Origin 2016 software environment, with a chi-squared minimization [129] performed by a Levenberg-Marquardt algorithm [130, 131].

The mean square charge radii $\delta\langle r^2\rangle^{198,A}$ was determined using the F factor $F_{254} = -55.36$ GHz/fm^2 obtained by ab initio MCDF calculations by Torbohm et al. [132]. The parameter k, from (the Seltzer moment) Equation 3.6 was also taken from [132] as $k = 0.938$. This is in close agreement with the determination of k from the coefficients of [37] ($k = 0.935$). The applied values are the same as those used by Ulm et al [7]. However, no attempt was made to scale F_{254} according to the mass number as was done in [7]. The specific mass shift coefficient S from Equation 3.3 was considered to be $S = 0$ [133], the normal mass shift contribution was calculated for each isotope.

In order to enable a comparison of the $\delta\nu^{198,A}$ for ^{182}Hg between this work and literature values, the isotope shift and uncertainty for the literature value of ^{182}Hg was determined from the reported $\delta\nu^{A,A'}$ in the 546 nm ($5d^{10}6s6p\ ^3P_2^\circ \rightarrow 5d^{10}6s7s\ ^3S_1$) line using the F factor conversion $\kappa = F_{546}/F_{254} = -0.1707(12)$ determined in [7].

9.3 Data analysis and the determination of experimental uncertainties

The ion rate at each laser frequency step was extracted from the MR-ToF MS mass spectrometry data by F. Wienholtz and from the Windmill decay spectroscopy data by S. Sels and E. Verstraelen. Following this, the count-rates were associated with the frequencies measured using two RILIS wavelength meters (WM): a Highfinesse WS7 and a LM-007 ATOS lambdameter. The laser and proton driver beam parameters were monitored continuously throughout the experiment and measurements were associated with each laser frequency step. These data were used determine the stability of the WMs, laser power, laser pulse timing synchronization and the proton driver beam during individual laser scans and over the period of the experiment. The corrected and uncorrected count rates were plotted against the laser frequencies and the plots were fitted using the program described in Section 9.2, the results were compared and the optimal choice and application of the CG of the ^{198}Hg reference value was investigated. A summary of the investigations is given below, the full analysis is detailed in Appendix A.1 to A.5.

- The WMs are compared in Appendix A.1. It was determined that there was a drift in the ATOS WM during the period of the experiment. Additionally there appears to have been an inconsistent illumination of the ATOS interferometers during individual laser scans. Consequently, all of the analysis proceeded using the frequencies measured with the WS7 WM.

- Three options for the application of the ^{198}Hg reference CG were investigated (Appendix A.2):
    - A global average of the CGs of all of the laser scans of ^{198}Hg.

  - An average of the CGs of the ^{198}Hg laser scans where the MR-ToF MS was used to determine the frequency dependent ion rate. This option was considered due to concerns about the effect on the CG of the multiple mercury isotopes present in the ion beam measured with the Faraday cup. This can be observed in the ^{198}Hg (198 FC) scan presented in Figure 9.2.
  - Interpolating between reference measurements to determine a ^{198}Hg reference value specific to the time of each laser scan.

  It was determined that taking a global average resulted in the closest agreement with literature and the smallest standard deviation between scans of the same element. This value was therefore used for the data analysis.

- An assessment of the saturation of the spectroscopic transition and the effect of correcting the ion rates for variations in the laser power is summarized in Appendix A.3. The optimal results were obtained without power correction, indicating the saturation of the spectroscopic transition. This mistake was a consequence of the saturation measurement taking place before the thick etalon was installed. A factor of ∼6 narrower laser linewidth following the installation of the thick etalon led to a different saturation threshold. This can be understood from Equation 4.1. Nevertheless, all of the HFS components are well resolved other than for ^{185g,m}Hg. Therefore the saturation does not appear to have been significantly detrimental to the experiment.

- The laser pulse timing remained synchronized during all of the laser scans other than the first scan of ^{179}Hg (Appendix A.4). The values extracted from this scan were omitted from the final results.

- Large fluctuations (>50%) in the current of the proton driver beam were identified during the laser scans of ^{184}Hg (Appendix A.5). Surprisingly, this did not appear to affect the measurements of this isotope. This indicates the lead target was in a solid state during this period of the experiment, thus significantly increasing the release time of isotopes created by the impinging protons.

Based on this analysis the isotope shifts, mean square charge radii and values for the hyperfine A and B factors were deduced. The final results are presented in

Section 9.5. A selection of the scans is presented in Figure 9.2.

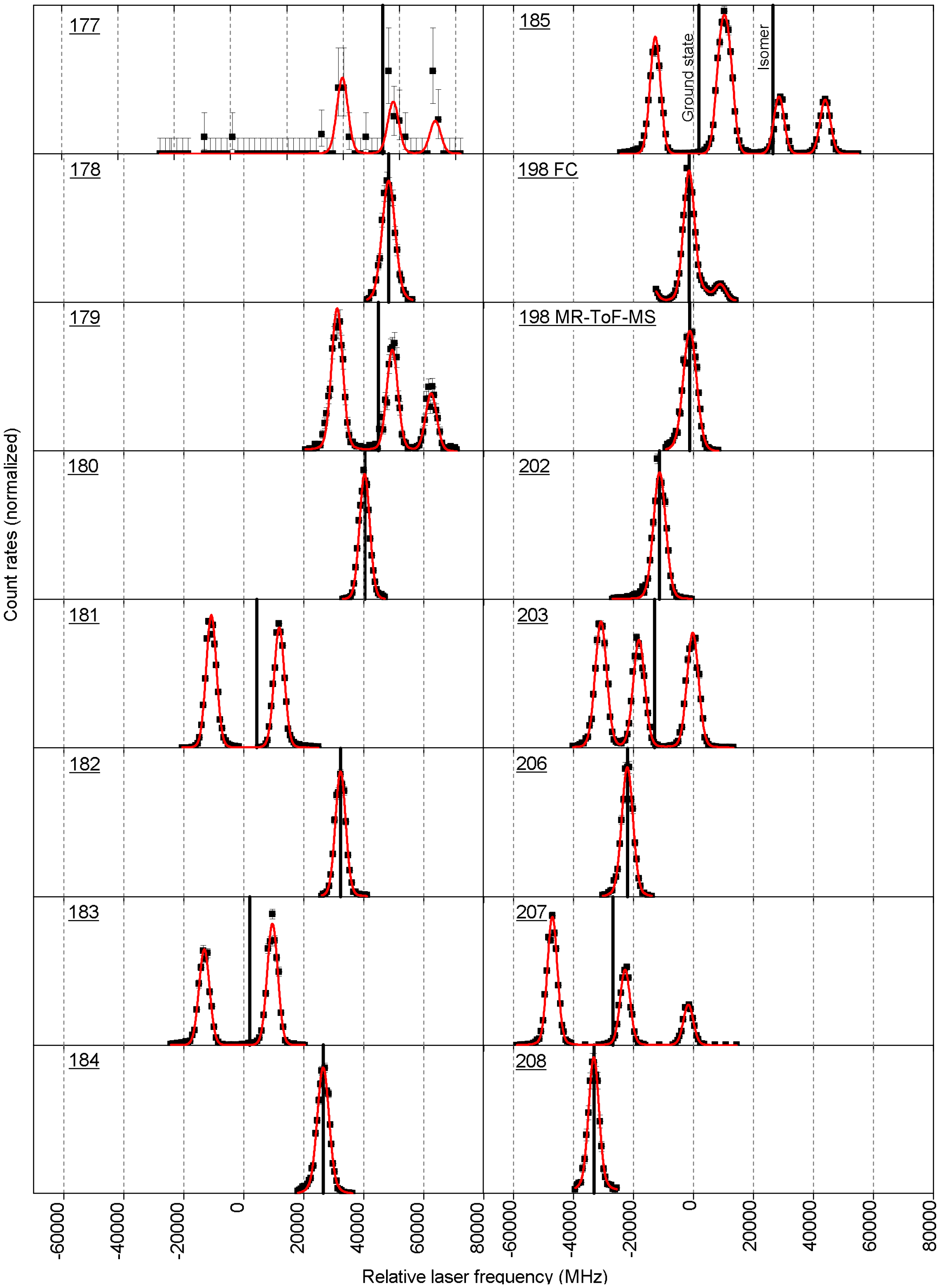

Figure 9.2: Fitted laser scans of each of the mercury isotopes investigated in this work.

9.4 Spin assignments

The nuclear spin I^{π} could not be unambiguously determined from this work because of the number of HFS components (the result of the spectroscopic transition exciting between atomic levels with J = 0 and J = 1). A spin and parity of $I^{\pi} = 9/2+$ was used for the analysis of the measurements of ^{207}Hg, based on reported systematics [134] and the neutron shell $g_{9/2}$ being the first shell above the N=126 shell closure. The ground state of ^{179}Hg was assigned as $I^{\pi} = 7/2$-, based on the proposed decay scheme and the study of the α-decay of ^{183}Pb [120]. The ground state of ^{177}Hg was also taken to be $I^{\pi} = 7/2$- based on the decay of the $I^{\pi} = 13/2+$ isomeric state [121]. The moments extracted from the HFS scans presented here support these spin assignments [135]. However, they are not discussed in this work and will form part of the thesis of S. Sels.

9.5 Summary of the extracted data

9.5.1 Isotope shifts

The extracted $\delta\nu^{198,A}$ and $\delta\langle r^2\rangle^{198,A}$ from this work are presented in Table 9.2, together with the literature values for the previously measured isotopes taken from [7]. The $\delta\nu^{198,A}$ are compared graphically to literature values in Figure 9.3. The uncertainties in the $\delta\nu^{198,A}$ of this work take into account the reproducibility of the CGs extracted from the ^{198}Hg reference measurements and the standard deviations of the CGs of each isotope (Appendix A.2.4). Additional weighting and uncertainty considerations for the CGs of ^{177}Hg and ^{208}Hg are discussed in Appendix A.6.

Figure 9.3 shows a reasonable agreement between the $\delta\nu^{198,A}$ from this work and the values reported by earlier studies and compiled in [7]. The significant uncertainty for the CG of ^{185}Hg from this work, can be at least partially attributed to the saturation of the detector of the MR-ToF MS hindering the deconvolution of ground state and isomer HFS components (Appendix A.3). The discrepancy for ^{206}Hg is discussed in Section 11.2. The full $\delta\langle r^2\rangle^{198,A}$ plot is presented in Figure 9.4.

Taking a global view of the mercury isotope chain as presented in Figure 9.4, it can be seen that the results of this work are in reasonable agreement with the earlier measurements, including for ^{185}Hg and ^{206}Hg where the discrepancy in $\delta\nu^{198,A}$

Table 9.2: Compilation of the extracted isotope shifts from this work and those compiled by [7]. The errors are purely experimental. To enable direct comparison, the literature values of $\delta\langle r^2\rangle^{198,A}$ are calculated from the $\delta\nu^{198,A}$ reported in [7], without scaling the electronic factor F_{254} for mass number A.

A	$\delta\nu^{198,A}$ (MHz)	$\delta\nu^{198,A}$ (lit.) (MHz)	$\delta\langle r^2\rangle^{198,A}$ (fm^2)	$\delta\langle r^2\rangle^{198,A}$ (lit.) (fm^2)
177	55 100 (520)	-	-1.0674 (100)	-
178	49 400 (280)	-	-0.9584 (54)	-
179	46 170 (260)	-	-0.8958 (48)	-
180	41 350 (280)	-	-0.8026 (54)	-
181	5 370 (270)	5 560 (200)	-0.1093 (52)	-0.1130 (39)
182	33 450 (240)	33 250 (340)	-0.6497 (46)	-0.6458 (65)
183	3 150 (210)	3 310 (100)	-0.0658 (40)	-0.0689 (19)
184	27 690 (285)	27 720 (90)	-0.5382 (54)	-0.5386 (17)
185	3 210 (450)	3 710 (30)	-0.0662 (87)	-0.0759 (6)
185m	27 860 (350)	27 720 (110)	-0.5409 (67)	-0.5382 (21)
198	0	0	0	0
202	-10 050 (260)	-10 102.4 (4.2)	0.1948 (50)	0.1958 (1)
203	-11 830 (210)	-11 750 (180)	0.2294 (40)	0.2278 (35)
206	-20 890 (230)	-20 420 (80)	0.4047 (44)	0.3957 (15)
207	-25 710 (230)	-	0.4979 (44)	-
208	-31 970 (280)	-	0.6187 (54)	-

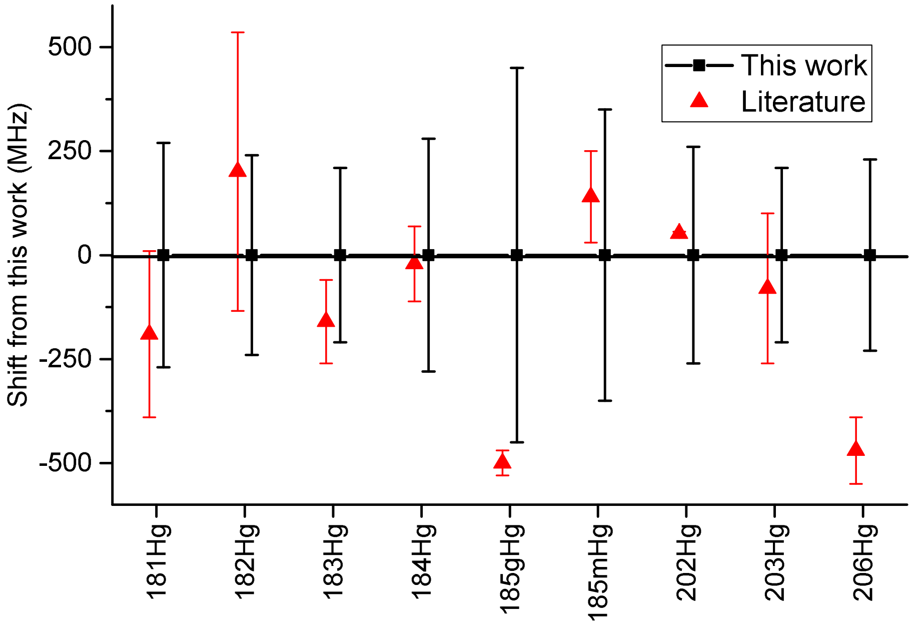

Figure 9.3: A comparison of the extracted isotope shifts to literature values compiled in [7]. The “This work” and “Literature” data points have been offset to aid clarity.

was ≈500 MHz. The agreement with the results of previous experiments, obtained through the application of different experimental methods, provides a validation of the technique of in-source RIS in a VADIS anode cavity. Crucially, this validates the

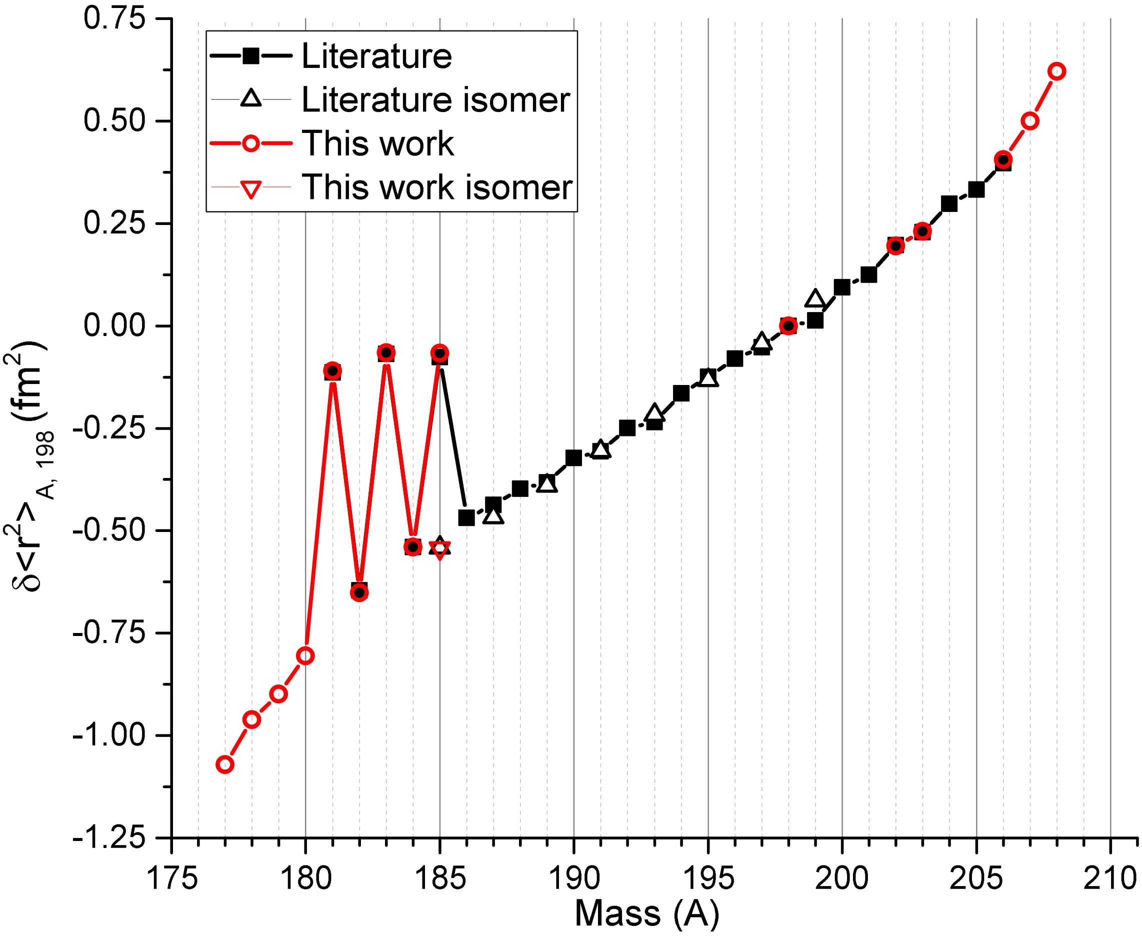

Figure 9.4: Changes of mean square charge radii $\delta\langle r^2\rangle^{198,A}$ in the isotopic chain ^{177}Hg-^{208}Hg as a function of the mass number A, taking ^{198}Hg as a reference. The literature values were calculated from [7]. Spin assignments are discussed in Section 9.4.

results for the newly measured isotopes.

9.5.2 Hyperfine A and B factors

The extracted hyperfine A and B factors from this work are presented in Table 9.3, with the literature values for the previously measured isotopes taken from [7]. The hyperfine A and B factors are compared graphically to literature values in Figure 9.5.

The uncertainties for the hyperfine A and B factors from this work consider the standard deviation of the extracted values for each isotope and the fitting errors. The extracted A and B factors from this work are in broad agreement with literature. However, there are discrepancies, particularly for the extracted A and B factors from ^{203}Hg. This indicates there may be an additional contribution to the uncertainty that was not identified. As noted in Section 9.4, the investigation of the magnetic dipole

Table 9.3: Compilation of the hyperfine A and B factors from this work and compiled by [7].

A	Spin I^{π}	A factor (MHz)	A factor (lit) (MHz)	B factor (MHz)	B factor (lit) (MHz)
177	7/2-	-4 170 (160)	-	-	-
179	7/2-	-3 960 (50)	-	-530 (210)	-
181	1/2-	+15 030 (120)	+14 960 (250)	-	-
183	1/2-	+15 150 (80)	+15 380 (30)	-	-
185	1/2-	+14 620 (220)	+14 960 (70)	-	-
185m	13/2+	-2 290 (40)	-2 305 (19)	+310 (240)	-140 (230)
203	5/2-	-5 100 (40)	-4 991.33 (0.04)	+50 (60)	-249.2 (0.3)
207	9/2+	-4 510 (40)	-	+600 (160)	-

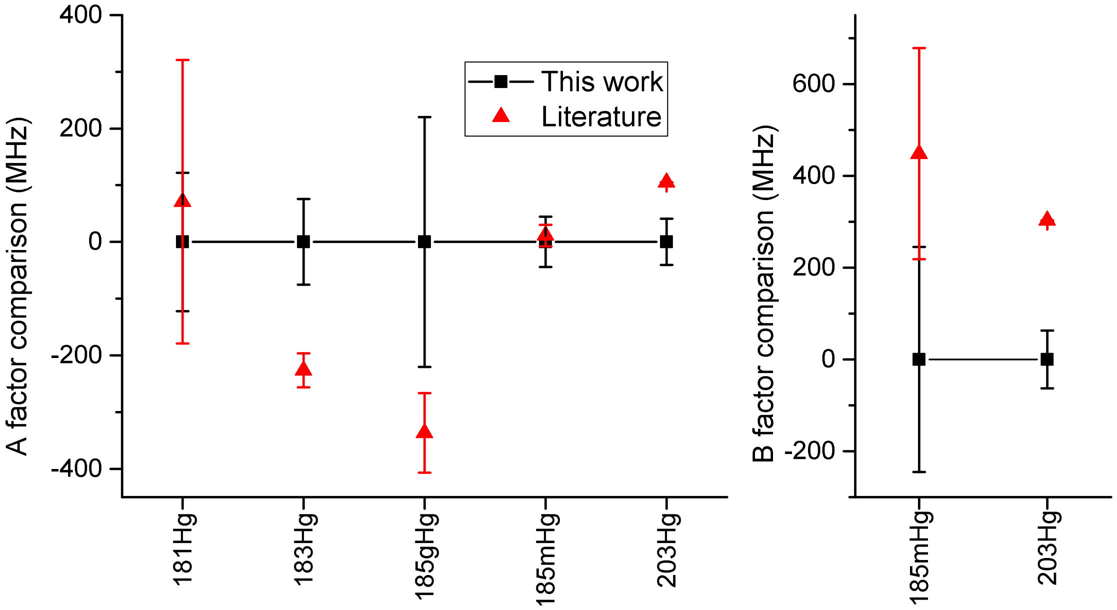

Figure 9.5: Comparison of the extracted hyperfine A and B factors to the literature values compiled in [7].

and electric quadrupole moments extracted from this work will form part of the thesis of S. Sels and therefore will not be discussed further.

Chapter 10

Charge radii of neutron deficient mercury

This chapter considers the results of the isotope shift measurements of neutron deficient mercury, with respect to the chain of mercury isotopes, the region below Z = 82 and the predictions and interpretation of nuclear models.

10.1 A cessation of extreme shape staggering

A cessation of the extreme shape staggering in neutron deficient mercury can be clearly observed in the chain of isotope shifts between ^{177}Hg and ^{187}Hg presented in Figure 10.1. These results represent the first definitive determination of the end point of the extreme shape staggering. The trend of the charge radii of neutron deficient mercury isotopes is overlaid on lines corresponding to the quadrupole deformation parameter β_2 defined in Equation 3.7, applying the revised coefficients of [17] for the calculation of the mean square radius of the spherical nuclei using the droplet model.

The strongly deformed ^{185,183,181}Hg nuclei correspond to $\beta_2 = 0.26 - 0.3$ and the weakly deformed nuclei to $\beta_2 = 0.13 - 0.17$. ^{181}Hg has the largest β_2 of the strongly deformed nuclei and ^{182}Hg the largest β_2 of the weakly deformed nuclei. The β_2 values decrease with decreasing N from A = 180, suggesting a decrease in the deformation of the weakly deformed isotopes.

The behaviour of the chain of mercury isotopes can additionally be considered in comparison to neighbouring elements, enabling a model-independent interpretation.

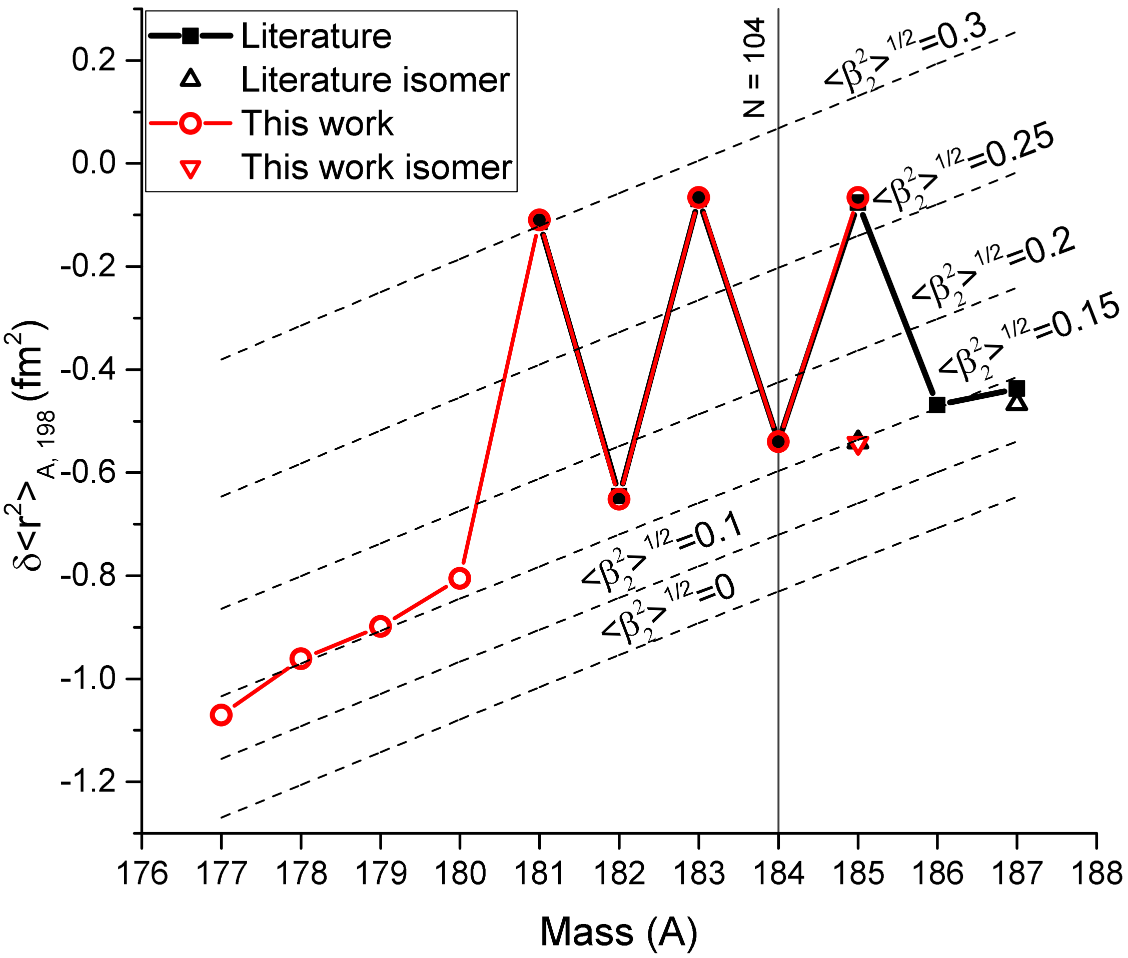

Figure 10.1: Isotope shifts of neutron deficient mercury between ^{177}Hg and ^{187}Hg. The data is overlaid on lines of β_2^2 deformation, using the predictions of the droplet model [16] with updated parameters from [17] to calculate the predicted radii of spherical nuclei.

This is presented in Figure 10.2, where the isotope chains of thallium, mercury, gold and platinum (Z = 81 to 78 respectively) are overlaid on the charge radii of the closed proton shell (Z = 82) lead isotopes.

Taking a macroscopic view of the region around mercury, the charge radii shown in Figure 10.2 could be understood as depicting the steadily decreasing influence of the Z = 82 shell closure. At Z = 81, the charge radii are near identical to that of the Z = 82 isotopes. Following the removal of one proton (Z = 80), the chain of isotopes exhibits extreme shape staggering between odd and even A isotopes, beginning at N = 106. In the isotope chain of Z = 79, there is a sudden isotope shift between N = 108 and N = 107. However, unlike its mercurial neighbour, the following even A isotopes remain deformed, resulting in an island of deformation. Finally, four protons from the Z = 82 shell closure (Z = 78), the isotopes steadily diverge from the trend

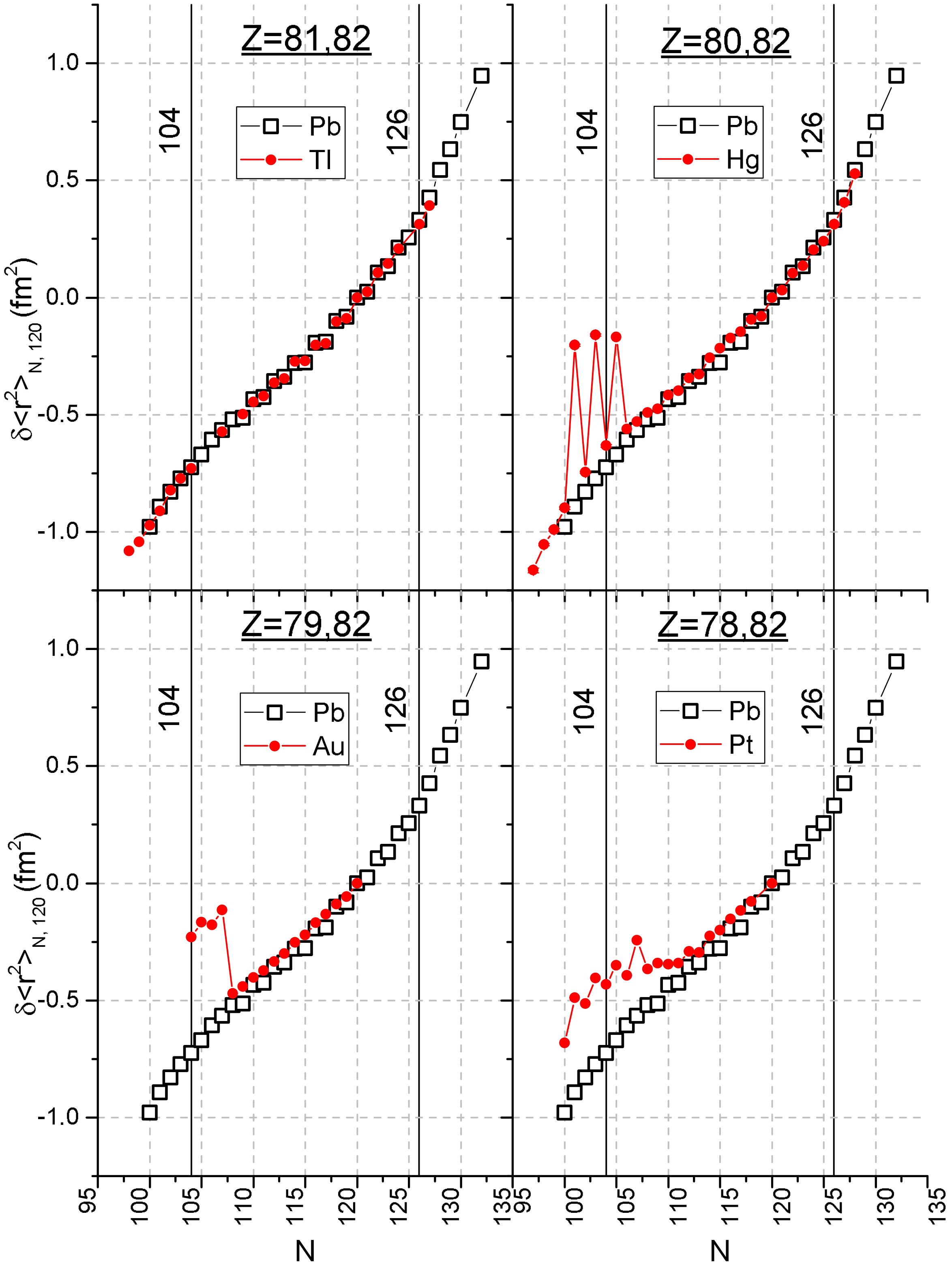

Figure 10.2: Isotope shifts for the chains of isotopes from Z = 78-82. Data taken from [128, 136, 137, 138] (Pb), [138, 139, 140] (Tl), [7] and this work (Hg), [138] (Au and Pt). The charge radii are all shown with respect to N = 120 for ease of comparison with the Au and Pt isotope chains.

of the lead charge radii, with a kink at N = 110.

Neutron shell effects can be inferred from the changes in charge radii with fixed

Z. The increase in deformation with decreasing N following the N = 126 shell closure could be expected as the result of increasing numbers of valence neutrons. There is a reduction of this deformation, most notably now in the mercury isotopes, following the N = 104 midshell region. This could be interpreted as evidence in favour of a shell closure around N = 82, well beyond the proton drip line. It is interesting to note that the return to a weak deformation in the mercury nuclei at N = 100, is somewhat mirrored in the platinum isotopes, where a sharp decrease in deformation between N = 101 and N = 100 can be observed.

10.2 Discussion of the results in the framework of non-optical studies

As discussed in Section 8.2, experimental methods other than optical spectroscopy have yielded insights into the behaviour of the chain of mercury isotopes. Coulomb excitation experiments confirmed the coexistence of two structures at low energy for the light mass mercury isotopes [141]. The results of γ-spectroscopy experiments on the mercury isotope chain are shown in Figure 10.3, reproduced from [30]. The level energies of the weakly deformed oblate band are shown in blue and the level energies of the strongly deformed prolate band are shown in red.

The intruder structure, understood to correspond to the deformed prolate deformation, is centred around N = 102. However, it is not completely symmetric, with the level energies of the intruder increasing more rapidly with decreasing N [119]. The level energies therefore indicate the disappearance of the coexisting prolate minima with decreasing N. However, it is not possible to determine from these results if the ground state shape staggering would cease at N = 100, or if there is sufficient symmetry around the N = 102 minima of the intruder level energies for the shape staggering to continue to N = 98. The suggestion of a weakly deformed ground state for the odd nuclei below A = 180, by [120, 121] and [122], is in agreement with the results presented in this work.

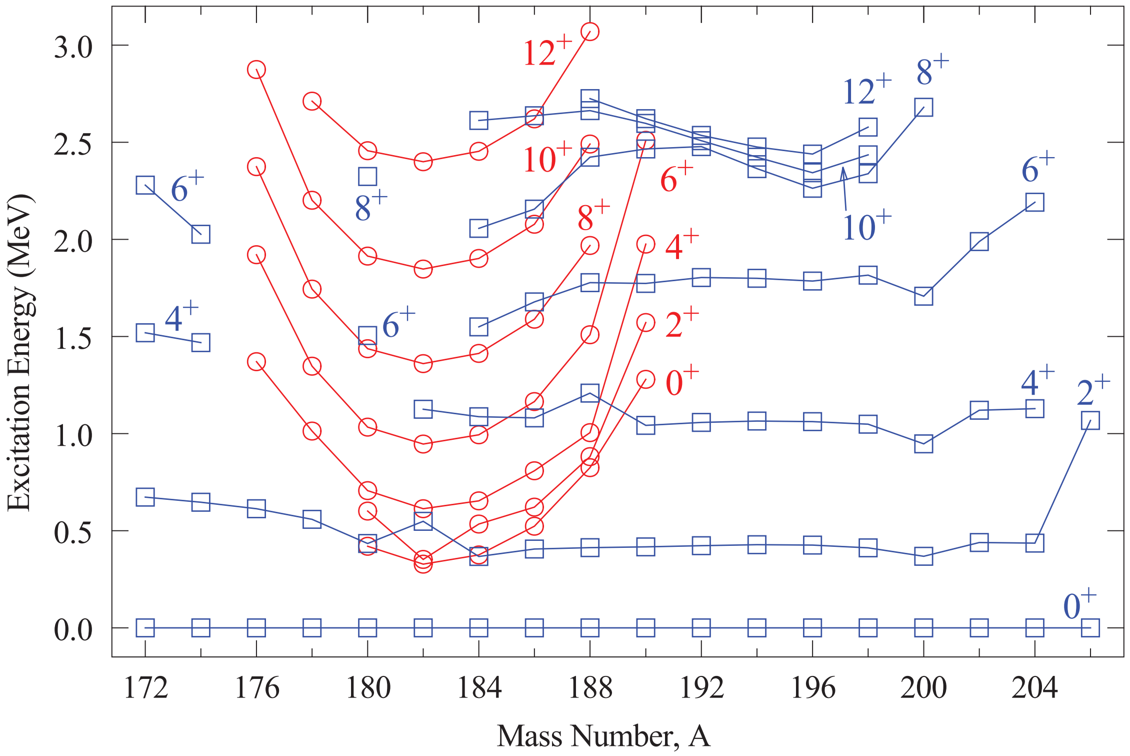

Figure 10.3: Level energy systematics of even mercury isotopes between ^{172}Hg and ^{206}Hg. The level energies assigned to the oblate deformation are depicted as blue squares, those assigned to the intruder are depicted as red circles. Figure taken from [30].

10.3 Discussion of the results in the framework of nuclear models

Charge radii systematics enable the predictive powers of state of the art nuclear models to be validated, equally these models have an important role in the interpretation of experimental results. A number of nuclear models are capable of reproducing the competing shape configurations of the neutron deficient mercury nuclei. However, they are as yet unable to reproduce the pronounced odd-even shape staggering observed between ^{186}Hg and ^{180}Hg. This can be understood as resulting from the complexity of the phenomena, where there are competing deformed shapes around the N = 104 mid shell, separated by a few hundred keV, with pairing effects sufficient to tip the balance between the two to determine the shape of the nuclear ground state.

10.3.1 Comparison with the FRLDM

In a wide ranging calculation, Möller et al. [18] used the FRLDM [142] to calculate the potential energy surfaces of 7206 nuclei between A = 31 and A = 290, with the results for 1224 even-even nuclei presented as potential energy contour plots of ϵ_2 Vs γ. Here ϵ_2 is the Nilsson quadrupole deformation parameter, which can be related to β_2 using an equation taken from [143], where

$$\beta_2 = \sqrt{\frac{\pi}{5}}\left(\frac{4}{3}\epsilon_2 + \frac{4}{9}\epsilon_2^2 + \frac{4}{27}\epsilon_2^3 + \frac{4}{81}\epsilon_2^4 + ...\right), \tag{10.1}$$

and γ describes the axial symmetry. $\gamma = 60$ corresponds to a purely oblate deformation, while $\gamma = 0$ corresponds to a purely prolate deformation. $0 < \gamma < 60$ corresponds to the degree of triaxial deformation. Contour plots taken from [18] for ^{176}Hg to ^{186}Hg are shown in Figure 10.4. Minima deeper than 0.05 MeV are marked on each plot with black circles and saddle points with crosses. The numbers labelling the bold contour lines correspond potential energies with units of MeV, each contour line corresponds to an energy difference of 0.2 MeV.

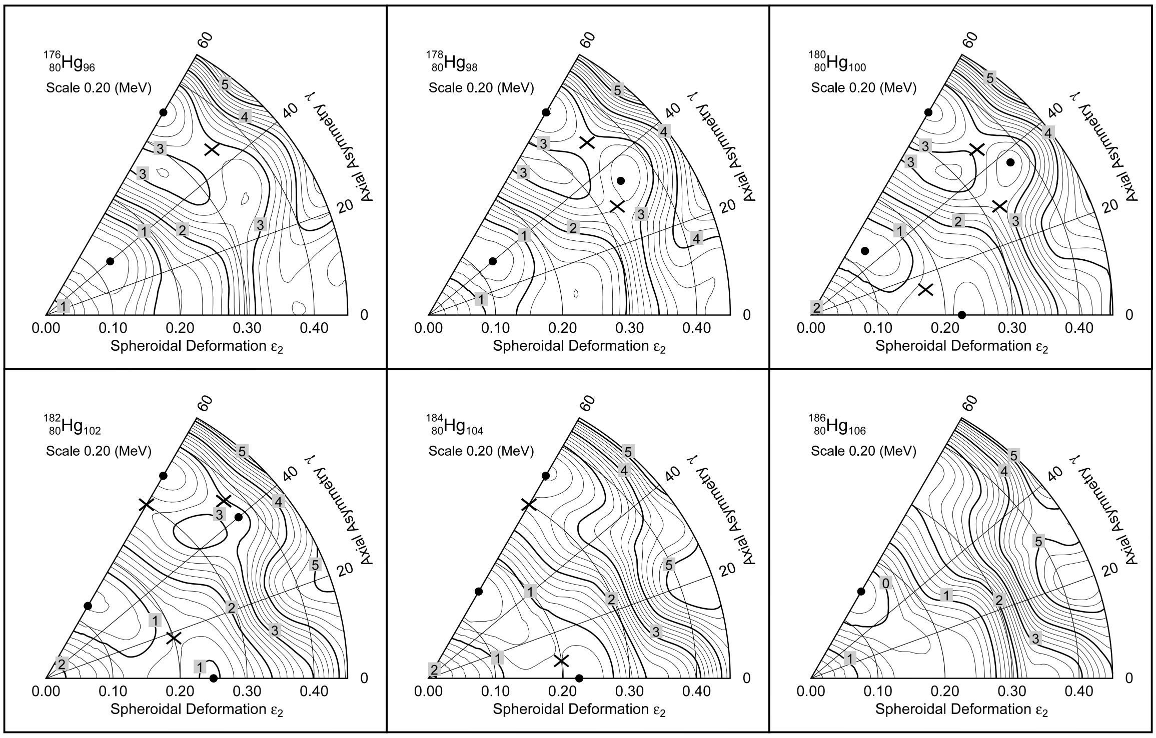

Figure 10.4: FRLDM potential energy surface contour plots predicting the evolution of shape coexistence in even mercury isotopes from ^{176}Hg to ^{186}Hg. Parameters are defined in the text. Figure taken from [18].

The contour plots shown in Figure 10.4 clearly depict competing oblate and prolate minima, with potential energies around 1 MeV. The prolate minima appears between N = 186 and N = 184 and disappears between N = 180 and N = 178. Were this to correspond exactly to the beginning and the end of the shape staggering, it would suggest the ground state of ^{179}Hg would have a strong prolate deformation. Applying Equation 10.1, it can be seen that the deformations are in broad agreement with the droplet model deformation lines presented in Figure 10.1. ^{185,183,181}Hg have β_2 = 0.26-0.3 (ϵ_2 = 0.23-0.26) which corresponds to the strongly deformed prolate minima in the contour plots, the other isotopes have β_2 = 0.13-0.17 (ϵ_2 = 0.12-0.16) corresponding to the weak oblate deformation in the FRLDM results. The contour plots enable the visualisation of the competing minima. However, the full results (included as a table in [18]) do not reproduce the odd-even shape staggering and indicate a weak oblate deformation of the nuclear ground state for both odd and even mercury isotopes around N = 104.

10.3.2 Comparison with the IBM

J.E. García-Ramos and K. Heyde applied the IBM to even A mercury isotopes [123]. The results were in good agreement with the energy level systematics shown in Figure 10.3, similarly the model was able to well reproduce isotope shifts of mercury isotopes, though only even isotopes between N = 104 and N = 114. Predictions were not reported beyond N = 104. The calculations indicated two competing shapes corresponding to a weak oblate deformation and a strong prolate deformation. However, the IBM results also indicated that the ground state of the even isotopes had a pronounced prolate deformation between $100 \leq N \leq 104$, with the energy minima degenerate at N = 106. This was in contradiction to their calculations for the isotope shift of ^{184}Hg. The IBM is heavily influenced by the experimental data used in the formulation of the model [144], a particularly good example being the determination of the lowest lying level energy of the intruder band observed in neutron deficient mercury [145].

10.3.3 Comparison with (relativistic) mean field calculations

The mercury isotopes have been investigated with both mean field and relativistic mean field calculations. Mean field calculations by J.M. Yao et al. [146] and K. Nomura et al. [147] were able to reproduce the competing oblate and prolate shapes. However, the results corresponded to a strongly deformed prolate ground state for the even isotopes between $100 \leq N \leq 106$ and $98 \leq N \leq 106$ respectively. In relativistic mean field calculations, T. Nikšić et al. [148] were able to reproduce the weakly oblate ground states for even mass neutron deficient mercury isotopes. However, this was only possible using an effective interaction parametrization tailored specifically to the Z = 78-82 region. Therefore the authors did not consider it to be a general effective relativistic mean-field interaction. The calculations were not extended to the odd mercury isotopes. A more recent and wide ranging set of calculations by S. E. Agbemava et al. [149] determined the even isotopes to have a strong prolate deformation for $100 \leq N \leq 108$.

Following the in-source spectroscopy results reported here, axial Hartree-Fock-Bogoliubov calculations were undertaken for both odd and even mercury isotopes by the Nuclear theory group at the University of York. This work is currently unpublished, but reported at [150]. Through a careful tuning of the parameters, their calculations were capable of reproducing the pronounced shape staggering behaviour.

10.4 Conclusion

The mean square charge radii measurements were extended four isotopes further into the neutron deficient region of the nuclear chart, down to ^{177}Hg. These measurements provided a definitive demonstration of the cessation of the extreme odd-even staggering in the neutron deficient mercury isotopes. This reduction in deformation could be interpreted as evidence for the robustness of a shell closure around N = 82, beyond the proton drip line.

Nuclear models are capable of demonstrating the competing oblate and prolate deformations, providing a valuable tool for the interpretation of the results. Nuclear models are also capable of reproducing the lowering of the potential energy of the well deformed prolate minima around the N = 104 midshell. Recent Hartree-Fock-Bogoliubov calculations, based on the results reported here, were able to reproduce the extreme shape staggering behaviour in the neutron deficient mercury isotopes.

Chapter 11

Charge radii of neutron rich mercury

The crossing of the N = 28, 50, 82 and 126 shell closures correspond to an increase in the gradient of the isotope shifts (a “kink”) with increasing N [138]. The reproduction of the kink is often used as a benchmark for nuclear models [151]. M. M. Sharma et al. [152] were the first to reproduce the kink, using relativistic mean field calculations. The applicability of relativistic mean field models to reproducing the kink is understood to be related to the automatic inclusion of the spin-orbit interaction [153]. The kink is the result of the attraction between protons and neutrons. The spin-orbit interaction affects the single particle neutron levels, the occupancy of which affects the proton wave function and thus the mean square charge radii. Optical spectroscopy data on the mean square charge radii of even lead and polonium isotopes, was used to investigate the gradient of the kink at the crossing of the N = 126 shell closure by P. Goddard et al. [154]. Their calculations determined that the occupation of the $1i_{11/2}$ neutron orbital was required to reproduce the gradient of the kink in the lead and polonium isotope chains.

This work, which extends the mercury isotope shift measurements further into the neutron rich region of the nuclear chart, reveals the characteristic kink and enables the determination of the change in the gradient of the isotope shifts. Mercury is only the third isotope chain for which both N=127 and N=128 have been measured after lead and bismuth (unpublished results [155]) and the first below the Z = 82 proton shell closure. The current capability of nuclear models in this region of the nuclear chart is often limited to even-even isotopes. Therefore, the determination of the isotope shifts of the even mercury isotopes is particularly important for the benchmarking of such models. The results reported here are presented in Figure 11.1 where the kink in the trend of the isotope shifts is clearly visible, a line is drawn through the even isotopes $\leqslant$ N = 126 to guide the eye.

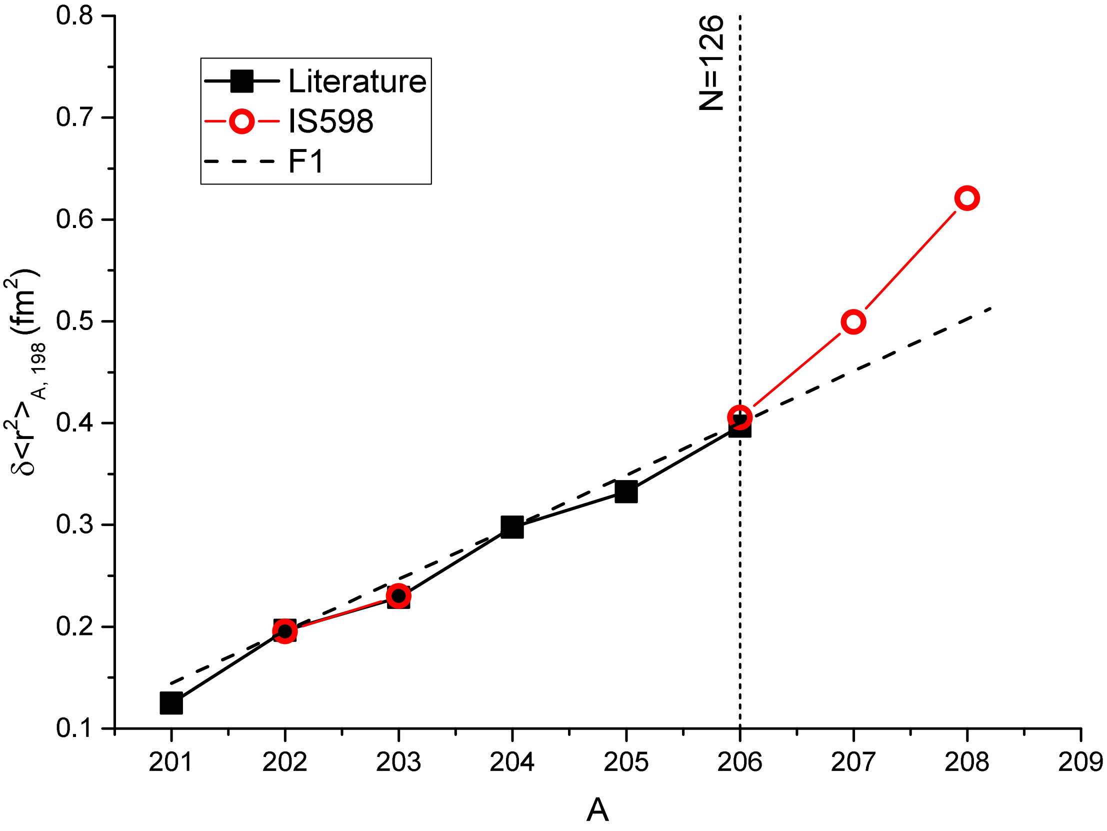

Figure 11.1: Isotope shifts of stable and neutron rich mercury isotopes ^{202}Hg - ^{208}Hg. Data taken from this work (hollow red circles) and calculated from the $\delta\nu^{198,A}$ reported in [7] (solid black squares).

Methods for defining the kink are presented in Section 11.1. The discrepancy between the $\delta\langle r^2\rangle^{198,206}$ reported in this work and the previously reported values is investigated in Section 11.2. Finally, the gradient of the kink in the trend of the charge radii of mercury isotopes at N = 126 is determined in Section 11.3 and compared to the predictions of nuclear models.

11.1 Defining the kink

Before investigating the magnitude of the kink in the charge radii systematics, it is necessary to find an objective definition of this phenomenon. There are a number of possible approaches:

- The change in gradient considering even-N isotopes adjacent to the kink $R(m_{(2N)})$ where

$$R(m_{(2N)}) = \frac{\delta\langle r^2\rangle^{N=126,124}}{\delta\langle r^2\rangle^{N=128,126}}. \tag{11.1}$$

  This approach offers the best determination of the kink, as no odd-even staggering effects are included and the gradient is not affected by increasing deformation moving away from the neutron shell closure. However, for $84 \leq \mathrm{Z} \geq 88$ $\mathrm{t}_{1/2}$ at $\mathrm{N} = 128$ is < 300 µs, hindering potential laser spectroscopy measurements.

- Determination of the change in gradient considering isotopes adjacent to the kink $R(m_{(1N)})$ where

$$R(m_{(1N)}) = \frac{\delta\langle r^2\rangle^{N=126,125}}{\delta\langle r^2\rangle^{N=127,126}}. \tag{11.2}$$

  Considering the adjacent odd-N isotopes expands the range of elements for which laser spectroscopy is feasible using conventional methods at thick-target ISOL facilities: for $80 \leq \mathrm{Z} \geq 88$ $\mathrm{t}_{1/2}$ at $\mathrm{N} = 127$ is > 1.5 ms. However, considering the adjacent odd-N isotopes includes a contribution from the odd-even staggering, which makes a direct comparison between isotope chains more challenging. The contribution of the odd-even staggering is additionally an issue when determining the kink in the trend of isotopes where there is a reversal of the odd-even staggering beyond the neutron shell closure, as has been reported for Z = 86,88 [82].

- A final option is a linear fit of the even-N isotopes before and after the kink $R(m_{(fit)})$. This method has the advantage of avoiding the influence of odd-even staggering. Additionally, even-N isotopes with longer half lives can be used to determine the gradient, enabling a gradient to be determined for $80 \leq \mathrm{Z} \leq 88$. However, changes in deformation moving away from the shell closure can result in a non-linear trend of isotope shifts, reducing the accuracy of the determination of the kink. Additionally, the gradient of the trend of isotope shifts is not consistent immediately prior to and following the N=126 shell closure. Considering the lead isotope chain, the gradient increases between N = 124 and N = 126 compared to the even-N isotopes between N = 120 and N = 124, the same behaviour is seen following the shell closure, with an increased gradient between and N = 126 and N = 128 compared to the even-N isotopes between N = 128 and N = 132. This is illustrated in Figure 11.3 for the lead isotope chain, with the gradients determined from the various fitting options presented in Table 11.1

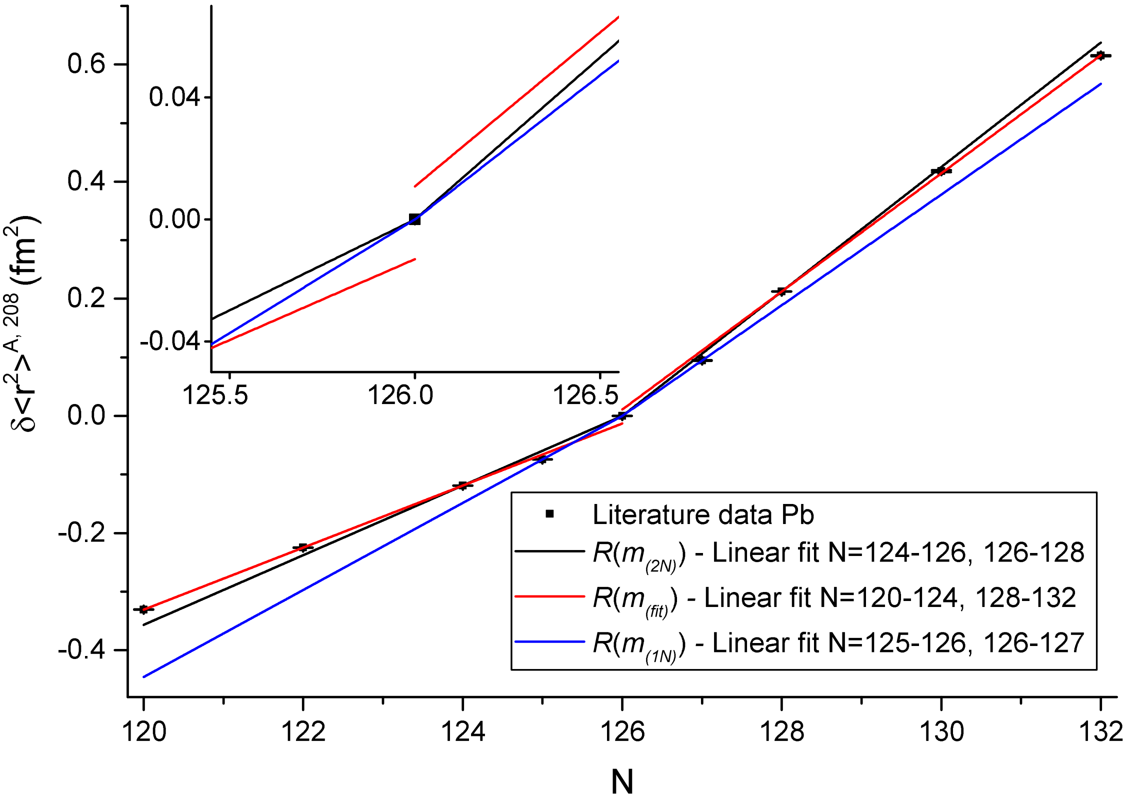

Figure 11.2: Linear fits of the mean square charge radii at the crossing of the N = 126 shell closure in the lead isotope chain (data from [138]). $R(m_{(2N)})$ is the change in gradient considering N = 126 and the adjacent even-N isotopes (N = 124, 126 and N = 126, 128), $R(m_{(fit)})$ is the change in gradient considering the even-N isotopes before and after N = 126 (N = 120, 122, 124 and N = 128, 130, 132) and $R(m_{(1N)})$ is the change in gradient considering N = 126 and the immediately adjacent isotopes (N = 125, 126 and N = 126, 127).

From Figure 11.2 and Table 11.1, it is evident the different approaches for defining the kink yield significantly differing values. In Figure 11.2 it can be seen linear fits of the even isotopes N = 120-124 and N = 128-132 (shown in red) do not meet at N = 126, therefore failing to provide a value for the kink at the shell closure. From

Table 11.1: A comparison of kink determination methods for the lead isotope chain, data from [138].

Element	$R(m_{(2N)})$	$R(m_{(fit)})$= $\frac{\delta\langle r^2\rangle^{N=120,124}}{\delta\langle r^2\rangle^{N=128,132}}$	$R(m_{(1N)})$
Pb	1.787 (6)	1.904 (11)	1.272 (8)

Table 11.1 it can be seen that the $R(m_{(fit)})$ method overestimated the kink defined as $R(m_{(2N)})$ by 6.5 (7)%. The effects of the odd-even staggering when considering $R(m_{(1N)})$ (shown in blue) are significantly more pronounced, using the values from Table 11.1 this method underestimates the kink defined as $R(m_{(2N)})$ by 29.1 (7)%. The $R(m_{(1N)})$ results require a multiplication factor to accurately reproduce the kink. However, the magnitude of the odd-even staggering varies along chains of isotopes and across shell closures, consequently any accurate correction would require knowledge of isotopes N = 124, 126, 128 which negates the usefulness of the correction.

The mercury isotope chain is therefore a particularly good case to investigate the kink at the N = 126 shell closure as it is possible to determine $R(m_{(2N)})$: the optimal method by which to benchmark nuclear models seeking to reproduce the trend in mean square charge radii at the shell closure.

11.2 ^{206}Hg

The most important isotope in the determination of the kink is N = 126 (^{206}Hg in the mercury isotope chain). Therefore the discrepancy between the $\delta\nu^{198,A}$ determined in this work and previous measurements (Figure 9.3) is of particular concern. The literature value $\delta\nu^{198,206}$ = -20420 (80) MHz, included in Table 9.2, was reported in the thesis of P. Dabkiewicz [156] and included in the 1986 mercury charge radii compilation of G. Ulm et al. [7]. However, the thesis value was not included in the 2005 compendium of charge radii by G. Fricke and K. Heilig [98], they instead used a previously published value of $\delta\nu^{204,206}$ = -4700 (500) MHz ≈ $\delta\nu^{198,206}$ = -20010 (500) MHz from [157]. These shifts are respectively 470 MHz and 880 MHz smaller than the ≈ $\delta\nu^{198,206}$ =-20890 (230)MHz reported in this work.

In this work there was no distinguishable difference between the experimental method for the $\delta\nu^{198,206}$ measurement and the measurements of the other isotopes.

It may therefore be reasonable to suggest the following explanation based upon a possible inaccuracy in the earlier measurements. There were multiple mercury isotopes present in the A = 206 mass selected ion beam during the previous measurements of ^{206}Hg [156, 157]. If the tail of the dominant ^{204}Hg signal was not fully accounted for in the fitting of the ^{206}Hg resonance, the effect would be a shift in the CG towards a smaller $\delta\nu^{198,A}$, and thus a smaller $\delta\langle r^2\rangle^{198,A}$. Such an issue would have the effect of shifting the value obtained in the same direction as that of the discrepancy described here.

Considering the systematics of the region, there is a reasonable agreement between the relative mean square charge radii of the lead (Z = 82) and polonium (Z = 84) isotopes approaching the N=126 shell closure. The relative mean square charge radii of mercury (Z = 80) isotopes from this work and the values reported in [7] are compared to the lead and polonium isotopes in Figure 11.3 a). Additionally, the difference in mean square charge radii of even-N isotopes of Z = 80-84, 85-88 is compared in Figure 11.3 b).

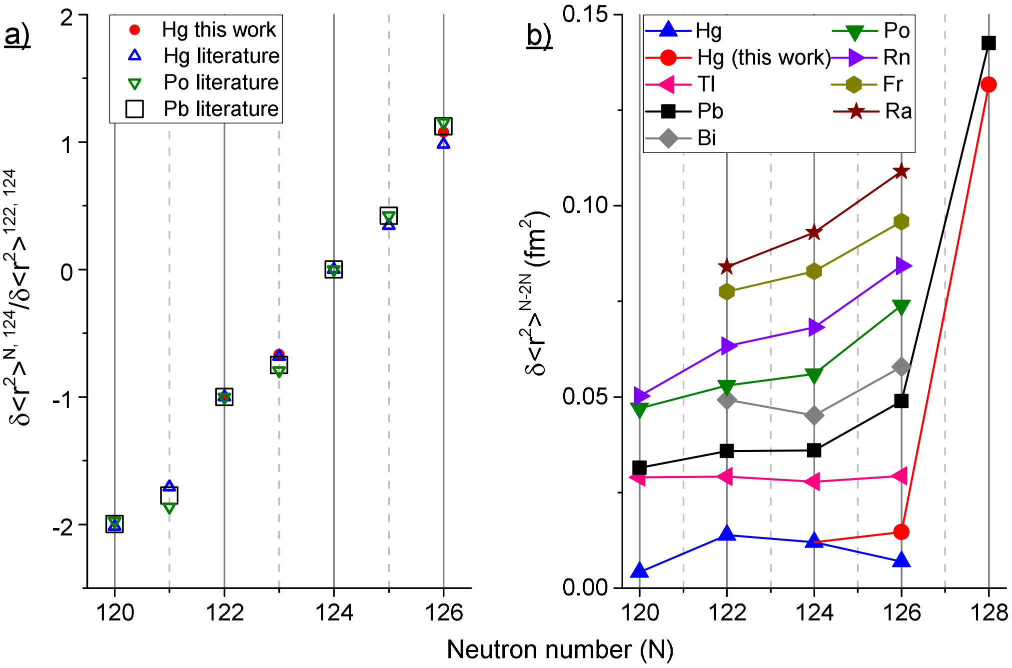

Figure 11.3: a) Relative variation in the mean square charge radii, comparing Hg (data from this work and calculated from the $\delta\nu^{198,A}$ reported in [7]), Pb (data taken from [138]), Po (data taken from [138]) between N=120 and N=128. b) The difference in mean square charge radii between even-N isotopes for Z = 80-84,86-88. The isotope chains are artificially displaced to aid interpretation. The mercury data is taken from this work and calculated from the $\delta\nu^{198,A}$ reported in [7], all other data is taken from [138].

In Figure 11.3a, it can be seen that there is increasingly good agreement for the odd-A and even-A isotopes approaching N=126 (isotopes of N = 122,124 are overlapped by the nature of the comparison). The value of $\delta\langle r^2\rangle^{A,126}$ for mercury obtained in this work is in better agreement with the systematics of the region than the previous value reported in [7]. From Figure 11.3b, it can be seen that the difference in the mean square charge radii increases between N = 124 and N = 126 in the isotope chains of Z = 81-84, 86-88. Prior to this work, only the mercury isotope chain exhibited a decrease. If we replace the earlier value for ^{206}Hg with the new value from this work, the mercury isotope chain is in agreement with the systematics of the region.

These discussions are not conclusive. However, since there is not an identified cause to doubt our measurements it is deemed appropriate to use the value determined in this work in the following determination of the kink.

11.3 Crossing the N=126 shell closure

The kink at the crossing of the N=126 shell closure is considered to be ubiquitous, having previously been observed (or inferred where measurements N=125-127 have not been made) for Z = 81-84, 86-88. However, as discussed in the introduction to this chapter, the only chain of charge radii measurements where N=124, 126, 128 have previously been published is the lead (Z=82) isotopes. The values of $R(m_{(2N)})$ and $R(m_{(1N)})$ calculated for mercury and lead are presented in Table 11.2, together with the kink predicted by covariant Density Functional Theory (DFT) calculations $R(m_{(2N_DFT)})$ from [149].

Table 11.2: The measured $R(m_{(2N)})$ the predicted $R(m_{(2N_DFT)})$ from [149] and the measured $R(m_{(1N)})$ in the mercury isotope chain at the crossing the N=126 shell closure. The measured values are from this work (Hg: N = 126, 127, 128), calculations of the $\delta\nu^{198,A}$ reported in [7] (Hg: N = 124, 125) and from [138] (Pb N=124-128).

Element	$R(m_{(2N)})$	$R(m_{(2N_DFT)})$	$R(m_{(1N)})$
Hg	1.980 (52)	2.86	1.267 (60)
Pb	1.787 (11)	2.51	1.271 (8)

It is clear from the values in Table 11.2, that the prediction of the covariant DFT calculations overestimate the gradient of the kink defined as $R(m_{(2N)})$. The uncertainty of $R(m_{(2N)})$ for mercury is <3%, sufficient for comparisons with nuclear models which consider an agreement to within 10% to be reasonable [154]. As expected, there is a significant difference between the values of $R(m_{(1N)})$ and $R(m_{(2N)})$ due to odd-even staggering contributions.

The kinks in the mercury and lead isotope chains are plotted in Figure 11.4, together with the predictions from Droplet model calculations using the parametrization from [17] and the results of covariant DFT calculations reported in [149]. Both sets of calculations are fixed to the experimental data points at N=126 and the isotope chains are arbitrarily displaced to facilitate comparison. The measured and predicted gradients $m_1^{(2N)}=\delta\langle r^2\rangle^{N=124,126}$ and $m_2^{(2N)}=\delta\langle r^2\rangle^{N=126,128}$ are also given in Table 11.3.

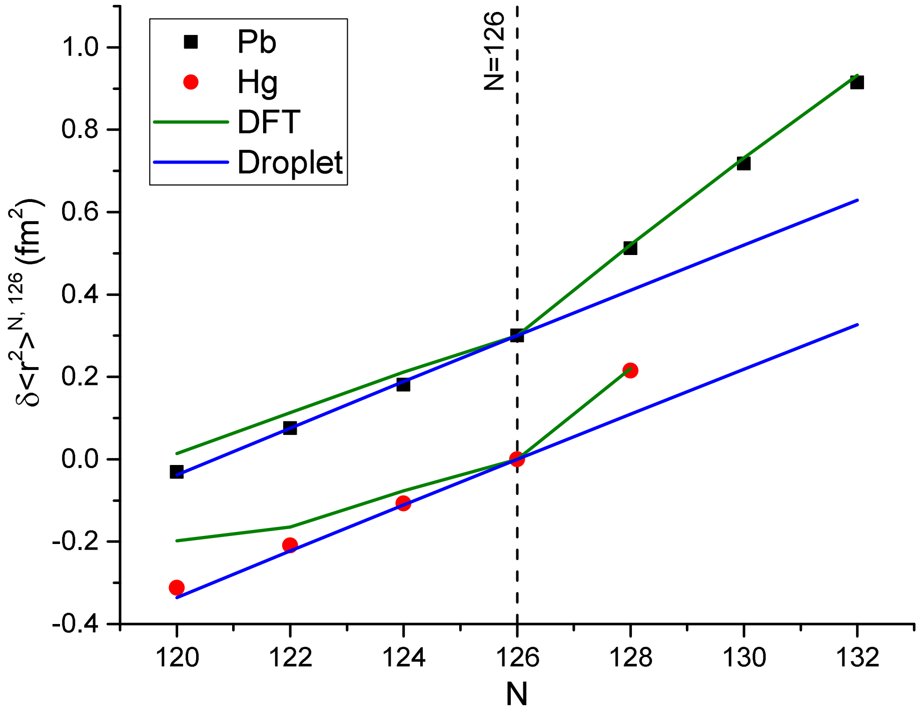

Figure 11.4: Isotope shifts of lead and mercury isotopes across the N = 126 shell closure, with the predictions of covariant Density Functional Theory (DFT) calculations from [149] and Droplet model calculations using the parametrization of [17]. The experimental data points are taken from this work (Hg: N = 126, 128), calculations of the $\delta\nu^{198,A}$ reported in [7] (Hg: N = 120, 122, 124,) and from [138] (Pb: N = 120, 122, 124, 126, 128). The lead and mercury isotopes are offset from each other for clarity.

Considering Figure 11.4, the Droplet model is capable of reproducing the trend of isotope shifts in both the mercury and lead isotope chains in the immediate vicinity below the N = 126 shell closure. However, it fails to reproduce the kink. This is to be expected as the Droplet model is not capable of reproducing shell effects and is based on a set of empirically determined parameters, this is a clear demonstration of the

Table 11.3: $m_1^{(2N)}$ and $m_2^{(2N)}$ gradients for mercury and lead isotopes presented in Figure 11.4, together with the predictions of [149] ($m_1^{(2NDFT)}$, $m_2^{(2NDFT)}$). The gradients are defined in the text.

Element	$m_1^{(2N)}$ (fm^2)	$m_1^{(2NDFT)}$ (fm^2)	$m_2^{(2N)}$ (fm^2)	$m_2^{(2NDFT)}$ (fm^2)
Hg	0.1080 (22)	0.0769	0.2140 (35)	0.2203
Pb	0.1179 (5)	0.0881	0.2107 (9)	0.2209

limitations of this model. The failure of the covariant DFT calculations to reproduce the trend of the lead and mercury isotopes below the N = 126 shell closure is recognised and partially attributed to the incorrect position of the proton $1h_{9/2}$ spherical subshell in the model [149]. It can be seen however, in Figure 11.4 and Table 11.3, that above the shell closure the covariant DFT calculations are well able to reproduce the trend in isotope shifts for both mercury and lead isotopes.

11.4 Conclusion

These measurements have enabled $R(m_{(2N)})$ to be determined for the mercury isotope chain. Used in combination with the previous measurements of lead, this will enable the benchmarking of the capability of nuclear models to reproduce shell effects in the heavier region of the nuclear chart. Compared to the results presented in Chapter 10, these results offer a comparatively lower-hanging fruit for theorists wishing to test the capabilities of their calculations, given that the values correspond to an unambiguous shell effect considering only even-even isotopes.

Chapter 12

Conclusion

This thesis presents both a series of developments for the ISOLDE RILIS and the results following their application for a study of the ground state properties of exotic mercury nuclei.

A new laser-atom interaction region was identified and characterized, coupling the RILIS with the VADIS, ISOLDE's variant of the FEBIAD-type arc discharge ion source. This has resulted in a truly versatile ion source the VADLIS (Versatile Arc Discharge and Laser Ion Source). This development has enabled the application of the RILIS with molten metal targets at ISOLDE, increased the flexibility of ISOLDE operation and opened a new direction for ion source development. In a separate series of developments, new RILIS ionization schemes are presented for tellurium, germanium, chromium, mercury and radium. In the course of the radium scheme development, autoionizing states were identified for the first time, in addition to the observation of optical pumping in the hot cavity environment.

The VADLIS development and the new RILIS ionization scheme for mercury were instrumental in the success of the in-source RIS of exotic mercury isotopes presented in this thesis. The increase in the ionization efficiency of a factor of 60 (compared to the previous RILIS ionization scheme) together with the sensitivity of the technique, enabled HFS measurements on the mercury isotope chain to be extended four isotopes further towards the proton drip line: down to ^{177}Hg and two isotopes further into the neutron rich region of the nuclear chart up to ^{208}Hg.

Analysis of the extracted mean square charge radii definitively determined ^{180}Hg to be the end point of the famous odd-even staggering in the light mercury isotopes.

The reduction in deformation offers possible evidence for the robustness of a neutron shell closure around N = 82, well beyond the proton drip line.

The extension of the isotope shift measurements at the neutron rich end of the mercury isotope chain, corresponded to the crossing of the N = 126 neutron shell closure. This enabled the determination of the characteristic kink in the gradient of the isotope shifts. This is the lowest Z isotope chain for which the mean square charge radii of isotopes with N = 127 and N = 128 has been studied and only the third overall after lead (Z = 82) and bismuth (Z = 83). Measurement of the N = 124, 126 and 128 isotopes is essential for the most accurate determination of the kink, as it enables the change in the gradient of the isotope shifts to be determined across the shell closure without the influence of odd-even staggering effects. In this region of the nuclear chart, it is typically only the even-even isotopes that are accessible to nuclear theory calculations. Thus these results are particularly applicable for the benchmarking of nuclear theory calculations as they attempt to reproduce shell effects in the trend of mean square charge radii.

Bibliography

[1] C. Müller, C. Vermeulen, U. Köster, K. Johnston, A. Türler, R. Schibli, and N.P. van der Meulen. Alpha-PET with terbium-149: evidence and perspectives for radiotheragnostics. *EJNMMI Radiopharmacy and Chemistry*, 1(1):5, 2017. `doi:10.1186/s41181-016-0008-2`.

[2] R.N. Wolf, D. Beck, K. Blaum, Ch. Böhm, Ch. Borgmann, M. Breitenfeldt, N. Chamel, S. Goriely, F. Herfurth, M. Kowalska, S. Kreim, D. Lunney, V. Manea, E. Minaya Ramirez, S. Naimi, D. Neidherr, M. Rosenbusch, L. Schweikhard, J. Stanja, F. Wienholtz, and K. Zuber. Plumbing Neutron Stars to New Depths with the Binding Energy of the Exotic Nuclide ^{82}Zn. *Physical Review Letters*, 110(4):041101, 2013. `doi:10.1103/PhysRevLett.110.041101`.

[3] A.T. Mecherikunnel, J.A. Gatlin, and J.C. Richmond. Data on total and spectral solar irradiance. *Applied Optics*, 22(9):1354, 1983. `doi:10.1364/AO.22.001354`.

[4] K. Heyde and J.L. Wood. Shape coexistence in atomic nuclei. *Reviews of Modern Physics*, 83(4):1467–1521, 2011. `doi:10.1103/RevModPhys.83.1467`.

[5] J. Bonn, G. Huber, H.J. Kluge, L. Kugler, and E.W. Otten. Sudden change in the nuclear charge distribution of very light mercury isotopes. *Physics Letters B*, 38(5):308–311, 1972. `doi:10.1016/0370-2693(72)90253-5`.

[6] T. Kühl, P. Dabkiewicz, C. Duke, H. Fischer, H.J. Kluge, H. Kremmling, and E.W. Otten. Nuclear Shape Staggering in Very Neutron-Deficient Hg Isotopes Detected by Laser Spectroscopy. *Physical Review Letters*, 39(4):180–183, 1977. `doi:10.1103/PhysRevLett.39.180`.

[7] G. Ulm, S.K. Bhattacherjee, P. Dabkiewicz, G. Huber, H.J. Kluge, T. Kühl, H. Lochmann, E.W. Otten, K. Wendt, S.A. Ahmad, W. Klempt, and R. Neugart. Isotope shift of ^{182}Hg and an update of nuclear moments and charge radii in the isotope range ^{181}Hg-^{206}Hg. *Zeitschrift für Physik A Hadrons and nuclei*, 325(3):247–259, 1986. `doi:10.1007/BF01294605`.

[8] K.S. Krane. *Introductory Nuclear Physics.* Wiley, 1987.

[9] R. Casten. *Nuclear Structure from a Simple Perspective.* Oxford University Press, 2000.

[10] B.R. Martin. *Nuclear and Particle Physics: An Introduction.* Wiley, 2009.

[11] B. Povh, K. Rith, C. Schulz, W. Rodejohann, and F. Zetsche. *Particles and Nuclei: An Introduction to the Physical Concepts*. Springer, 2015.

[12] G. Gamow. Mass Defect Curve and Nuclear Constitution. *Proceedings of the Royal Society A: Mathematical, Physical and Engineering Sciences*, 126(803):632–644, 1930. `doi:10.1098/rspa.1930.0032`.

[13] C.F.v. Weizsacker. Zur Theorie der Kernmassen. *Zeitschrift fur Physik*, 96(7-8):431–458, 1935. `doi:10.1007/BF01337700`.

[14] W.D. Myers and W.J Swiatecki. Average nuclear properties. *Annals of Physics*, 55(3):395–505, 1969. `doi:10.1016/0003-4916(69)90202-4`.

[15] W.D. Myers and W.J. Swiatecki. The nuclear droplet model for arbitrary shapes. *Annals of Physics*, 84(1-2):186–210, 1974. `doi:10.1016/0003-4916(74)90299-1`.

[16] W.D. Myers and K.H. Schmidt. An update on droplet-model charge distributions. *Nuclear Physics A*, 410(1):61–73, 1983. `doi:10.1016/0375-9474(83)90401-3`.

[17] D. Berdichevsky and F. Tondeur. Nuclear core densities, isotope shifts, and the parametrization of the droplet model. *Zeitschrift für Physik A Hadrons and nuclei*, 322(1):141–147, 1985. `doi:10.1007/BF01412027`.

[18] P. Möller, A.J. Sierk, R. Bengtsson, H. Sagawa, and T. Ichikawa. Nuclear shape isomers. *Atomic Data and Nuclear Data Tables*, 98(2):149–300, 2012. `doi:10.1016/j.adt.2010.09.002`.

[19] R.D. Woods and D.S. Saxon. Diffuse Surface Optical Model for Nucleon-Nuclei Scattering. *Physical Review*, 95(2):577–578, 1954. `doi:10.1103/PhysRev.95.577`.

[20] O. Haxel, J.H.D. Jensen, and H.E. Suess. On the ”Magic Numbers” in Nuclear Structure. *Physical Review*, 75(11):1766–1766, 1949. `doi:10.1103/PhysRev.75.1766.2`.

[21] M.G. Mayer. On Closed Shells in Nuclei. II. *Physical Review*, 75(12):1969–1970, 1949. `doi:10.1103/PhysRev.75.1969`.

[22] M.G. Mayer. Nuclear Configurations in the Spin-Orbit Coupling Model. I. Empirical Evidence. *Physical Review*, 78(1):16–21, 1950. `doi:10.1103/PhysRev.78.16`.

[23] S.G. Nilsson, C.F. Tsang, A. Sobiczewski, Z. Szymański, S. Wycech, C. Gustafson, I.L. Lamm, P. Möller, and B. Nilsson. On the nuclear structure and stability of heavy and superheavy elements. *Nuclear Physics A*, 131(1):1–66, 1969. `doi:10.1016/0375-9474(69)90809-4`.

[24] R. Bengtsson, J. Dudek, W. Nazarewicz, and P. Olanders. A systematic comparison between the Nilsson and Woods-Saxon deformed shell model potentials. *Physica Scripta*, 39(2):196–220, 1989. `doi:10.1088/0031-8949/39/2/002`.

[25] A. Arima and F. Iachello. Interacting boson model of collective states I. The vibrational limit. *Annals of Physics*, 99(2):253–317, 1976. `doi:10.1016/0003-4916(76)90097-X`.

[26] F. Iachello and A. Arima. Boson symmetries in vibrational nuclei. *Physics Letters B*, 53(4):309–312, 1974. `doi:10.1016/0370-2693(74)90389-X`.

[27] A.N. Andreyev, M. Huyse, P. Van Duppen, L. Weissman, D. Ackermann, J. Gerl, F.P. Hessberger, S. Hofmann, A. Kleinböhl, G. Münzenberg, S. Reshitko, C. Schlegel, H. Schaffner, P. Cagarda, M. Matos, S. Saro, A. Keenan, C. Moore, C.D. O'Leary, R.D. Page, M. Taylor, H. Kettunen, M. Leino, A. Lavrentiev, R. Wyss, and K. Heyde. A triplet of differently shaped spin-zero states in the atomic nucleus ^{186}Pb. *Nature*, 405(6785):430–433, 2000. `doi:10.1038/35013012`.

[28] J.L. Wood and K. Heyde. A focus on shape coexistence in nuclei. *Journal of Physics G: Nuclear and Particle Physics*, 43(2):020402, 2016. `doi:10.1088/0954-3899/43/2/020402`.

[29] H. Morinaga. Interpretation of Some of the Excited States of 4n Self-Conjugate Nuclei. *Physical Review*, 101(1):254–258, 1956. `doi:10.1103/PhysRev.101.254`.

[30] L.P. Gaffney, M. Hackstein, R.D. Page, T. Grahn, M. Scheck, P.A. Butler, P.F. Bertone, N. Bree, R.J. Carroll, M.P. Carpenter, C.J. Chiara, A. Dewald, F. Filmer, C. Fransen, M. Huyse, R.V.F. Janssens, D.T. Joss, R. Julin, F.G. Kondev, P. Nieminen, J. Pakarinen, S.V. Rigby, W. Rother, P. Van Duppen, H.V. Watkins, K. Wrzosek-Lipska, and S. Zhu. Shape coexistence in neutron-deficient Hg isotopes studied via lifetime measurements in 184,186Hg and two-state mixing calculation. *Physical Review C*, 89(2):024307, 2014. `doi:10.1103/PhysRevC.89.024307`.

[31] W.H. King. *Isotope Shifts in Atomic Spectra.* Springer US, Boston, MA, 1984. `doi:10.1007/978-1-4899-1786-7`.

[32] E.W. Otten. Nuclear Radii and Moments of Unstable Isotopes. In *Treatise on Heavy Ion Science*, pages 517–638. Springer US, Boston, MA, 1989. `doi:10.1007/978-1-4613-0713-6_7`.

[33] J. Billowes and P. Campbell. High-resolution laser spectroscopy for the study of nuclear sizes and shapes. *Journal of Physics G: Nuclear and Particle Physics*, 21(6):707–739, 1995. `doi:10.1088/0954-3899/21/6/003`.

[34] B. Cheal and K.T. Flanagan. Progress in laser spectroscopy at radioactive ion beam facilities. *Journal of Physics G: Nuclear and Particle Physics*, 37(11):113101, 2010. `doi:10.1088/0954-3899/37/11/113101`.

[35] B. Cheal, T.E. Cocolios, and S. Fritzsche. Laser spectroscopy of radioactive isotopes: Role and limitations of accurate isotope-shift calculations. *Physical Review A*, 86(4):042501, 2012. `doi:10.1103/PhysRevA.86.042501`.

[36] P. Campbell, I.D. Moore, and M.R. Pearson. Laser spectroscopy for nuclear structure physics. *Progress in Particle and Nuclear Physics*, 86:127–180, 2016. `doi:10.1016/j.ppnp.2015.09.003`.

[37] E.C. Seltzer. K X-Ray Isotope Shifts. *Physical Review*, 188(4):1916–1919, 1969. `doi:10.1103/PhysRev.188.1916`.

[38] P. Dabkiewicz, F. Buchinger, H. Fischer, H.J. Kluge, H. Kremmling, T. Kühl, A.C. Müller, and H.A. Schuessler. Nuclear shape isomerism in ^{185}Hg detected by laser spectroscopy. *Physics Letters B*, 82(2):199–203, 1979. `doi:10.1016/0370-2693(79)90735-4`.

[39] R.V. Ambartsumyan, V.N. Kalinin, and V.S. Letokhov. Two-step selective photoionization of rybidium atoms by laser radiation. *JETP Letters*, 13(6):217, 1971. URL: `http://jetpletters.ac.ru/ps/1572/article{_}24089.shtml`.

[40] R.V. Ambartzumian and V.S. Letokhov. Selective Two-Step (STS) Photoionization of Atoms and Photodissociation of Molecules by Laser Radiation. *Applied Optics*, 11(2):354, 1972. `doi:10.1364/AO.11.000354`.

[41] V.S. Letokhov. *Laser Photoionization Spectroscopy.* ACADEMIC PRESS INC., London, 1987.

[42] W. Demtröder. *Atoms, Molecules and Photons.* Graduate Texts in Physics. Springer Berlin Heidelberg, Berlin, Heidelberg, 2010. URL: `http://link.springer.com/10.1007/978-3-642-10298-1`, `doi:10.1007/978-3-642-10298-1`.

[43] V.S. Letokhov and V.I. Mishin. Laser photoionization pulsed source of radioactive atoms. *Book of abstracts, On-line in 1985 and beyond a workshop on the ISOLDE programme*, page D7, 1984. URL: `http://cds.cern.ch/record/152322`.

[44] G.D. Alkhazov, E.Ye. Berlovich, and V.N. Panteleyev. A new highly efficient selective laser ion source. *Nuclear Instruments and Methods in Physics Research Section A: Accelerators, Spectrometers, Detectors and Associated Equipment*, 280(1):141–143, 1989. `doi:10.1016/0168-9002(89)91282-5`.

[45] V.I. Mishin, V.N. Fedoseyev, H.J. Kluge, V.S. Letokhov, H.L. Ravn, F. Scheerer, Y. Shirakabe, S. Sundell, and O. Tengblad. Chemically selective laser ion-source for the CERN-ISOLDE on-line mass separator facility. *Nuclear Instruments and Methods in Physics Research Section B: Beam Interactions with Materials and Atoms*, 73(4):550–560, 1993. `doi:10.1016/0168-583X(93)95839-W`.

[46] B.A. Marsh. Resonance ionization laser ion sources for on-line isotope separators (invited). *Review of Scientific Instruments*, 85(2):02B923, 2014. `doi:10.1063/1.4858015`.

[47] V.N. Fedosseev, D.V. Fedorov, R. Horn, G. Huber, U. Köster, J. Lassen, V.I. Mishin, M.D. Seliverstov, L. Weissman, and K. Wendt. Atomic spectroscopy studies of short-lived isotopes and nuclear isomer separation with the ISOLDE RILIS. *Nuclear Instruments and Methods in Physics Research Section B: Beam Interactions with Materials and Atoms*, 204:353–358, 2003. `doi:10.1016/S0168-583X(02)01959-6`.

[48] K. Blaum, J. Dilling, and W. Nörtershäuser. Precision atomic physics techniques for nuclear physics with radioactive beams. *Physica Scripta*, T152:014017, 2013. `doi:10.1088/0031-8949/2013/T152/014017`.

[49] S.A. Blundell, P.E.G. Baird, C.W.P. Palmer, D.N. Stacey, G.K. Woodgate, and D. Zimmermann. A re-evaluation of isotope shift constants. *Zeitschrift für Physik A Atoms and Nuclei*, 321(1):31–33, 1985. `doi:10.1007/BF01411940`.

[50] M.D. Seliverstov, T.E. Cocolios, W. Dexters, A.N. Andreyev, S. Antalic, A.E. Barzakh, B. Bastin, J. Büscher, I.G. Darby, D.V. Fedorov, V.N. Fedoseyev, K.T. Flanagan, S. Franchoo, S. Fritzsche, G. Huber, M. Huyse, M. Keupers, U. Köster, Yu. Kudryavtsev, B.A. Marsh, P.L. Molkanov, R.D. Page, A.M. Sjødin, I. Stefan, J. Van de Walle, P. Van Duppen, M. Venhart, and S.G. Zemlyanoy. Charge radii of odd-A ^{191211}Po isotopes. *Physics Letters B*, 719(4-5):362–366, 2013. `doi:10.1016/j.physletb.2013.01.043`.

[51] K.T. Flanagan, K.M. Lynch, J. Billowes, M.L. Bissell, I. Budinčević, T.E. Cocolios, R.P. de Groote, S. De Schepper, V.N. Fedosseev, S. Franchoo, R.F. Garcia Ruiz, H. Heylen, B.A. Marsh, G. Neyens, T.J. Procter, R.E. Rossel, S. Rothe, I. Strashnov, H.H. Stroke, and K.D.A. Wendt. Collinear Resonance Ionization Spectroscopy of Neutron-Deficient Francium Isotopes. *Physical Review Letters*, 111(21):212501, 2013. `doi:10.1103/PhysRevLett.111.212501`.

[52] E. Kugler. The ISOLDE facility. *Hyperfine Interactions*, 129(1/4):23–42, 2000. `doi:10.1023/A:1012603025802`.

[53] B.W. Allardyce. ISOLDE Today and Tomorrow. In Richard A. Meyer and Daeg S. Brenner, editors, *Nuclei Off the Line of Stability*, ACS Symposium Series, chapter 61, pages 406–413. American Chemical Society, Washington, DC, 1986. `doi:10.1021/bk-1986-0324.ch061`.

[54] J.R. McConnell and W.L. Talbert. The Tristan on-line isotope separator facility. *Nuclear Instruments and Methods*, 128(2):227–243, 1975. `doi:10.1016/0029-554X(75)90672-2`.

[55] B. Jonson and A. Richter. More than three decades of ISOLDE physics. *Hyperfine Interactions*, 129(1/4):1–22, 2000. `doi:10.1023/A:1012689128103`.

[56] Y. Blumenfeld, T. Nilsson, and P. Van Duppen. Facilities and methods for radioactive ion beam production. *Physica Scripta*, 2013(T152):14023, 2013. `doi:10.1088/0031-8949/2013/T152/014023`.

[57] E. Boltezar, H. Haseroth, W. Pirkl, G. Plass, T.R. Sherwood, U. Tallgren, P. Tetu, D. Warner, and M. Weiss. Performance of the New CERN 50 MeV Linac. *IEEE Transactions on Nuclear Science*, 26(3):3674–3676, 1979. `doi:10.1109/TNS.1979.4330576`.

[58] K.H. Reich. The CERN PS booster, a flexible and reliable injector. In *5th All-Union Conference on Charged-particle Accelerators*, pages 221–225, Dubna, 1976. URL: `https://cds.cern.ch/record/1035486`.

[59] S. Lukić, F. Gevaert, A. Kelić, M.V. Ricciardi, K.H. Schmidt, and O. Yordanov. Systematic comparison of ISOLDE-SC yields with calculated in-target production rates. *Nuclear Instruments and Methods in Physics Research Section A: Accelerators, Spectrometers, Detectors and Associated Equipment*, 565(2):784–800, 2006. `doi:10.1016/j.nima.2006.04.082`.

[60] R. Kirchner. Progress in ion source development for on-line separators. *Nuclear Instruments and Methods in Physics Research*, 186(1-2):275–293, 1981. `doi:10.1016/0029-554X(81)90916-2`.

[61] P. Sortais, T. Lamy, J. Medard, J. Angot, L. Latrasse, and T. Thuillier. Ultracompact/ultralow power electron cyclotron resonance ion source for multipurpose applications. *Review of Scientific Instruments*, 81(2):02B314, 2010. `doi:10.1063/1.3272878`.

[62] M. Kronberger, A. Gottberg, T.M. Mendonca, J.P. Ramos, C. Seiffert, P. Suominen, and T. Stora. Production of molecular sideband radioisotope beams at CERN-ISOLDE using a Helicon-type plasma ion source. *Nuclear Instruments and Methods in Physics Research Section B: Beam Interactions with Materials and Atoms*, 317:438–441, 2013. `doi:10.1016/j.nimb.2013.07.032`.

[63] R. Kirchner. On the thermoionization in hot cavities. *Nuclear Instruments and Methods in Physics Research Section A: Accelerators, Spectrometers, Detectors and Associated Equipment*, 292(2):203–208, 1990. `doi:10.1016/0168-9002(90)90377-I`.

[64] Y. Liu, H.Z. Bilheux, and Y. Kawai. Characterization of a tubular hot-cavity surface ion source. In *Proceedings of the 2005 IEEE Particle Accelerator Conference (PAC 05). 16-20 May 2005, Knoxville, Tennessee. 21st IEEE Particle Accelerator Conference, p.1581*, pages 1581–1583, Knoxville, 2005. URL: `http://accelconf.web.cern.ch/AccelConf/p05/PAPERS/TPPE018.PDF`.

[65] É. Ya. Zandberg and N. I. Ionov. Surface ionization. *Soviet Physics Uspekhi*, 2(2):255–281, 1959. `doi:10.1070/PU1959v002n02ABEH003123`.

[66] J. Lettry, R. Catherall, G. J. Focker, O.C. Jonsson, E. Kugler, H. Ravn, C. Tamburella, The ISOLDE Collaboration, V. Fedoseyev, V.I. Mishin, G. Huber, V. Sebastian, M. Koizumi, and U. Koster. Recent developments of the ISOLDE laser ion source. *Review of Scientific Instruments*, 69(2):761, 1998. `doi:10.1063/1.1148978`.

[67] V.N. Fedosseev, B.A. Marsh, D.V. Fedorov, U. Köster, and E. Tengborn. Ionization Scheme Development at the ISOLDE RILIS. In *Laser 2004*, pages 15–27. Springer-Verlag, Berlin/Heidelberg, 2005. `doi:10.1007/3-540-30926-8_2`.

[68] CRC. *"Physical Constants of Organic Compounds," in CRC Handbook of Chemistry and Physics*. CRC Press/Taylor & Francis, Boca Raton, FL, 2017. URL: `http://hbcponline.com/`.

[69] V.N. Fedosseev, L.E. Berg, D.V. Fedorov, D. Fink, O.J. Launila, R. Losito, B.A. Marsh, R.E. Rossel, S. Rothe, M.D. Seliverstov, A.M. Sjodin, and K.D.A. Wendt. Upgrade of the resonance ionization laser ion source at ISOLDE on-line isotope separation facility: New lasers and new ion beams. *Review of Scientific Instruments*, 83(2):02A903, 2012. `doi:10.1063/1.3662206`.

[70] S. Rothe, T. Day Goodacre, D.V. Fedorov, V.N. Fedosseev, B.A. Marsh, P.L. Molkanov, R.E. Rossel, M.D. Seliverstov, M. Veinhard, and K.D.A. Wendt. Laser ion beam production at CERN-ISOLDE: New features More possibilities. *Nuclear Instruments and Methods in Physics Research Section B: Beam Interactions with Materials and Atoms*, 376:91–96, 2016. `doi:10.1016/j.nimb.2016.02.024`.

[71] U. Köster, M. Argentini, R. Catherall, V.N. Fedoseyev, H.W. Gäggeler, O.C. Jonsson, and R. Weinreich. Off-line production of intense $^{7,10}\mathrm{Be}^{+}$ beams. *Nuclear Instruments and Methods in Physics Research Section B: Beam Interactions with Materials and Atoms*, 204:343–346, 2003. `doi:10.1016/S0168-583X(02)01952-3`.

[72] B.A. Marsh, B. Andel, A.N. Andreyev, S. Antalic, D. Atanasov, A.E. Barzakh, B. Bastin, Ch. Borgmann, L. Capponi, T.E. Cocolios, T. Day Goodacre, M. Dehairs, X. Derkx, H. De Witte, D.V. Fedorov, V.N. Fedosseev, G.J. Focker, D.A. Fink, K.T. Flanagan, S. Franchoo, L. Ghys, M. Huyse, N. Imai, Z. Kalaninova, U. Köster, S. Kreim, N. Kesteloot, Yu. Kudryavtsev, J. Lane, N. Lecesne, V. Liberati, D. Lunney, K.M. Lynch, V. Manea, P.L. Molkanov, T. Nicol, D. Pauwels, L. Popescu, D. Radulov, E. Rapisarda, M. Rosenbusch, R.E. Rossel, S. Rothe, L. Schweikhard, M.D. Seliverstov, S. Sels, A.M. Sjödin, V. Truesdale, C. Van Beveren, P. Van Duppen, K. Wendt, F. Wienholtz, R.N. Wolf, and S.G. Zemlyanoy. New developments of the in-source spectroscopy method at RILIS/ISOLDE. *Nuclear Instruments and Methods in Physics Research Section B: Beam Interactions with Materials and Atoms*, 317:550–556, 2013. `doi:10.1016/j.nimb.2013.07.070`.

[73] R. Kirchner and E. Roeckl. Investigation of gaseous discharge ion sources for isotope separation on-line. *Nuclear Instruments and Methods*, 133(2):187–204, 1976. `doi:10.1016/0029-554X(76)90607-8`.

[74] L. Penescu, R. Catherall, J. Lettry, and T. Stora. Development of high efficiency Versatile Arc Discharge Ion Source at CERN ISOLDE. *The Review of scientific instruments*, 81(2):02A906, mar 2010. `doi:10.1063/1.3271245`.

[75] S. Sundell and H. Ravn. Ion source with combined cathode and transfer line heating. *Nuclear Instruments and Methods in Physics Research Section B: Beam Interactions with Materials and Atoms*, 70(1-4):160–164, 1992. `doi:10.1016/0168-583X(92)95926-I`.

[76] S. Rothe, V.N. Fedosseev, T. Kron, B.A. Marsh, R.E. Rossel, and K.D.A. Wendt. Narrow linewidth operation of the RILIS Titanium:Sapphire laser at ISOLDE/CERN. *Nuclear Instruments and Methods in Physics Research Section B: Beam Interactions with Materials and Atoms*, 317:561–564, 2013. `doi:10.1016/j.nimb.2013.08.058`.

[77] R.E. Rossel. *A Distributed Monitoring and Control System for the Laser Ion Source RILIS at CERN-ISOLDE*. PhD thesis, Hochschule RheinMain, 2015. `doi:10.17181/CERN.L5N9.2GCS`.

[78] R.N. Wolf, D. Beck, K. Blaum, Ch. Böhm, Ch. Borgmann, M. Breitenfeldt, F. Herfurth, A. Herlert, M. Kowalska, S. Kreim, D. Lunney, S. Naimi, D. Neidherr, M. Rosenbusch, L. Schweikhard, J. Stanja, F. Wienholtz, and K. Zuber. On-line separation of short-lived nuclei by a multi-reflection time-of-flight device. *Nuclear Instruments and Methods in Physics Research Section A: Accelerators, Spectrometers, Detectors and Associated Equipment*, 686:82–90, 2012. `doi:10.1016/j.nima.2012.05.067`.

[79] R.N. Wolf, F. Wienholtz, D. Atanasov, D. Beck, K. Blaum, Ch. Borgmann, F. Herfurth, M. Kowalska, S. Kreim, Yu. A. Litvinov, D. Lunney, V. Manea, D. Neidherr, M. Rosenbusch, L. Schweikhard, J. Stanja, and K. Zuber. ISOLTRAP's multi-reflection time-of-flight mass separator/spectrometer. *International Journal of Mass Spectrometry*, 349-350:123–133, 2013. `doi:10.1016/j.ijms.2013.03.020`.

[80] M.D. Seliverstov, T.E. Cocolios, W. Dexters, A.N. Andreyev, S. Antalic, A.E. Barzakh, B. Bastin, J. Büscher, I.G. Darby, D.V. Fedorov, V.N. Fedosseev, K.T. Flanagan, S. Franchoo, G. Huber, M. Huyse, M. Keupers, U. Köster, Y. Kudryavtsev, B.A. Marsh, P.L. Molkanov, R.D. Page, A.M. Sjödin, I. Stefan, P. Van Duppen, M. Venhart, and S.G. Zemlyanoy. Electromagnetic moments of odd-A Po193203,211 isotopes. *Physical Review C*, 89(3):034323, 2014. `doi:10.1103/PhysRevC.89.034323`.

[81] D.A. Fink, S.D. Richter, B. Bastin, K. Blaum, R. Catherall, T.E. Cocolios, D.V. Fedorov, V.N. Fedosseev, K.T. Flanagan, L. Ghys, A. Gottberg, N. Imai, T. Kron, N. Lecesne, K.M. Lynch, B.A. Marsh, T.M. Mendonca, D. Pauwels, E. Rapisarda, J.P. Ramos, R.E. Rossel, S. Rothe, M.D. Seliverstov, M. Sjödin, T. Stora, C. Van Beveren, and K.D.A. Wendt. First application of the Laser Ion Source and Trap (LIST) for on-line experiments at ISOLDE. *Nuclear Instruments and Methods in Physics Research Section B: Beam Interactions with Materials and Atoms*, 317:417–421, 2013. `doi:10.1016/j.nimb.2013.06.039`.

[82] D.A. Fink, T.E. Cocolios, A.N. Andreyev, S. Antalic, A.E. Barzakh, B. Bastin, D.V. Fedorov, V.N. Fedosseev, K.T. Flanagan, L. Ghys, A. Gottberg, M. Huyse, N. Imai, T. Kron, N. Lecesne,

K.M. Lynch, B.A. Marsh, D. Pauwels, E. Rapisarda, S.D. Richter, R.E. Rossel, S. Rothe, M.D. Seliverstov, A.M. Sjödin, C. Van Beveren, P. Van Duppen, and K.D.A. Wendt. In-Source Laser Spectroscopy with the Laser Ion Source and Trap: First Direct Study of the Ground-State Properties of ^{217,219}Po. *Physical Review X*, 5(1):011018, 2015. `doi:10.1103/PhysRevX.5.011018`.

[83] T. Day Goodacre, J. Billowes, R. Catherall, T.E. Cocolios, B. Crepieux, D.V. Fedorov, V.N. Fedosseev, L.P. Gaffney, T. Giles, A. Gottberg, K.M. Lynch, B.A. Marsh, T.M. Mendonça, J.P. Ramos, R.E. Rossel, S. Rothe, S. Sels, C. Sotty, T. Stora, C. Van Beveren, and M. Veinhard. Blurring the boundaries between ion sources: The application of the RILIS inside a FEBIAD type ion source at ISOLDE. *Nuclear Instruments and Methods in Physics Research Section B: Beam Interactions with Materials and Atoms*, 376:39–45, 2016. `doi:10.1016/j.nimb.2016.03.005`.

[84] Charged Particle Optics Ltd. CPO, 2015. URL: `http://simion.com/cpo/`.

[85] TECH-X. VSim, 2016. URL: `https://www.txcorp.com/vsim`.

[86] L. Penescu, R. Catherall, J. Lettry, and T. Stora. Numerical simulations of space charge effects and plasma dynamics for FEBIAD ion sources. *Nuclear Instruments and Methods in Physics Research Section B: Beam Interactions with Materials and Atoms*, 266(19-20):4415–4419, 2008. `doi:10.1016/j.nimb.2008.05.071`.

[87] R. Courant, K. Friedrichs, and H. Lewy. On the Partial Difference Equations of Mathematical Physics (Republished). *IBM Journal of Research and Development*, 11(2):215–234, 1967. `doi:10.1147/rd.112.0215`.

[88] R. Kirchner and E. Roeckl. A novel isol ion source. *Nuclear Instruments and Methods*, 139:291–296, 1976. `doi:10.1016/0029-554X(76)90687-X`.

[89] M. Breitenfeldt, D. Atanasov, K. Blaum, T. Eronen, P. Finlay, F. Herfurth, M. Kowalska, S. Kreim, Yu. Litvinov, D. Lunney5, V. Manea5, D. Neidherr, T. Porobic, M. Rosenbusch, L. Schweikhard, N. Severijns, F. Wienholtz, R.N. Wolf, and K. Zuber. Q-values of Mirror Transitions for fundamental interaction studies. Technical report, CERN-INTC, Geneva, 2013. URL: `http://cds.cern.ch/record/1551494`.

[90] U. Köster, V.N. Fedoseyev, A.N. Andreyev, U.C. Bergmann, R. Catherall, J. Cederkäll, M. Dietrich, H. De Witte, D.V. Fedorov, L. Fraile, S. Franchoo, H. Fynbo, U. Georg, T. Giles, M. Gorska, M. Hannawald, M. Huyse, A. Joinet, O.C. Jonsson, K.L. Kratz, K. Kruglov, Ch. Lau, J. Lettry, V.I. Mishin, M. Oinonen, K. Partes, K. Peräjärvi, B. Pfeiffer, H.L. Ravn, M.D.

Seliverstov, P. Thirolf, K. Van de Vel, P. Van Duppen, J. Van Roosbroeck, and L. Weissman. On-line yields obtained with the ISOLDE RILIS. *Nuclear Instruments and Methods in Physics Research Section B: Beam Interactions with Materials and Atoms*, 204:347–352, 2003. URL: `http://linkinghub.elsevier.com/retrieve/pii/S0168583X02019560`, `doi:10.1016/S0168-583X(02)01956-0`.

[91] S. Rothe, R. Catherall, B. Crepieux, T. Day Goodacre, V.N. Fedosseev, T. Giles, B.A. Marsh, J.P. Ramos, and R.E. Rossel. Advances in surface ion suppression from RILIS: Towards the Time-of-Flight Laser Ion Source (ToF-LIS). *Nuclear Instruments and Methods in Physics Research Section B: Beam Interactions with Materials and Atoms*, 376:86–90, 2016. `doi:10.1016/j.nimb.2016.02.060`.

[92] T. Day Goodacre, D. Fedorov, V.N. Fedosseev, L. Forster, B.A. Marsh, R.E. Rossel, S. Rothe, and M. Veinhard. Laser resonance ionization scheme development for tellurium and germanium at the dual Ti:SaDye ISOLDE RILIS. *Nuclear Instruments and Methods in Physics Research Section A: Accelerators, Spectrometers, Detectors and Associated Equipment*, 830:510–514, 2016. `doi:10.1016/j.nima.2015.10.066`.

[93] K.M. Lynch, J. Billowes, M.L. Bissell, I. Budinčević, T.E. Cocolios, T. Day Goodacre, R.P. de Groote, V.N. Fedosseev, K.T. Flanagan, S. Franchoo, R.F. Garcia Ruiz, H. Heylen, T. Kron, B.A. Marsh, G. Neyens, R.E. Rossel, S. Rothe, I. Trashnov, H.H. Stroke, and K.D.A. Wendt. Collinear resonance ionization spectroscopy of radium ions. Technical report, CERN-INTC, Geneva, 2014. URL: `https://cds.cern.ch/record/1704513`.

[94] T.E. Cocolios, H.H. Al Suradi, J. Billowes, I. Budinčević, R.P. de Groote, S. De Schepper, V.N. Fedosseev, K.T. Flanagan, S. Franchoo, R.F. Garcia Ruiz, H. Heylen, F. Le Blanc, K.M. Lynch, B.A. Marsh, P.J.R. Mason, G. Neyens, J. Papuga, T.J. Procter, M.M. Rajabali, R.E. Rossel, S. Rothe, G.S. Simpson, A.J. Smith, I. Strashnov, H.H. Stroke, D. Verney, P.M. Walker, K.D.A. Wendt, and R.T. Wood. The Collinear Resonance Ionization Spectroscopy (CRIS) experimental setup at CERN-ISOLDE. *Nuclear Instruments and Methods in Physics Research Section B: Beam Interactions with Materials and Atoms*, 317:565–569, 2013. `doi:10.1016/j.nimb.2013.05.088`.

[95] S. Raeder, J. Lassen, H. Heggen, and A. Teigelhöfer. In-source spectroscopy on astatine and radium for resonant laser ionization. *Hyperfine Interactions*, 227(1-3):77–83, 2014. `doi:10.1007/s10751-014-1040-9`.

[96] U. Dammalapati, K. Jungmann, and L. Willmann. Compilation of Spectroscopic Data of Radium (Ra I and Ra II). *Journal of Physical and Chemical Reference Data*, 45(1):013101, 2016. `doi:10.1063/1.4940416`.

[97] K.P. Birch and M.J. Downs. An Updated Edlén Equation for the Refractive Index of Air. *Metrologia*, 30(3):155–162, 1993. `doi:10.1088/0026-1394/30/3/004`.

[98] G. Fricke and K. Heilig. 80-Hg Mercury. In *Nuclear Charge Radii*, pages 1–9. Springer-Verlag, Berlin/Heidelberg, 2005. `doi:10.1007/10856314_82`.

[99] K. Zuber. Separation of the Mercury Isotopes by a Photochemical Method. *Nature*, 136(3446):796–796, 1935. `doi:10.1038/136796a0`.

[100] S. Mrozowski. Bemerkungen über die Leuchtdauer der Quecksilberresonanzlinie 2537 Å. *Zeitschrift für Physik*, 78(11-12):844–846, 1932. `doi:10.1007/BF01342045`.

[101] A.C. Melissinos. Determination of the Dipole Moment and Isotope Shift of Radioactive ^{197}Hg by Double Resonance. *Physical Review*, 115(1):126–129, 1959. `doi:10.1103/PhysRev.115.126`.

[102] D.P. Sumner, T. Aung, and H. Kleiman. Isotope Shifts of Neutron-Deficient Mercury Isotopes. *Physical Review*, 147(3):861–866, 1966. `doi:10.1103/PhysRev.147.861`.

[103] W.G. Schweitzer. Hyperfine Structure and Isotope Shifts in the 2537-Å Line of Mercury by a New Interferometric Method. *Journal of the Optical Society of America*, 53(9):1055, 1963. `doi:10.1364/JOSA.53.001055`.

[104] J. Bonn, G. Huber, H.J. Kluge, U. Köpf, L. Kugler, and E.-W. Otten. Optical pumping of neutron deficient 187Hg. *Physics Letters B*, 36(1):41–43, 1971. `doi:10.1016/0370-2693(71)90315-7`.

[105] P. Hornshøj, P.G. Hansen, B. Jonson, A. Lindahl, and O.B. Nielsen. Search for rotational fine structure in the nucleus 184Hg. *Physics Letters B*, 43(5):377–379, mar 1973. `doi:10.1016/0370-2693(73)90376-6`.

[106] S.G. Nilsson, J.R. Nix, P. Möller, and I. Ragnarsson. How much of a bubble is there in ^{184}Hg? *Nuclear Physics A*, 222(2):221–234, apr 1974. `doi:10.1016/0375-9474(74)90389-3`.

[107] A. Faessler, U. Götz, B. Slavov, and T. Ledergerber. Strongly deformed nuclei near the magic proton shell 82? *Physics Letters B*, 39(5):579–582, 1972. `doi:10.1016/0370-2693(72)90001-9`.

[108] F. Dickmann and K. Dietrich. Variable collective inertia and the transition from spherical to deformed shapes in the Hg-isotopes. *Zeitschrift für Physik A Hadrons and nuclei*, 263(3):211–225, 1973. `doi:10.1007/BF01392563`.

[109] F. Dickmann and K. Dietrich. Coexistence and mixing of spherical and deformed states in the region of light Hg-isotopes. *Zeitschrift für Physik*, 271(4):417–426, 1974. `doi:10.1007/BF02126197`.

[110] M. Cailliau, J. Leterssier, H. Flocard, and P. Quentin. Self consistent calculations of a possible shape transition in neutron deficient mercury isotopes. *Physics Letters B*, 46(1):11–14, 1973. `doi:10.1016/0370-2693(73)90461-9`.

[111] D. Kolb and C.Y. Wong. Shape isomerism in mercury isotopes. *Nuclear Physics A*, 245(2):205–220, 1975. `doi:10.1016/0375-9474(75)90173-6`.

[112] S. Frauendorf and V.V. Pashkkevich. On oblate-prolate transition in the ground state rotational band of light mercury isotopes. *Physics Letters B*, 55(4):365–368, 1975. `doi:10.1016/0370-2693(75)90360-3`.

[113] D. Proetel, R.M. Diamond, P. Kienle, J.R. Leigh, K.H. Maier, and F.S. Stephens. Evidence for Strongly Deformed Shapes in ^{186}Hg. *Physical Review Letters*, 31(14):896–898, 1973. `doi:10.1103/PhysRevLett.31.896`.

[114] N. Rud, D. Ward, H.R. Andrews, R.L. Graham, and J.S. Geiger. Lifetimes in the Ground-State Band of ^{184}Hg. *Physical Review Letters*, 31(23):1421–1423, 1973. `doi:10.1103/PhysRevLett.31.1421`.

[115] M. Brack, J. Damgaard, A.S. Jensen, H.C. Pauli, V.M. Strutinsky, and C.Y. Wong. Funny Hills: The Shell-Correction Approach to Nuclear Shell Effects and Its Applications to the Fission Process. *Reviews of Modern Physics*, 44(2):320–405, 1972. `doi:10.1103/RevModPhys.44.320`.

[116] G. Huber, J. Bonn, H.J. Kluge, and E.W. Otten. Nuclear Radiation Detected Optical Pumping of neutron-deficient Hg isotopes. *Zeitschrift für Physikr Physik A Atoms and Nuclei*, 276(3):187–202, 1976. `doi:10.1007/BF01412097`.

[117] C. Duke, H. Fischer, H.J. Kluge, H. Kremmling, Th. Kühl, and E.W. Otten. Determination of the isotope shift of ^{190}Hg by on-line laser spectroscopy. *Physics Letters B*, 68(2):129–132, 1977. `doi:10.1016/0370-2693(77)90183-6`.

[118] K. Heyde and J.L. Wood. Nuclear shapes: from earliest ideas to multiple shape coexisting structures. *Physica Scripta*, 91(8):083008, 2016. `doi:10.1088/0031-8949/91/8/083008`.

[119] R. Julin, K. Helariutta, and M. Muikku. Intruder states in very neutron-deficient Hg, Pb and Po nuclei. *Journal of Physics G: Nuclear and Particle Physics*, 27(7):R109–R139, 2001. `doi:10.1088/0954-3899/27/7/201`.

[120] F.G. Kondev, M.P. Carpenter, R.V.F. Janssens, C.J. Lister, K. Abu Saleem, I. Ahmad, H. Amro, J. Caggiano, C.N. Davids, A. Heinz, B. Herskind, T.L. Khoo, T. Lauritsen, W.C. Ma, J.J. Ressler, W. Reviol, L.L. Riedinger, D.G. Sarantites, D. Seweryniak, S. Siem, A.A. Sonzogni, P.G. Varmette, and I. Wiedenhöver. First observation of excited structures in neutron-deficient ^{179}Hg: evidence for multiple shape coexistence. *Physics Letters B*, 528(3-4):221–227, 2002. `doi:10.1016/S0370-2693(02)01221-2`.

[121] A. Melerangi, D. Appelbe, R.D. Page, H.J. Boardman, P.T. Greenlees, P. Jones, D.T. Joss, R. Julin, S. Juutinen, H. Kettunen, P. Kuusiniemi, M. Leino, M.H. Muikku, P. Nieminen, J. Pakarinen, P. Rahkila, and J. Simpson. Shape isomerism and spectroscopy of ^{177}Hg. *Physical Review C*, 68(4):041301, 2003. `doi:10.1103/PhysRevC.68.041301`.

[122] D.G. Jenkins, A.N. Andreyev, R.D. Page, M.P. Carpenter, R.V.F. Janssens, C.J. Lister, F.G. Kondev, T. Enqvist, P.T. Greenlees, P.M. Jones, R. Julin, S. Juutinen, H. Kettunen, P. Kuusiniemi, M. Leino, A.P. Leppännen, P. Nieminen, J. Pakarinen, P. Rahkila, J. Uusitalo, C.D. O'Leary, P. Raddon, A. Simons, R. Wadsworth, and D.T. Joss. Confirmation of triple shape coexistence in 179Hg. *Physical Review C*, 66(1):011301, 2002. `doi:10.1103/PhysRevC.66.011301`.

[123] J.E. García-Ramos and K. Heyde. Nuclear shape coexistence: A study of the even-even Hg isotopes using the interacting boson model with configuration mixing. *Physical Review C*, 89(1):014306, 2014. `doi:10.1103/PhysRevC.89.014306`.

[124] L.P. Gaffney, T. Day Goodacre, A. Andreyev, M. Seliverstov, N. Althubiti, B. Andel, S. Antalic, D. Atanasov, A.E. Barzakh, J. Billowes, K. Blaum, T.E. Cocolios, J. Cubiss, G. Farooq-Smith, V.N. Fedosseev, D.V. Fedorov, R. Ferrer, K.T. Flanagan, L. Ghys, A. Gottberg, C. Granados, F. Herfurth, M. Huyse, D.G. Jenkins, D. Kisler, S. Kreim, T. Kron, Y. Kudryavtsev, D. Lunney, K.M. Lynch, V. Manea, B.A. Marsh, T.M. Mendonca, P.L. Molkanov, D. Neidherr, R. Raabe, S. Raeder, J.P. Ramos, E. Rapisarda, M. Rosenbusch, R.E. Rossel, S. Rothe, L. Schweikhard, S. Sels, T. Stora, I. Tsekhanovich, C. Van Beveren, P. Van Duppen, M. Veinhard, R. Wadsworth, F. Wienholtz, A. Welker, K. Wendt, G.L. Wilson, S. Witkins, R. Wolf, and K. Zuber. In-source laser spectroscopy of mercury isotopes. *CERN INTC*, (P-424), 2014. `doi:10.17181/CERN.DUGM.L69R`.

[125] J. Lettry, R. Catherall, G. Cyvoct, P. Drumm, A.H.M. Evensen, M. Lindroos, O.C. Jonsson, E. Kugler, J. Obert, J.C. Putaux, J. Sauvage, K. Schindl, H. Ravn, and E. Wildner. Release from ISOLDE molten metal targets under pulsed proton beam conditions. *Nuclear Instruments and Methods in Physics Research Section B: Beam Interactions with Materials and Atoms*, 126(1-4):170–175, 1997. `doi:10.1016/S0168-583X(96)01088-9`.

[126] J. Lettry, R. Catherall, P. Drumm, P. Van Duppen, A.H.M. Evensen, G.J. Focker, A. Jokinen, O.C. Jonsson, E. Kugler, and H. Ravn. Pulse shape of the ISOLDE radioactive ion beams. *Nuclear Instruments and Methods in Physics Research Section B: Beam Interactions with Materials and Atoms*, 126(1-4):130–134, 1997. `doi:10.1016/S0168-583X(96)01025-7`.

[127] J. Lettry, G. Arnau, M. Benedikt, S. Gilardoni, R. Catherall, U. Georg, G. Cyvogt, A. Fabich, O. Jonsson, H. Ravn, S. Sgobba, G. Bauer, H. Brucherstseifer, T. Graber, C. Güdermann, L. Ni, and R. Rastani. Effects of thermal shocks on the release of radioisotopes and on molten metal target vessels. *Nuclear Instruments and Methods in Physics Research Section B: Beam*

Interactions with Materials and Atoms, 204:251–256, 2003. `doi:10.1016/S0168-583X(02)01919-5`.

[128] H. De Witte, A.N. Andreyev, N. Barré, M. Bender, T.E. Cocolios, S. Dean, D. Fedorov, V.N. Fedoseyev, L.M. Fraile, S. Franchoo, V. Hellemans, P.H. Heenen, K. Heyde, G. Huber, M. Huyse, H. Jeppessen, U. Köster, P. Kunz, S.R. Lesher, B.A. Marsh, I. Mukha, B. Roussière, J. Sauvage, M. Seliverstov, I. Stefanescu, E. Tengborn, K. Van de Vel, J. Van de Walle, P. Van Duppen, and Y. Volkov. Nuclear Charge Radii of Neutron-Deficient Lead Isotopes Beyond N=104 Midshell Investigated by In-Source Laser Spectroscopy. *Physical Review Letters*, 98(11):112502, 2007. `doi:10.1103/PhysRevLett.98.112502`.

[129] OriginLab. 15.5.3 Theory of Nonlinear Curve Fitting. URL: `http://www.originlab.com/doc/Origin-Help/NLFit-Theory`.

[130] K. Levenberg. A method for the solution of certain non-linear problems in least squares. *Quarterly of Applied Mathematics*, 2(2):164–168, 1944. URL: `http://www.jstor.org/stable/43633451`.

[131] D.W. Marquardt. An Algorithm for Least-Squares Estimation of Nonlinear Parameters. *Journal of the Society for Industrial and Applied Mathematics*, 11(2):431–441, 1963. `doi:10.1137/0111030`.

[132] G. Torbohm, B. Fricke, and A. Rosén. State-dependent volume isotope shifts of low-lying states of group-II a and -II b elements. *Physical Review A*, 31(4):2038–2053, 1985. `doi:10.1103/PhysRevA.31.2038`.

[133] G. Fricke and K. Heilig. Introduction. In *Nuclear Charge Radii*, chapter 1, pages 1–36. Springer-Verlag, Berlin/Heidelberg, 2005. `doi:10.1007/10856314_1`.

[134] B. Jonson, O.B. Nielsen, L. Westgaard, and J. Zylicz. The decay of ^{207}Hg to ^{207}Tl. In *4th International Conference on Nuclei Far from Stability V2*, pages 640–643, Helsingør, Denmark, 1981. CERN. `doi:10.5170/CERN-1981-009.640`.

[135] A.E. Barzakh. Private communication. Technical report, 2016.

[136] M. Anselment, W. Faubel, S. Göring, A. Hanser, G. Meisel, H. Rebel, and G. Schatz. The odd-even staggering of the nuclear charge radii of Pb isotopes. *Nuclear Physics A*, 451(3):471–480, 1986. `doi:10.1016/0375-9474(86)90071-0`.

[137] S.B. Dutta, R. Kirchner, O. Klepper, T. Kühl, D. Marx, G.D. Sprouse, R. Menges, U. Dinger, G. Huber, and S. Schröder. Measurement of isotope shift and hyperfine splitting of ^{190,191,193,197}Pb isotopes by collinear laser spectroscopy. *Zeitschrift für Physik A Hadrons and nuclei*, 341(1):39–45, 1991. `doi:10.1007/BF01281272`.

[138] I. Angeli and K.P. Marinova. Table of experimental nuclear ground state charge radii: An update. *Atomic Data and Nuclear Data Tables*, 99(1):69–95, 2013. `doi:10.1016/j.adt.2011.12.006`.

[139] A.E. Barzakh, L.K. Batist, D.V. Fedorov, V.S. Ivanov, K.A. Mezilev, P.L. Molkanov, F.V. Moroz, S.Y. Orlov, V.N. Panteleev, and Y.M. Volkov. Changes in the mean-square charge radii and magnetic moments of neutron-deficient Tl isotopes. *Physical Review C*, 88(2):024315, 2013. `doi:10.1103/PhysRevC.88.024315`.

[140] C. Van Beveren. *Laser-assisted decay and optical spectroscopy studies of neutron-deficient thallium isotopes*. PhD thesis, KU Leuven, 2016. URL: `https://lirias.kuleuven.be/handle/123456789/529374`.

[141] N. Bree, K. Wrzosek-Lipska, A. Petts, A. Andreyev, B. Bastin, M. Bender, A. Blazhev, B. Bruyneel, P.A. Butler, J. Butterworth, M.P. Carpenter, J. Cederkäll, E. Clément, T.E. Cocolios, A. Deacon, J. Diriken, A. Ekström, C. Fitzpatrick, L.M. Fraile, C. Fransen, S.J. Freeman, L.P. Gaffney, J.E. García-Ramos, K. Geibel, R. Gernhäuser, T. Grahn, M. Guttormsen, B. Hadinia, K. Hadyńska-Klek, M. Hass, P.H. Heenen, R.D. Herzberg, H. Hess, K. Heyde, M. Huyse, O. Ivanov, D.G. Jenkins, R. Julin, N. Kesteloot, Th. Kröll, R. Krücken, A.C. Larsen, R. Lutter, P. Marley, P.J. Napiorkowski, R. Orlandi, R.D. Page, J. Pakarinen, N. Patronis, P.J. Peura, E. Piselli, P. Rahkila, E. Rapisarda, P. Reiter, A.P. Robinson, M. Scheck, S. Siem, K. Singh Chakkal, J.F. Smith, J. Srebrny, I. Stefanescu, G.M. Tveten, P. Van Duppen, J. Van de Walle, D. Voulot, N. Warr, F. Wenander, A. Wiens, J.L. Wood, and M. Zielińska. Shape coexistence in the neutron-deficient even-even $^{182-188}$Hg isotopes studied via Coulomb excitation. *Physical Review Letters*, 112(16):162701, 2014. `doi:10.1103/PhysRevLett.112.162701`.

[142] P. Moller, J.R. Nix, W.D. Myers, and W.J. Swiatecki. Nuclear Ground-State Masses and Deformations. *Atomic Data and Nuclear Data Tables*, 59(2):185–381, 1995. `doi:10.1006/adnd.1995.1002`.

[143] R. Firestone. *Table of Isotopes (1999 update with CD-ROM)*. Wiley, 1999. URL: `http://eu.wiley.com/WileyCDA/WileyTitle/productCd-0471356336.html`.

[144] K. Wrzosek-Lipska and L.P. Gaffney. Unique and complementary information on shape coexistence in the neutron-deficient Pb region derived from Coulomb excitation. *Journal of Physics G: Nuclear and Particle Physics*, 43(2):024012, 2016. `doi:10.1088/0954-3899/43/2/024012`.

[145] A.F. Barfield and B.R. Barrett. The interacting boson model and the structure of ^{182}Hg. *Physics Letters B*, 149(4-5):277–278, 1984. `doi:10.1016/0370-2693(84)90405-2`.

[146] J.M. Yao, M. Bender, and P.H. Heenen. Systematics of low-lying states of even-even nuclei in the neutron-deficient lead region from a beyond-mean-field calculation. *Physical Review C*, 87(3):034322, 2013. `doi:10.1103/PhysRevC.87.034322`.

[147] K. Nomura, R. Rodríguez-Guzmán, and L.M. Robledo. Shape evolution and the role of intruder configurations in Hg isotopes within the interacting boson model based on a Gogny energy density functional. *Physical Review C*, 87(6):064313, 2013. `doi:10.1103/PhysRevC.87.064313`.

[148] T. Nikšić, D. Vretenar, P. Ring, and G.A. Lalazissis. Shape coexistence in the relativistic Hartree-Bogoliubov approach. *Physical Review C*, 65(5):054320, 2002. `doi:10.1103/PhysRevC.65.054320`.

[149] S.E. Agbemava, A.V. Afanasjev, D. Ray, and P. Ring. Global performance of covariant energy density functionals: Ground state observables of even-even nuclei and the estimate of theoretical uncertainties. *Physical Review C*, 89(5):054320, 2014. `doi:10.1103/PhysRevC.89.054320`.

[150] A. Pastore, J. Dobaczewski, and A. Andreyev. Charge radii in Hg isotopes close to proton drip-line. *Book of abstracts, international nuclear physics confernce (INPC) 2016*, page 132, 2016. URL: `http://inpc2016.com/abstracts/pdf/abstract_132.pdf`.

[151] J.R. Stone and P.G. Reinhard. The Skyrme interaction in finite nuclei and nuclear matter. *Progress in Particle and Nuclear Physics*, 58(2):587–657, 2007. `doi:10.1016/j.ppnp.2006.07.001`.

[152] M.M. Sharma, G.A. Lalazissis, and P. Ring. Anomaly in the charge radii of Pb isotopes. *Physics Letters B*, 317(1-2):9–13, 1993. `doi:10.1016/0370-2693(93)91561-Z`.

[153] K. Kreim, M.L. Bissell, J. Papuga, K. Blaum, M. De Rydt, R.F. Garcia Ruiz, S. Goriely, H. Heylen, M. Kowalska, R. Neugart, G. Neyens, W. Nörtershäuser, M.M. Rajabali, R. Sánchez Alarcón, H.H. Stroke, and D.T. Yordanov. Nuclear charge radii of potassium isotopes beyond N=28. *Physics Letters B*, 731:97–102, 2014. `doi:10.1016/j.physletb.2014.02.012`.

[154] P. M. Goddard, P. D. Stevenson, and A. Rios. Charge radius isotope shift across the N=126 shell gap. *Physical Review Letters*, 110(3):032503, 2013. `doi:10.1103/PhysRevLett.110.032503`.

[155] A.E. Barzakh, L.K. Batist, D.V. Fedorov, V.S. Ivanov, P.L. Molkanov, F.V. Moroz, S.Y. Orlov, V.N. Panteleev, M.D. Seliverstov, and Y.M. Volkov. Changes in the mean square charge radii and electromagnetic moments of neutron-deficient Bi isotopes. In *Nuclear Structure and Dynamics '15*, page 030011, 2015. URL: `http://scitation.aip.org/content/aip/proceeding/aipcp/10.1063/1.4932255`, `doi:10.1063/1.4932255`.

[156] P. Dabkiewicz. *Laserspektroskopische bestimmung der formisomerie in ^{185}Hg und der isotopieverschiebung von ^{206}Hg.* PhD thesis, The Johannes Gutenberg University of Mainz, 1980.

[157] P. Dabkiewicz, C. Duke, H. Fischer, T. Kuehl, and H.J. Kluge. Nuclear shape staggering in very neutron deficient Hg isotopes detected by laser spectroscopy. *Journal of the Physical Society of Japan*, 44 (suppl):503–508, 1978.

Appendix A

Data extraction and analysis

A.1 Reference measurements and wavelength meter (WM) comparison

Long term drifts and short term fluctuations in the measurement of the laser wavelengths typically occur due to temperature changes in the laser room influencing the interferometer-based WM. The periodically repeated scans of the ^{198}Hg reference isotope enable the determination of the stability of the reference value over the period of the experiment. In all but one case, pairs of ^{198}Hg reference measurements were made, scanning the laser frequency in opposite directions enabling the evaluation of any scan-direction bias or hysteresis. For the first nine reference scans, the ion rate was determined with a Faraday cup. The method of ion rate determination was switched to the MR-ToF MS following the identification of multiple mercury isotopes, simultaneously present in the ion beam. The ^{198}Hg reference scans, where a Faraday cup was used for ion detection might therefore be considered less reliable.

The final ^{198}Hg reference scan was made 64 hours after the beginning of the experiment, however, the final laser scan took place 19 hours after the last ^{198}Hg reference measurement at an experiment time of 83 h. This did not follow the established experimental protocol of regular scans of the reference isotope, however, laser scans of ^{181}Hg and ^{180}Hg took place near the beginning and near the end of the experiment at 10 h, 13 h and 81 h and 1 h, 2 h, 78.5 h and 79.5 h respectively. These scans can therefore be additionally used to determine the stability of the experimental set-up and identify potential WM drifts or fluctuations during the period of the experiment. The full timeline of the experiment is presented in Figure A.1.

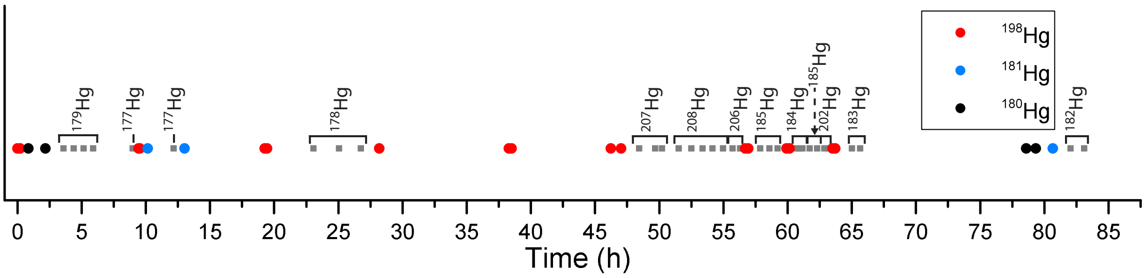

Figure A.1: The measurements are plotted according to the time at which they took place, the first scan is considered to have started at experiment hour 0. The ^{198}Hg reference scans are highlighted in red. Additionally, the ^{181}Hg and ^{180}Hg scans are highlighted in blue and black respectively.

The performance of the two WM can be compared by considering the spread of the CG frequencies extracted from the scans of ^{198}Hg, ^{181}Hg and ^{180}Hg about their respective average values. This is presented in Figure A.2.

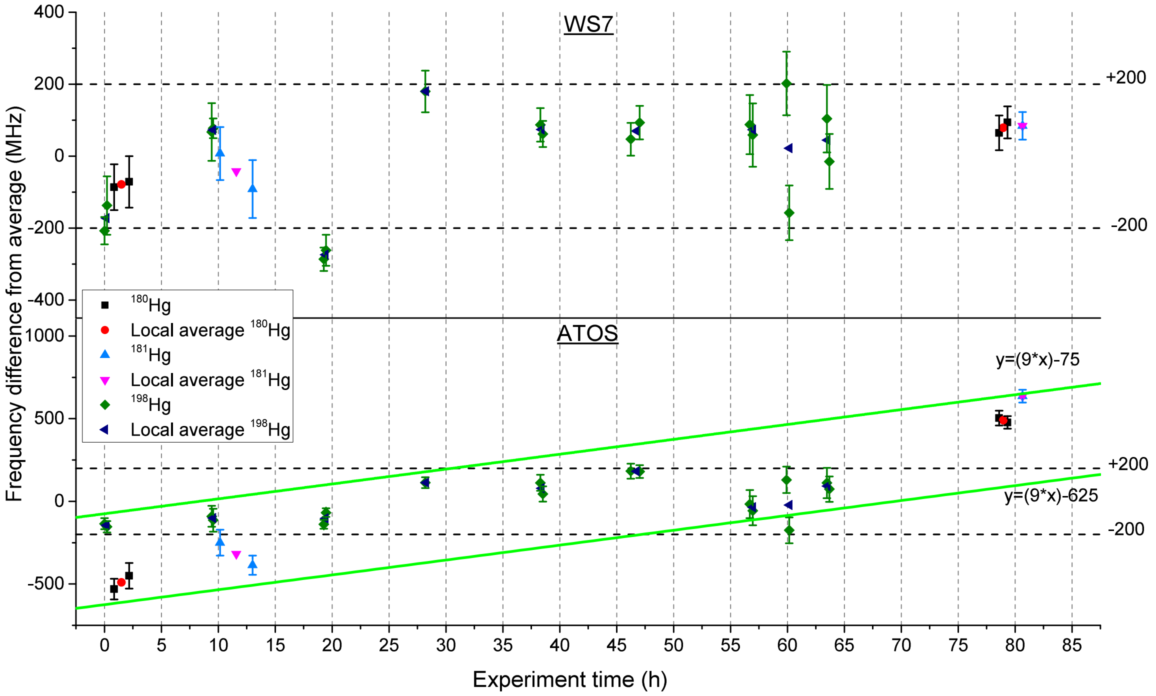

Figure A.2: The CG values extracted from the fits of the measurements of ^{198}Hg, ^{181}Hg, ^{180}Hg, using with the WS7 and ATOS WM, with respect to their respective average CG positions. The error bars correspond to the fit error on each data point. Dashed lines 200 MHz either side of the average for both the WS7 and ATOS WMs and diagonal green lines for the ATOS WM are included to aid comparison.

Figure A.2 depicts the reasonable agreement between the extracted centroid values of the measurements when using the frequencies recorded with the WS7 WM, particularly given the potential inaccuracy of the ^{198}Hg Faraday cup measurements due to the presence of multiple mercury isotopes in the ion beam. All of the ^{198}Hg CGs extracted from the scans where the MR-ToF MS was used to determine the ion rate lie within 200 MHz of the global average of the ^{198}Hg reference scan CGs.

The spread of the CGs when the recorded ion rates are associated with the ATOS WM measurements is also depicted in Figure A.2. There is reasonable agreement over the time frame of the experiment for the ^{198}Hg measurements. However, when the measurements of ^{180}Hg and ^{181}Hg are considered, a drift is revealed.

The drift in the ATOS WM is highlighted in Figure A.3. Where the difference in the recorded frequency between the WS7 and ATOS WMs is plotted against the frequency recorded by the WS7 WM for the scans of ^{180}Hg at experiment times 1 h and 78.5 h.

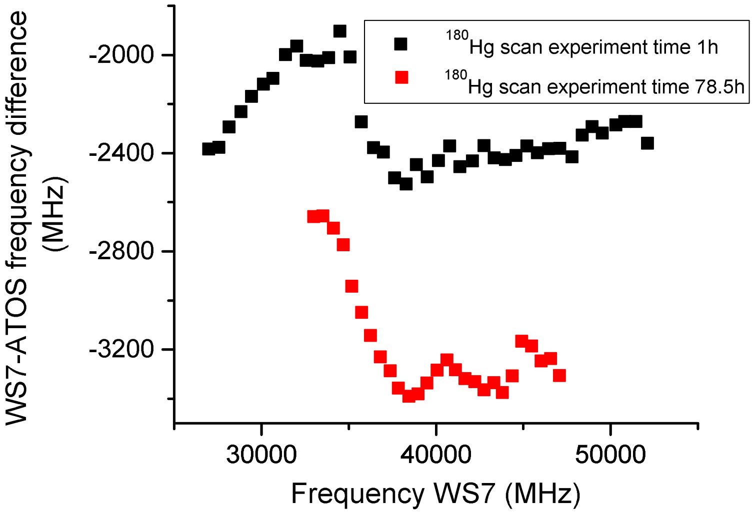

Figure A.3: The frequency measured by the WS7 WM during the hyperfine structure scans of ^{180}Hg at experiment times 1 h and 78.5 h, plotted against the difference between the frequencies measured by the WS7 WM and the ATOS WM. The scan durations were 24 minutes and 36 minutes for the scans at experiment times 1 h and 78.5 h respectively.

A significant (~1 GHz) shift, in addition to mid-scan fluctuations, can be observed in Figure A.3. The mid-scan variation in the frequency difference between the two WM could be attributed to the ATOS switching between measuring with three or four interferometers. Due to the drift over the period of the experiment and what is understood to be non-linearities in the measured wavelengths, the ATOS measurements were disregarded and only the laser frequencies measured with the WS7 WM were considered for the analysis.

A.2 Application of reference measurements

A reference value for the CG of ^{198}Hg is required, as all of the extracted isotope shifts are determined relative to this isotope. A global average of all of the reference values can be used, alternatively it is possible to interpolate between each reference measurement.

A.2.1 Determination of an averaged ^{198}Hg reference value

A comparison was made between using a global average of the ^{198}Hg reference measurements and using the average of just the ^{198}Hg reference measurements made using the MR-ToF MS to determine the ion rate. This was deemed necessary due to the already stated potential for an increased uncertainty in the CGs of the ^{198}Hg reference scans measured with a Faraday cup. The extracted CGs using the two methods are presented in Figure A.4.

The shift in the ^{198}Hg reference value, between considering the global average, or only the reference scans where the MR-ToF MS or the Faraday cup was used to determine the ion rate can be seen in Figure A.4. The difference between the ^{198}Hg MR-ToF MS average and the ^{198}Hg FC average is 99 MHz.

A.2.2 Interpolation between reference measurements

An alternative method for the determination of the ^{198}Hg experimental reference value is to interpolate between each pair of reference measurements R_a and R_b, in an attempt to correct for instabilities in the experimental set-up or drifts in the calibration of the WM. This approach results in a reference value R_S specific to each HFS scan. This was implemented using Equation A.1

$$R_S = R_a - \left(\left(\frac{R_a - R_b}{T^{R_b} - T^{R_a}} \right) \times (T^S - T^{R_a}) \right), \tag{A.1}$$

where T^{R_a} is the central time of the earlier pair of reference measurements, T^{R_b} is the central time of the later pair of reference measurements and T^S is the central time

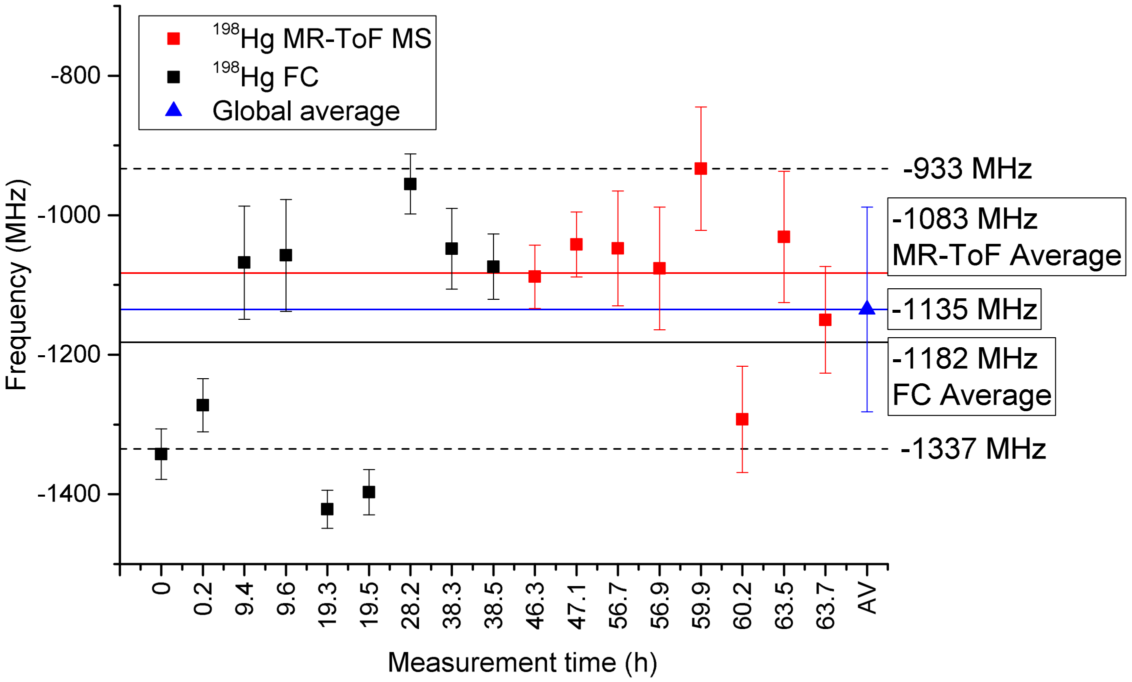

Figure A.4: The spread of the CGs of the ^{198}Hg reference measurements. The errors on the data points correspond only to the fit error. The blue line represents the average of all of the CGs, the red line is the average of the measurements where the MR-ToF MS was used for ion detection and the black line is the average of the measurements where the Faraday cup was used for ion detection. The error bars on the global average are the standard deviation of all the ^{198}Hg CGs, equal to 147 MHz. The dashed lines represent the maximum distance of the ^{198}Hg MR-ToF MS CGs from the global average of the measurements (202 MHz).

of the HFS scan. The standard deviation of the extracted centroids was compared to investigate the validity of interpolating between pairs of reference measurements. This is presented in Figure A.5.

From Figure A.5, the only significant reduction in standard deviation when interpolating between pairs of reference measurements is seen in the extracted CGs of ^{181}Hg. For ^{180}Hg, the reduction in standard deviation is the result of taking just the first two of the four scans, as the third and fourth scans were made following the final reference scans of ^{198}Hg, thus interpolation was not possible. There was an increase in the standard deviation for the extracted CGs of ^{178}Hg and ^{177}Hg. Interpolation between reference points actually raised the average standard deviation rather than lowered it, although only by 6 MHz.

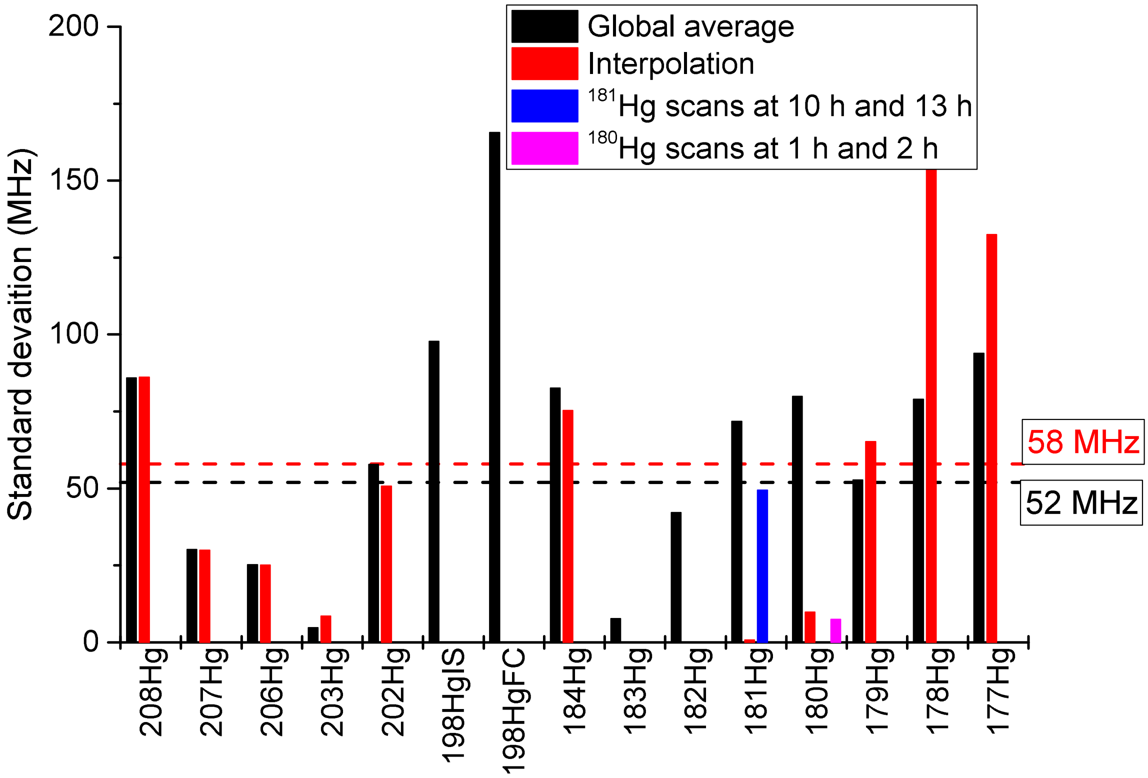

Figure A.5: The standard deviation of the extracted CGs for each isotope, using the frequencies from the WS7 WM and either a global average of the ^{198}Hg reference values or interpolating between each pair of reference measurements. The standard deviation for the first two scans of both ^{181}Hg and ^{180}Hg is additionally included as the later scans were made following the final ^{198}Hg measurement, thus interpolation was not possible. The red and black dashed lines show the average standard deviation when using the interpolated and global average reference values respectively (for the isotopes for which it is possible to compare).

A.2.3 Comparison with literature values

The validity of the different reference options was investigated by a comparison with literature values for isotope shifts compiled by Ulm et al. [7]. This is presented graphically in Figure A.6.

The resulting shift due to the application of the different reference options is between 50 and 200 MHz as presented in Figure A.6. Figure A.7, shows an average absolute shift from the literature values for the three reference options. It is clear that taking an overall global average results in the closest agreement with literature values. Interpolating between reference points is additionally problematic as there were no ^{198}Hg reference measurements for the final 20 hours of the experiment. Consequently, the global average of the ^{198}Hg measurements was chosen as the reference value for the isotope shifts.

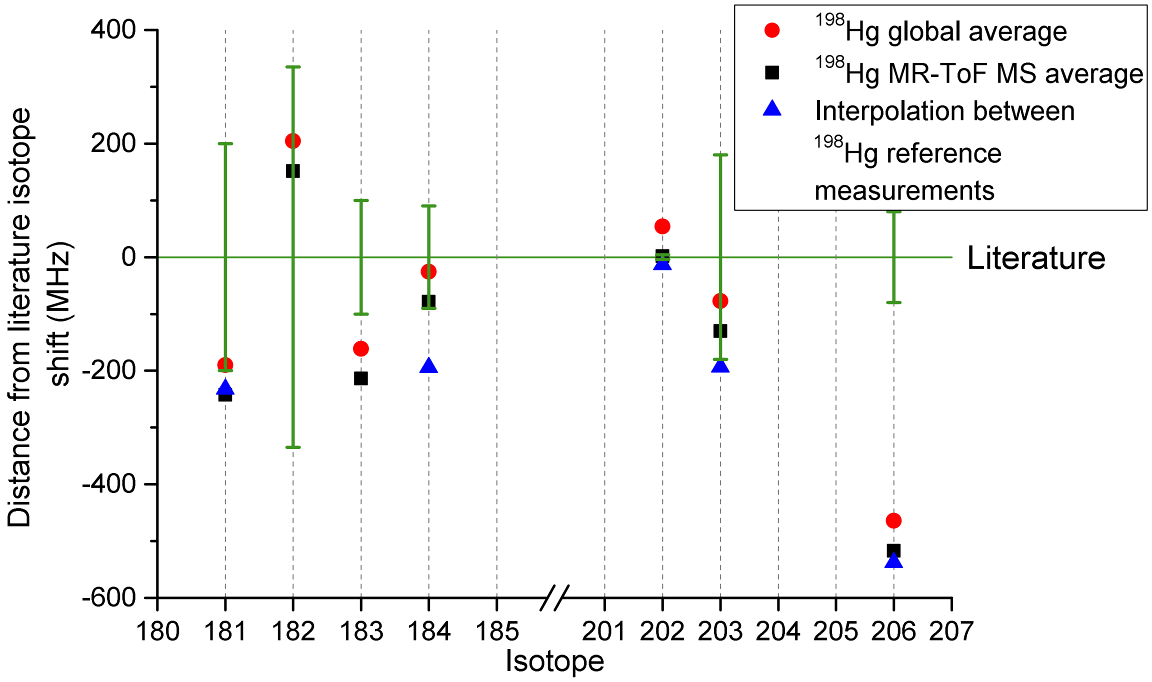

Figure A.6: The difference in the average CG of each isotope when using a global average of the ^{198}Hg reference values, an average of the ^{198}Hg measurements using the MR-ToF MS for ion counting or interpolating between each pair of reference measurements.

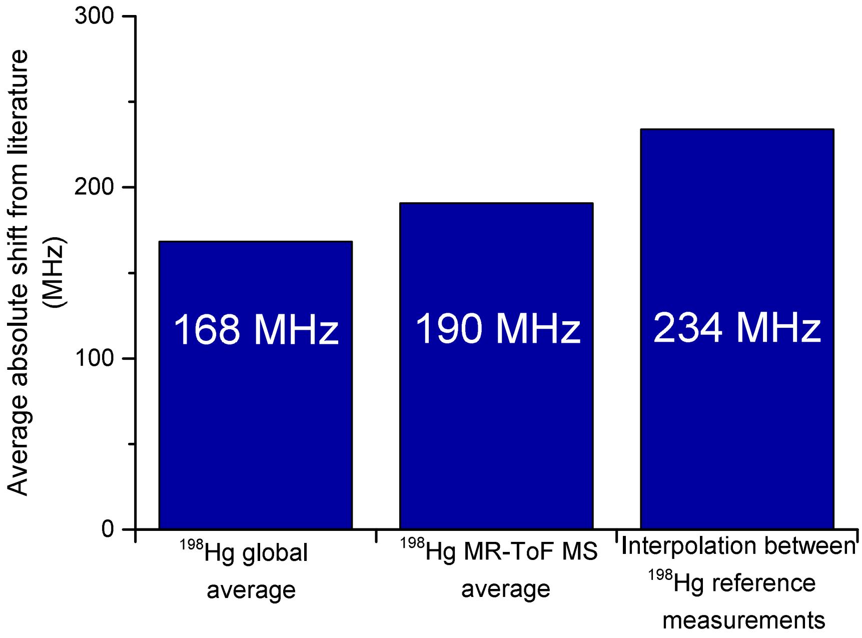

Figure A.7: The average absolute shift from the literature data compiled by [7], taking either a global average of the ^{198}Hg reference scans, an average of the ^{198}Hg measurements using the MR-ToF MS to determine the ion rate or interpolating between pairs of ^{198}Hg reference measurements. The isotopes considered in this comparison were ^{181}Hg, ^{182}Hg, ^{183}Hg, ^{184}Hg, ^{202}Hg, ^{203}Hg and ^{206}Hg.

A.2.4 Experimental uncertainty

The standard deviation of the ^{198}Hg reference measurements depicted in Figure A.4 is 147 MHz. A larger error contribution is reasonable due to the multiple mercury isotopes simultaneously present in the ion beam when the Faraday cup was used to determine the ion rate. This consideration is not relevant to the measurement of the isotopes where either time of flight mass spectrometry or decay spectroscopy was used to identify the signals. Consequently, taking the maximum deviation of the ^{198}Hg reference measurements using the MR-ToF MS to determine the ion rate is appropriate, corresponding to a contribution to the total uncertainty of 202 MHz. An additional contribution to the uncertainty of the extracted values is the standard deviation of the extracted CGs, presented in Figure A.5.

The sum of the spread of the ^{198}Hg reference measurements using the MR-ToF MS to determine the ion rate (202 MHz) and the standard deviation of the extracted CGs was used as the uncertainty of each isotope shift. An additional uncertainty was considered for ^{185g,m}Hg and ^{177}Hg, this is discussed in Sections A.3 and A.6 respectively.

A.3 Saturation effects and correction for laser power

For unsaturated atomic transitions, the ion rate scales linearly with laser power, consequently the laser power is recorded at each frequency step to enable correction in the post experiment analysis. Saturation of either the scanning laser power or the ion rate determination set-up, can result in a distortion of the measured hyperfine structure. If the atomic transition is saturated, then correcting for laser power incorrectly distorts the HFS. By calculating the expected relative intensities of the HFS components, it is possible to determine the validity of the laser power correction. The power of the scanning laser was measured in three locations as described in 5.3.1.

Saturation of the detector system used to measure the ion rate can also result in the distortion of the HFS. The MR-ToF MS detector is considered to be unsaturated when the recorded count rate is below 10 counts/shot. A shot is defined as a single filling of the MR-ToF MS device from the pre-injection radio frequency quadrupole cooler and buncher. The saturation limit was exceeded during a the majority of the laser scans, the maximum count/shot rate is summarized in Figures A.8 and A.9.

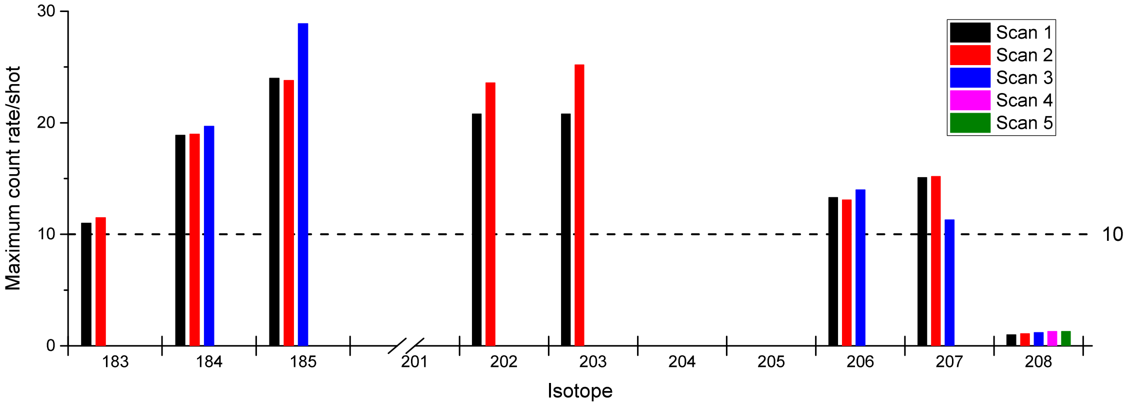

Figure A.8: The maximum count rate per shot for each of the HFS scans using the MR-ToF MS for to determine the laser frequency dependent ion rate. The saturation limit of the MR-ToF MS detector is indicated by a dashed line.

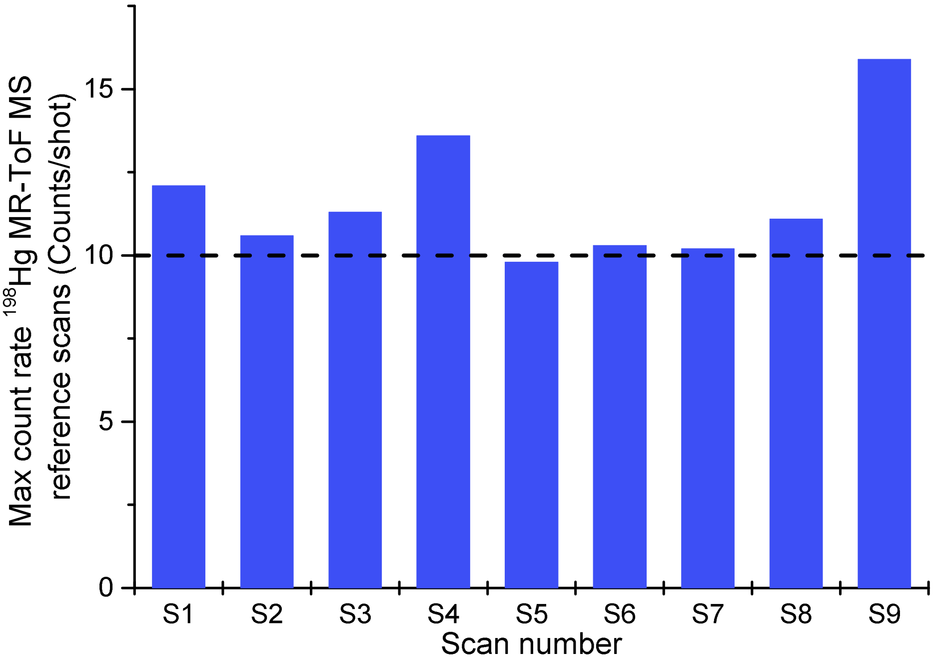

Figure A.9: The maximum count rate per shot for the ^{198}Hg reference measurements using the MR-ToF MS to determine the ion rate. The saturation limit of the MR-ToF MS detector is indicated by a dashed line.

Considering Figure A.8, the limit was exceeded for all scans other than those of ^{208}Hg. This must therefore be considered when evaluating the ratios of the hyperfine structure components. Figure A.9 demonstrates that the count rate was maintained at or around the saturation limit for the majority of the ^{198}Hg reference scans using the MR-ToF MS to determine the ion rate.

A.3.1 Correcting for laser power

The laser scans of ^{185g}Hg and ^{185m}Hg are the optimal test cases for the investigation of saturation effects, due to the multiple HFS components that cover the majority of the scanning range used in the experiment. Additionally, ^{185}Hg was the only isotope studied where there are overlapping HFS components, resulting from the F=3/2 level of ^{185g}Hg lying just 1.6 GHz from the F=15/2 level of ^{185m}Hg (depicted in Figure 3.1).

The effect of scaling the ion rates of the first scan of ^{185}Hg based on the scanning laser power measurements following frequency conversion is presented in Figure A.10. The measurements of the fundamental laser power were not considered as a reasonable option for power correction, due to the non-linear correlation of the efficiency of the frequency conversion process with laser power.

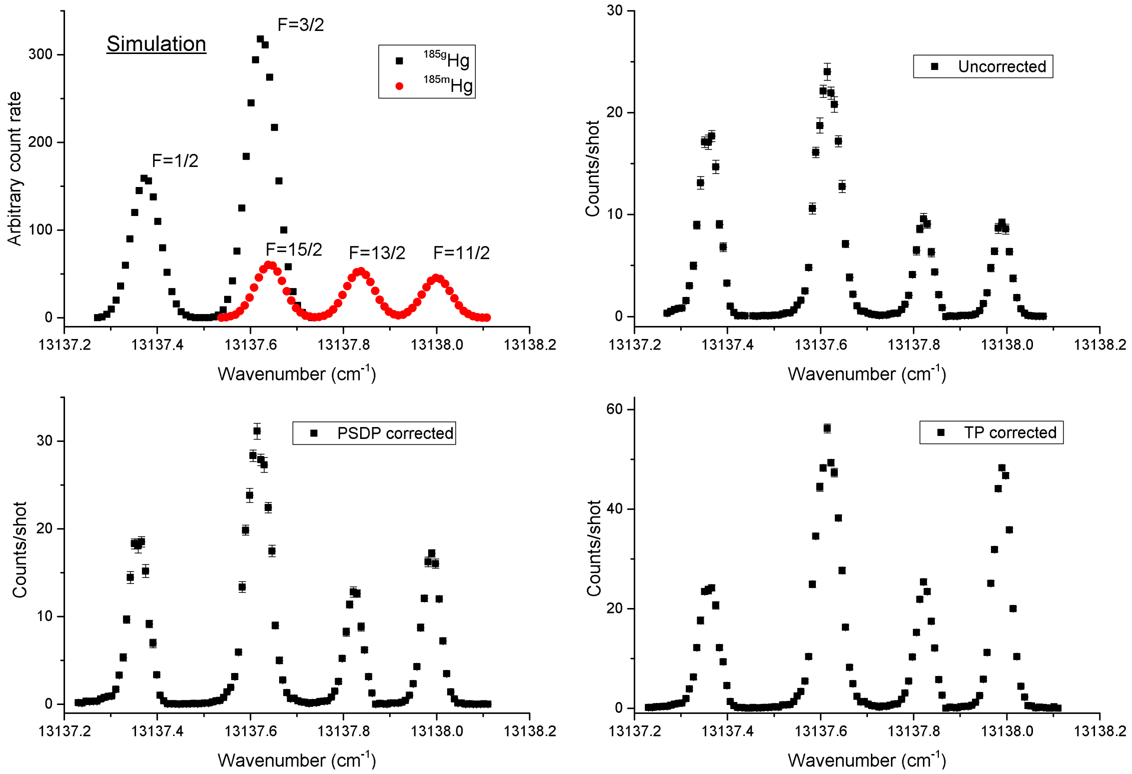

Figure A.10: The effects of correcting the first scan of ^{185g,m}Hg for the UV laser power monitored on the laser table (TP corrected) and the PSD in the reference area (PSDP corrected), compared the uncorrected and the simulated spectra.

Compared to the simulation shown in Figure A.10, the amplitudes of the resonances in the uncorrected spectra corresponding to the F=13/2 and F=11/2 levels of ^{185m}Hg appear reasonable with respect to one another. However, the amplitude of the resonance corresponding to the overlapped F=3/2 and F=15/2 components of the ground state and isomer is substantially less than expected. Correcting for laser power destroys the reasonable respective amplitudes of the resolved HFS of ^{185m}Hg, however, it does improve the amplitude of the overlapped components of the ground state and the isomer.

The overlapped resonances have an amplitude of 25 counts per shot, therefore it could be understood that the overlapped resonance is lower than expected due to a saturation of the MR-ToF MS detector. This will lead to an increase in the uncertainty of the extracted CGs, hyperfine A and B factors, as it hinders the possibility of a deconvolution of the overlapped resonances. The additional uncertainty was taken into account by the inclusion of a contribution of the fitting error into the uncertainty of ^{185g,m}Hg.

If all of the transitions were saturated by laser power across the scanning range, then it would correspond to a negligible effect from variations in the power of the scanning laser. This is observed in the respective amplitudes of the resonances corresponding to the F=13/2 and F=11/2 states of the isomer, suggesting a saturation of the transitions.

A.3.2 Comparison to literature values

In order to determine the validity of correcting the measurement points for variations in the power of the scanning laser, the measurements where the MR-ToF MS was used to determine the ion rate were corrected based on the recorded power at each measurement point. The CGs, hyperfine A and B factors were extracted and a global average of the MR-ToF MS ^{198}Hg measurements (also corrected for the laser power) was used as a reference. Figure A.11 presents a comparison of the data extracted from the power corrected laser scans, to the values extracted from the uncorrected scans and the literature values compiled by Ulm et al. [7].

It can be observed that there is a more pronounced shift in the extracted CGs when correcting for the laser power measured on the laser table, compared to correcting for the laser power measured on the PSD. Considering all of the isotopes, the uncorrected power appears to be systematically closer to the literature values. While based on the extracted A and B factors, there appears to be no significant effect of the power correction.

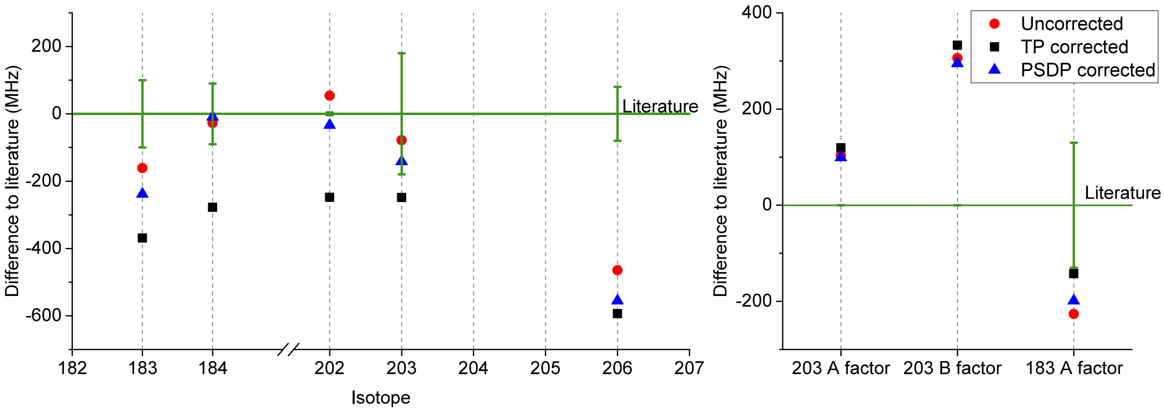

Figure A.11: Comparison of the extracted isotope shifts, hyperfine A and B factors, following correction based on the power of the scanning laser measured on the laser table (TP corrected) and in the reference area (PSDP corrected). Literature values were calculated from [7], the error bars correspond to the uncertainties reported in literature.

Determining the average absolute shift from literature values provides a further opportunity to investigate the efficacy of correcting for laser power variations. This is presented in Figure A.12.

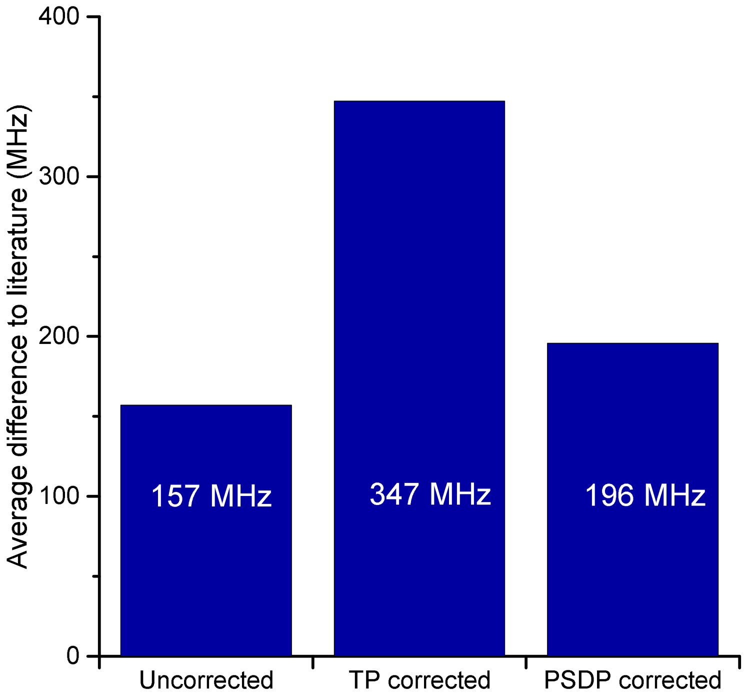

Figure A.12: The average absolute shift from literature data between the uncorrected data and correcting for variations in the power of the scanning laser over the scanning range. The laser power was measured on the laser table (TP corrected) and in the reference area (PSDP corrected). The isotopes considered for this comparison were ^{183}Hg, ^{184}Hg, ^{202}Hg, ^{203}Hg and ^{206}Hg.

The results presented in Figure A.12, confirm the conclusions based on Figure A.11, that the uncorrected data has the closest agreement with literature values. Consequently the uncorrected values were used for the final analysis.

A.4 Synchronization of the laser timing

The timing of the pulsed lasers must remain synchronised throughout the measurement. This is the consequence of the laser pulse length and atomic excitation lifetimes typically being of the order of 10 ns and a time difference between the temporally overlapped laser pulses of 100 µs. A loss of synchronization between the timing of the scanning laser and the other excitation steps results in a reduction in ionization efficiency unrelated to the laser frequency.

The pulse timing synchronization of the scanning laser was monitored throughout the experiment and stabilized with respect to the master clock. The only laser scan where this method failed was the first measurement of ^{179}Hg, where the magnitude of an instability in the scanning laser was too great to be fully compensated by the timing stabilization. The desynchronization of the first excitation step is presented in Figure A.13.

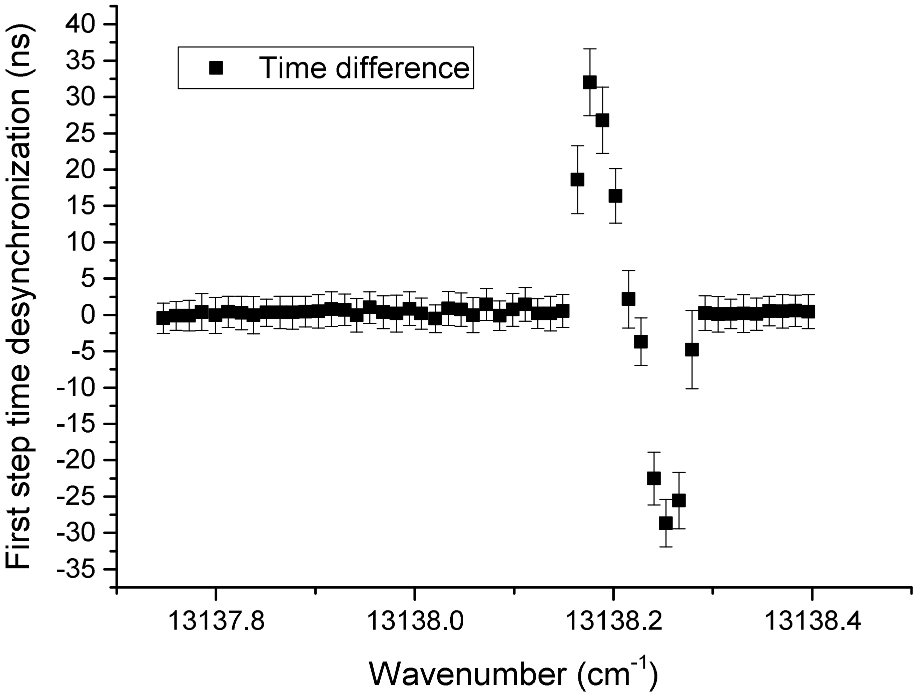

Figure A.13: The de-synchronization of the scanning laser with respect to the laser pulses of the other excitation steps during the first HFS scan of ^{179}Hg.

The response time of the stabilization program was decreased to prevent a repetition of the problem in the subsequent three scans of ^{179}Hg. The fluctuations of up to ±30 ns are likely to have adversely affected the laser scan, therefore the first scan was not considered in the final results of ^{179}Hg.

A.5 Proton driver beam stability

The ion rate is directly related to the proton current impinging on the ISOLDE target. Consequently fluctuations in the proton current or the number of protons per pulse during a laser scan, could result in fluctuations in the ion rate unrelated to the frequency of the scanning laser. The current of the proton beam impinging on the target was stable (variations <10%) during all of the laser scans discussed in this work, other than for the scans of ^{184}Hg, where there were significant variations in the average number of protons per pulse. This is presented in Figure A.14.

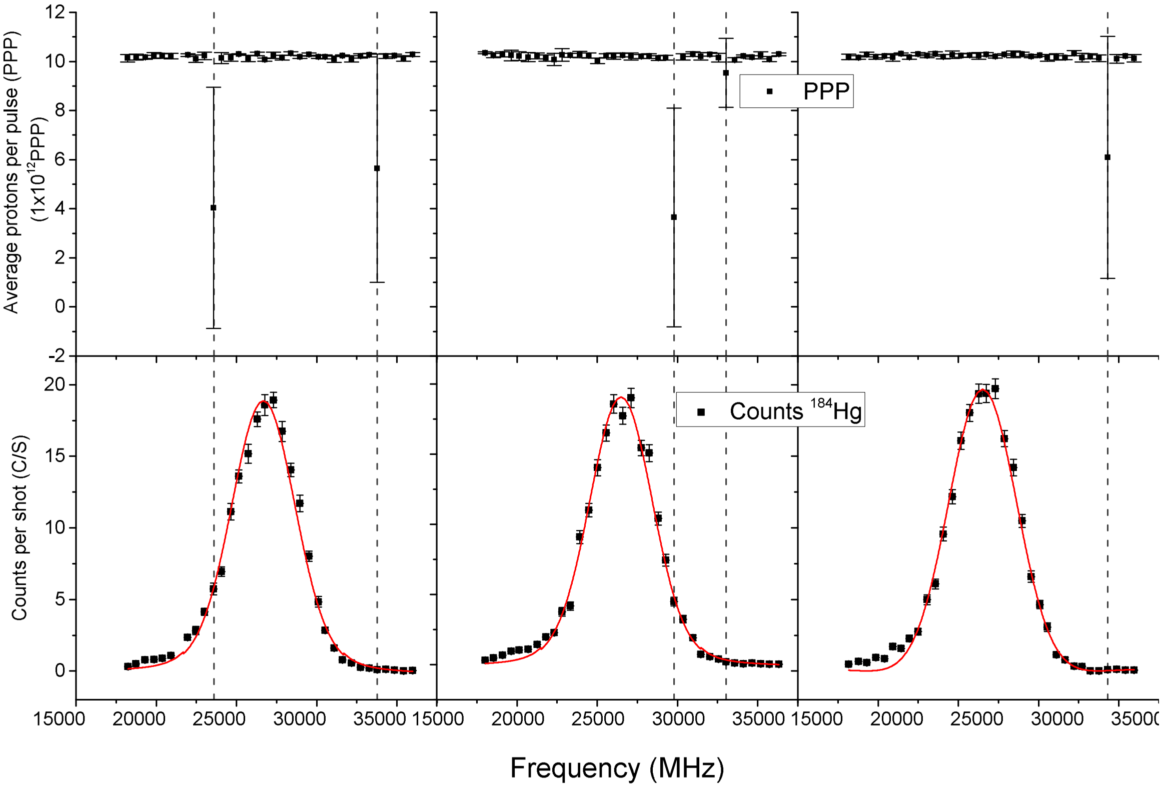

Figure A.14: Instability in the average number of protons per pulse during the HFS scans of ^{184}Hg. The error bars represent the standard deviation of the number of protons per pulse for the five proton pulses incident during the period of each measurement point.

Considering the scans presented in Figure A.14, the instability in the number of the protons per pulse does not appear to have affected the HFS measurements. This could be understood to be the result of the lead target being in a non-liquid state during this period of the experiment. The target heating was reduced due to a requirement to cool the target by the ISOLDE target group. This arose from concerns about ^{208}Pb ion beams in excess of 1 nA coating the extraction electrode (such limits have since been relaxed to <50 nA). Considering Figure A.14, there appears to have been a significantly longer release time than the 10 s reported for mercury from a molten lead target in 1997 [125]. While the cold target aided the experiment for the scans of ^{184}Hg (with the laser related ion rate insensitive to fluctuations in the number of protons per pulse) it severely hampered the measurement of the more exotic mercury isotopes.

A.6 Weighting of extracted data

The number of measurement points per scan and the count rate per measurement point, influences the precision of the measurement. Weighting the extracted CGs, hyperfine A and hyperfine B factors is required where there are significant variations in the number of measurement points or the count rates between scans of the same isotope. There were five successful scans of ^{208}Hg, the first two had 50% of the number of measurement points per scan compared to the final three. Consequently, a weighting was applied for the average of the extracted CGs and a weighted standard deviation determined for the isotope specific contribution to the experimental uncertainty for ^{208}Hg. The spread of the CGs of ^{208}Hg are presented in Figure A.15.

In the scans of ^{177}Hg, a maximum usable count rate of 0.02 counts per second resulted in between two and six counts in the peaks of the resonances for the two laser scans of ^{177}Hg. The standard deviation of the two extracted CGs is 94 MHz. However, to consider this as the isotope specific uncertainty would underestimate the uncertainty related to the fitting error, due to the number of counts per HFS component. The fit error was therefore considered, it was also used to weight the centroid contribution to the average CG of ^{177}Hg. This is presented in Figure A.16. The average of the extracted hyperfine A factor from the ^{177}Hg scans was weighted in the same manner.

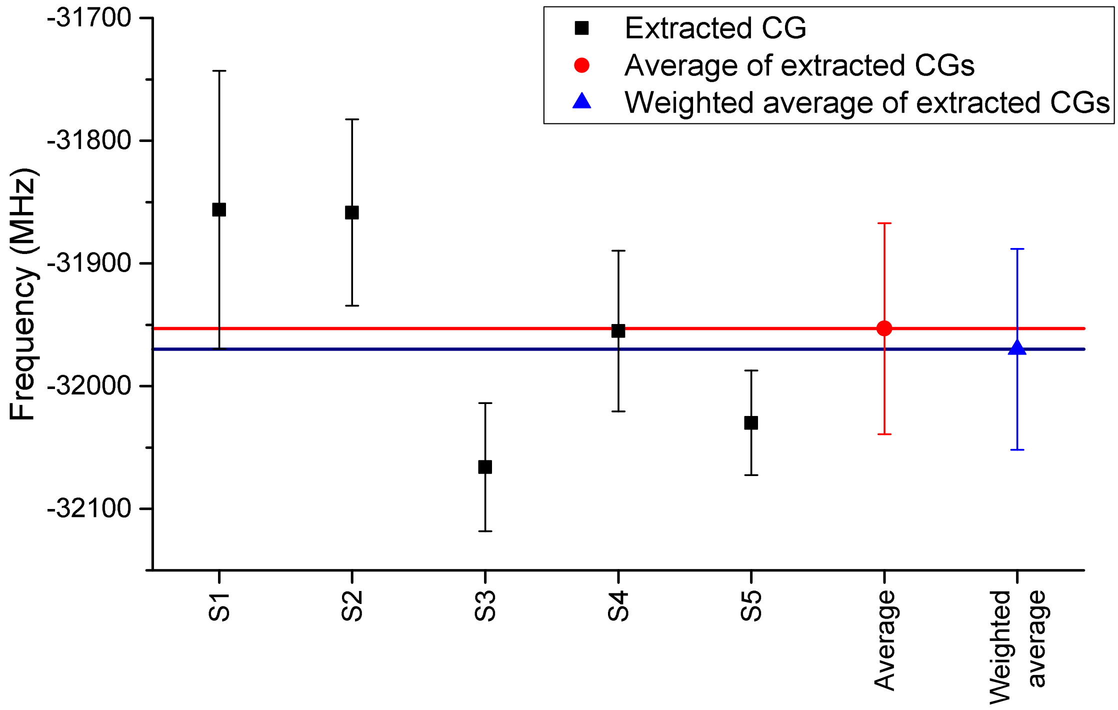

Figure A.15: The extracted CGs of ^{208}Hg, the average of the CGs is highlighted in red and the weighted average considering the number of measurement points per scan is highlighted in blue.

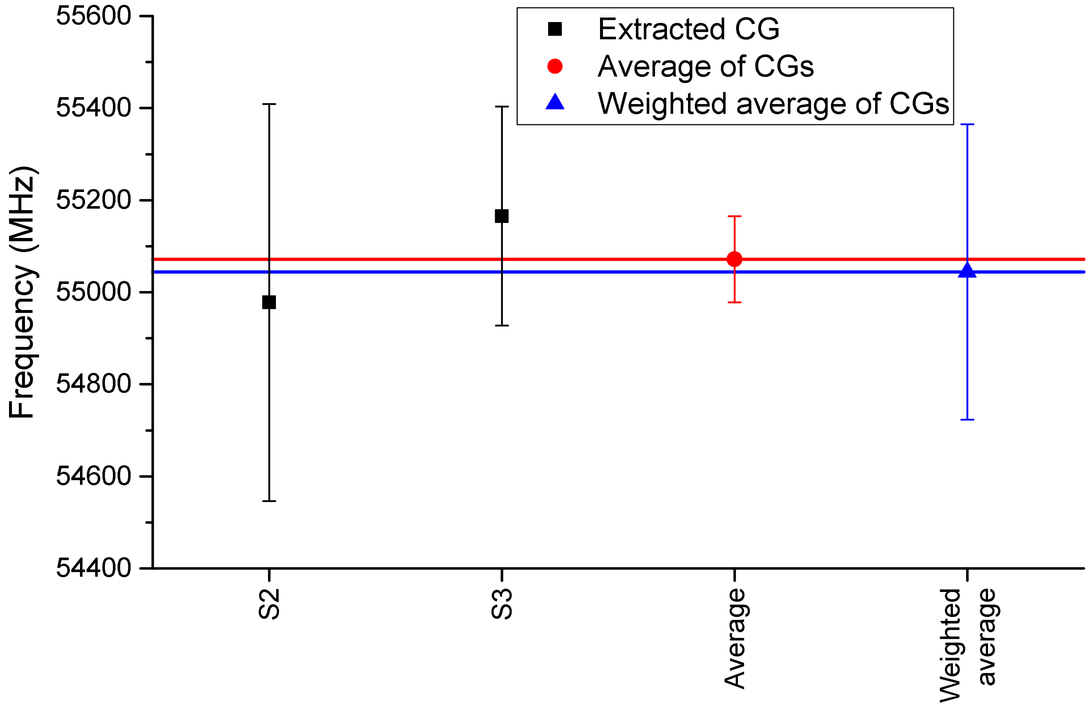

Figure A.16: The dominance of the fit errors over the standard deviation of the two extracted CGs of ^{177}Hg.